INTERFACIAL MODIFICATION OF NANOPARTICLES FOR BIOMEDICAL APPLICATIONS

By

Santosh Lala Gawali

CHEM01201504019

Bhabha Atomic Research Centre, Mumbai

A thesis submitted to the

Board of Studies in Chemical Sciences

In partial fulfillment of requirements

for the Degree of

DOCTOR OF PHILOSOPHY

of

HOMI BHABHA NATIONAL INSTITUTE

October, 2019

Homi Bhabha National Institute

Recommendations of the Viva Voce Committee

As members of the Viva Voce Committee, we certify that we have read the dissertation prepared by **Santosh Lala Gawali** entitled "**Interfacial Modification of Nanoparticles for Biomedical Applications**" and recommend that it may be accepted as fulfilling the thesis requirement for the award of Degree of Doctor of Philosophy.

Chairman - Prof. K. I. Priyadarsini	K. Indira Priyadarsini	**Date:** 12.8.2020
Guide / Convener – Prof. P. A. Hassan		**Date:** 12.08.2020
Examiner - Prof. Jayesh R. Bellare		**Date:** 12-Aug-2020
Member 1– Prof. S. K. Ghosh		**Date:** 12/8/2020.
Member 2– Prof. V. K. Aswal		**Date:** 12-08-2020
Member 3- Prof. S. N. Sawant	SNSawant	**Date:** 12/8/2020
Technology Adviser- Dr. K. C. Barick		**Date:** 12-08-2020

Final approval and acceptance of this thesis is contingent upon the candidate's submission of the final copies of the thesis to HBNI.

I hereby certify that I have read this thesis prepared under my direction and recommend that it may be accepted as fulfilling the thesis requirement.

Date: 12.08.2020

Place: Mumbai

(P. A. Hassan)
Guide

STATEMENT BY AUTHOR

This dissertation has been submitted in partial fulfillment of requirements for an advanced degree at Homi Bhabha National Institute (HBNI) and is deposited in the Library to be made available to borrowers under rules of the HBNI.

Brief quotations from this dissertation are allowable without special permission, provided that accurate acknowledgment of source is made. Requests for permission for extended quotation from or reproduction of this manuscript in whole or in part may be granted by the Competent Authority of HBNI when in his or her judgment the proposed use of the material is in the interests of scholarship. In all other instances, however, permission must be obtained from the author.

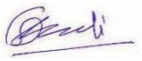

Santosh L. Gawali

DECLARATION

I, hereby declare that the investigation presented in the thesis has been carried out by me. The work is original and has not been submitted earlier as a whole or in part for a degree/diploma at this or any other Institution / University.

Santosh L. Gawali

List of Publications

Publications arising from the thesis

1. "Altering the X-ray Scattering Contrast of Triton X-100 Micelles and Its Trapping in a Supercooled Solvent", **Santosh L. Gawali,** K. C. Barick, V. K. Aswal, M. Basu, and P. A. Hassan, *J. Phys. Chem. B,* **2020**, *124*, 3418–3427.

2. "Discerning the Structure Factor of Charged Micelles in Water and Supercooled Solvent by Contrast Variation X-ray Scattering", **Santosh L. Gawali,** M. Zhang, S. Kumar, D. Ray, M. Basu, V. K. Aswal, D. Danino, and P. A. Hassan, *Langmuir*, **2019**, *35*, 9867–9877.

3. "pH-Labile Magnetic Nanocarriers for Intracellular Drug Delivery to Tumor Cells", **Santosh L. Gawali,** K. C. Barick, N. Shetake, V. Rajan, B. Pandey, N. N. Kumar, K.I. Priyadarsini, and P. A. Hassan, *ACS Omega*, **2019**, *4*, 11728–11738.

4. "Dynamically Arrested Micelles in a Supercooled Sugar-Urea Melt", **Santosh L. Gawali,** M. Zhang, S. Kumar, V. K. Aswal, D. Danino, and P. A. Hassan, *Communications Chemistry*, **2018,** *1*, 33.

5. "Effect of Sugar Alcohol on Colloidal Stabilization of Magnetic Nanoparticles for Hyperthermia and Drug Delivery Applications", **Santosh L. Gawali**, B. K. Barick, K. C. Barick, and P. A. Hassan, *J. Alloy. Compd.*, **2017**, *725*, 800–806.

6. "Jammed Micelles in High Solid Content Sucrose Solutions", **Santosh L**. **Gawali,** S. Kumar, and P. A. Hassan, *J. Nanofluids*, **2017**, *6*, 596–602.

7. "Immobilization of protein on Fe_3O_4 nanoparticles for magnetic hyperthermia application". Santosh L. Gawali, S. B. Shelar, K. C. Barick, J. Gupta, and P. A. Hassan, (***Manuscript submitted***).

Invited review articles

1. "Directing Amphiphilic Self Assembly: From Microstructure Control to Interfacial Engineering", P. A. Hassan and **Santosh L. Gawali**, *Langmuir*, **2019**, *35(30)*, 9635–9646.

2. “Surface Engineering of Iron Oxide Nanoparticles for Cancer Therapy”, **Santosh L. Gawali,** B. Dutta, K. C. Barick, and P. A. Hassan, *Biomed Res. J.,* **2017**, *4(1)*, 49–66.

Other publications from collaborative research

1. “Phenylseleno N-acetyl α-amino acids conjugated magnetic nanoparticles: Synthesis, characterization and radical scavenging ability”, K. C. Barick, B. Dutta, **Santosh L. Gawali**, P. Phadnis, K. I. Priyadarsini, V. Jain, and P. A. Hassan, *Chemistry Letters,* **2020**, **(Accepted).**

2. “pH dependent aggregation and conformation changes of rituximab using SAXS and its comparison with the standard regulatory approach of biophysical characterization”, A. Narvekar, **Santosh L. Gawali**, P. A. Hassan, R. Jain, and P. Dandekar, *Int. J. Biol. Macromol*., **2020**, *164*, 3084-3097.

3. “An investigation of morphological, microscopic dynamics, fluidity, and physicochemical variations in Cu-decorated metallosomes with cholesterol”, B. Kaur, G. Kaur, G. R.Chaudhary, V. K. Sharma, H. Srinivasan, S. Mitra, A. Sharma, **Santosh L.Gawali**, and P. A. Hassan, *J. Mol. Liq.*, **2020**, *318,* 114034.

4. “Electrostatically bound lanreotide peptide–gold nanoparticle conjugates for enhanced uptake in SSTR2-positive cancer cells”, S. B. Shelar, **Santosh L. Gawali,** K. C. Barick, A. Kunwar, A. Mohan, I. K. Priyadarsini, and P. A. Hassan, *Mater. Sci. Eng. C*, **2020,** *117*, 111272**.**

5. “High antimicrobial photodynamic activity of photosensitizer encapsulated dual-functional metallocatanionic vesicles against drug-resistant bacteria S. aureus”, B. Sharma, G. Kaur, G. R. Chaudhary, **Santosh L. Gawali**, and P. A. Hassan, *Biomater. Sci.,* **2020,** *8*, 2905–2920.

6. “Thermo-switchable de novo ionogel as metal absorbing and curcumin loaded smart bandage material”, M. Kuddushi, N. K. Patel, **Santosh L. Gawali**, J. P. Mata, H. Montes-Campos, L. M. Varela, P. A. Hassan, and N. I. Malek, *J. Mol. Liq.,* **2020,** *306*, 112952.

7. “Fluorescent MoS2 Quantum dot-DNA Nanocomposite Hydrogels for Organic Light-Emitting Diodes”, P. K. Pandey, H. Ulla, M. N. Satyanarayan, K. Rawat, A. Gaur, **Santosh L. Gawali**, P. A. Hassan, and H. B. Bohidar, *ACS Appl. Nano Mater.,* **2020,** *3*, 1289–1297.

8. “A Study of Synthesis, Characterization and Metalloplex Formation Ability of Cetylpyridinium Chloride Based Metallosomes”. G. Kaur, B. Kaur, P. Garg, G. R. Chaudhary, **Santosh L. Gawali**, and P. A. Hassan, *J. Mol. Liq.*, **2020**, *300*, 112326.

9. “Symmetrical Dialkylsulphoxides in Ionic Liquid as Extractants for Uranyl Ion: Extraction Efficacy and Aggregation Behavior”, M. S. Murali, **Santosh L. Gawali,** P. A. Hassan and R. B. Gujar, *J. Radioanal. Nucl. Chem.,* **2019**, *320*, 577–585.

10. “Thermodynamics of Mixing of TEHDGA with Isodecanol in Dodecane: Effect of Equilibration with Aqueous Nitric Acid”, M. Basu, P. Sinharoy, J. Ramkumar, **Santosh L. Gawali,** B. Dutta, and J. N. Sharma, *J. Solution Chem.,* **2019**, *48*, 1318–1335.

11. “Structural and SAXS Analysis of Protein Folding/unfolding with Cationic Single Chain Metallosurfactants”, P. Garg, G. Kaur, G. R. Chaudhary, **Santosh L. Gawali,** and P. A. Hassan, *J. Mol. Liq.*, **2018**, *271*, 157–165.

12. “Investigating the Structural Integrity of Bovine Serum Albumin in Presence of Newly Synthesized Metallosurfactants”, P. Garg, G. Kaur, G. R. Chaudhary, S. Kaur, **Santosh L. Gawali,** and P. A. Hassan, *Colloids Surf. B Biointerfaces,* **2018**, *164*, 116–124.

13. “PEG Mediated Shape-Selective Synthesis of Cubic Fe_3O_4 Nanoparticles for Cancer Therapeutics”, B. Dutta, N. G. Shetake, **Santosh L. Gawali**, B. K. Barick, K. C. Barick, P. D. Babu, B. N. Pandey, K. I. Priyadarsini, and P. A. Hassan, *J. Alloy. Compd.,* **2018**, *737*, 347–355.

14. “Cationic Double Chained Metallosurfactants: Synthesis, Aggregation, Cytotoxicity, Antimicrobial Activity and Their Impact on Structure of Bovine Serum Albumin”, G. Kaur, P. Garg, B. Kaur, G. R. Chaudhary, S. Kumar, N Dilbaghi, P. A. Hassan, and **Santosh L. Gawali**, *Soft Matter***, 2018**, *14*, 5306–5318.

15. "Fabrication of Metalosomes (Metal Containing Cationic Liposomes) Using Single Chain Surfactant as Precursor via Formation of Inorganic Organic Hybrids", P. Garg, G. Kaur, G. R. Chaudhary, **Santosh L. Gawali**, and P. A. Hassan, *Phys. Chem. Chem. Phys.,* **2017**, *19*, 25764–25773.

16. "Pluronic Stabilized Fe_3O_4 Magnetic Nanoparticles for Intracellular Delivery of Curcumin", K. C. Barick, Ekta*****, **Santosh L. Gawali***, A. Sarkar, A. Kunwar, K. I. Priyadarsini, and P. A. Hassan, *RSC Adv*., **2016**, *6*, 98674–98681. (*= Equal contribution)

Journal Cover Art

1. "Surface Modification and Nanostructure Formation Using Self-Assembly", *Langmuir,* **2019,** *35 (30).*

Conference Proceedings

1. "Triton X-100 functionalized Fe_3O_4 nanoparticles for biomedical applications", **Santosh L. Gawali***,* D. P. Madan*,* K. C. Barick*,* R. Somani*,* and P. A. Hassan, *AIP Conference Proceedings*, **2018**, *1942*, 040020.

2. "Surface decorated Fe_3O_4 nanoparticles for magnetic hyperthermia", **Santosh L. Gawali**, K. C. Barick and P. A. Hassan, *AIP Conference Proceedings,* **2017**, *1832*, 050101.

Book Chapters

1. "Synthesis and Surface Functionalization of Nanostructured Biomaterials", **Santosh L. Gawali**, B. Dutta, J. Gupta, P. A. Hassan, and K. C. Barick, in Synthesis Strategies for Advanced Materials, Eds: A. K. Tyagi and R. S. Ningthoujam, *Springer Publisher*. **(Accepted)**

2. "Advances in Amphiphilic Assemblies and its Immobilization in Room Temperature Supercooled Matrices", **Santosh L. Gawali,** S. B. Shelar, S. D. Kulkarni, and P. A. Hassan, in Immobilization Strategies: Biomedical, Bioengineering and Environmental Applications, Eds: A. Tripathi and J. S. Melo, *Springer-Nature, Singapore Pte Ltd*. **2020. (*In Press*)**

Patent

1. "Liposomes Entrapping Hydrophobic or Hydrophilic Drugs and a Process for Preparing the Same Using Supercooled Micelle and Emulsion", **Santosh L. Gawali**, K. C. Barick, K. I. Priyadarsini and P. A. Hassan, [File sent for approval of TT&CD BARC, Indian patent].

Oral/Poster Presentation in Conferences

Oral Presentations

1. "Altering the X-ray Scattering Contrast of Core-shell Micelles and Its Trapping in a Supercooled Solvent", *Mumbai-Pune Soft Matter Meet,* **Oct-2018**, NCL, Pune, India.

2. "Arresting self-assembly of surfactants in supercooled sugar-urea melts", *Mumbai-Pune Soft Matter Meet,* **Feb-2018**, IITB, Mumbai, India.

3. "Surface functionalization of Fe_3O_4 nanoparticles for biomedical applications", *Research Scholar Meet,* **2016**, Jai Hind College, Mumbai, India.

Poster Presentations

1. "Melting, Micelle Formation and Supercooling of Surfactant Crystals in a Water-free Matrix", **Santosh L. Gawali**, M. Pardeshi, R. V. Jayarama, and P. A. Hassan, *22nd Workshop & Symposium on Thermal Analysis* (**THERMANS-2020**), BARC, Mumbai, India.

2. "Contrast Variation X-ray Scattering of Triton X-100 Micelles in a Room Temperature Supercooled Melts", **Santosh L. Gawali** and P. A. Hassan, *International SAXS Symposium 2019* (**SAXSexcites: 2019**), Graz University of Technology, Graz, Austria.

3. "Ascorbic Acid Functionalized Fe_3O_4 Nanoparticles for Chemotherapeutic Application", **Santosh L. Gawali**, K. C. Barick, and P. A. Hassan, *National Symposium on Materials in Healthcare,* **2018**, GITAM University, Hyderabad, India ***(Best poster award)*****.**

4. "Covalent Conjugation of Organoselenium Compounds on the Surface of Fe_3O_4 Nanoparticles", **Santosh L. Gawali**, K. C. Barick, B. Dutta, P. P. Phadnis, V. K. Jain, K. I. Priyadarsini and P. A. Hassan, *Symposium on Selenium Chemistry and Biology* **(SSCB-2017)**, BARC Mumbai, India ***(Best poster award)***.

5. "Triton X-100 Functionalized Fe_3O_4 Nanoparticles for Biomedical Applications", ***Santosh L. Gawali****, D. P. Madan, K. C. Barick, R. Somani, and P. A. Hassan, DAE Solid State Physics Symposium* **(DAE-SSPS-2017),** BARC, Mumbai, India.

6. "Water-free Micelles in a Supercooled Liquid Formed by Glucose-Urea Mixture", **Santosh L. Gawali** and P. A. Hassan, **Compflu-2017**, IIT Madras, Chennai, India.

7. "Surface Engineered Magnetic Nanoparticles for Hyperthermia Therapy", **Santosh L. Gawali**, K. C. Barick, and P. A. Hassan, *DAE Solid State Physics Symposium 2016***(DAE-SSPS: 2016),** KIIT University, Bhubaneswar, India.

8. "Protein Conjugated Glutaric Acid Functionalized Fe_3O_4 Magnetic Nanoparticles for Hyperthermia Therapy", **Santosh L. Gawali**, K. C. Barick, and P. A. Hassan, *6thInterdisciplinary Symposium in Materials Chemistry* **(ISMC-2016)**, BARC, Mumbai, India.

9. "Vitamin-C Functionalized Fe_3O_4 Nanoparticles for Cancer Therapeutics Application", **Santosh L. Gawali**, K. C. Barick, and P. A. Hassan, *2nd International Conference on Material Science and Technology* **(ICMST-2016),** St. Thomas College, Palai, Kerala, India ***(Best poster award)***.

10. "Ascorbic Acid Functionalized Fe_3O_4 Nanoparticles for Delivery of Anticancer Drug", **Santosh L. Gawali**, K. C. Barick, and P. A. Hassan, **NMIMS-2015**, Mitibai College Santacruz, Mumbai, India.

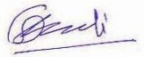

Santosh L. Gawali

DEDICATED

TO

"NATURE"

ACKNOWLEDGEMENTS

First of all, I would like to express my sincere gratitude to my research supervisor Prof. Puthusserickal A. Hassan, Head, Nanotherapeutics and Biosensors Section, Chemistry Division, Bhabha Atomic Research Centre, Mumbai, for his active involvement, support, encouragement, caring, motivation, constructive criticism and valuable advices during my Ph.D. period. Without him, this thesis would not have materialized.

I would also like to thank Dr. K. C. Barick, Chemistry Division BARC, for helpful guidance throughout my research work, giving me a deep insight on certain topics, and constant support when I needed most in times of low and high that I experienced throughout. I put on record my appreciation to Dr. K. Indira Priyadarsini, Former Head, Chemistry Division, BARC for her constructive suggestions and encouragement during the course of this thesis. Thanks, are also due to Dr. V. K. Aswal, Solid State Physics Division, BARC for his constant support and guidance in performing Small Angle Neutron Scattering (SANS) experiments at BARC. Special thanks to Dr. Sugam Kumar, and Dr. Debes Ray for constructive discussions on SANS. I gratefully acknowledge the support from Prof. Dganit Danino and Dr. Mingming Zhang, Technion, Israel for their support in TEM experiments. Thanks, are also due to Dr. Shilpa Sawant, Chemistry Division for her constant encouragement and support. I also thank Dr. S. K. Ghosh, Head, Food Technology Division for his constructive comments.

I owe a great many thanks to all fellow colleagues in the lab, especially Dr. C. A. Betty, Dr. M. Basu, Dr. Gunjan Verma, Dr. R. Ganguly, Dr. S. Choudhury, Dr. C. A. Amarnath, Dr. S. B. Shelar, Mr. Bijaideep Dutta, and Ms. Pallavi for their constant

support during the period of my research. The inspirations, learning and help received from them in the lab are beyond words. I would like to express a deep sense of gratitude to Dr. Suman Rana and Dr. Bhawana Thakur, our earlier research scholars in the lab, for their help, advice, and teaching during the initial periods of my research. Their enthusiasm and zeal have been a major source of inspiration to me throughout my work.

I take the opportunity to thank all my friends, fellow research scholars and other staff members in Chemistry Group, BARC who directly or indirectly helped me in achieving my goals. It has been a great privilege to work in a multi-disciplinary organization like BARC where I could meet people with a broad spectrum of technical expertise. At some point or other, I had interacted with many of them and it has been a wonderful experience throughout.

Last but not the least, I would like to thank my parents, son, wife, sister, brother, and all the family members for being supportive in my endeavor and extending encouragement throughout the work. Without their support, patience, understanding, caring, and encouragement this would not have been easy.

Santosh L. Gawali

CONTENTS

LIST OF FIGURES

LIST OF TABLES

CHAPTER 7

SUMMARY AND FUTURE PERSPECTIVES

Summary

In summary, this thesis discussed a few novel surface functionalization strategies that can be adopted for commercial implementation of magnetic nanoparticles in cancer therapy. Also, a new methodology for the production of surface charge tuned organic nanocarriers were developed for effective drug encapsulation and delivery.

The effects of different biocompatible ingredients such as sugar alcohols and ascorbic acid as surface passivation agents for Fe_3O_4 MNPs were investigated. The effects of these coating materials on particle size, surface potential and colloidal stability were successfully investigated. For that Fe_3O_4 MNPs were synthesized through co-precipitation of Fe^{+2} and Fe^{3+} ions in basic medium followed by in-situ coating. XRD and TEM analysis revealed the formation of a highly crystalline spinel nanostructure of Fe_3O_4 MNPs with an average crystallite size of 10 nm. The surface passivation of these MNPs was evident from FTIR spectra, TGA, and zeta-potential measurements. Light scattering measurements indicate that such approaches provide nano-formulations with good colloidal stability and pH-dependent charge reversal behavior. This offers an efficient route for electrostatic binding of drugs like doxorubicin hydrochloride and protein resistant characteristics in the physiological medium. The loading efficiency of the drug as well as their pH-triggered release is strongly dependent on the drug to particle ratio and the coating agent. These functionalized MNPs showed a high loading affinity for DOX and their pH-dependent sustained release, which makes them suitable for drug delivery. In addition, the functionalized exterior of these MNPs having free hydroxyl groups can provide the available sites for conjugation of various bioactive molecules for a variety of

biomedical applications.

Further, covalent immobilization of anticancer drug DOX to Fe_3O_4 MNPs were carried out using pH-labile linkages for sustained delivery of anticancer drug DOX to the tumor cells with minimal side effects. The covalent conjugation DOX through carbamate and hydrazone linkage resulted in a slow and sustained drug release profile at different environmental conditions. The drug-loaded nanocarriers exhibit sustained pH-triggered release of drug molecules at mildly acidic environment of tumor, due to the faster hydrolysis of carbamate and hydrazone linkage and substantial cellular internalization with significant toxicity towards the proliferation of mouse skin fibrosarcoma (WEHI-164) cells, human breast cancer (MCF-7), and human lung cancer (A549) cells. Moreover, it showed significantly lower toxicity in human normal lung (WI26VA) cells, which is essential for cancer therapy. Specifically, the developed drug-nanocarrier conjugate would minimize the amounts of drug leaching out in the blood (pH 7.4) and enable intracellular drug release upon internalized by the target cells (pH 5). The covalent conjugation and pH-triggered drug release make the nanocarriers more specific towards the targeting site and minimize premature drug release from carriers at the physiological conditions.

The application of surface-functionalized Fe_3O_4 MNPs in magnetic hyperthermia has also been investigated. The magnetic studies demonstrated that the presence of the coating layer reduces the magnetic saturation of the MNPs. Nevertheless, this passivation does not change the superparamagnetic nature of the Fe_3O_4 nanoparticles, as shown by the absence of coercivity and remanence magnetization at 300 K. These MNPs shows the very high magnetic response for external magnetic field and shows self-heating ability under AC magnetic field. The

effects of surface modification on the heating efficacy of these MNPs are monitored by time-dependent induction heating studies under the AC magnetic field. These studies revealed that the heating efficacy and specific absorption rate (SAR) of these MNPs strongly dependent on the concentration of particles and stabilizing matrix. Further, serum proteins such as BSA can be used as a coating material for MNPs with enhanced heating efficacy.

An organic solvent-free process for the preparation of surface charge controlled liposomes were developed using supercooled micelles and emulsions. Room temperature supercooled solvents comprising sugars and other additives have been explored for the first time as a solvent for micellization. Hydrogenated soya lecithin is solubilized using cationic, anionic and non-ionic surfactants as emulsifiers. Dissolution of the supercooled micelle and emulsion in water leads to the spontaneous formation of liposomes with controlled surface charge. To investigate the suitability of this method for drug encapsulation, curcumin is employed as a model hydrophobic compound. Curcumin loaded formulations show 10 fold enhanced cellular uptake in cancer cells, as compared to that of pure curcumin. Thus, the liposomal formulations prepared by this route have a good capability of incorporating active pharmaceutical agents. This offers a scalable method for the productions of liposomes through the spontaneous dissolution of supercooled micelles or emulsions in water or buffer.

Future Perspectives

Inspired by the extensive research on nano-drug delivery systems and its application in cancer therapy, very few have reached commercial deployment. This is primarily due to the lack of specificity of the carrier to the tumor cells. Therefore, it is necessary to put more efforts to develop new modalities that will specifically target

the site of action. Photodynamic/thermal therapy using efficient photosensitizers with target specific receptors or immunotherapy agents are some of the new modalities that are not yet explored. Among the immunotherapy options, a MUC1 glycoprotein is an attractive option for cancer therapy. MUC1 is often found overexpressed in tumor cells from various cancer types. Since its discovery MUC1 has been an attractive target for antitumor immunotherapy. Recent studies indicate the possibility of new T-cell vaccine strategies capable of inducing MUC1-specific cytotoxicity in tumor cells. Another key research area includes the separation of circulating tumor cells (CTC) from cancer patients and offers a personalized medicine platform. Despite their potential role in cancer healthcare, CTC methods are still at its infancy due to the difficulties caused by CTC heterogeneity, unavailability of unique CTC separation methods from the blood, and a lack of thorough clinical validation. Therefore, it is necessary to pursue extensive research on standardization and clinical application of various CTC technologies for cancer diagnosis and therapy. Dual-modality drug delivery-contrast agent systems that can track and treat cancer will emerge as a new modality for advanced health care. One such strategy will be to employ existing imaging techniques such as MRI or ultrasound to track the delivery system and release the cargo upon an external stimulus such as ultrasound. This area is also not yet fully explored. Ultrasound mediated delivery of drugs in a precisely controlled manner could pave the way for effective chemotherapy in a clinical environment. Another approach is to use functionalized particles with proteins or peptides that can translocate across the plasma membrane and intracellularly deliver the payload. Often a peptide residue that contains domains of less than 20 amino acids, mostly basic, termed as cell-penetrating peptides (CPPs) are used to target tumor cells. CPPs have been recognized as a promising strategy as they possess the ability to translocate

across the cell membrane. Different therapeutic moieties that are mostly hydrophilic in nature and/or are of high molecular weight can be tagged to CPPs and transported across the cell membrane.

Production of organic nanoparticles using biocompatible ingredients such as cholesterol or lipoproteins with controlled size distribution and a surface charge is still a challenge. Room temperature supercooled solvents have been identified as a new solvent matrix for self-assembly of amphiphiles. These matrices have the ability to arrest the motion of preformed nuclei during nanoparticle synthesis. Thus, the application of supercooled solvent for the production of organic as well as inorganic particles will emerge as a new area for research in nanotherapeutics.

.

SYNOPSIS

The thesis entitled, **"Interfacial Modification of Nanoparticles for Biomedical Applications"** deals with the development and characterization of nanostructured materials with desired surface functionality, and their potential applications in cancer therapeutics.

Improving the efficacy of drugs and minimizing its side effects have been a topic of great interest and this has been attempted using different approaches such as delivering drugs in a controlled manner or selective targeting to the site of action and so on. Some of the other issues encountered in many potentially valuable drug candidates are low aqueous solubility, lack of stability in the physiological medium, and rapid metabolism. A promising strategy to overcome these limitations has been to employ a suitable drug delivery vehicle that can achieve the release of payloads at the target site in a controlled manner. Some of the desirable features one should keep in mind while designing such drug carriers are (i) sufficient biocompatibility and biodegradability; (ii) good colloidal stability in physiological conditions; (iii) high drug loading capacity and low toxicity; and (iv) stimuli-responsive characteristics for the delivery of pharmaceuticals. In this respect, interfacial modification of nanoparticles plays a crucial role to achieve improved delivery of drugs, targeted delivery specifically targets cancer cells with a minimal side effect on normal tissue or co-delivery of two or more drugs for combination therapy.

In view of this, the present thesis deals with the structural, physico-chemical evaluation, and drug delivery characteristics of a series of biocompatible nanocarriers like functionalized Fe_3O_4 magnetic nanoparticles and surface charge controlled liposomes. These nano-drug delivery systems composed of biodegradable materials

show great promise in fulfilling the stringent requirements placed in smart drug delivery systems and increase patient compliance. The dimensions and surface characteristics of these particles allows efficient uptake by a variety of cell types and selective drug accumulation at target sites thereby enhancing the bioavailability of active ingredients.

The main objectives of the present study are:

1) Explore the use of biocompatible ingredients such as sugar-alcohols, vitamins, and proteins for surface functionalization of magnetic nanoparticles and assess their colloidal stability and magnetic properties for cancer therapy
2) Develop suitable surface functionalization strategies for Fe_3O_4-based magnetic nanoparticle system that can selectively release anticancer drugs like doxorubicin hydrochloride (DOX) at the tumor site due to changes in intracellular pH.
3) Exploration of new matrices for self-assembly of amphiphiles to prevent agglomeration of nano-drug delivery systems during production and storage and to develop a suitable methodology to prepare colloidally stable liposomal formulations with tunable surface charge and improved drug loading efficacy.

The experimental findings to meet the abovementioned objectives and inferences derived from them are included in this thesis. The thesis comprises seven chapters the details of which are indicated below.

Chapter 1: Introduction

In this introductory chapter, a short review of drug delivery systems for cancer therapy and the historical background of different functionalized nanocarriers for biomedical applications, especially for drug delivery, is presented. A comprehensive literature survey including various research articles, review articles, and books that

trace the present understanding of functionalized nanoparticles, micelles, and liposome-based drug carriers and exploration of their biomedical applications is presented. The systems that have been chosen for the investigation are also described in detail in this chapter. The gap areas in this field of research have been identified and the objective of the present investigations is clearly brought out.

Chapter 2: Experimental Techniques

A brief overview of the different experimental techniques used in the current thesis has been illustrated in this chapter. The working principle of different scattering techniques employing light, X-rays, and neutrons, were explained in detail. X-ray diffraction (XRD), Zeta potential, UV-Visible spectroscopy, Fourier Transform Infrared Spectroscopy (FTIR), and Hyperthermia studies have also been explained. A brief description of other complementary techniques employed for the characterization of nanoparticles such as Thermogravimetric Analysis (TGA), Transmission Electron Microscope (TEM), Magnetic measurements, Cell Viability Measurements, Optical Microscopy, etc. are also included.

Chapter 3: Surface Passivation of Fe_3O_4 Nanoparticles for Electrostatic Binding of Doxorubicin

This chapter deals with the utilization of biocompatible ingredients such as ascorbic acid, mannitol, and sorbitol as appropriate coating materials for surface passivation of Fe_3O_4 magnetic nanoparticles. The effects of sugar-alcohols and vitamin-C on particle size, surface potential and colloidal stability were investigated. Such approaches provide nano-formulations with good colloidal stability for the binding of cationic anticancer drug, doxorubicin. Adsorption of organic molecules imparts negative charge on the surface of magnetic nanoparticles, providing the

conjugation site for positively charged anticancer drug, doxorubicin hydrochloride (DOX) by electrostatic interactions. The functionalized Fe_3O_4 magnetic nanoparticles (MNPs) have been synthesized by a facile soft-chemical approach and are resistant to protein adsorption in the physiological medium. XRD and TEM analysis revealed that the formation of highly crystalline Fe_3O_4 nanostructure with an average crystallite size <10 nm. The passivation of Fe_3O_4 nanoparticles were investigated by FTIR spectra, DLS, TGA, and zeta-potential measurements. These MNPs exhibit superparamagnetic behavior at room temperature. The drug loading and release behavior of these MNPs were investigated by using DOX as a model drug to evaluate their potential as a carrier system. Results show a high loading affinity of anticancer drug and their sustained release in the mild acidic environments.

Chapter 4: Covalent Immobilization of Doxorubicin to Fe_3O_4 Using pH Labile Linkages for Specific Release in Cancer Cells.

This chapter includes the development of Fe_3O_4 magnetic nanocarriers with pH labile linkages for sustained delivery of anticancer drug DOX to the tumor cells with minimal side effects. The uniqueness of this drug delivery system lies in the covalent conjugation of DOX through carbamate and hydrazone linkage, resulting in slow and sustained drug release profiles at different environmental conditions. The drug-loaded nanocarriers exhibit sustained pH triggered release of drug molecules at the mild acidic environment of tumor, due to the faster hydrolysis of carbamate and hydrazone linkage and substantial cellular internalization with significant toxicity towards the proliferation of mouse skin fibrosarcoma (WEHI-164) cells, human breast cancer (MCF-7), and human lung cancer (A549) cells. However, it showed significantly lower toxicity in human normal lung (WI26VA) cells, which is essential for cancer

therapy. Specifically, the developed drug-nanocarrier conjugate would minimize the amounts of drug leaching out in the blood (pH 7.4) and enable intracellular drug release upon internalized by the target cells (pH 5).

Chapter 5: Fabrication of Biocompatible Fe_3O_4 Magnetic Nanoparticles for Improved Hyperthermia Applications

This chapter includes the exploration of different biocompatible ingredients such as sugar-alcohols, ascorbic acid, and proteins as appropriate coating materials for surface passivation of Fe_3O_4 magnetic nanoparticles and their application in hyperthermia. The magnetic studies demonstrated that the presence of the coating layer reduces the magnetic saturation of the MNPs. Nevertheless, this passivation does not change the superparamagnetic nature of the Fe_3O_4 nanoparticles, as shown by the absence of coercivity and remanence magnetization at 300 K. These MNPs shows the very high magnetic response for an external magnetic field. The effects of surface modification on the heating efficacy of MNPs are monitored by time-dependent calorimetric measurements under the AC magnetic field. Our induction heating studies revealed the heating efficacy and specific absorption rate (SAR) of these MNPs were found to be strongly dependent on the concentration of particles and stabilizing media. The AC magnetic field mediated heating capacity with high SAR value makes these novel nanoparticles as an effective heating source for magnetic hyperthermia treatment in thermal therapy.

Chapter 6: A New Organic Solvent Free Process for the Production of Surface Charge Tuned Liposomes

This chapter will discuss an organic solvent-free process for the preparation of liposomes using solid matrices with embedded nanostructures. This has been

attempted by immobilizing micelles in solid ingredients. Freezing of disordered micellar structure is difficult without cryogenic quenching, due to crystallization of the solvent or surfactant, leading to micelle destruction. A new method has been developed to create disordered, dynamically arrested water-free micelles, trapped in a supercooled state. The micelle formation is monitored by using small angle X-ray scattering (SAXS), Small angle neutron scattering (SANS), DLS, and HR-TEM. To explore the utility of supercooled micelles for liposome production, hydrogenated soya lecithin is solubilized using different types of surfactants such as cationic, anionic, and non-ionic. Dissolution of the supercooled matrix in water leads to the spontaneous formation of vesicles or liposomes with controlled surface charge. These nano-formulations were characterized using SAXS, Cryo-TEM, Zeta potential, DLS, and HR-TEM. To investigate the suitability of this method for drug encapsulation, curcumin is employed as a model hydrophobic compound. It was observed that up to 5 mg/ml of curcumin loading can be achieved in a 10% lipid matrix. It was also observed that curcumin loaded formulations show 10 fold enhanced cellular uptake in cancer cells, as compared to that of pure curcumin.

Chapter 7: Summary and Future Perspectives

This chapter summarizes the important inferences derived from the present investigation. Some of the key findings are sugar alcohol, ascorbic acid and proteins as effective passivating agents for magnetic nanoparticles, covalent binding of doxorubicin to MNPs with acid-labile linkages, functionalized MNPs for hyperthermia applications and supercooled micelles as efficient matrices for surface charge tuned liposome production. Future scope for extension of this work has also been discussed.

CHAPTER 1

INTRODUCTION

1.1. Introduction

Nanostructured materials find intriguing applications in the biomedical field, especially for cancer therapeutics and diagnostics. Different types of materials with at least one dimension in the sub-micron/nm range have evolved for the treatment of cancer as well as for the delivery of chemotherapeutic agents to achieve an optimal clinically efficacious response. The design of such drug delivery systems (DDSs) depends on the nature of the material used and its compositions. Depending on that, the nanocarriers are widely categorized into different classes namely: inorganic, organic, organic-inorganic hybrid and polymeric nanocarriers. These nanostructured carriers are particularly used for drugs which have poor solubility and less absorption ability.[1] Some of the most widely researched nanocarriers for drug delivery applications are shown in Fig. 1.1. However, the efficacy of these nanostructures as a carrier depends on the size, shape, surface functionality and other inherent biophysical/chemical characteristics. Some of the important nanocarriers systems include metals, metal-oxides, micelles, liposomes, dendrimers, carbon nanotubes, solid lipid particles, polymeric nanocarriers, etc.

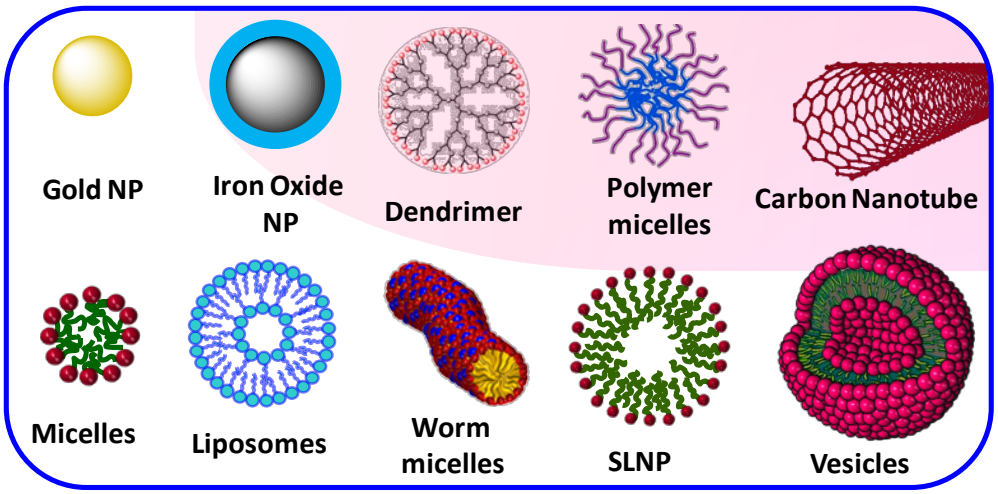

Figure 1.1 *Different types of nanocarriers used as drug delivery systems for cancer therapy*

To date, much effort has been made to develop efficient approaches that can enhance the therapeutic efficacy in the management of cancer.[2] The efficacy of chemotherapy can be maximized by two approaches: first, inhibition of drug to healthy non-cancer cells, and the second, direct entry of drugs selectively into the tumor site. This can be achieved to some extent through the systematic development of various targeted drug delivery systems using nanostructured materials. There have been extensive efforts to develop/modify the DDS thereby minimizing the side effects of chemotherapy.

1.2. Characteristics of Nano Drug Delivery Systems

Although great advancements have been made in the treatment and control of cancer progression, significant deficiencies, and room for improvement remain. For a successful DDS, there are several requirements that must satisfy so that it is compatible with the biological system and deliver the material of interest.[3] Some of the important characteristics of an ideal drug delivery vehicle that should be considered while designing the drug carrier are discussed below (Fig. 1.2).

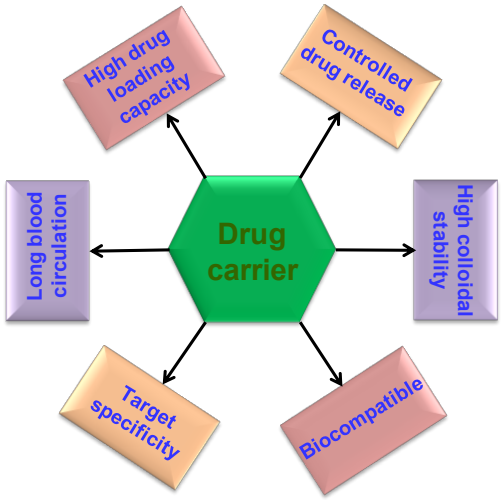

Figure 1.2 *Schematic representation of ideal characteristics of a carrier for the drug delivery system.*

Biocompatibility and Immunocompatibility: Biocompatibility in the context of drug delivery can be defined as "an expression of the benignity of the relation between a material and its biological environment".[4] The ability of a material to interact in the body with the surrounding cells, tissues, and other factors are often expressed in terms of biocompatibility. A material is considered to be having good biocompatibility if it does not generate a vigorous immune response, resists the build-up of proteins and other substances on its surface that would hinder its function and is resistant to infection. It is now well known that surface properties of drug carriers play an important role for DDS, and greatly affect their properties while in the bloodstream. The factors such as the interaction with blood components, carrier accumulation, and clearance in organs, etc. are indeed important. The biocompatibility and immunocompatibility of the materials depends on their structure, chemical composition, formulation, and many other factors which often result in a total effect on the organism.

High Colloidal Stability in Biological Fluids: It is important that the developed carrier should have sufficient stability in the biological medium so that the physicochemical properties are retained until it reaches the site of interest. The carrier aggregations will significantly alter both *in vitro* and *in vivo* behaviors such as uptake, cytotoxicity, pharmacokinetics, organ toxicity, and bio-distribution. When drug carriers are delivered into cell culture media, their colloidal and chemical properties are altered due to the presence of proteins and high ion content, which are responsible for collapsing the colloidal stability due to screening of the electrostatic interactions and result in aggregation.[5] Therefore, it is important to develop a robust understanding of the factors governing the colloidal stability of the drug carrier and aggregation in physiological

environments. The surface functionalization of the drug carriers is one of the most widely accepted methods to prevents the agglomeration of nanocarriers. The different approaches designed to avoid the formation of aggregates in complex biological media include electrostatic, steric, or electro-steric stabilization.[6] The colloidal stability often depends on inter-particle interactions and characterized by estimation of surface charge, particle size and sedimentation rate. The influence of physicochemical properties of drug carrier on the cellular interaction is routinely assessed using *in vitro* systems. It follows that media composition can vary based on the metabolic and nutritional needs of different cell types, and this may in turn impact the colloidal stability of engineered drug carriers.

High Drug Loading Capacity: Another factor that needs to be taken into account while developing the carrier is its drug loading capacity. Current DDS are hampered by poor delivery of cargo to tumors, in part due to poor encapsulation ability of drug carriers and easy release from the cargo. Although drug carriers have high colloidal stability and do not aggregate/precipitate in bulk solution, drug carriers with low encapsulation ability and poor drug binding can lose their ingredient during circulation in the blood due to interactions with blood cells, cellular membranes, serum proteins, and other bio-macromolecules. The resulting premature drug release from carriers limits the therapeutic efficacy at target sites. To attain minimum carrier toxicity, it is desirable that the drug-loading capacity and encapsulation efficiency of the carrier be as high as possible. Most of the existing drug carriers possess meager drug-loading/encapsulation (generally <10%) associated with more carrier materials.[7]

The drug loading capacity is usually expressed in weight percentage of the carrier material, while the drug loading efficiency is given by weight percent of the drug-loaded to the carrier:

$$\text{Drug loading capacity (wt.\%)} = \frac{\text{Mass of drug in carrier}}{\text{Mass of the carrier}} \text{ X } 100\% \quad (1.1)$$

$$\text{Drug loading efficiency (wt.\%)} = \frac{\text{Mass of drug in carrier}}{\text{Mass of the drug in feed}} \text{ X } 100\% \quad (1.2)$$

The drug-loading efficiency reflects the utilization of drugs in feed during the drug carrier preparation process. Many hydrophobic drugs have poor water solubility and hence, limited applications. The functionalization or coating agent act as gatekeepers on drug carrier with a high loading capacity for hydrophobic as well as hydrophilic drugs. Surface coatings on the carrier can also enhance *in vivo* therapeutic efficacy by preventing premature release of cargo. For intravenous administration, the extensive use of carrier materials might cause systemic toxicity and impose an extra burden of degradation, metabolism, and excretion of the materials for patients. Therefore, on the premise of guaranteeing therapeutic effect and function, improvement of drug loading is a promising approach to overcome toxicity or side effects.

Target Specificity: Targeted drug delivery to the tumor site is an active area of research, presently under intense investigation. Multiple routes and various methods, devices, and formulations of both pharmaceutical agents and biologics are being investigated for cancer therapy over the past decade. The cancerous state is a highly stimulating environment of metabolically active cells, and hence these cells are overexpressed for selective receptors to assimilate factors essential for growth and transformation. Such receptors would serve as potential targets for the specific ligand-mediated transport of pharmaceutically active molecules. Due to the active metabolism of tumor cells, the tumor micro-environment is highly acidic compared to normal tissues; hence pH-sensitive drug carrier systems have now been developed in

which drug release is specifically triggered by the acidic tumor environment. Conventional drug formulations administered through routes such as intravenous or oral, cannot deliver enough drug molecules to the target site. A good fraction of drugs are excreted or accumulated in unspecific sites where the drug expresses side effects. Hence, the induction of spatial control is needed to deliver therapeutic agents to specific target sites to increase drug efficiency and minimize the side effects. Targeted DDS is a method for expanding the therapeutic windows of drugs by increasing delivery to the desired target.

Principal schemes of drug targeting investigated in various experimental and clinical settings can be mainly divided into the following types:[8,9]

a) Passive Targeting: Passive targeting refers to the preferential accumulation of a drug or drug-carriers at the target site due to: a) Pathophysiological factors: inflammation or infection, and the enhanced vascular permeability and retention (EPR) effect, b) Physicochemical factors: size and molecular weight, c) Anatomical intervention: catheterization and direct injection and d) Chemical approaches: pro-drugs and chemical delivery systems.[10] Typically, tumor vessels are highly disorganized and dilated with a high number of pores, resulting in enlarged gap junctions between endothelial cells and compromised lymphatic drainage. The passive targeting is a result due to this characteristic of leaky vasculature of tumors,[11] which refers to the EPR effect and hence allows the accumulation of the drug or drug carriers at the cancerous site up to 400 nm in diameter by convection or passive diffusion.[12] Maeda et al. originally described the concept of EPR and this theory is based on the characteristics of tumor vasculature of leaky blood vessels and lack of lymphatic

drainage.[13,14] Factors that influence EPR include the long circulation time, size of tumors, degree of tumor vascularization, and angiogenesis.

b) Active Targeting: In this method, the specific markers in the cancerous cell, which are not expressed by healthy/normal cells, are targeted. This targeting method employs a specific modification of a drug or drug-carrier system with "active" agents having a selective affinity for recognizing and interacting with a specific cell, tissue, or organ in the body. This strategy comprises use of a targeting ligand or a specific molecule attached on the surface of drug carrier, which recognizes and enables the drug carrier to bind to receptors (tumor-specific epitope) overexpressed on cancer cells, like folate receptor, Her-2, transferrin receptor, the epidermal growth factor receptor (EGFR), glycoprotein receptoretc., or antibodies that is raised against that particular antigen, such as anti-CEA antibody. CA-125 is expressed in more than 85% cases of ovarian cancer and is one of the best biomarkers for active targeting.[15] These receptors serve as tumor markers which are not/less expressed on normal cells. Another example of such a targeting approach is to utilize peptides ligands. A typical example involves RGD-containing peptides which are particularly helpful in targeting tumor angiogenesis.[16] Also, some widely used targeting moieties are: proteins mainly as antibodies and their fragments, peptides, nucleic acid (aptamers), vitamins, carbohydrates, or others. Such molecules or antibodies are conjugated to the surface of drug-carriers and forms the basis of active targeting. In spite of the many advantages of active targeting, the technology has resulted in only a few clinically validated drug-carrier formulations to date. The schematic representation of drugs entering the tumor through passive and active targeting methods and by stimuli triggered release are shown in Fig. 1.3.

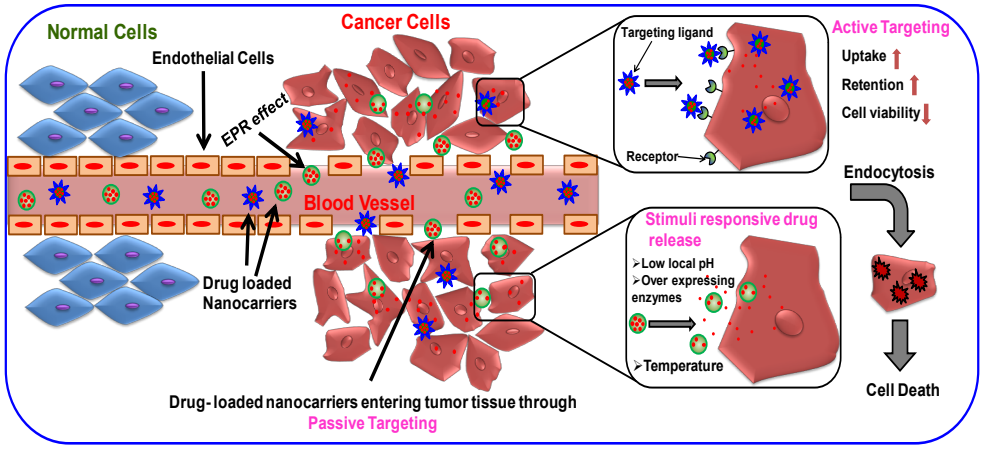

Figure 1.3 *Schematic of Passive and active targeting approaches.* ***Passive targeting:*** *In which drugs may be released in the extracellular matrix due to leaky vascularization and diffuse throughout the tumor.* ***Active targeting:*** *Exploits surface-modified nanoparticles; which can enhance the therapeutic efficacy of drugs by increasing accumulation and cellular uptake of drug carriers through receptor-mediated endocytosis.* ***Triggered release:*** *It is based on stimuli-responsive nanoparticles.*

Long Blood Circulation: For chemotherapeutic or diagnostic agents, prolonged blood circulations are advantageous, since longer circulation time ensures longer contact of drug carrier with the tumor tissue and allow them to reach their target site. One major barrier preventing the progress of this approach is the rapid clearance of foreign particles from the blood circulation by the reticulo-endothelial system (RES). Upon administration of drug-carriers into the blood, they are quickly opsonized and cleared by the macrophages, thereby limiting their circulation times.[17] The rapid clearance of carrier is the cause of several limitations of DDSs including short half-life and limited accumulation at the target site. To overcome this problem, the particle size and surface properties including charge, hydrophobicity, the state of hydration, and the dynamic motion of the hydrophilic surface-attached chain molecules, are the controlling factors for the prevention of opsonization and prolong particle circulation in the biological milieu.[18] The surface modification of NPs by polyethylene glycol

(PEG) was developed as the first strategy to prolong NPs circulation. Also, polysaccharides and PEG-derived copolymers have been extensively used. Though PEGylation has preferred for prolonged blood circulation, it has several limitations including transient nature of the effect and compromised carrier-target interactions. Accordingly, several other approaches have been developed, these include, modulation of mechanical properties, engineering particle morphology and hitch-hiking on red blood cells etc.[19]

Controlled Drug Release: To achieve predictable and reproducible drug release rate, extended duration of activity for short half-life drugs, decreased toxicity, and reduction of required dose, optimized therapy, and better patient compliance, in addition to targeting, a sustained drug release is desirable.[9] In the sustained release, the drug is released over a period of time in a controlled manner from a carrier. The first controlled-release polymer composition, marketed as Zoladex®, was approved by the US FDA in 1989 for the treatment of certain types of prostate and breast cancers.[20] These controlled-release polymer-drug compositions, allow a drug to be trapped inside a polymer matrix and release over an extended period of time as it slowly diffuses out of the polymer matrix. There are a few carriers used in sustained drug release such as liposomes, biodegradable microspheres, inorganic NPs and drug-polymer conjugates, etc. In addition, polymer-drug complex as sustained delivery are still limited by their non-biodegradability and the undesirable fate of polymers after *in vivo* administration.[21]

Recent research shows that once the drug-carrier reaches to the tumor site, a controlled release of the therapeutic agents from carriers was triggered by various stimuli responsible mechanism like pH, osmolality, temperature, glucose, magnetic

field, or *via* an enzymatic activity; leading to the improved antitumor activity of the drug in tumor.

a) pH-Responsive Release: Intracellular and extracellular pHs in tissues affect the function of the cells and play an important role in cancer therapy. In the normal cells, metabolism is done by aerobic pathway; and glucose is fully metabolized to produce carbon dioxide, water, and energy. However, in the cancer cells, the glucose is mostly metabolized through the anaerobic pathway, which produces a large amount of lactic acid and releases limited energy due to a high level of pyruvate and hypoxia in the tumor environment. During the process, compared to the normal tissue, the tumor growth requires a large amount of energy, which produces more carbon dioxide and lactic acid in the tumor, resulting the acidic condition in the tumor micro-environment.[22] This offers a methodology to trigger the release of drugs through judicious changes in cellular pH. To attain the pH-responsive drug release, anticancer agents can be attached to the surface or encapsulated into pH-sensitive materials, such that the drug can be released when it reaches the acidity of the tumor micro-environment.

b) Temperature and Magnetic Field Responsive Release: The temperature in a specific area can be increased by using external sources of heat that can be applied on the skin or can be remotely induced via irradiation of metals or by applying the alternating magnetic field (AMF) to magnetic materials. Temperature-sensitive DDSs are based on components that modify their structural morphology (the swelling or shrinking of the network or disintegrate the carrier) as a function of temperature. There are varieties of temperature-sensitive drug delivery carriers prepared using polymers such as poly(methyl vinyl ether), Poly-N-isopropyl acrylamide (p-NIPAM),

poly-N,N-diethyl acrylamide, poly-N-vinyl caprolactam, poly(methylvinyl ether), poly(ethylene oxide)–poly(propylene oxide) block copolymers, etc. because their critical solubility temperature is near the body temperature or can be easily tuned with minor changes in their composition. One of the most encouraging temperature-sensitive liposome formulation "ThermoDox®" is perhaps the elegant DDS that has been more clinically evaluated so far. Increased temperature makes the blood vessels leakier, and the drug carrier will disintegrate, and it will eliminate the drug rapidly. If one can control the temperature raise during treatment, the sustained release of the drug can be achieved.[23]

c) Light Responsive Release: Recently, DDSs which are responsive to lights have gained much attention. Visible and UV light may activate the drug release, and near-infrared radiation (NIR) can go deeper in the body and possess the ability to discharge the drug in a localized place of tissue. Gold nanoparticles (AuNPs) are one of the most efficient systems for the application of light-mediated therapy. Under the NIR irradiation, the surface plasmon resonance of AuNPs increases the temperature up to several degrees and causes the drug release as well as cell cytotoxicity. In this context, Park et al. reported that poly(lactic-co-glycolic acid) matrix particles loaded with DOX and the gold films were coated on this drug-loaded NPs.[24] It was found that NIR irradiation will cause the delivery of DOX that will lead to the death of cancerous cells, as the gold surface absorbs light energy and converts it to cytotoxic heat and photothermal treatment was also achieved.

d) Ultrasound Mediated Release: Low-frequency ultrasound can penetrate deeper into the body with very low scattering. Cavitations formed due to ultrasound cause disassemblies of carriers like polymeric micelles, polymersomes and liposomes

containing gas-filled micro-bubbles and disruption of networks, responsible for drug release. There are varieties of commercially available micro-bubble based contrast agents clinically used in ultrasound imaging and that can be adapted to perform as ultrasound responsive DDSs.[25]

The Development of functional NPs for advanced drug delivery systems can serve as the successful tools for anticancer therapy. To improve patient management in the near future, recent research has focused on the new ways of using currently available therapeutic agents. A variety of nanostructures have been recently investigated such as synthetic biodegradable polymers, lipids (liposomes, solid lipid NPs), mesoporous silica NPs, micelles, dendrimers, quantum dots, carbon nanotubes, protein-based NPs, metal/metal oxide NPs, etc. for the treatment of cancer. In the proceeding section, recent literature relevant to a few types of nanocarriers with controlled composition, size, structural morphology and improved surface functionality are discussed in terms of their fabrication, targeting, and different properties relevant to the biomedical applications.

1.3. Different Types of Nanocarriers

a) Inorganic Nanocarriers

The employment of inorganic nanostructured materials for the construction of efficient functionalized DDSs for cancer therapy has gained increasing importance in recent years.[26] Metals, metal oxides, or metal/metal oxide composites constitute the major fraction in inorganic-based carriers. These nanocarriers are often stabilized by a shell region composed mainly of an organic ligand that provides suitable surface functionalization for the conjugation of biomolecules. The organic coating agents also

protect the core region and loaded cargo from unwanted physicochemical interactions from the external biological environment, and also for enhanced the colloidal stability. Mesoporous and hollow inorganic materials are also the most attractive drug delivery carriers as they can easily entrap drug molecules especially hydrophobic drugs in their voids. Further, the unique intrinsic characteristics of some inorganic particles at the nanoscale such as electrical, magnetic, and plasmonic properties could be used for creating multifunctional materials for simultaneous applications in therapy as well as diagnostic purposes. Examples of such dual functionality include diagnostics using magnetic resonance imaging (MRI), computed tomography (CT), or positron emission tomography (PET).[26] The shape, size, and surface properties of inorganic nanocarriers can be tuned to achieve desired properties. However, so far, only a few of them have been accepted for its clinical use in cancer diagnostics or therapy. A large number of them are still in the clinical trial stage, due to their critical issues connected with limited amounts of active drug transportation and a high degree of *in-vivo* toxicity.

Metallic nanocarriers are one of the most widely studied inorganic materials for drug delivery. They are purely made-up from the metal precursors and advancements in their fabrication provide tools to fine-tune their physicochemical properties. NPs of the alkali and noble metals i.e. Rubidium, Cesium, Copper, Silver Gold, etc. shows applications in many research areas, mostly in therapy and diagnosis purpose due to their good biocompatibility and versatility when it comes to surface functionalization. After Faraday's work, gold NPs have generated escalating interest and in the last few decades more and more controllable synthesis methods and applications in diverse nano-systems have been developed.[27] Specifically, gold and silver NPs have gained increasing interest in the biomedical field due to their special features, such as extraordinary optical and electronic properties, localized surface plasmon resonance

(SPR), high colloidal stability, and biocompatibility, tunable size and morphology, and easy surface functionalization. Appropriate drugs can be conjugated to gold NPs surfaces via ionic, covalent or physical absorption, and hence can be used in drug delivery, targeting, and imaging applications.[28] Though silver NPs exhibited excellent antimicrobial activity, for drug delivery applications, very few studies have been carried out. Prusty and Swain et al. reported the chemically cross-linked and porous polyacrylamide/dextran nano-hydrogels hybrid system with incorporations of silver NPs for the stimuli-responsive in vitro release of Ornidazole.[29] The physicochemical properties, like luminescence, conductivity, and catalytic activity of inorganic NPs can be controlled by tuning their size. However, an unavoidable problem associated with these NPs is their intrinsic instability over longer periods of time, and they tend to form agglomerates to reduce the energy associated with the high surface area to volume ratio. To prevent the particle aggregation and provide sites for bio-functionalization, metallic NPs need to be further passivated using appropriate stabilizers. The advantage with small size is that due to the large surface area to volume ratio, these NPs can have high drug loading capability, which can significantly lower the matrix concentration and hence minimize any adverse effect associated with the matrix. Dhar et al. reported that DOX-coupled gold NPs could lower the effective dose to patients during treatment due to their higher uptake as compared to free DOX molecules and it further helps to cross the blood-brain barrier (BBB).[30]

Metal oxide NPs have also been investigated as an effective platform for controlled drug delivery applications in cancer therapy. Some of the widely studied metal oxides NPs are iron oxide, SiO_2, CeO_2, ZnO, and their composites. Being highly biocompatible material, iron oxide nanoparticles (IONPs) are the most researched and commonly used materials for biomedical applications, due to its interesting magnetic

properties. Though maghemite (γ-Fe_2O_3) and magnetite (Fe_3O_4) are highly biocompatible IONPs, magnetite is the most commonly used in drug delivery.[31] Since naked IONPs are highly chemically active and are easily oxidized in the air; resulting loss in magnetism and dispersibility, hence surface passivation with a biocompatible shell is required. IONPs have been investigated for use in targeted drug delivery, controlled drug release, magnetic hyperthermia treatment, and as contrast agents in MRI. The magnetic properties of IONPs can be improved by doping with magnetically susceptible elements such as manganese (Mn), cobalt (Co), and nickel (Ni). The metal ferrite of these NPs ($MnFe_2O_4$, $CoFe_2O_4$, and $NiFe_2O_4$) also have been investigated for possible use in magnetic hyperthermia and as contrast agents for MRI.[32] Other metal oxide NPs such as CeO_2, ZnO, TiO_2, SiO_2, etc. are also gaining interest in the biomedical field. Recently, Renu et al. and Sahu et al. reported that CeO_2 NPs have many defects on their surface mainly due to the oxygen vacancies, which result in a mixed valance of cerium(IV) and (III) oxidation states. This results in a redox couple which provides the catalytic activity and leads to an increased interest in biological antioxidant potential.[33] The use of porous silica (SiO_2) NPs is widely increasing due to its large specific surface area, pore-volume, controllable particle size, and good biocompatibility. The influence of the microstructure of mesoporous silica on drug loading capacity was studied theoretically and experimentally.[34] Andersson et al. have reported the application of mesoporous silica for delivery of ibuprofen[35] Huang et al. reported the covalent conjugation of DOX to mesoporous silica NPs via pH-sensitive hydrazone linkage and controlled release of DOX in both *in vitro* and *in vivo* conditions.[36] The fluorescent properties of ZnO NPs can be exploited for simultaneous detection and photodynamic therapy of tumor. Barick et al. investigated the drug-loading efficacy of mesoporous ZnO nanocarriers

using DOX as a model drug.[37] They observed that the release of drug strongly depends on the nature of the coating agent and strategy of stimuli used. Further, combination therapy involving anticancer drug and quantum dot technology has received much attention. Yuan et al. synthesized blue-light emitting ZnO quantum dots and combined them with biodegradable chitosan to use in targeted drug delivery.[38] Tripathy et al. reported that the enhancement of anticancer potency using an acid-responsive ZnO-incorporated liposomal DDS. They have reported that ZnO NPs rapidly decomposed in the acidic environment of cancer cell and thereby released entrapped drug molecules from the nano-complexes.[39]

Specific surface passivation of inorganic NPs through organic materials has been utilized to improve the selectivity and efficiency of antitumor agents. This can also lead to several hybrid particles with dual functionalities. The meticulous construction of composite systems of lipid bilayers supported on solid material has attracted significant interest owing to their superior biocompatibility. Desai et al. reported the development of a mesoporous silica NPs-lipid bilayer hybrid system, for improved retention and intracellular delivery of zoledronic acid in breast cancer.[40] Han et al. developed DOX loaded, hybrid, lipid-capped mesoporous silica NPs with pH and redox-responsive release of DOX within the tumor cells.[41] Vivero-Escoto et al. developed mesoporous silica capped gold NPs for intracellular controlled delivery of paclitaxel inside of human fibroblast and liver cells.[42] Bikram et al. reported the photothermal modulated hybrid DDS consisting of a silica core surrounded by a gold shell. Further, they embedded these SiO_2-Au hybrid NPs into thermally sensitive hydrogels to achieve the temperature-controlled drug release using light.[43] Chen et al. developed a novel magnetic DDS by embedding DOX conjugated Fe_3O_4 NPs in a PEG functionalized porous silica shell (Fe_3O_4-DOX/pSiO_2-PEG). They have

demonstrated that the porous silica shell not only creates a protective layer for DOX and Fe_3O_4 but also provides a barrier for the release of drug from the nanocarrier. The surface anchored PEG may prevent the recognition of the drug-loaded carrier by RES as well as their opsonization.[44] Combination of luminescent and magnetic properties into a single entity would enable the engineering of unique nano-sized devices which can exhibit multifunctionality and could be manipulated using an external magnetic field. Recently, Barick et al. developed luminescent magnetic NPs composed of Fe_3O_4 and YPO_4:Eu hybrid nanostructure by covalent bridging for simultaneous imaging and therapy.[45] Other metallic hybrid nanomaterials such as silica-coated Pd@Ag nanoplates, carboxymethyl chitosan stabilized Fe_3O_4 NPs and Fe_3O_4@polypyrrole nanocomposites were also explored as carriers for the drug delivery purpose.[46,47]

b) Organic and Polymeric Nanocarriers

Organic and polymeric NPs are also being extensively investigated for biomedical applications. The organic nanocarriers are basically carbon-based nanostructured materials that possess high biocompatibility and improved drug loading capacity. They allow versatile control of both structural morphology and chemical composition, while their high colloidal stability and amorphous structure allow the incorporation of a wide combination of various hydrophilic/hydrophobic drugs. A range of naturally occurring polymers such as dextran, gelatin, guar gum, collagen, proteins, chitosan, etc. and synthetic biocompatible polymers like polyvinyl alcohol, PEG, poly (lactic acid), poly(lactic-co-glycolic acid) (PLGA), poly(ε-caprolactone), poly(styrene-maleic anhydride) copolymer, and N-(2-hydroxypropyl)-methacrylamide copolymer (HPMA), etc. have been gained increasing interest among the scientific community for the fabrication of different types of nanocarriers for drug

delivery applications.[48] Drugs can easily be encapsulated either through dispersion in the polymer matrix or conjugation to polymer molecules. The controlled delivery of the drugs can be achieved through surface or bulk erosion, diffusion through the polymer matrix, swelling followed by diffusion, or as a response to local stimuli. They are also explored for targeted drug delivery by conjugating them with specific targeting moieties.

Chitosan is a naturally derived biopolymer employed for various drug delivery applications and used via different routes of administration, including treatment of dermatologic and gastrointestinal diseases, pulmonary diseases, and drug delivery to the brain and ocular infections.[49] Several studies indicated that chemical modification of chitosan NPs can improve their targeting and bioavailability, and appreciably enhance the delivery of therapeutic agents. Recent advances highlight the use of chitosan NPs for tumor targeting, imaging, and theranostic applications.[8] A range of chitosan-based materials in the forms of micro and NPs, gels, tablets, etc. have been prepared by different routes such chemical or ionic gelation, spray-drying, emulsion route as well as coacervation etc.[50] Due to good bio-adhesive and sustained release properties, chitosan particles have been employed in topical delivery systems as well. It showed improved microbiological activity when evaluated for topical sustained release of cetylpyridinium chloride (CPC).[51] Mitra et al. prepared DOX-dextran conjugate and subsequently encapsulated into a chitosan hydrogel using a reverse microemulsion technique to improve therapeutic efficacy in the treatment of solid tumors.[52] Chitosan-based nanocarriers have also been evaluated for the delivery of drugs to ocular mucosa using Cyclosporin A as a model drug.[53]

Poly lactic-*co*-glycolic acid (PLGA) is a highly biodegradable and biocompatible, FDA approved polymer extensively used to fabricate systems for sustained drug delivery and biomedical applications. Lupron is a commercially available drug delivery material made up of PLGA employed for the treatment of advanced prostate cancer.[54] K. Tomoda et al. investigated PLGA NPs for transdermal delivery of estradiol in order to avoid the problems associated with oral and intravenous administration of a drug such as metabolization in gastrointestinal tract and liver, the rapid increase of drug levels in the blood, fast clearance and resultant side effects including thrombosis, endometriosis, and uterus carcinoma.[55] Cheng et al. developed the multifunctional Taxol-loaded PLGA NPs and showed chemotherapeutic and NIR photothermal destruction of cancer cells *in vitro* and *in vivo*.[56]

Albumin-based nanocarriers have been found very promising for the targeted delivery of antitumor drugs. It is a protein that can be obtained from a variety of sources, including egg white (ovalbumin), human serum albumin, (HSA), and bovine serum albumin, (BSA), and is also available in milk, soybeans, grains, and has been considered as an ideal material for biomedical applications. Furthermore, due to the easy preparation, high loading capacity for various drugs, non-toxic, non-immunogenic, biocompatible, and biodegradable properties, as well as a long half-life in circulating plasma, these nanocarriers have a great interest in drug delivery. Due to the presence of functional groups like amine and carboxylic groups makes it easy to bind targeting ligands and other surface modifications. Ruttala et al. reported paclitaxel-loaded albumin NPs encapsulated in curcumin containing PEGylated hybrid liposomes to investigate the potential of a combination drug therapy.[57] The nanocarriers composed of proteins like BSA or HSA with si-RNA have been

employed for systemic tumor-targeted delivery of si-RNA. These proteins enhance the intracellular delivery of si-RNA and its accumulation in the tumor side and shield it from degradation.[58,59] Elzoghby et al. reported that the nanocarriers prepared from milk protein casein and loaded with flutamide were found to show very good anticancer activity for prostate cancer in rats.[60]

Hydrogels are another important class of materials that gained interest among the drug delivery community. They are three-dimensional networks composed of hydrophilic polymer chains and can absorb large amounts of water or biological fluids, and are a special class of natural and synthetic polymeric materials. These structures have the ability to swell in water without dissolving. Generally, hydrogels are prepared by various methods like chemical cross-linking, photo-polymerization or irradiated cross-linking. These are widely used for numerous biomedical applications, such as biosensors, for 3D cell culture, and bio-adhesive and/or controlled drug delivery. The key success of hydrogel development is the gelation process, and the constitution of these materials mainly involves weak interactions so their swelling behavior changes drastically in response to external environment such as pH, temperature, ionic strength of the medium, composition of the complexing agent, electrical and magnetic stimuli, light, etc.[61] The development of pH-sensitive hydrogels has attracted a lot of attention as they offer a novel way of therapeutic agents delivery to tumor sites. The lower extracellular pH of the tumor site helps in the ionization of acid and basic functionalities present on the polymer chains. This results in the changes of swelling and shrinkage of the hydrogels and the corresponding increase in the extent of drug release.[62] Similarly, for temperature-sensitive hydrogels, the solubility and swelling behavior of hydrogels changes in

response to external temperature, and have a special feature to control the drug release by changing the gel structure. Ghosh et al. reported that poly(vinyl pyrrolidone) stabilized fluorescent red copper nano-clusters can be converted into hydrogel nanocarriers through cross-linking with PVA to deliver the anticancer drug Cis-platin to cervical cancer cells (HeLa), thereby inducing apoptotic cell death.[63] The high encapsulating efficiency is attributed to molecule loading on the surface and inside the hydrogel particle, followed by strong interactions using various functionalities.

c) Amphiphilic Assemblies

Amphiphilic assemblies are also an important class of materials that are widely explored for drug delivery. Amphiphiles are molecules that possess distinct hydrophilic and hydrophobic parts. Due to this nature, they have the ability to accumulate at the interface in a specific orientation as well as form self-assembled structures such as micelles, vesicles, worm-like micelles, etc. in selected solvents. Such association phenomenon arises from the balance of various non-covalent forces acting among the molecules, such as electrostatic interactions, hydrogen bonding, hydrophobic interactions, solvophobic, van der Waals, steric and depletion interactions, π-π stacking, etc.[64] The self-assembly phenomenon is highly solvent dependent. There are widespread interest in water as a solvent for self-assembly due to its importance in both nature (e.g., biological) and engineered systems. Association of lipids to form cell membranes, bile salt aggregation during digestion, stabilization of fat globules in milk, and attainment of the tertiary structure of proteins from linear strands of covalently linked amino acids, etc. are the well-known examples of self-assembly in nature. The amphiphilic macromolecules provide unique and still effective opportunities for designing novel materials for advanced applications in the

biomedical field. Amphiphilic macromolecules possess both a hydrophilic and a lipophilic (or hydrophobic) portion. The hydrophilic part can be uncharged or charged (anionic, cationic, or zwitter-ionic) and interacts favorably with the surrounding water, while the hydrophobic part is usually composed of hydrocarbon chains that tends to minimize its exposure to water. The association of amphiphiles will happen only when the given concentrations exceed above a certain concentration called critical micelle concentration (CMC). Often, a large number of lyotropic phases are observed as a function of concentration of amphiphilic molecules in the solvents, as schematically shown in Fig 1.4. Below the CMC, amphiphiles are molecularly dispersed in the solvent, but with increasing the concentrations they exhibit a rich phase behavior with an entire gamut of structures such as micelles, which can be of the spherical, disk, ribbons, hollow capsules, rod type, and so on depending on the molecular structure. At even higher concentrations, these micellar aggregate changes to more ordered structures and can form hexagonal, cubic or lamellar phases, also of the inverse type at very high concentrations. The observed phase diagrams can be quite complex and characteristics of these aggregates not only depend on concentration, but also on solvent, pH, temperature, ionic strength, type and concentration of additives and so on.[65,66]

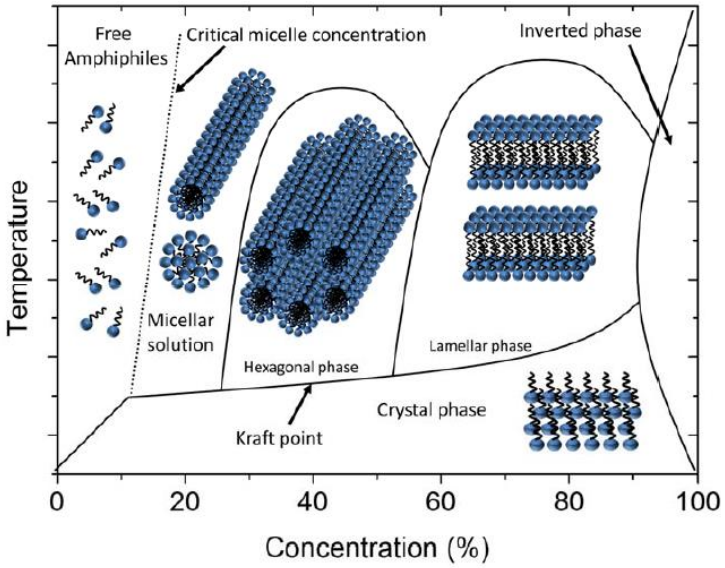

Figure 1.4 *Schematic illustrations of concentration dependent phase diagram of an amphiphilic surfactant in the solvent. [This figure is taken from ref:*[66]*]*

The fundamental principles of the self-assembly process have been described in detail by various authors. The occurrence of equilibrium structures with finite aggregation number and its dependence on molecular structure of amphiphiles has been envisaged in the primary work of Tanford[67] and later extended by Israelachivli.[68] According to Tanford, the standard free energy change per molecule upon aggregation can be written as a sum of the three terms, namely the transfer free energy, interfacial free energy and the repulsive interaction energy between the head groups.[67,69]

$$\left(\frac{\Delta\mu_g^0}{kT}\right) = \left(\frac{\Delta\mu_g^0}{kT}\right)_{Transfer} + \left(\frac{\Delta\mu_g^0}{kT}\right)_{Interface} + \left(\frac{\Delta\mu_g^0}{kT}\right)_{Head} \quad \text{..... (1.3)}$$

The first term accounts for the changes in free energy associated with the transfer of the hydrocarbon tail form an unfavorable contact with water to that of a lipophilic environment in the micelles core. Obviously, this leads to a negative contribution to the free energy. The second term represents the positive free energy due to the formation of an interface between the lipophilic core of the micelle and the polar

solvent. The third term accounts for the repulsive interactions arising from the steric effects of solvated head groups which will tend to keep the hydrophilic part away from each other. In the case of ionic surfactants, there is an additional contribution from the electrostatic repulsion of the charged head groups. These factors tend to increase the free energy of the system. The optimum geometry of the aggregate can be obtained from the minimization of the total free energy per molecule and this optimal packing of the molecules in the aggregate can be linked to the effective head group area of surfactant. Considering the transfer free energy to be independent of head group area of the surfactant, one can see that the effective area per molecules is decided by the interplay of head-head repulsion and the interfacial tension (γ). Since the interfacial free energy per molecule is a product of interfacial tension and the area per molecule (a), and the repulsive energy is assumed to vary inversely with the area per molecule, one can write the above free energy expression [1.3] as,

$$\left(\frac{\Delta\mu_g^0}{kT}\right) = \left(\frac{\Delta\mu_g^0}{kT}\right)_{Transfer} + \left(\frac{\gamma}{kT}\right)a + \left(\frac{\alpha}{kT}\right)\frac{1}{a} \quad \ldots\ldots\ldots\ldots\ldots\ldots\ldots\ldots (1.4)$$

where α is the repulsion parameter, T is the temperature and k is the Boltzmann constant. An illustration of the variation of free energy per molecule as a function of a is given in Fig. 1.5, at different values of the repulsion parameter, α/kT, keeping the first term $\left(\frac{\Delta\mu_g^0}{kT}\right)_{Transfer}$ and γ/kT constant. It can be seen that the free energy goes through a minimum corresponding to the equilibrium area per molecule (a_0). This equilibrium area increases with an increase in the repulsive interaction parameter α/kT, as indicated in Fig.1.5.

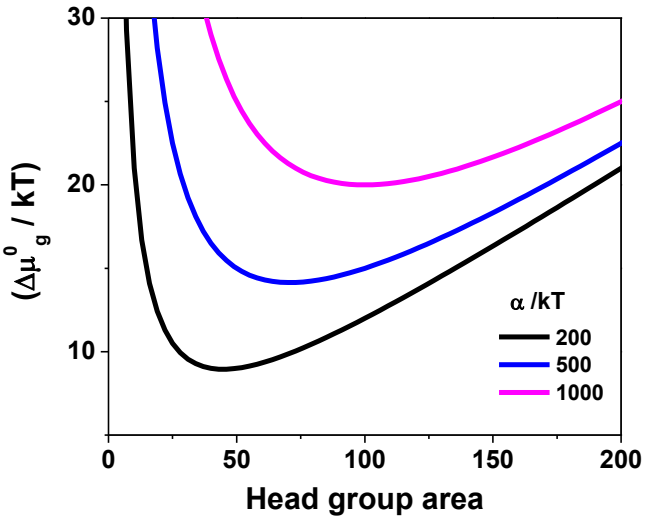

Figure 1.5 *Simulated curves of change in the free energy per molecule in aggregate as a function of the head group area per amphiphile, as per above equation 1.4. The transfer-free energy is taken as zero, the interface energy term (γ/kT) as 0.1 units and the repulsive interaction term (α/kT) as 200, 500, and 1000 units. [This image is taken from ref:*[70]*]*

The optimal packing of molecules in the aggregate led to the development of a predictive geometrical parameter known as critical packing parameter (CPP) which is used as a guiding principle to forecast the geometry of aggregates. The packing parameter of amphiphiles can be defined by a ratio of the volume of the hydrophobic part (v) to the length of the hydrophobic chain (l) and the effective head group area (a_0) of the surfactant molecule (shown in Fig. 1.6). Schematic illustration of the corresponding changes in the packing of molecules to form structures such as spheres, rods, vesicles, and bilayers are shown in Fig. 1.6. Thus, one can modulate the equilibrium area and hence the CPP by changing the molecular repulsion parameter. This offers an opportunity to develop and manipulate nanostructure architectures ranging from spherical micelles ($C_{pp}\leq 1/3$) to rod-like micelles ($1/3\leq C_{pp}\leq 1/2$), vesicles ($1/2\leq C_{pp}\leq 1$) and lamellar structures ($C_{pp}=1$), while for larger values ($C_{pp}>1$), the amphiphiles will assemble into "inverted" phases.[64]

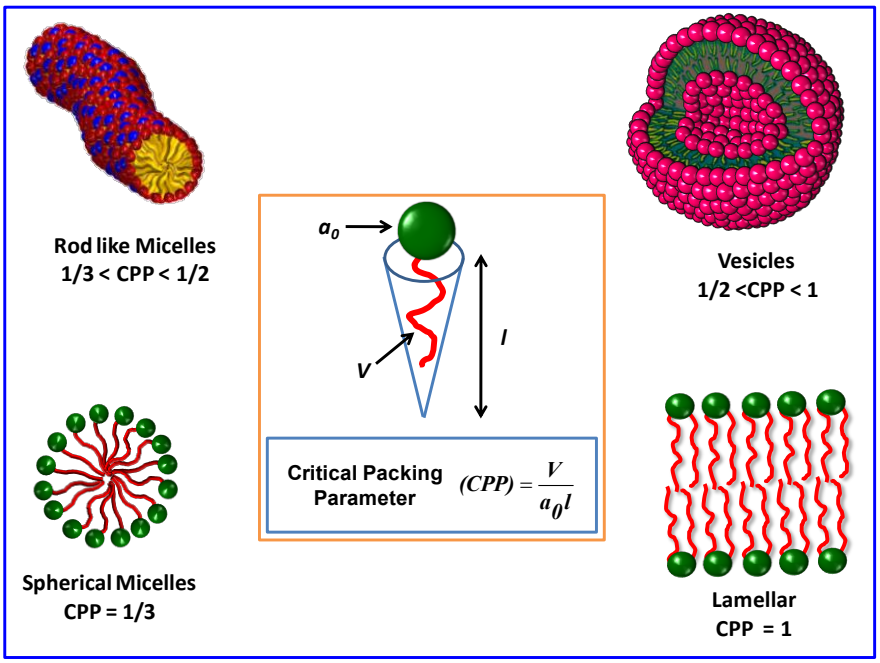

Figure 1.6 *Schematic representation of the relation between critical packing parameter and relevant shape factors that influence the morphology of amphiphilic nanocarriers.*

The amphiphilic self-assembly is not limited to water, but it can be observed in a wide variety of solvents like glycerol, ethylene glycol, formamide, molten salts, ionic liquids, deep eutectic solvents, etc. and the driving force for such association has been termed as "solvophobic effect" rather than the more specific hydrophobic effect found in water.[71] The advantage of self-assembly-based approach in creating functionalized surfaces is its ability to form equilibrium structures. Conventional nano-phase material production from the bottom-up approach involves the nucleation process from a supersaturated solution followed by the growth of the particles, and it imparts a maximum in the free energy vs particle size curve and hence particles are prone to agglomeration. This agglomeration or growth is prevented by competitive adsorption of stabilizing agents on the surface of particles. On the other hand, self-assembled structures such as micelles and microemulsions are the equilibrium

structures and hence possess a potential energy minimum. However, these structures are dynamic in nature. The dynamic processes involve an exchange of monomers with bulk and Brownian motion mediated collision of the aggregates. The ability of amphiphiles to adsorb at the interface or form structures with diverse morphologies makes it attractive candidates for the production of nanoscale materials in diverse applications including pharmaceutical formulations. An in-depth understanding about the factors governing the self-assembly and its ability to modulate the surface as well as bulk nanostructure goes a long way in designing materials for healthcare applications. Their advantage is in trapping drugs physically within the hydrophobic cores or linking drugs covalently to component molecules of the micelle.[72,73] Additionally, they proved to be an excellent novel drug delivery system due to their high stability in physiological conditions, high loading capacity, and high accumulation of drug at the target site.

1.4. Preparation of Nanocarriers

1.4.1 Synthesis Protocols for Nanoparticles

The synthesis of NPs is the most important component of nanotechnology and nanoscience. A high-throughput scalable process for NPs with controlled quality is required for their commercialization in various fields of applications. In the last decades, a lot of effort has been made into developing various methodologies for the preparation of NPs from a diverse range of materials. There are basically two approaches commonly employed to synthesize NPs: top-down (physical) and bottom-up (chemical) approaches. In top-down approach, the NPs synthesis is initialized with the bulk counterpart that leaches out systematically bit-after-bit leading to the production of fine NPs.[74] However, the bottom-up approach is the energy-efficient and preferred

method for fabricating a miscellaneous range of NPs which involves the assembling or coalescence of atoms and molecules.[74] Also some authors have reported the biological route (use of algae, bacteria, fungi, or plants) for synthesizing NPs.[75] The overview of different methods used for producing NPs is shown in Fig. 1.7 below.

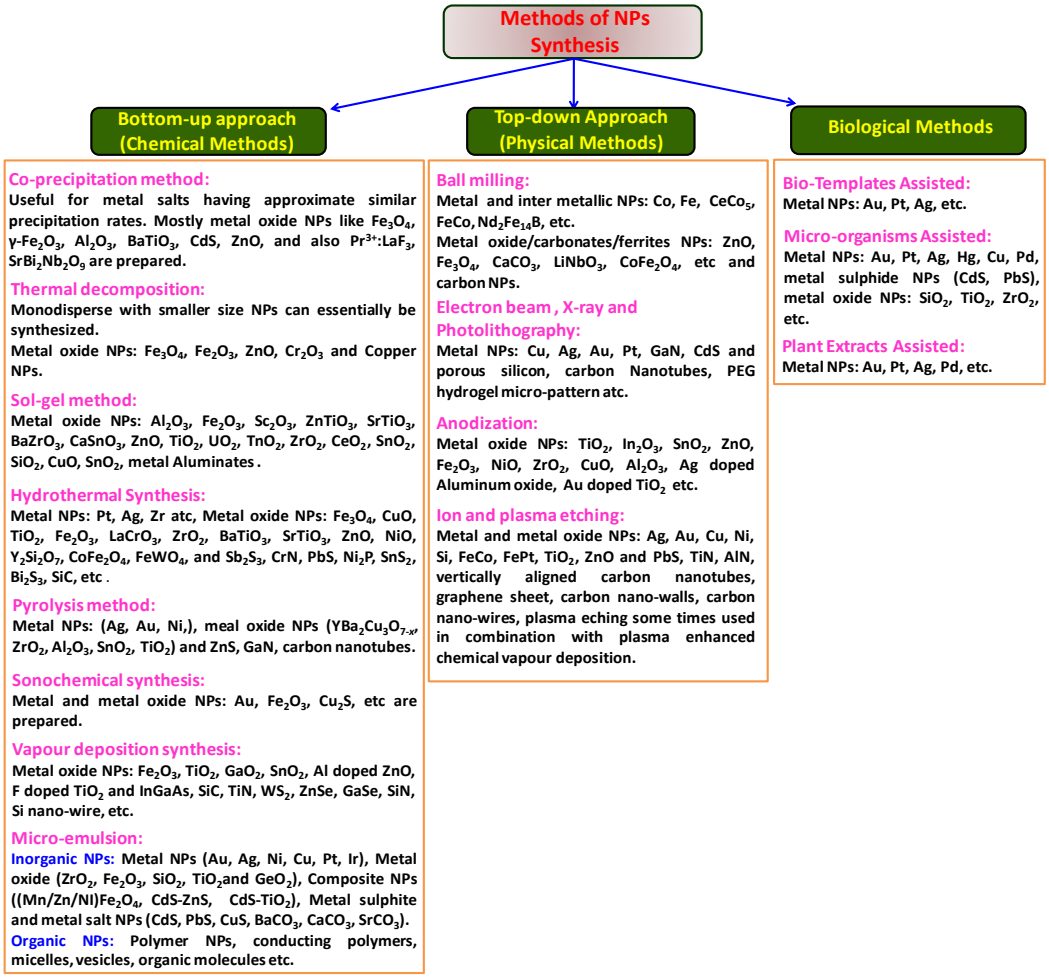

Figure 1.7 *Overview of different synthesis methods to produce a variety of NPs.*

a) Co-precipitation Method

The co-precipitation method is a convenient technique for attaining the required stoichiometry and phase purity in particles. Generally, it is a very effective method for the reactant's having good aqueous solubility and very similar

precipitation rates. However, this method can produce wide particle size distributions with mean sizes ranging from nm to a few microns, if the necessary precautions are not taken. A number of experimental factors such as ionic strength of the solvent, type of salts used, the ratio of molar ions, pH value of solvent, and kinetics of the reaction have a significant impact on the size, crystalline phase and structural morphology of NPs. By controlling these experimental parameters, one can easily tune the size, shape, and composition of the NPs.[76] The key steps involved in the co-precipitation method are:(1) achieving the conditions of high supersaturation by changes in experimental conditions (2) nucleation of a large number of tiny particles and (3) Ostwald ripening and/aggregation or growth of the particles. In fact, this method is a facile and convenient approach to prepare various types of inorganic NPs like metals, oxides, and their composite. Mostly, inorganic metal salt, like chloride, sulfate, and nitride, etc. are used as a precursor for the synthesis of inorganic NPs. The dissolved metal ions in water exist in the form of metal hydrate species and NPs precipitated out by the addition of reducing agents or alkaline bases such as aqueous ammonia or ammonium hydroxide or sodium hydroxide at mild temperature (60-90 ^{o}C). To avoid the critical oxidation of formed metal oxide NPs, inert gas (Argon/Nitrogen) was purged through the reaction solvent. Purging of inert gas not only protects against oxidation of the NPs but also helps to reduce the particle size.[77]

A typical chemical reaction for the formation of oxide by co-precipitation method is:

$$A^{2+}\,(aq.) + B^{3+}\,(aq.) + 8OH^{-}\,(aq.) \rightarrow AB_2O_4\downarrow\,(solid) + 4H_2O$$

Where A and B are the metal salts of Fe, Mn, Co, Cu, Mg, Zn, Ni, etc. AB_2O_4 be the insoluble metal oxide NPs formed in the solvent.

Massart et al. reported the synthesis of magnetic nanoparticles (MNPs) in acid and alkaline media, way back in 1981.[78] Till date, this approach is followed to obtain

the MNPs, especially, iron oxide and its composites.[79] Kang et al. reported that a mono-dispersed, and narrow size distribution IONPs can be prepared by co-precipitation method without any surface passivation in an alkaline aqueous solution (pH = 11-12) with a molar ratio of Fe^{2+}/Fe^{3+}= 0.5. The colloidal suspensions of γ-Fe_2O_3 can be obtained by aeration of Fe_3O_4.[80] It may be noted that metal oxide NPs obtained by this way are often not colloidally stable and hence surface passivation is required. In recent years, several reports have described the use of various coating agents such as multi-functional organic and inorganic entities like sugars, polyols, vitamins, amino acids, polysaccharides, surfactants, functionalized polymers, proteins, peptides, antibodies, silica and gold etc. to obtain stable metal oxide NPs. These coating ligands act as protecting agent for controlling the particle size and stabilizing the colloidal dispersions. Providing a proper coating and developing effective protection strategies is the key to the successful application of NPs.

The advantages of the co-precipitation method are high yield and product purity, lack of necessity to use organic solvents, and low cost. However, this method also have some disadvantages such as inapplicability to insoluble precursors, contamination by trace impurities precipitated with the product, problems in batch-to-batch reproducibility, etc.

b) Thermal Decomposition Method

Thermal decomposition is a non-aqueous, innovative method to synthesize stable inorganic NPs. In this method, high-boiling organic solvents (260-320 ^oC) are used for the thermal decomposition of metal salt or precursors which often leads to size-controlled NPs.[81] Mostly, in this method the precursors/molecules containing zero-valent metals such as metal carbonyls (e.g. $Fe(CO)_5$, $Mn(CO)_5$), acetate salt

($Fe(acac)_3$) (acac=acetylacetonate), etc. are used for the thermal decomposition.[82] To control the size distribution of metal oxide NPs using this method, experimental factors like reaction time, temperature, concentrations of the reactants, stabilizers, and capping agents needs to be optimized.[83] The stabilizer molecules used in this reaction are usually long-chain fatty acids with at least one functional group. This functional group, either an amine group or a carboxylic acid, usually bound to the NPs surface and provide the hydrophobicity to synthesized NPs. Rao et al. reported that capping agents, such as carboxylic acids and alkyl amines, influence the polydispersity of NPs obtained from the same method.[81] Sun et al. demonstrated that thermal decomposition of $Fe(acac)_3$, with 1,2 hexadecanediol in the presence of oleic acid and oleylamine can be used to make monodisperse and highly crystalline IONPs with size ~20 nm and high magnetization ability.[82]

Although the thermal decomposition method has many advantages for producing highly monodispersed NPs with a narrow size distribution, it has the big disadvantage that it employs relatively expensive organic compounds as precursors, and the reaction process requires elevated temperature and tedious procedure. Further, the obtained NPs are mostly dispersed in non-polar solvents (such as hexane or cyclohexane). For use in biomedical applications, adequate further surface modifications are essential to enable the water-dispersibility and biocompatibility of these NPs. In this context, Lattuada and Hatton demonstrated the ligand-exchange method in which hydrophobic capping agent initially present on the NPs surfaces were replaced via reaction with various capping agents bearing reactive moieties.[84] This route was proposed as a flexible methodology for the preparation of various types of monodisperse, water-soluble NPs.

c) Hydrothermal/Solvothermal Method

The hydrothermal method is also a popular soft-chemical approach to synthesize inorganic NPs from aqueous solution under relatively high temperature (from 130 to 250 ºC) and at high pressure (from 0.3 to 4 MPa) in a sealed pressure vessel.[85] This reaction can be performed in batch or continuous mode. If the aqueous solution is replaced by the organic solvent under similar conditions to fabricate NPs, then it is called as solvothermal method. In general, this method employs an inorganic salt, reducing agent/oxidizing agent, and one or more stabilizers in a reaction system under high temperature to prepare NPs. The reaction parameters such as temperature, pressure, time, reactant concentration, and pH of solvent can be tuned to attain satisfactory nucleation rates and particle size distribution. Inorganic NPs of metals, metal oxides, chalcogenides, and various materials have been prepared by using the hydrothermal or solvothermal process. This method is normally inexpensive and has the capability to synthesize a huge amount of NPs with controlled size, morphology, composition and surface chemistry. For instance, Du et al. reported the single-step synthesis of Pt NPs using the hydrothermal method and observed excellent electro-catalytic activity.[86] Wang et al. described the hydrothermal method to prepare IONPs having size ~40 nm and possessed a maximum saturation magnetization of 85.8 emu g^{-1}.[87] Qiu et al. fabricated core-shell Fe_3O_4@ZnO@$mSiO_2$ nanocarriers with a mean particle size of 170 nm using the solvothermal method and used as DDS in cancer therapy.[88]

Although the hydrothermal technique is very versatile, one of the main disadvantages is the slow reaction kinetics (by 1-2 orders of magnitude). Komarneni et al. introduced the microwave heating during the hydrothermal synthesis and this has been found to increase the kinetics of crystallization. He revealed that the introduction

of microwaves into a reaction system there is a dramatic increment in the reaction kinetics, under hydrothermal conditions, due to the localized superheating of the solution.[89]

d) Sol-Gel Method

The sol-gel processing method is a cost-effective colloidal technology, mostly employed for the preparations of metal oxide NPs as well as metal oxide nano-composites. This method consists of the chemical transformation of a liquid (sol) into a gel state and with subsequent post-treatment, it transforms into solid oxide material. The steps involved in the sol-gel method are mixing, casting, gelation, aging, drying, and densification. This process involves the hydrolysis and condensation of metal precursors in which the former uses a solvent to disintegrate the bonds of the precursor while the latter process leads to the formation of nanomaterials. The synthesis of NPs using this process can be done either in the aqueous or non-aqueous medium. In the aqueous sol-gel method, water molecules are the source for the supply of oxygen in the formation of the oxide. In the non-aqueous process, oxygen is provided by a solvent (ethers, alcohols, ketones, or aldehydes) or by an organic constituent of the precursor (alkoxides or acetylacetonates).

The reactions in a typical sol-gel process using organometallic precursors can be given as follows:

$$M(OR)_x + mH_2O \longrightarrow M(OH)_x + mROH \text{ (hydrolysis)}$$

If *x* and *m* are equal, the reaction is said to be of total hydrolysis. This can happen in two stages, either by water or alcohol condensation.[90]

$$2M(OH)_x \longrightarrow M\text{-}O\text{-}M + xH_2O \text{ (water condensation)}$$

$$M(OR)_x + M(OH)_x \longrightarrow M\text{-}O\text{-}M + xROH \text{ (alcohol condensation)}$$

where, M = Si, Zr, Ti, Zn, Fe, etc.

The preparation of NPs by this method has gained increasing interest, due to simplicity, low cost, reliability, repeatability and relatively mild conditions of synthesis. Optimization of the synthesis parameters such as precursors, solvent percentage, water percentage, reflux temperature, reflux time, calcination temperature, sol drying method, etc. are important for the fabrication of NPs by this method.[91] Barick et al. developed pure and doped ZnO nano-assemblies by heating acetate precursors in diethylene glycol medium.[92] He observed that the incorporation of dopant and co-dopants into the ZnO structure can modulate the local electronic structure due to the formation/activation of defects, which are responsible for significant changes in their structural, vibrational, optical and magnetic properties. del Monte et al. obtained γ-Fe_2O_3 NPs in a size range of 6-15 nm by direct heat treatment of gels at 400 °C.[93] Apart from them, sol-gel is also a promising method for the synthesis of a variety of NPs such as iron oxide, metal-aluminate, Fe-Co, ZrB_2, $GdVO_4$, Ta_2O_5, etc.[74]

e) Sonochemical Method

Production of NPs by passing the ultrasound to the chemical reaction medium is called as sonochemical process. It is a competitive alternative extensively used to generate novel materials with unusual properties. In this method, a high-intensity ultra-sonication is used to from acoustic cavitations, that is, the formation, growth, and implosive collapse of bubbles in the liquid. When sonicating liquids at high intensities, the sound waves that propagate into the liquid media result in alternating low-pressure (rarefaction) and high-pressure (compression) cycles, with rates depending on the frequency. During the low-pressure cycle, high-intensity ultrasonic

waves create small vacuum bubbles or voids in the liquid. When these bubbles attain a volume at which they can no longer absorb energy, they collapse violently during a high-pressure cycle. This phenomenon is termed cavitation. The implosive collapse of the bubble generates a localized hotspot through shock wave formation or adiabatic compression within the gas phase of the collapsing bubble. The conditions formed in these hotspots have been experimentally determined, with transient temperatures of 5000 K, pressures of 1800 atm, and cooling rates over 1010 K/s.[94] The physical effects of cavitation are being used for the top-down generation of NPs, where particle size is reduced by the forces of cavitation. This includes the breaking of agglomerates and aggregates. The physical effects are used in combination with the chemical effects in the bottom-up production of NPs and crystals, i.e. during precipitation or crystallization. The nuclei formation and growth of NPs take place at this temperature and pressure via collapsing of bubbles, which is prone to prepare the highly mono-dispersive NPs. Here, ultrasound serves a number of roles in the initiation of seeding and subsequent crystal formation and growth. The majority of nanomaterials produced by this method are pure metals and metal oxide NPs having a variety of size and structural morphology.[95,96]

A major advantage of this methodology is that the shape and size of the NPs can be adjusted by varying the operating parameters like ultrasonic power, current density, deposition potential and the ultrasonic vs electrochemical pulse times. Together with these, it is also possible to adjust the pH, temperature, and the composition of the electrolyte in the sono-electrochemistry cell.[97] Even though various metal and metal oxide NPs have been prepared by the sonochemical approach, their large-scale synthesis is still not yet achieved.

1.4.2 Surface Functionalization of Nanoparticles

For biomedical applications and the storage of NPs, stability is of the utmost important factor. Due to the high surface to volume ratio, NPs have a particular tendency to lower their surface energy, which is the origin of their thermodynamic instability. Bare NPs tend to stabilize themselves by decreasing their surface energy either by sorption of molecules from the surroundings or by lowering the surface area through coagulation and agglomeration. In order to avoid the latter, NPs can be kinetically stabilized with repulsive interactions (like electrostatic, steric, and their combination electro-steric repulsive) by using appropriate stabilizers. The type of stabilizer used affects the selection of further bio-functionalization strategies, as for certain strategies, the good colloidal stability at a broad range of pH and ionic strength is required. Selecting the most adequate bio-functionalization strategy is not an easy task since no universal methodologies exist to cover the wide variety of NPs and biomolecules available for this purpose. A functionalization protocol that works well for one type of nanoparticle may not work for another, since they could be very different in terms of size, charge, surface area, colloidal stability, density and type of reactive groups, etc. Furthermore, biomolecules vary significantly in terms of size, chemical composition, three-dimensional complexity and location of its biological active site. Each particular case of NPs conjugated to biomolecules requires optimization of the protocol. Thus, in addition to the synthesis of NPs, it is vital to focus on the development of smart multi-functionalization strategies. These NPs should be able to deliver a therapeutic agent based on environmental changes or remote stimuli. Although a wide variety of NPs can be stabilized by a verity of stabilizers, mostly they can be classified under inorganic or organic stabilizers.

a) Organic Stabilizers

Organic compounds are often employed to functionalize the surface of the NPs during or after the synthesis to avoid agglomeration. In the absence of any proper surface coating, van der Waals interactions between the NPs will cause them to aggregate and form large clusters, resulting in increased particle size. Mostly used organic compounds for the functionalization of inorganic NPs are small chain organic ligands (like vitamins, amino acids, sugars, sugar alcohol, etc), polysaccharides, surfactants, functionalized polymers, dendrimers, and biomolecules like proteins, peptides, antibodies, etc. Moreover, these organic stabilizers can provide the reactive functional groups, e.g. hydroxyl, thiol, aldehyde, amino, and carboxyl groups, which can conjugate to the active biomaterials such as protein, antibody, DNA, enzyme, etc., in order to expand the potential biomedical application of NPs in several areas. The structure of organic compounds functionalized NPs consists of two major parts: core and shell. The core part preserves the characteristic properties of NPs, while the shell part imparts colloidal stability and conjugation moiety.

The ligand molecules bound to the NPs surface not only control the growth of the particles during the synthesis but also prevent the aggregation of the NPs. The colloidal stability to the particle may be provided by electrostatic repulsion, steric exclusion or a hydration layer on the surface. Depending on the NPs system, i.e. the core material and the solvent in which the particles are dispersed, the choice of the ligand is important to yield stable particles. The ligand molecules are bound with NPs surface by different modes such as attractive interaction, chemisorptions, electrostatic attraction or hydrophobic interaction. Large varieties of chemical functional groups possess a certain affinity to NPs surfaces. For instance, the most famous example is the passivation of gold NPs by using carboxyl and thiolated stabilizers.[98] Ibrahim et al.

prepared the gold NPs at room temperature by using gallic acid as a reducing agent in the presence of polyethyleneimine as a stabilizer. He observed that the particle size of the prepared gold NPs was decreased with an increase in the concentrations of polyethyleneimine.[99] He revealed that polyethyleneimine is not only acted as a stabilizer but also as a reducing agent. P Díaz-Núñez et al. prepared the highly concentrated silver NPs using femtosecond laser ablation in the presence of organic stabilizers like cetyltrimethylammonium bromide (CTAB), and polyvinyl pyrrolidone.[100] From the last few decades, several authors have reported the fabrication of IONPs by using organic ligand as a stabilizer. Shaoo et al. reported the surface-modified IONPs with an average diameter of < 10 nm by using oleic acid, lauric acid, dodecyl phosphonate, hexadecyl phosphonate, and dihexadecyl phosphate, etc., they found that alkyl phosphonates and phosphates could be used for obtaining thermodynamically stable dispersions of IONPs.[101] Polysaccharides such as dextran, starch, carrageenan, etc. are also known to passivate the surface of Fe_3O_4 NPs and render them colloidally stable.[102]

b) Inorganic Stabilizers

Although there have been many significant progresses in the preparation of organic materials functionalized NPs, simultaneous control of their shape, stability, biocompatibility, surface structure, and characteristic properties are still a challenge. As an alternative, inorganic compound functionalized NPs were also explored to enhance the anti-oxidation properties of naked NPs. The applied coating of inorganic materials includes silica, metal, non-metal, metal oxides, and sulfides. The interest arises from the possibility of combining the different properties by entrapping NPs in other inorganic compound layers, in a core-shell fashion. With a controlled structure

and interface interactions, nanocomposites can exhibit novel physical and chemical properties that will be essential for different biomedical applications.

Among the others, Silica is the most common material for preparing the surface-functionalized metal oxide NPs. Silica coating provides not only the stability to the NPs in solution, but also possess good biocompatibility, hydrophilicity, and stability. In addition, silica-coating helps in binding the various biological molecules at the NPs surface using silane chemistry. For instance, Ashtari et al. have reported an effective method for recovery of target ss-DNA-based on amino-modified silica-coated Fe_3O_4 NPs.[103] Yi et al. have developed a pathway to synthesize magnetic quantum dots-based on silica coating nanocomposite of γ-Fe_2O_3 NPs and CdSe quantum dots (SiO_2/γ-Fe_2O_3-CdSe), which have unique combination of magnetic and optical properties.[104] Noble metal such as gold is also often employed to passivate the surface of IONPs to avoid oxidation. It may be noted that the diameter of metallic or non-metallic functionalized IONPs is prone to tailoring, and the necessary diameter can be obtained by controlling the reduction time. For instance, Mandal et al. reported the coating of gold and silver on Fe_3O_4 MNPs by directly reducing the Au^+ and Ag^+, respectively, to achieve a long time stability of the MNPs.[105] The coating of gold not only provides the stability to the NPs but also provides the binding sites for biomolecules through the thiol group. Recently, Wu et al. have adopted this approach to prepare the monodispersed gold-coated Fe_3O_4 NPs via the sonolysis of a solution mixture of gold ions and amino-modified Fe_3O_4 NPs.[106] Stoeva et al. skillfully used core-shell type functionalized NPs (SiO_2/Fe_3O_4) that electrostatically attract 1-3 nm gold NPs seeds which act in a subsequent step as nucleation sites for the formation of a continuous gold shell around the NPs upon $HAuCl_4$ reduction.[107] Hong et al. synthesized the ZnO coated magnetite core-shell NPs by coating the Fe_3O_4 NPs with

direct precipitation using zinc acetate and ammonium carbonate.[108] He observed that the functionalized NPs have much better anti-oxidation ability than the naked Fe_3O_4 NPs.

Having noticed that both organic and inorganic coatings can be introduced to colloidal carriers, the main outcomes of the surface passivation can be summarized as follows: (a) Improves the biocompatibility, chemical stability and tailors the dispersibility in water, (b) Endows the NPs new physico-chemical properties that are advantageous for biomedical applications, and (c) Provides new functional groups to NPs for the subsequent binding with biomolecules such DNA, antibody, protein, etc.

1.5. Recent Developments in Nanotherapeutics

The quest for developing new therapeutic approaches and effective delivery systems for cancer management led to increasing interest in a wide range of nanomaterials. Some of the physicochemical properties that have been exploited for cancer therapy includes magnetic hyperthermia, magnetic targeting, photothermal therapy, photodynamic therapy, radiosensitization, receptor-mediated targeting, stimuli responsiveness, etc. In this context, magnetic nanoparticle-based targeting/therapy and amphiphilic DDS have taken a prominent place in terms of recent exploratory research.

1.5.1. Magnetic Nanoparticle-Based Therapy

Magnetic nanocarriers (MNCs) have become one of the key materials for cancer therapy due to its attributes such as high biocompatibility, superparamagnetic nature, superior heating ability under the AC field, etc.[109] Mostly, ferromagnetic or ferrimagnetic materials shows superparamagnetic behavior, having a single magnetic

domain and a high magnetic moment with isothermal magnetization against applied field with zero coercivity and remanence. These properties make it an attractive material for diagnosis, thermal therapy and a platform for combination therapy. Based on the response of the material under the influence of a magnetic field, materials properties can be classified as diamagnetism, paramagnetism, ferromagnetism, antiferromagnetism, and ferrimagnetism. The ratio of magnetization (M) to the applied magnetic field (H) is a measure of how susceptible the material is to become magnetized. This ratio is called the magnetic susceptibility (χ_m) of the material: $M= \chi_m H$. Diamagnetism occurs in materials possessing atoms and molecules that have no permanent magnetic moment. Diamagnetic materials have a very weak negative susceptibility, typically of the order of -10^{-6}. Some atoms or molecules, however, do have a permanent magnetic moment due to the presence of unpaired electron spins and such materials are paramagnetic. Often what one describes as magnetic materials are technically ferromagnetic. They too have permanent magnetic moments, but with the difference that these moments are not randomly oriented but are strongly aligned due to coupling between individual spins. This leads to the presence of magnetic domains in which the moments are parallel and are aligned with a particular direction. In an adjacent domain, again all the moments are parallel to each other but aligned in a different axis. The domains are separated by domain boundaries within which the orientation of the magnetic moments gradually changes from one to the next. The susceptibilities of ferromagnetic materials are typically of the order of 10^3 or 10^4 or even greater. The ferromagnetic susceptibility of a material is temperature-sensitive. Above a certain temperature known as the Curie temperature, the material ceases to become ferromagnetic, and it behaves as paramagnet.

Compared to others, iron oxide-based MNPs have gained momentum among cancer therapy researchers.[110] Typically, there exist six oxides composed of Fe and O such as magnetite (Fe_3O_4), hematite (α-Fe_2O_3), maghemite (γ-Fe_2O_3, β-Fe_2O_3, ε-Fe_2O_3) and Wüstite (FeO). Out of that Fe_3O_4 and γ-Fe_2O_3 are most studied and in particular Fe_3O_4 is found to be highly promising.[31,111] Below the curie temperatures (850 K) it is ferrimagnetic in nature and it has a cubic inverse spinel structure with oxygen (O^{2-}) forming a face centered cubic (FCC) lattice and Fe cations occupying interstitial tetrahedral (T_d) and octahedral (O_h) sites, as shown in Fig. 1.10. The bivalent Fe^{2+} ions occupy O_h sites and trivalent Fe^{3+} ions are equally distributed between O_h and T_d sites.[112] Below the Curie temperature, magnetic moments on T_d sites, occupied by Fe^{3+} are ferromagnetically aligned while on O_h sites, occupied by Fe^{2+} and Fe^{3+} are antiferromagnetic. Such combined effects are responsible for the ferrimagnetic nature of Fe_3O_4,[113] and that exhibits different magnetic properties depending on their particle size.

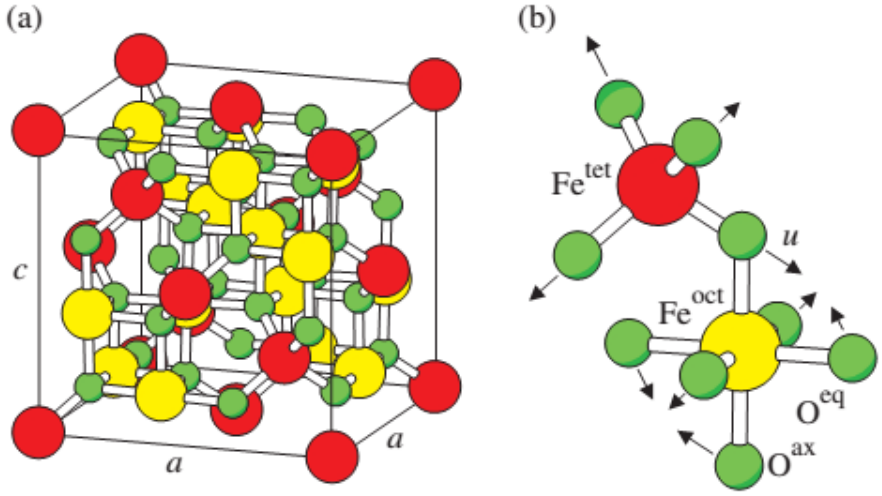

Figure 1.8 *(a) Inverse spinel FCC structure of Fe_3O_4, (b) Magnified view of one tetrahedron and one adjacent octahedron sharing an oxygen atom. Large spheres labeled by Fe^{tet} and Fe^{oct} represent iron atoms at T_d and O_h sites, respectively. Oxygen atoms are shown as small green spheres. [Figure is taken from ref:*[114]*]*

For effective utilization of Fe_3O_4-based MNPs in cancer therapy, several challenges needs to be met. The low stability of IONPs in aqueous solution and their destabilization due to the adsorption of plasma proteins are perhaps the first significant constraints for their therapeutic applications. Also, IONPs tend to lose their dispersity after long-term due to aggregation of particles and their magnetism gets diminished due to air oxidation. The next step is to achieve selective targeting of the system to the site of interest for the in-vivo studies. Thus different approaches are implemented to stabilize the IONPs in an inert atmosphere and also to make them water-dispersible at physiological pH, for applications in nanomedicine. Recent advancements in nano-medicine have made it possible to provide treatment modalities that are more effective for cancer therapy. Superparamagnetic iron oxide nanoparticles (SPIONs) can easily gain access to various areas of the body without interfering into normal functions and it has enjoyed widespread attention for numerous *in-vitro* and *in-vivo* applications using targeted drug delivery and temperature-based repression of cancer cells. For instance, Islamian et al. reported the superparamagnetic mesoporous hydroxyapatite coupled DOX and deoxy-D-glucose nanocomposites to boost breast cancer chemo and radiotherapy.[115] Compared to radiotherapy alone, such a combination approach showed significant improvement with minimum side effects and damage to normal healthy cells. In another approach, Ye et al. recommended that Fe_3O_4 NPs can increase the efficacy of Cryo-ablation; a process that uses extreme cold conditions to treat cancerous cells.[116] Fe_3O_4 NPs show promising results to enhance the cryoablation which can be successfully applied to effectively treat tumors. The drug resistance shown by cancer cells restricts their chemotherapeutics success. In this context, Yan Zhang et al. synthesized a nanocomposite comprising of Fe_3O_4 core and polymeric shell covered with PEG, and folate groups and the chemotherapeutic drug

Cis-platin was encapsulated into the shell through coordination of amino groups.[117] They reported the cytotoxic response in HeLa cells through ligand-mediated targeting of folate receptors which is overexpressed on HeLa cells. Furthermore, Ebrahimi et al. have established a PLGA-PEG copolymer system by emulsion method, which encapsulated Fe_3O_4 NPs with DOX, and showed the controlled release of DOX in tumor cells.[118] Both Yan Zhang et al. and Ebrahimi et al. reported the high drug release at acidic pH and their formulations were found to be effective as a chemopreventive and chemotherapeutic agent for the treatment of lung and other solid tumors. For targeted chemotherapy, Xupeng et al. fabricated a multifunctional nanocomposite consisting of polydopamine passivated Fe_3O_4 NPs conjugated with epidermal growth factor receptor antibody, and loaded with anticancer agent DOX. This nanocomposite exhibited wide applications in the diagnosis, targeting, and chemo and photothermal therapy of cancer.[119] Jia et al. constructed a nanocarrier with PLGA polymer encapsulating IONPs and DOX, and performed the drug internalization study in multiple cancer cell lines such as human osteosarcoma (OS-732), Lewis lung carcinoma (LLC), and murine-leukemic monocyte-macrophage (RAW-264.7) cell lines.[120] It was reported that IONPs-DOX composite was internalized in cells in higher amount with respect to DOX alone. To cross the BBB and treat the leukemia and neuroblastoma effectively, Xuhua et al. synthesized Daunorubicin functionalized Fe_3O_4 NPs and reported that it has the ability to cross the BBB by increasing the barrier permeability.[121]

In addition to its use as a carrier, the MNPs capacity of converting the energy of AMF into heat and the extra sensitiveness of tumor cells to an increase in temperature opens new opportunities for cancer care. Since the late 50's, when Gilchrist et al. first reported the use of MNPs to heat tissue samples,[122] magnetic

hyperthermia has evolved considerably and is a key area of interest in cancer therapy with several studies showing the benefit of employing magnetic materials in hyperthermia strategies. Several groups have reported noteworthy results in clinical trials where magnetic hyperthermia shows effectiveness in tumor cell destruction with impressive targeting, thus minimizing the side effects of chemotherapy.[123,124] Magnetic nanoparticle-mediated hyperthermia is a therapeutic technique used for cancer treatment by deactivation/killing (dead or driven to apoptosis) without affecting the healthy (normal cells). Typically, the superparamagnetic Fe_3O_4 NPs are injected into the tumor site and are subjected to an external ACMF which raises the temperature of the tumor up to 42-48 ^oC. In combination therapy, at this temperature range, the generated heat can also increase the efficacy of different chemotherapeutic drugs. Therefore, the combination of conventional chemotherapy with hyperthermia provides a promising strategy, which can have synergistic therapeutic effects on tumor cells and reduce the required effective doses of anticancer drugs. The applications of an external AMF on MNPs evoke magnetization reversal, and the production of thermal energy is continuously measured in terms of the specific absorption rate (SAR) as the NPs return to their relaxed states. In this context, the development of a novel hyperthermia agent with both high biocompatibility and high heat transfer efficiency is of utmost importance for the application of magnetic hyperthermia.

The contrast mechanism for probing the tumor vasculature, including the use of exogenous MR contrast agents, is a result of changes in the MR signal intensity by changes in tissue relaxation times (T_1 and T_2). Briefly, T_1, be the spin-lattice or longitudinal relaxation time, and it is the time constant that characterizes the exponential process by which the magnetization returns or relaxes to its equilibrium position. T_1 relaxation occurs at the molecular levels including interactions between

protons in tissue water and those on macromolecules or proteins, and by interactions with paramagnetic substances. However, as protons diffuse through the inhomogeneous microscopic field, they also lose phase coherence due to their Brownian random motions through the magnetic field gradients, which result in phase dispersion that cannot be reversed by the application of a refocusing pulse. This process is known as T_2 relaxation. IONPs have also been used as T_2 contrast agents for more than 25 years. During the last decades, superparamagnetic IONPs were developed for limited and well-defined clinical applications such as MR angiography, tissue perfusion studies, and atherosclerotic plaque and tumor imaging. Several superparamagnetic IONPs formulations for intravenous or oral administration have been approved for clinical use as MRI contrast agents by the EMEA and FDA.[125] Gastromark® (AMAG Pharmaceuticals, Waltham, MA, USA: ferumoxytol, silicone-coated superparamagnetic IONPs), is a currently marketed formulation for gastrointestinal bowel marking using MRI. The most widely applied coatings for FDA-approved superparamagnetic IONPs are dextran and carboxydextran. Further, it enables the non-invasive MRI of cell trafficking, gene expression, and cancer. In addition, the FDA approval of iron supplement ferumoxytol (Feraheme) has led to a renaissance of ultra-small SIONPs for a variety of imaging applications and gained considerable interest as an MR contrast agent. Ferumoxytol is composed of SIONPs with strong T_1 and T_2 relaxivities, and therefore can be used "off label" to enhance soft-tissue contrast on MR images. In fact, ferumoxytol was originally designed as an MR contrast agent but was later developed for anemia treatment.[126] The ultra-small SIONPs have been tested as blood-pool agents because they are readily distributed in the intravascular extracellular space. In this way, USIONPs are used as a contrast for lymphography[127] and angiography,[128] as a bone marrow contrast, or as a perfusion

agent in the brain and kidney. The SIONPs with a core of < 10 nm in diameter are capable of producing positive contrast in T_1-weighted images when administered in moderate concentrations,[129] and this benefit is at the expense of their T_2 effects.[130] Despite the extensive reports and commercialization of IONPs as MRI contrast agents, its application in hyperthermia and combination therapy are still in the research stage. This is primarily because of the lack of stability, specificity, and poor drug loading ability. Therefore, efforts are needed to develop a suitable surface functionalization strategy for IONPs so as to make them amenable for targeted hyperthermia and site-specific delivery of active ingredients.

1.5.2. Amphiphile-Based Drug Delivery Systems

The association of amphiphiles in solvents gives rise to a rich variety of structures such as micelles, vesicles, solid lipid nanoparticles, microemulsions, liquid crystalline dispersions, etc. These phases have a unique structure in which the hydrophilic or hydrophobic compartments with a dimension of a few nm to sub-micrometer are dispersed in a solvent. It is noteworthy that some of these structures exist in a thermodynamic equilibrium state, as opposed to kinetically stabilized NPs. These structural features of amphiphilic assemblies make them efficient carriers for the encapsulation of several drug molecules. The most common structures used in drug delivery applications include micelles, liposomes, and lipid particles. One of the classic examples of micelles in clinical trials is NK911, developed from a block copolymer of PEG and polyaspartic acid and bound anticancer drug doxorubicin for metastatic pancreatic cancer treatment.[131] Another example is NK105, consisting of paclitaxel which was investigated for pancreatic, colonic and gastric tumor treatment.[132] To develop polymer-drug conjugates mostly used polymers are PEG,

PLGA, HPMA, gelatin, and Dextran. As a result of the high surface area to volume ratio of these nanoparticles; it is quite possible to achieve high ligand density on the surface of these nano-carriers for active targeting purposes. Several mixed micelle formulations comprising amphiphiles, lipids and block copolymers were also explored for improving the therapeutic efficacy of various drugs through different routes of administration. Mixed micelles usually have diameters < 60 nm, which prevents their uptake by the RES, increases it's *in-vivo* circulation and facilitates their extravasations in sites with leaky vasculature such as tumors.[133] Therefore, they have been particularly employed for parenteral delivery of hydrophobic drugs. The interaction between micelles and lipophilic drugs leads to the formation of swollen micelles and sufficiently stable to be used for drug delivery. The classical example of the mixed micelle-based formulations currently available in the pharmaceutical market are, Valium®MM and Konakion®MM.[134] Also the bile salts micelles and derived mixed systems are intensively investigated as drug-carrier systems to enhance the transport of lipophilic drugs across biological membranes and thereby enhance oral bioavailability.[135]

Liposomes are closed vesicles surrounded by a lipid bilayer membrane composed of phospholipids. These vesicles are uni/muti-lamellar and have the potential to carry both hydrophilic and lipophilic drugs. Their hydrophilic core can be used for the entrapment and delivery of water-soluble drugs, while lipid bilayer entraps the lipophilic drug molecules. A hydrophobic wall, or a barrier, protects the loaded molecules from the external solution. The wall can also act as a "gate" that controls the diffusion of molecules in and out of the vesicle. By tuning the permeability of this "gate", the extent of loading and release from vesicles can be controlled. A separate field of liposomal technology research was started by the

approval of first nano-sized liposomal product Doxil® for IV administration which is a big hit in the market. Doxil® was approved by the U.S. FDA in 1995 for the treatment of Kaposi's sarcoma, refractory ovarian cancer, and breast cancer.[136] Later, Nexstar Pharmaceuticals USA also developed a liposomal product, DaunoXome®, for the delivery of daunorubicin, which was approved in 1996 by the U.S. FDA for the management of advanced HIV-associated Kaposi's sarcoma. Subsequently, a few more products have become available for the management of various cancers. These products include Depocyt® by SkyPharma Inc., Mepact® by Takeda Pharmaceutical, Myocet® by Elan Pharmaceuticals and Marqibo® by Talon Therapeutics.[137] Surface modification of the liposomal system with hydrophilic PEG coating enables to escape the uptake of RES efficiently and increases the circulation time in the blood. Coatings of hydrophilic polymers create a cloud of chains at the liposomal surface which repels plasma proteins and inhibits their adsorption, resulting in evading RES uptake. Formulations of PEGylated liposomal doxorubicin known as Doxil have shown to escape RES uptake and prolong liposome circulation time significantly. Non-PEGylated liposomes undergo the greater breakdowns in blood and more rapid clearance via the RES compared with PEGylated liposomes. In spite of these developments, number of chemotherapeutic drugs that use amphiphiles-based carriers are still limited. This is primarily due to the increased productions cost of ingredients and technologies that add enormous cost to the product. Thus, there exists a demand for identifying suitable amphiphiles and processes that can efficiently encapsulate anticancer drugs and deliver them to the site of action. The superior biocompatibility of lipids and many natural amphiphiles makes it an attractive candidate for future studies.

1.6. Gap Areas and Objectives of the Thesis

From the above discussions, it is obvious that MNPs and amphiphiles-based delivery systems offer an attractive options in the management of cancer. Although drug delivery systems result in a substantial improvement in the therapeutic index of anticancer agents, still further improvements need to be required. As a result, further development and refinement of therapeutic modes and drug delivery systems are essential for improving therapeutic outcomes. Some of the desirable features one should keep in mind while designing such drug carriers are (i) sufficient biocompatibility and biodegradability; (ii) good colloidal stability in physiological conditions; (iii) high drug loading capacity and low toxicity; and (iv) stimuli-responsive characteristics for the delivery of pharmaceuticals. Though there have been various reports on synthesis and surface modification of nanoparticles, as discussed above, there is a pressing need to develop various biocompatible coatings, in a cost-effective and scalable manner. Moreover, the effect of surface modification on the inherent properties of the material needs to be investigated so as to fine-tune the formulation for efficacy and biodistribution. Improved colloidal stability, resistance to protein adsorption, good specific absorption rate, effective heat transport, controlled drug release, minimize side effects, etc. are some of the important points that are envisaged in a new formulation. This has stimulated the quest for new protocols and binding ligands in the preparation of MNPs. Further, the main drawbacks connected with currently available methods used for liposomes preparation are the use of one or more organic solvents to achieve adequate distribution of the constituents of the lipid bilayer. When liposomes are administered intravenously, as a drug delivery vehicle, it should be free from any organic solvents. Due to the toxicity and flammability, the uses of organic solvents are undesirable and also have negative implications in terms

of cost, safety, and environmental impact. The use of water-immiscible organic solvents puts additional constraints with respect to workplace safety and release to the environment. In addition, the stability of liposomes during production, long-term storage and reproducibility for scale-up are also a matter of concern.[138,139] The surface charge of the liposomes needs to be controlled to enhance transfection efficiency. Thus, there is a need to devise methods for producing liposomes having improvements in safety, stability, and desired interfacial properties.

In view of this, this thesis attempts to address some of these issues. The main objectives of the current thesis are:

1. Explore the use of biocompatible ingredients such as sugar-alcohols, vitamins, and proteins for surface functionalization of magnetic nanoparticles and assess their colloidal stability and magnetic properties for cancer therapy.
2. Develop suitable surface functionalization strategies for Fe_3O_4-based magnetic nanoparticle system that can selectively release anticancer drugs like doxorubicin hydrochloride (DOX) at the tumor site due to changes in intracellular pH.
3. Exploration of new matrices for self-assembly of amphiphiles to prevent agglomeration of nano-drug delivery systems and to develop a suitable methodology to prepare colloidally stable liposomal formulations with tunable surface charge and improved drug loading efficacy.

The experimental findings to meet the above mentioned objectives and inferences derived from them are included in this thesis. Specifically, this thesis addresses the development of a biocompatible coating on Fe_3O_4 MNPs for site-specific release of chemotherapy drugs and hyperthermia. Moreover, attempts were made to develop surface charge controlled liposomes without using volatile/toxic and flammable organic solvents.

CHAPTER 2

EXPERIMENTAL TECHNIQUES

2.1. Introduction

This chapter provides a brief overview of key experimental techniques employed to reveal the topographic, morphological, structural, chemical or physical details and interfacial characterization of nanocarriers reported in the current thesis. From the perspective of structural and morphological evaluation, a wide variety of techniques are employed depending on the length scale of investigation. Fig. 2.1 shows a schematic illustration of the length scales associated with different nanocarriers and appropriate tools that can be employed to probe these structures. The different characterization techniques can probe different size objects, at a length scale from the Angstrom level to the micrometers. Some of the materials that are commonly employed for pharmaceutical applications, with a size range in the submicron level are also indicated in the scheme. It may be noted that both electron microscopy and scattering techniques complement each other in deducing the structural information of sub-micron size objects.

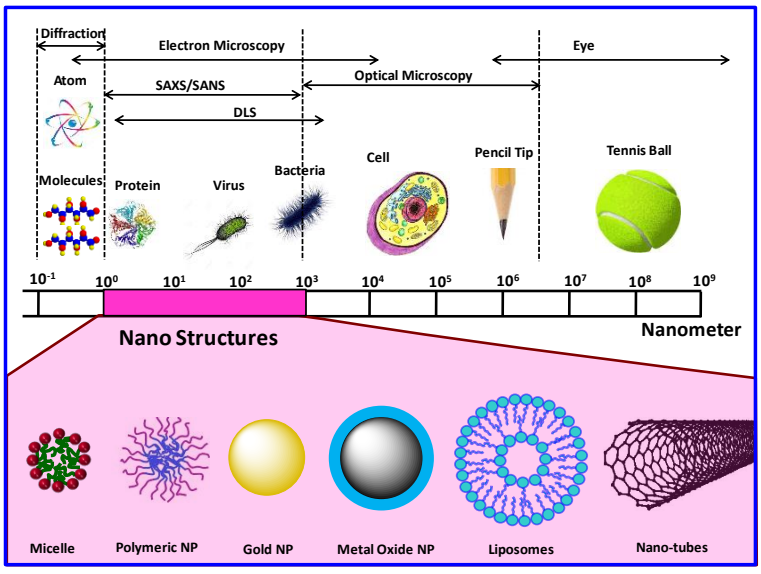

Figure 2.1 *Overview of typical characterization tools and the corresponding size range of various objects. A few colloidal drug delivery vehicles are also indicated as an inset.*

Since the present thesis deals with a variety of colloidal structures with a size range of 1–10^3 nm length scale, the emphasis has been given to those techniques that can probe such structures. Some of the nanocarriers discussed in the current work are functionalized Fe_3O_4 MNPs, micelles, liposomes, etc. In order to explore their potentials as a drug carrier or for other therapeutic purposes, it is important to get detailed knowledge about the physicochemical properties of these systems. The morphology and structural properties of inorganic materials such as MNPs were obtained from TEM, X-ray diffraction, etc. while organic materials such as micelles and liposomes were probed by small angle scattering (SAS); i.e small angle X-ray scattering (SAXS) and small angle neutron scattering (SANS). Transmission Electron Microscopy (Cryo-TEM, HR-TEM, and TEM) was also used to complement the results obtained from scattering. The colloidal stability and hydrodynamic radii of nanocarriers were monitored by dynamic light scattering (DLS) measurements. The changes in the interfacial characteristics of the nanocarriers, presence of organic moieties as well as the functional groups and their surface ionization, etc. were obtained from zeta-potential, thermogravimetric analysis (TGA) and FTIR spectroscopy. UV-visible and Fluorescence spectroscopy have been adopted to investigate the drug loading and release behavior of these nanocarriers. In addition to the above-mentioned characterizations, some of the specific nanocarriers were subjected to Magnetic susceptibility measurements, optical microscopic studies, protein adsorption studies, and biocompatibility investigations. The fundamental principles and necessary equations employed in interpreting the data, especially scattering studies, were incorporated in this chapter.

2.2. Scattering Techniques

Scattering of electromagnetic radiations such as light, X-rays, or neutrons (wave-particle duality) provides useful information about size, shape, and interactions among particles. The characteristic scattering pattern will be observed due to the difference in the scattering power of the specimen with respect to the matrix and interference of the waves from different regions of the scattering objects. The scattering power of the objects depends on the nature of radiation used; viz difference in refractive index in case of light, electron density in case of X-rays and neutron scattering length density in the case of neutrons. The theoretical basis of scattering remains the same, irrespective of the nature of the radiation, the only difference being the probing length scale due to the difference in wavelength and the scattering power of the objects. Early light scattering experiments started in the late 19th century, with research in colloidal suspensions by John Tyndall, leading to the manifestation of the Tyndall effect.[140] Lord Rayleigh (John William Strutt) reported the wavelength dependence of light scattering with particles whose dimensions smaller than its wavelength and explained the blue color of the sky due to scattering by atmospheric particles.[141] For larger particles relative to the wavelength of light, Gustav Mie developed a theory to study the light scattering from absorbing and non-absorbing particles, considering particle shape and the difference in refractive index between particles and the medium where they are dispersed.[142] The small particles tend to scatter light more evenly in all directions whereas larger particles tend to favor scattering in the forward direction. Moreover, the particle size has a strong dependence on the absolute intensity of light scattered; colloidal particles scatter incident light proportional to the 6th power of their radii.[143] The angular dependence of scattered light and its impact on particle size has also been reported. For the particles,

with dimensions <1/10th of the incident light wavelength (i.e. λ/10), the scattered light is isotropic in all directions, i.e angle independent (Rayleigh scattering).[144] However, when the size of the particles exceeds this threshold of λ/10 then Rayleigh scattering is replaced by anisotropic Mie scattering where the scattered light is angle-dependent.[145] For large particles, in the Mie scattering region, due to constructive interference in the forward direction, scattered light is most intense towards the direction of the incident light.[146]

To describe the interaction of light, X-rays and neutrons with the matter, one has to consider dual nature (particular as well as a wave) of the radiation. It is fairly simple to understand the origin of the light scattering phenomenon by using the classical wave nature of light. An electromagnetic wave consists of periodic oscillation of electric and magnetic field strength both in space and time (t). The variation in the electric field strength of a linearly polarized light of wavelength λ, and velocity c, propagating in the x-direction, can be written as.

$$E(x,t) = E_0\left\{sin\left(\frac{2\pi x}{\lambda}\right) + sin\left(\frac{2\pi\frac{c}{\lambda}}{t}\right)\right\} \quad (2.1)$$

Such an oscillating electric field induces fluctuation in the spatial charge distribution. The magnitude of this effect is given by the polarizability of the molecule, that is, the ease of shifting electron cloud within the molecule. The charge distribution follows the time-modulation of the electric wave vector of the incident light radiation, and therefore the molecule constitutes an electric oscillator or oscillating dipole. This oscillating dipole acts as an emitter of secondary electromagnetic waves of the same wavelength as the incident one and the process is called “elastic scattering”, emitted isotropically in all directions perpendicular to the oscillator. These scattered waves can be coherent or incoherent. The coherent scattering from ordered scatterers

produces patterns of constructive and destructive interference that contains structural information, while incoherent scattering results from random events and can provide dynamic information.

Typically, in scattering experiments, a monochromatic beam is directed to the sample and either the angular distribution of scattered light (elastic scattering) or energy changes associated with scattered radiation (inelastic scattering) is measured. The increasing success of scattering techniques for characterizing different nanoparticle/macromolecule systems is due to the fact that it provides detailed information about spatial and/or temporal correlations within the sample without severe sample preparation. Hence, it attracted considerable interest both in industry and academia for structural characterizations of colloids, condensed matter systems, including biological systems and material chemistry. Though X-rays, neutrons, and light are used as electromagnetic radiation to probe sub-micron structures, here we discuss the general principle of small angle scattering with special emphasis on X-ray and scattering.

2.2.1. Small Angle X-rays/Neutrons Scattering

i. Basic Principles

The small angle scattering (SAS) of X-rays and neutrons, abbreviated as SAXS and SANS respectively, measures the scattered intensity as a function of wave vector transfer or also called momentum transfer vector (q), typically in the range of 10^{-3} to 1 $Å^{-1}$. To probe length scales in the range of 1-50 nm by using radiations with a wavelength of ~1 Å, the scattering needs to be monitored at angles as small as 0.2°, hence the technique is called as small-angle scattering.[147] The typical schematic representation of a small angle scattering experiment is shown in Fig. 2.2. In the scattering experiment, the scattering vector $q = k_s - k_i$, represents the difference

between the wave vectors of the scattered (k_s) and incident radiations (k_i). In the SAS experiment, for elastic scattering, the magnitude of the incident and scattered wave vectors are given as $|k_s| = |k_i| = \frac{2\pi n}{\lambda}$, where n is the refractive index of the medium, in water n= 1.33 for light, but in case of X-rays and neutrons it is very close to unity. Consequently, the modulus of the momentum transfer vector or scattering vector (q) is related to scattering angle (θ), and the wavelength (λ) of the incident radiation as:

$$|q| = 2|k_i| \sin\frac{\theta}{2} = \frac{4\pi}{\lambda} sin\frac{\theta}{2} \qquad (2.2)$$

The magnitude q has the dimension of reciprocal length and the commonly used unit for SAXS/SANS is Å^{-1}. A fundamental theorem in the theory of wave scattering by an extended object relates the real space (r-space) density distribution of the scattering objects to the reciprocal space (q-space) scattered intensity distribution, through Fourier transform. This theorem shows that the characteristic size R in the r-space is reciprocally related to the characteristic width of the scattered intensity distribution in q-space. Therefore, to characterize the size R in r-space, one needs to do a scattering experiment in which q spans in a range of $q=2\pi/R$. Large structures scatter to low q (and angle) and small structure at higher q values.

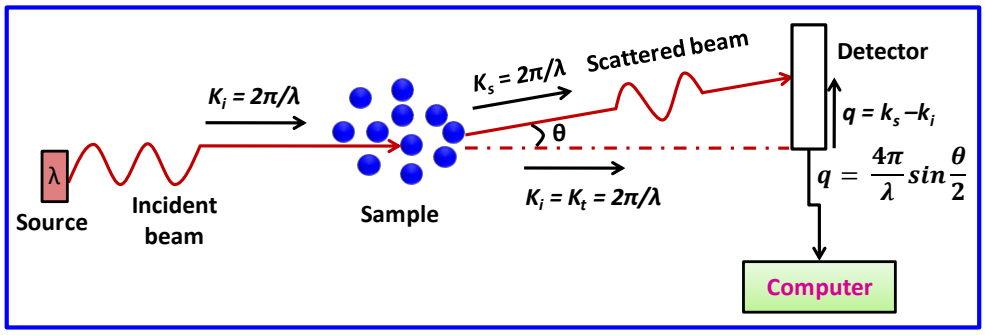

Figure 2.2 *Schematic representation of a small angle scattering (SAS) experiment, and illustration of the scattering process with the incoming and outgoing beam, the wave vectors, k_i and k_s, and the scattering vector q are shown.*

The basics and the data analysis methods used in the SAXS and SANS techniques are similar and hence a common procedure can be employed to extract structural information.[148] In SANS techniques, neutrons interact with the atomic nucleus via strong nuclear forces operating at very short range ($\lambda \sim 10^{-5}$ Å), which is much smaller than the incident neutron wavelength ($\lambda \sim 4$ to 10 Å). Therefore, each nucleus acts as a point scatterer to the incident neutron beam, which may be considered as a plane wave. Due to the magnetic moment of neutrons, in addition to the nuclear interaction, it can interact with the magnetic moments of the individual atoms. Therefore, neutron scattering is also used to study magnetic structures. The strength of interaction of free neutrons with the bound nucleus can be quantified by the scattering length (b) of the atom, which is isotope dependent and allows isotopes of the same element to have substantially different scattering lengths for neutrons. However, in the case of X-rays, the electromagnetic radiation (X-ray) interacts with the electron cloud of the atom, which oscillates with the same frequency as that of the incident X-rays. These oscillating electrons act as a source of coherent secondary radiation of the same frequency. Table 2.1 shows the coherent scattering length values of few selected atoms for X-ray and neutrons. In the case of neutrons, the scattering power of an atom vary in a random way, without any dependence on its atomic number, while for X-rays, the scattering power increases in proportion to the atomic number, and it is isotope independent.

Table 2.1 The coherent scattering length of few atoms for X-ray and neutrons scattering.

Element	**H**	**D**	**C**	**N**	**O**	**S**
$b_{x\text{-}ray}$ (10^{-12} cm)	0.282	0.282	1.690	1.972	2.252	4.508
$b_{neutron}$(10^{-12} cm)	-0.3741	0.6674	0.6648	0.936	0.5805	0.2847

Contrast Variation in SAS

In small-angle scattering, when the positions of the individual atoms are uncorrelated, it is convenient to represent the scattering from a particle, in terms of continuous distribution of the scattering length density (SLD) $\rho(r)$, where $\rho(r) = b(r)/V_M$. The SLD of a molecule can be obtained as:

$$\rho = \sum_i^j \frac{b_i}{V_M} \quad (2.3)$$

Where bi is the bound coherent scattering length of atom i in a molecule of molecular volume V_M.

$$V_M = \frac{1}{N_A}\frac{M}{\rho_m} \quad (2.4)$$

Where N_A is Avogadro's number, M is the molar mass and ρ_m is the mass density.

In the case of X-rays, the SLD can be obtained as the electron number density function multiplied by the scattering length of a single electron, i.e. its classical radius. Therefore, the SLD for X-rays can be estimated using the equation:

$$\rho = \sum_i^j \frac{Z_i r_e}{V_M} \quad (2.5)$$

where Z_i is the atomic number of the i^{th} of j atoms in a molecule of molecular volume V_M and r_e is the classical electron radius or Thomson scattering length (2.8179×10^{-15} m). The differences in ρ values for neutrons and X-rays arise from the fact that neutrons are scattered by the nucleus of an atom, while X-rays are scattered by the electron clouds around the nucleus. Thus, it is possible to calculate the SLD of the particle or solvent by determining the molecular volume, V_M. The values of $\rho_{particle}$ and $\rho_{solvent}$ depend on the chemical composition of the scatterer and the solvent.[149]

In both SAXS and SANS techniques, the wave vector dependent scattering amplitude from a particle arises when there is a difference in scattering length density between the particle and its solvent medium or matrix, and the term $\Delta\rho^2 = (\rho_{particle}-$

$\rho_{solvent})^2$, is called as contrast factor, also called the excess SLD, which decides the visibility of that component in the measurement.[150] Since scattering length is proportional to the atomic number in the case of X-rays, high Z elements in a hydrogenous matrix show good contrast. In case of neutrons, the scattering length values between hydrogen and deuterium are significantly different, and hence it is possible to make a very good contrast between the hydrogenous particle and the solvent by deuterating either the particle or solvent and also by using mixed hydrogenated and deuterated solvents. This has been made use of in simplifying the complex scattering patterns observed in SAXS/SANS. For example, for micelles having a core-shell type of morphology, the pattern can be significantly different for SAXS and SANS (Fig. 2.3). For X-rays, it has different electron density for the hydrophobic core part and hydrophilic shell part, which gives rise to its characteristic scattering in SAXS. To achieve a good contrast between hydrocarbon core and solvent matrix, often D_2O is used as the solvent, instead of water, in SANS. As opposed to SAXS, the SANS pattern does not show features of the core-shell particles, due to poor scattering contrast between the solvated shell of micelles and solvent.

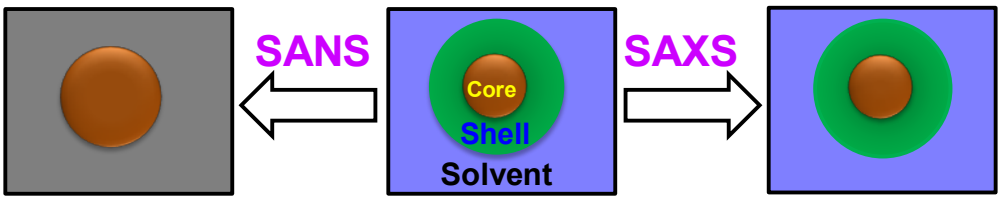

Figure 2.3 *Schematic illustration of scattering contrast in the core-shell type micelles comprising a solvated shell, as observed by SANS and SAXS.*

Contrast variation can be achieved by using appropriate additives or solvent mixtures such that one of the components in a multicomponent system can be masked. A mixture of D_2O and H_2O can be used to vary the solvent SLD in SANS. Similarly,

additives such as glucose, sucrose, etc. can be used to increase the solvent SLD in SAXS. Due to the advantage of contrast variation, SANS/SAXS has been used to study multi-component complex structures at various length scales. Since most of the measurements are performed in solution, these techniques provide unique structural information under different conditions. SAXS is particularly useful for studying nanostructures wherein at least one of the components has high electron density (Z value). These techniques are often used as complementary tools with each other, providing detailed information about the system.

ii. Detailed Analysis of Small-angle Scattering Data

If the wave vectors of the incident and scattered waves are k_i and k_s respectively, then a scattered wave by a scatterer at a point r in the sample will thus be phase-shifted with respect to that scattered at the origin by a phase factor (φ), given by $\varphi=-qr$, where q is the scattering vector and r is the position vector. Now the scattering amplitude by the collection of atoms within the scatterer can be obtained by summing up all the secondary waves, represented by a term e^{-iqr} corresponding to each point scatterer. But considering the enormous number of electrons and the fact that a single electron cannot be exactly localized, it will be convenient to introduce the concept of average electron density in the region of interest. This may be defined as the number of electrons per unit volume and denoted by $\rho(r)$ as discussed in the above section. A volume of element dV at position r will then contain $\rho(r)dV$ electrons. So the amplitude of the scattered radiation (A) can be expressed as:

$$A(q) = \iiint_{V_{sample}} \rho(r) e^{-iqr} \cdot dV \qquad (2.6)$$

Therefore, the scattering amplitude is the Fourier transform of the electron density distribution within the object in a certain direction (specified by q). V_{sample} is the whole

volume irradiated by the incident radiation. Since the detectors measure the scattering intensity, rather than the amplitude, the corresponding equation for scattered intensity *I(q)* becomes:

$$I(q) = AA^* = \iiint \iiint_{V_{sample}} \rho(r_1) \cdot \rho(r_2) \cdot e^{-iq(r_1 - r_2)} \cdot dV_1 \cdot dV_2 \qquad (2.7)$$

A^* be the complex conjugate of A. To summarize all pairs with equal relative distance, and to integrate overall relative distance, including the phase factor, and normalization over the total scattering volume above equation becomes;

$$I(q) = \frac{1}{V} \iiint \bar{\rho}^2(r) \cdot e^{-iqr} \cdot dV \qquad (2.8)$$

where, $\bar{\rho}^2(r)$ is the correlation between the scattering length densities at all points in the sample separated by a distance *r,* ($r = (|\boldsymbol{r}_1 - r_2|)$ = constant). Thus, the intensity distribution in reciprocal space or q is uniquely determined by the structure of the object, as expressed by $\bar{\rho}^2(r)$, and can be obtained from *I(q)* by the Inverse Fourier Transform (IFT).

The scattering expressions for both the SAXS and SANS experiments can have contributions from both intra-particle interference and inter-particle interference. The general equation treating the scattered intensity versus the momentum transfer q of a mono-disperse, homogeneous and isotropic particles can be written as:

$$I(q) = \Phi P(q) \mathrm{S(q)} + Background \qquad (2.9)$$

where Φ is the volume fraction of the particles and *P(q)* is the intra-particle form factor corresponds to the intra-particle structure contribution and is decided by the shape and size of particles. *S(q)* is the structure factor, includes the inter-particle contribution to the scattering, which depends on the spatial arrangement of particles.

For a low particle concentration, the inter-particle interactions can be neglected, and the value of $S(q)$ becomes equal to 1 and, therefore the data analysis is primarily based on $P(q)$. Fig. 2.4 shows the typical plot of *P(q), S(q),* and the corresponding scattering intensity *I(q).*

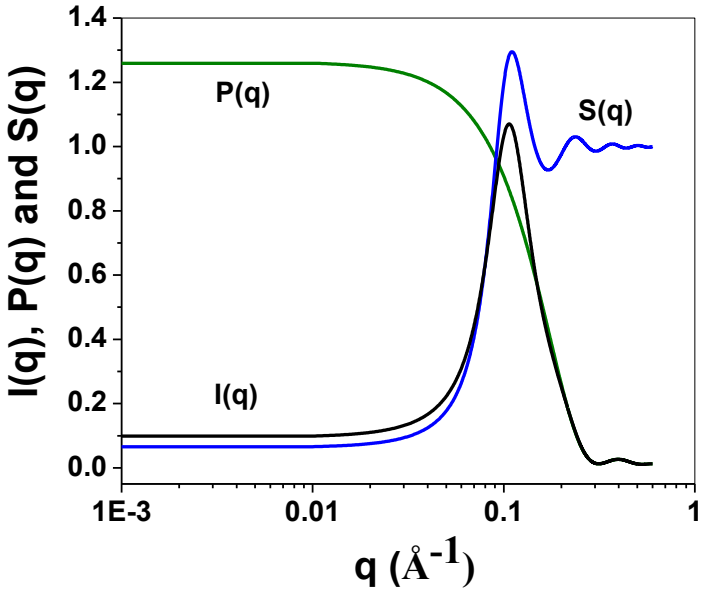

Figure 2.4 *Typical plot of I(q), P(q), and S(q) indicating the contributions to scattering from interparticle and intraparticle interferences.*

In general, two different approaches are used for the treatment of small-angle scattering data. First, a model-independent "Indirect Fourier transformation (IFT)" of the reciprocal space data to obtain the Pair-Distance Distribution Function (PDDF), *p(r)* from which information regarding particle structure can be deduced.[147] This method is advantageous to get preliminary information about the structure, without any a priori approximations about the shape of the objects. In this method, $p(r)$ is expressed as a linear combination of orthogonal functions in the range $(0, D_{max})$ where the coefficient of expansions are obtained by fitting the experimental data. In principle, the scattering intensity $I(q)$ and PDDF contain the same information, but the

real space representation in terms of $p(r)$ is more intuitive and can be used as a guide for model-dependent analysis. The particle shape and size of some simple geometric bodies can often be deduced by straightforward visual inspection of $p(r)$.[151] The *p(r)* function represents the histogram of distances within pairs of scattering centers in the particle weighted by the SLD's of the points connected by the vector$(\bar{r})$. Furthermore, the *p(r)* is also critical in real space 3D model constructions. For example, the DAMMIF program permits, visualization of the real space structures, by fitting the p(r) function.[152]

The *I(q)* and *p(r)* are closely related by the equation:

$$I(q) = \int_0^{D_{max}} p(r) \frac{\sin(qr)}{qr} dr \qquad (2.10)$$

which can be derived from the Debye formula,[153] and the inverse Fourier transformation allows one to calculate *p(r)* function as:

$$p(r) = \frac{r}{2\pi^2} \int_0^{D_{max}} q \cdot I(q) \cdot \sin(qr) \cdot dq \qquad (2.11)$$

This interpretation is limited to non-periodic structures at low concentrations, where the interparticle interactions are negligible. The value of D_{max} obtained for a scattering pattern provides an approximate value of the maximum dimension of the particles. The information obtained from the PDDF can be used to develop a suitable shape-dependent model to define the detailed structural information. Attempts were also made to extract the PDDF of particles from concentrated suspension using a generalized IFT analysis.[147,154]

The second approach consists of direct modeling of reciprocal space data using shape-dependent models and the experimental scattering data is directly fitted to a mathematical model. These models can be used with both dilute and concentrated solutions, hence giving the possibility of evaluating both the size of the particles and

their interparticle interactions i.e. structure factor. It was assumed that the particles are randomly oriented in the sample so that the theoretical form factors for anisotropic particles have to be averaged overall orientation. However this method requires the fitting of several parameters, therefore some a priori information is required to obtain reliable results.

Now, the essence of analyzing scattering data lies in comparing the experimentally observed scattering pattern with simulated curves for an appropriate shape/size. For some of the regular shapes, having an axis of symmetry, the analytical expressions for $P(q)$ are available in the literature.[147,155] Here $P(q)$ expressions for frequently used shapes in the current thesis are described.

a) Core-Shell Ellipsoid With a Sharp Interface

This is one of the commonly used models for SAXS analysis of self-assembled structures like micelles. The core comprises the hydrocarbon part and the shell can be of polyoxyethylene chains or condensed counterions. The elliptical structure is advantageous to consider the one-dimensional growth of micelles and it can also capture a spherical shape under the limiting condition, $r_{min} = r_{maj}$. Often the electron density of the shell is more than that of core or solvent Fig. 2.5 shows a schematic illustration of the core-shell ellipsoid where the shell has high scattering length density compared to the core and solvent with a sharp interface.

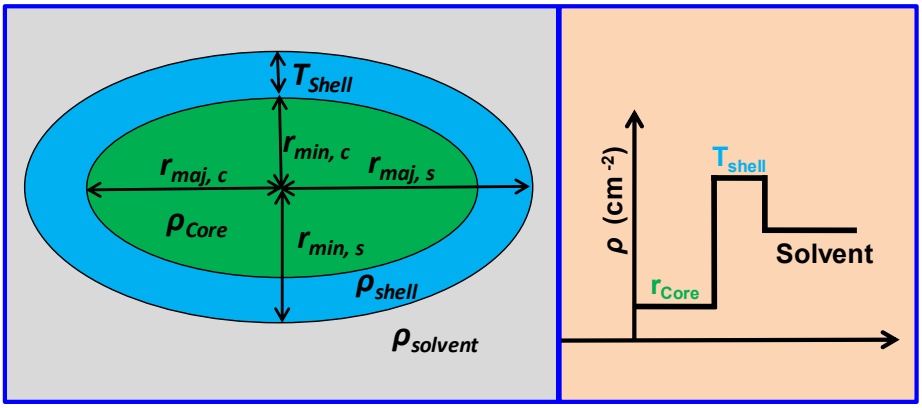

Figure 2.5 *Schematic of the core-shell ellipsoid particle with its geometric parameters and the corresponding SLD profile (here r_{core} is the effective core radius; T_{shell} is the thickness of shell).*

The particle form factor, normalized by the total volume ellipsoid, for such geometry can be given as:

$$P(q) = \frac{Scale}{V}\int_0^1 |F(q, r_i, \alpha)|^2 \, d\alpha + Background \qquad (2.12)$$

where, $F(q, r_i, \alpha)$, is the single-particle scattering amplitude for core-shell ellipsoid of revolution and its analytical expression is given by,

$$|F(q, r_i, \alpha)| = V_{core}(\rho_{core} - \rho_{shell})\left(\frac{3j_1(u_{core})}{u_{core}}\right) + V_{shell}(\rho_{shell} - \rho_{solv})\left(\frac{3j_1(u_{shell})}{u_{shell}}\right) \qquad (2.13)$$

where, $V_{core} = (4\pi/3) r_{maj,c} {r^2}_{min,c}$

$$V_{shell} = (4\pi/3) r_{maj,s} {r^2}_{min,s}$$

$$u_{core} = q\left[{r_{maj,c}}^2 \alpha^2 + {r_{min,c}}^2 (1 - \alpha^2)\right]^{\frac{1}{2}}$$

$$u_{shell} = q\left[{r_{maj,s}}^2 \alpha^2 + {r_{min,s}}^2 (1 - \alpha^2)\right]^{\frac{1}{2}}$$

$j_1(u_i)$ is the first-order Bessel function of the first kind. r_{maj} is the semi-major axis and r_{min} is the semi-minor axis. α is the angle between the axis of the ellipsoid and vector q, while ρ represents the SLD of the core, shell or solvent.

b) Core-shell Particles With the Graded Interface

It may be noted often real samples do not possess a sharp interface between two regions of different SLDs. Instead, the SLD varies in a continuous fashion and this will have implications in the scattering pattern. Therefore, a gradually varying SLD at the interface (graded interface) is often used to model SAS data. A typical SLD profile of core-shell spheres with the graded interface is shown in Fig. 2.6. In this model, instead of sharp interfaces between successive layers, the interface between each neighboring shells can be described by an error function, power-law, or exponential functions. The scattering intensity is computed by building a continuous custom SLD profile along the radius of the particle. The SLD profile is composed of a number of uniform shells with interfacial shells between them. The form factor for such an object can be calculated in the following way:

$$P(q) = \frac{f^2}{V_{particle}} \tag{2.14}$$

where $f = f_{core} + f_{dry\ shell} + f_{shell\ interface} + f_{solvent}$

For spherically symmetric particles with an SLD profile $\rho_{x(r)}$ the form factor due to each term can be defined as:

$$f_x = 4\pi \int_0^\infty \rho_x(r) \frac{sin(qr)}{qr} r^2 dr \tag{2.15}$$

So that individual terms can be calculated (see SasView documentation[156] and references therein). Here we assume that the SLDs of the core and the solvent are constant against r and considered the sharp interface between the core and

dry shell while the diffused interface has been considered between dry shell and solvent. The SLD at the interface between shell and solvent is computed using an error function with a characteristic width (thickness of the interface).

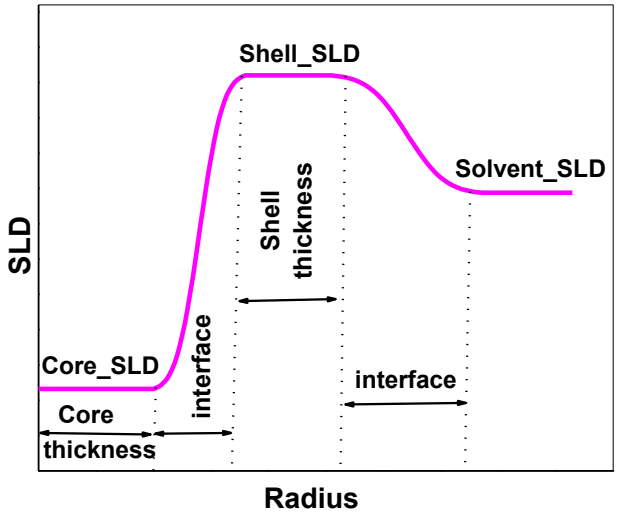

Figure 2.6 *Schematic illustration of the SLD profile for the core-shell sphere with graded SLD at the interface.*

Polydispersity Index: Another factor that contributes to the scattering pattern is the polydispersity in size. Often, the polydispersity is taken into account by invoking certain known distribution functions. The choice of the distribution function is best made according to theoretical expectations. The Schulz distribution is one the asymmetric distribution function is expected to be suitable to account for polydispersity in the core radius (R), and can be given as,

$$f(R) = \left(\frac{Z+1}{R_M}\right)^{Z+1} R^Z exp\left[-\left(\frac{Z+1}{R_M}\right)R\right]\frac{1}{\Gamma(Z+1)} \tag{2.16}$$

where R_M is the mean value of distribution and Z is a parameter characterizing the width distribution. The polydispersity of this distribution is given by,

$$\frac{\Delta R}{R} = \frac{1}{\sqrt{Z+1}} \tag{2.17}$$

For finite Z, the Schulz distribution has the realistic feature that it is skewed towards large sizes. With increasing Z, Eq. (2.16) asymptotically approaches a Gaussian and, in the limit of Z→∞, tends to a delta function at R_M the Schultz distributions possess a long tail in the higher *R* region and hence more suitable for practical purposes.

Structure Factor S(q): The interparticle interference term, also called structure factor *S(q)* becomes important for concentrated suspensions. For ionic micelles, this becomes significant even at volume fractions as low as 3 %. The *S(q)* is related to the total correlation function,

h(r) = g(r)–1, as,

$$S(q) = 1 + 4\pi n \int_0^\infty [g(r) - 1]\, r^2 \frac{sin(qr)}{qr} dr \qquad (2.18)$$

where g(r) is their pair-correlation function.

The structure factor can be computed using different approximations. One of the widely used models to calculate the structure factor of ionic particles in water is the screened coulomb interaction model proposed by Hayter and Penfold in the rescaled mean spherical approximation (RMSA).

It may be noted that for anisotropic particles as well as for polydisperse systems, the structure factor calculated by this approach should be considered as an effective structure factor S'(q) only, as polydispersity and particle anisotropy can influence the oscillations in the structure factor.[157] Using the decoupling approximation, the apparent structure factor *S'(q)* is related to the true structure factor *S(q)* by the relation:

$$S'(q) = 1 + \beta(q)[S(q) - 1] \qquad (2.19)$$

$$\beta(q) = |\langle F(q)\rangle|^2 / \langle |F(q)|^2 \rangle \qquad (2.20)$$

where $P(q) = \langle |F(q)|^2 \rangle$ and β is a q-dependent factor between zero and one that accounts for the deviation of the true structure factor *S(q)* in the observed scattering spectrum from a polydisperse or non-spherical system of particles. From a detailed analysis of the effect of axial ratio and polydispersity on the interparticle structure factor, The contribution from anisotropy effects in structure factor can be neglected, when qr_{maj} is less than 3.5 and the axial ratio for the ellipsoid core is about <1.3. Throughout the analysis, we consider an apparent structure factor to model the experimental data.

Finally, the experimental data needs to be compared with the simulated curves with the minimum number of parameters as the variable in the fit. The quality of the fit in the SAXS/SANS data analysis can be ascertained from the reduced χ^2 test. The reduced χ^2 is given by,

$$\chi^2 = \left[\sum_{i=1}^{N} \left(\frac{(O_i - E_i)^2}{S_i^2}\right)\right] * 1/N \qquad (2.21)$$

where O_i is an observed (measured) value, E_i is an expected (theoretical) value, S_i is the standard deviation in the experimental data and N is the number of data points. Some fit parameters can be simply estimated from the sample composition and have been fixed for the fitting process. If the models are chosen poorly then the reduced-chi square value will be high suggesting re-assessment of the models. This approach is very useful for structure as well as interaction determination through the proper modeling of form factor and structure factor.

2.2.2. Dynamic Light Scattering

Dynamic Light Scattering (DLS) is a technique which is used to determine the hydrodynamic size of nearly spherical particles by measuring the random changes in

the intensity of light scattered from a suspension and it is also known as Quasi-Elastic Light Scattering (QELS) or Photon Correlation Spectroscopy (PCS). In this technique, the scattered intensity of light is measured as a function of time and the time-dependent intensity fluctuations arising from the Brownian motion of colloidal particles are used to extract particle size. The scattered intensity fluctuations are processed by a digital correlator to obtain the intensity autocorrelation function. This correlation function can be analyzed to get the information of diffusion coefficients associated with the mean hydrodynamic size and distribution width (polydispersity) of the nanoparticles in suspension. This time dependence or the fluctuations in the net scattered intensity forms the basis of the DLS experiment.[158] The schematic of the typical experimental setup is shown in Fig. 2.7.

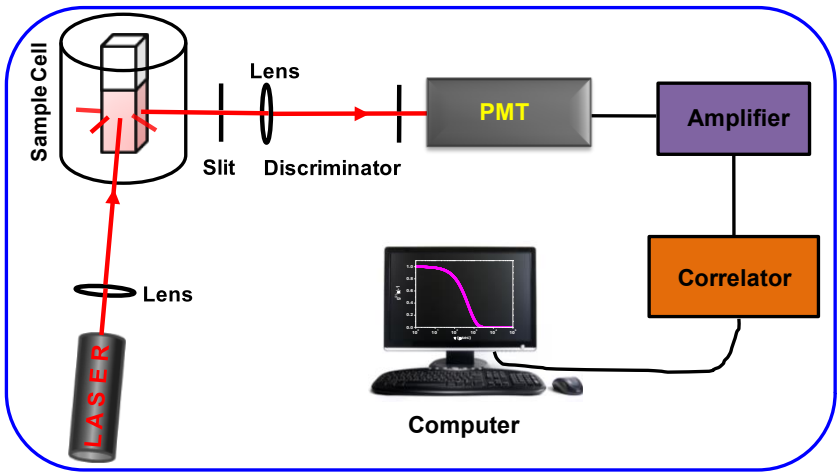

Figure 2.7 *Schematic of typical dynamic light scattering experimental setup.*

The basic principle of DLS is based on the Brownian motion of particles. Since the nanoparticles in a colloidal suspension are not stationary but move or diffuse in a random walk fashion called Brownian motion, the relative position of the particles changes over time. As a result of this, the net intensity seen by the detector will be a

superposition of all the waves scattered from the scattering volume. Therefore, the intensity fluctuates randomly in time as the phases of the scattered waves fluctuate randomly. The rate of these scattered intensity fluctuations depends on the mobility of the particles and will, therefore be related to the size of diffusing particles. For a large area detector, the scattered intensity (speckle) pattern observed by the detector contains bright as well as dark patches, due to the constructive and destructive interference respectively. Since the distance between particles affects the phase difference of the scattered light, the brightness of spots on the speckle pattern will fluctuate in intensity as the particles change position with respect to each other. Fig. 2.8a shows a representative time-dependent scattered intensity profile for small and large sized particles as observed on the same time scales, with the result of variations in the position of an essentially fixed number of particles in the scattering volume.

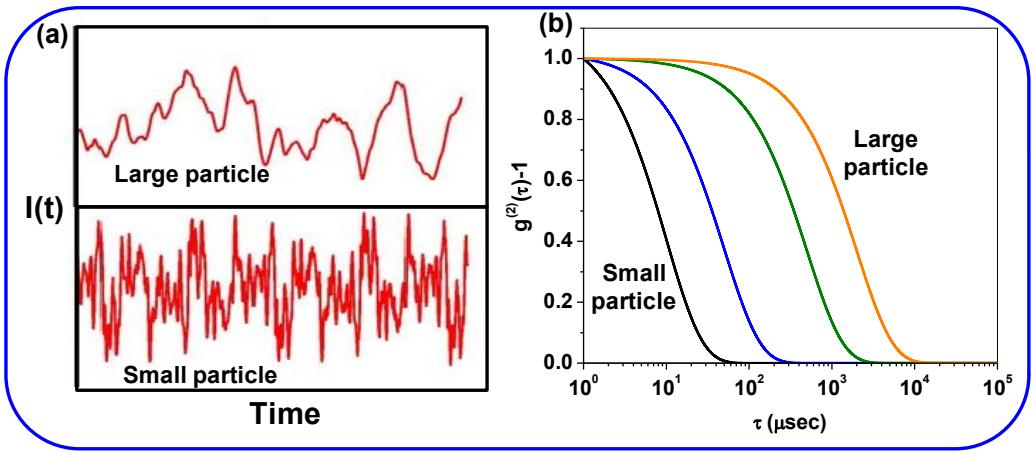

Figure 2.8 *(a) Typical intensity fluctuations in scattered intensity for large and small particles and (b) the variation of intensity correlation functions with increasing nanoparticle size. The decay of the function slows down for larger sized particles.*

The observed intensity pattern is processed in real-time with a digital signal processing device known as a correlator and the dynamic information of the particles is derived from an autocorrelation function as a function of delay time (τ). Once the

autocorrelation data have been generated, different mathematical approaches can be employed to determine particle size information from it. As shown in Fig. 2.8b the autocorrelation function decay shift, to a longer time (i.e. slows down) as the particle size increases. Analysis of the scattering data is based on the assumption that the particles are dilute and interparticle interactions can be neglected. For concentrated suspensions, this can be achieved by dilution, and for charged particles, interparticle effects are reduced by the use of salts to reduce the thickness of the electrical double layer. As dust particles can scatter strongly, it is very important to remove dust from the solution during the sample preparation either by filtration or centrifugation.

The autocorrelation function, denoted by C(τ), represents the correlation between the values of the scattered intensity at a given time *t* and at a later time (*t*+*τ*). By representing intensity at an arbitrary time as *I(t)* and those at a later time τ as *I(t+τ),* the autocorrelation function can be written as,

$$C(\tau) = \langle I(t) \cdot I(t+\tau) \rangle \tag{2.22}$$

when the sampling interval *τ* becomes very large, there should not be any correlation between the pairs of sampled intensities and hence the above equation reduces to

$$C(\infty) = \langle I(t) \rangle^2 \tag{2.23}$$

An autocorrelator accepts the digital photo counts from the detector which represents the light scattering intensity *I(t)* and computes the second-order correlation function, normalized with the long time correlation data $\langle I \rangle^2$. The normalized time correlation function $g^2(\tau)$ of the scattered intensity is given by,

$$g^2(\tau) = \frac{\langle I(t) \cdot I(t+\tau) \rangle}{\langle I(t) \rangle^2} \tag{2.24}$$

For photo counts obeying Gaussian statistics, the relationship between $g^2(\tau)$ and the first-order correlation function of the electric field $g^1(\tau)$ is:

$$g^2(\tau) = \beta + A|g^1(\tau)|^2 \quad (2.25)$$

where β is the baseline and A is an adjustable parameter which is dependent on the scattering geometry and independent of τ. This parameter A is one important characteristic of the experimental set-up or more specifically the light receiver optics and is often called the spatial coherence factor which is ≤1. It is a measure of the amplitude of the normalized correlation function, and the resolution of the measurement is dependent on the amplitude. A high value of the amplitude can be achieved by decreasing the detector aperture size. Since small particles move faster than larger ones, their autocorrelation decay constant is large. For a suspension of monodisperse, rigid, spherical particles undergoing the Brownian diffusion, first-order autocorrelation function follows a single exponential decay with the decay constant Γ (units of inverse seconds) and is given as,

$$G(\tau) = e^{-\Gamma\tau} \quad (2.26)$$

Γ is related to the diffusion coefficient of the particle as, $\Gamma = Dq^2$

Then equation 2.26 becomes,

$$g^1(\tau) = \exp(-Dq^2\tau) \quad (2.27)$$

where $g^1(\tau)$ is the autocorrelation function at a particular wave vector, $q = \frac{4\pi n}{\lambda} sin\frac{\theta}{2}$ and delay time τ, where λ is the incident laser wavelength, n is the refractive index of the sample and θ is the angle at which the detector is located with respect to the sample cell.

For small, dilute, non-interacting spheres the hydrodynamic radius R_h can be related to the translational diffusion coefficient D by means of Stokes-Einstein relationship,

$$D = \frac{kT}{6\pi\eta R_h} \quad (2.28)$$

where k is the Boltzmann constant, η is the viscosity of the sample, T is the temperature at which measurements are taken and R_h be the hydrodynamic radius of the particles under study. If the particle is non-spherical then R_h is often taken as the apparent hydrodynamic radius. The viscosity of the solvent is very much dependent on the temperature, so in DLS measurements precise temperature control is essential. For the double exponential behavior of the correlation function was fitted by using the equation,

$$g^2(\tau) - 1 = A_1 exp\left(-\frac{\tau}{\tau_1}\right) + A_2\, exp\left(-\frac{\tau}{\tau_2}\right)^{\beta} \quad (2.29)$$

where the parameters A_1 and A_2 are amplitudes of the two relaxation modes, τ_1 is the fast relaxation time connected to the microscopic motion of particles, τ_2 is the slow relaxation time related to the structural rearrangement, and β is the stretching exponent which measures the distribution width of the slow relaxation. Here, the amplitudes, relaxation times, and the stretching exponent of the slow mode are used as variables.

For polydisperse samples, the particle size distribution and the polydispersity index of the distribution can be obtained from advanced data analysis procedures. Some of the commonly used data analysis methods include cumulants analysis, exponential sampling, CONTIN, etc.

The hydrodynamic diameter that is measured in DLS is a value that refers to how a particle moves within a medium with its associated solvent. Therefore this size could be different for the sizes obtained by other methods such as electron microscopy. Moreover, for polydisperse systems, DLS measures the z-average diameter, as opposed to the number average diameter obtained by microscopy. For these reasons, often the size obtained from DLS is higher than that is observed by

TEM. Fig 2.9 shows a typical representation of the hydrodynamic size of inorganic particles with an organic shell attached to it.

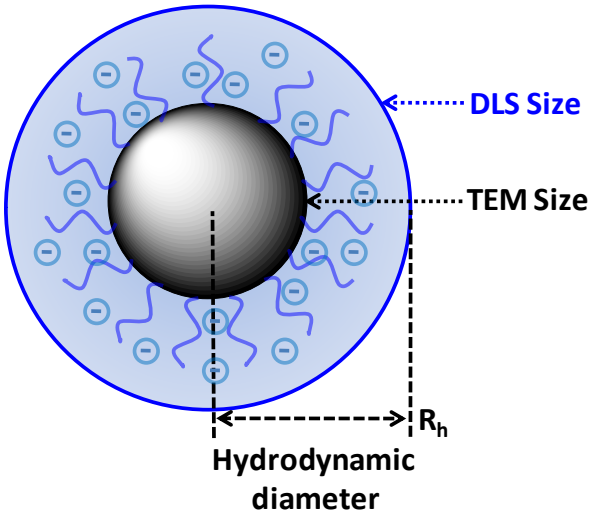

Figure 2.9 *Schematic representation of hydrodynamic diameter and TEM size.*

2.2.3. Zeta-potential Measurements

The interfacial charges on colloidal particles can be quantified in terms of the zeta potential. For an electrically charged interface in a solvent, the counterions surrounding a charged particle surface exists as two regions; an inner region (Stern layer) where the ions are strongly bound and an outer region (diffuse layer) where they are less firmly associated. Within the diffuse layer, there is a notional boundary inside where the ions and the particles form a stable entity. Due to the unequal charge distribution near the surface, an electrostatic potential is developed at the surface and it decreases with increasing distance from the surface. When a particle undergoes electrophoretic motion (e.g. due to applied electric field), ions within the notional boundary also move with the particle. Those ions beyond the boundary stay with the bulk dispersant. The potential at this boundary (surface of hydrodynamic shear) is called the zeta (ζ) potential (Fig. 2.10).

The characterization of a particle's surface properties is necessary to optimize the conjugation chemistry as well as to assess kinetic stability. The magnitude of zeta potential gives an indication of the potential stability of the colloidal system under study. If all the particles in suspension have a large positive or negative zeta potential (more than +30 or -30 mV) then they will tend to repel each other and there will be less probability for the particles to come together and hence is considered a stable suspension. However, if the particles have low zeta potential values, then there will not be sufficient kinetic barrier to prevent the particles from coming together and flocculating. However, if the particles have a density different from the dispersant, they will eventually sediment forming a close-packed bed. Also, there is one term called isoelectric point referred to as PZC (point of zero charge), at which the particles in suspension have a net charge of zero and no mobility in the electric field. The general method used to estimate the zeta potential is by electrophoretic mobility measurements.

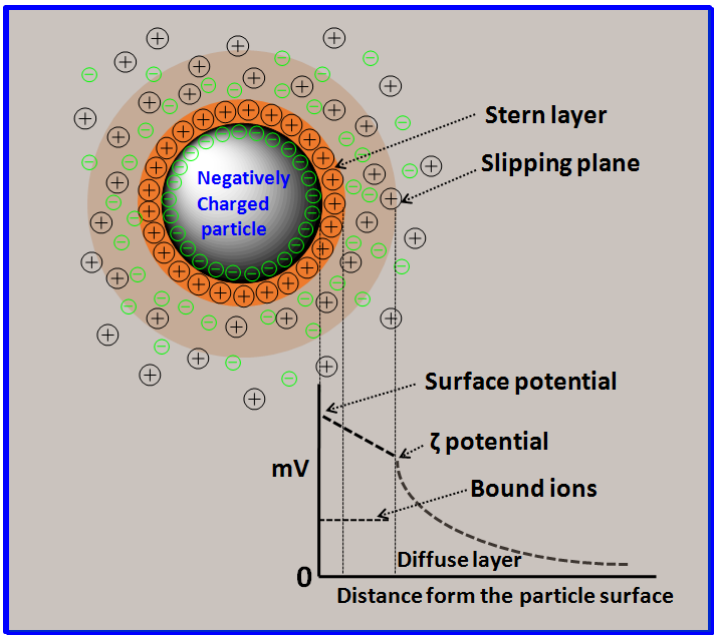

Figure 2.10 *Schematic representation of the electric double layer surrounding nanoparticle and electrostatic potential near a negatively charged spherical particle.*

When an electric field is applied across a colloidal suspension, charged particles suspended in the electrolyte are attracted towards the electrode of the opposite charge. But the viscous forces acting on the particles tend to oppose this movement. After reaching equilibrium between these two opposing forces, the particles move with constant velocity. The velocity is dependent on various factors such as the strength of the electric field or voltage gradient, the dielectric constant of the medium, the viscosity of the medium, and the zeta potential. The velocity of a particle in a unit electric field is referred the electrophoretic mobility of that particle, which is related with Zeta potential by the Henry equation as:

$$U_E = \frac{2\varepsilon\zeta f(\kappa a)}{3\eta} \qquad (2.29)$$

Where U_E = electrophoretic mobility, ζ = zeta potential, ε = dielectric constant, η = viscosity and $f(\kappa a)$ = Henry's function. The units of κ, termed the Debye length, are the reciprocal length and κ^{-1} is often taken as a measure of the "thickness" of the electrical double layer. The parameter 'a' refers to the radius of the particle and therefore κa measures the ratio of the particle radius to the electrical double layer thickness. Electrophoretic determinations of zeta-potential are most commonly used in aqueous media and moderate electrolyte concentration. In this case, the value of $f(\kappa a)$ is 1.5, and this is referred to as the Smoluchowski approximation. Therefore calculation of zeta-potential from the mobility is simple for systems that fit the Smoluchowski model, i.e. particles larger than about 0.2 microns dispersed in electrolytes containing more than 10^{-3} molar salt. Also, for small particles in low dielectric constant media like non-aqueous media, $f(\kappa a)$ becomes 1.0 and allows an equally simple calculation and this is referred to as the Huckel approximation.

2.3. X-Ray Diffraction (XRD)

X-rays are electromagnetic radiations, discovered by WC Röntgen in 1895, with frequencies in between ultra-violet (UV) and gamma radiations, and their wavelength (λ) range from 0.4 nm to 100 nm. X-rays are generated when fast-moving electrons collide with the hard metallic targets such that the inner core electrons get knocked out and higher energy level electrons get transferred to the empty core orbits and the difference in energy between the two orbits is emitted as a X-rays. These characteristic X-rays are superimposed over a broad background also known as white radiation or Bremsstrahlung radiation which arises due to the deceleration occurring with the incident electron beam due to its interaction with the electric field of the target metal.

When an X-ray beam is incident on crystalline substances (which can also act as three-dimensional diffraction gratings), they are either coherently/incoherently scattered or absorbed. The coherent scattering of X-rays can interfere with each other producing constructive interference (bright) and destructive interference (dark fringes). When λ is fixed, the scattered rays will become constructive only at a particular angle and this phenomenon is termed as X-ray Diffraction. Fig. 2.11 represents the crystallographic planes (separated by a distance *d*), and the path traversed by the incident and scattered rays, indicating the path difference between the two rays[159]

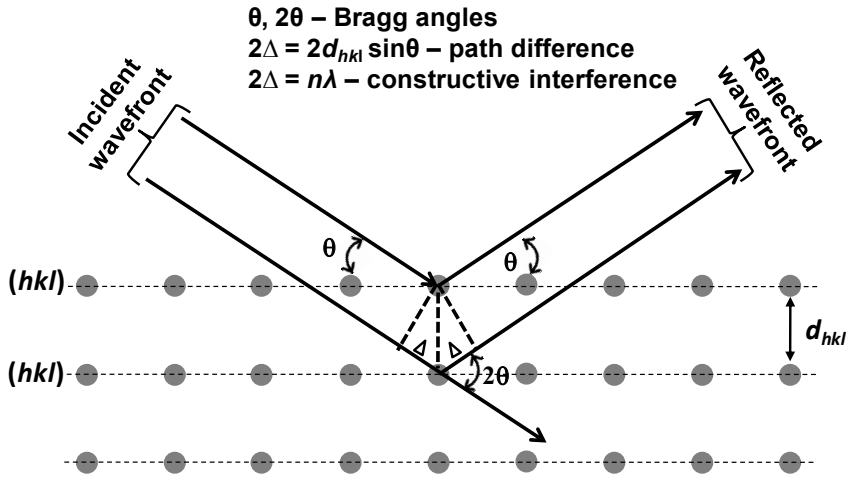

Figure 2.11 *Schematic representation of the diffraction of X-rays from crystallographic planes.*

The necessary condition for constructive interference of X-rays and its relation to the inter-planar separations of the lattice is given by the classical Bragg's law of diffraction as:

$$n\lambda = 2dSin\theta \qquad (2.30)$$

where λ is the wavelength of X-rays, θ is the glancing angle (also called as Bragg's angle), d is interplanar separations, and n is the order of diffraction. Each plane is characterized by Miller indices (hkl). The experimental measurements give the intensity of the reflections for (*hkl*) planes and the corresponding scattering angles (2θ). By knowing the wavelength of radiation and the diffraction angle, the inter-planar spacing can be easily determined from the diffraction pattern.

X-ray diffraction (XRD) technique is one of the most widely used non-destructive tools for crystal structure characterization of a wide range of materials. It is an indispensable method for the characterization of materials and quality control in materials research, development, and production. This technique was first proposed in 1912 by the German physicist Max von Laue,[160] and aided by Walter Friedrich and

Paul Knipping who directed an X-ray beam toward a copper sulfate crystal and analyzed the observed diffraction pattern.[161] In 1913, William Henry Bragg and William Lawrence Bragg (father and son) determined the first crystal structures of NaCl using XRD. The XRD method is also applied to powders of crystalline samples with random orientations and is called X-ray powder diffraction (XPD). In this case, it is assumed that for crystallographic planes with an interplanar distance d_{hkl}, there is always a significant fraction of properly oriented crystals that satisfy Bragg's law, and, therefore, all reflections that meet the $|F_{hkl}|\neq 0$ criterions will be observed experimentally.

The XPD is usually based on the Bragg-Brentano geometry and it consists of an X-ray source, sample holder, X-ray slits, and a detector, which is located on the focusing circle to pick up the diffracted X-rays. During measurements, the detector moves by angle 2θ with respect to the sample which is placed at the center of the measuring circle. The main use of powder diffraction is to identify components in a sample by a search/match procedure, and the observed diffraction patterns were compared with JCPDS (Joint Committee on Powder Diffraction Standards) files available for reported crystalline samples. Furthermore, the areas under the peak are related to the amount of each phase present in the sample. In 1919 A.W. Hull[162] pointed out that, every crystalline substance gives a pattern and the same substance always gives the same pattern, and in a mixture of substances each produces its pattern independently of the others. Therefore the X-ray diffraction pattern of a pure crystalline substance is, like a fingerprint of that substance.

Nanostructured materials exhibit broad diffraction peaks as the assumption of an ideal, perfect, and infinite crystal is not satisfied, with the limited number of lattice planes within the grains. The line width of the diffraction peak depends on the size of

the crystallites and shows the inverse correlation with average crystallite size. The average crystallite size of the nanoparticles was estimated from the full width at half maximum (FWHM) of the intense diffraction peaks in the XRD pattern using the Debye Scherrer's formula, which is given as

$$Crystallite\ size\ (D) = \frac{0.89\lambda}{\beta cos\theta} \quad (2.31)$$

where D is the average crystallite size (in Å), λ is the X-ray wavelength used (in Å), β is the angular line width at half maximum intensity and θ be the Bragg's angle. The Scherrer's constant accounts for the shape of the particle and is generally taken to the value 0.89.[163] The interplanar spacing d and the lattice parameter a was used to distinguish phases between the material, and are related as,

$$a = d_{hkl}\sqrt{(h^2 + k^2 + l^2)} \quad (2.32)$$

To understand and explain the properties of nanomaterials, knowledge regarding its crystal structure and coordination environment around the atoms in the lattice is essential.

2.4. Transmission Electron Microscopy (TEM)

By using conventional light microscopy, it is not possible to resolve the nanoscale structure of the materials, due to the long wavelength associated with visible light. TEM offers a powerful tool to exam some fine features of materials whose characteristic dimensions are less than 100 nm in size (or even down to atomic scale in some cases), and it works with the same basic principles as that of a light microscope, using small wavelength electron beam as a source, instead of light. TEM is the unique technique as it can focus on a single nanoparticle and can determine its crystallite size, morphology, particle size, shape, etc. This enabled the use of TEM for a wide verity of materials in the material science, nanotechnology, semiconductors,

polymers, cancer research, biological and engineering field to observe different features of materials such as the crystal structure, grain boundaries and features in the structure like dislocations; high-resolution imaging, shape, size, etc.[164] Due to the lower wavelength of electrons compared to that of light, we get high-resolution images in TEM as compared to a light microscope image. The electromagnetic lenses are used in TEM rather than glass lenses to focus the electrons into a very thin beam and transmitted through an ultra-thin specimen, depending on the density of the material, out of which some are scattered and disappears from the beam. An image is formed from the interaction of the electrons transmitted through the specimen; the image is magnified and focused onto an imaging device such as a fluorescent screen, which gives rise to a "shadow image" of the specimen with its different parts displayed in varied darkness according to their density. The image can be studied directly by the operator or photographed with a CCD camera. In TEM, contrast formation depends greatly on the mode of operation. In conventional TEM, contrast is obtained by two modes namely the mass-thickness contrast and the diffraction contrast and both are based on amplitude contrast. In the case of high-resolution transmission electron microscopy (HR-TEM), the phase contrast is used for the imaging to obtain structural information of materials, and it has great benefits since it gives deep information about the complicated structures, crystal defects, etc. High-resolution images are formed by the interference of elastically scattered electrons, leading to a distribution of intensities that depends on the orientation of the lattice planes in the crystal relative to the electron beam. Therefore, at certain angles, the electron beam is diffracted strongly from the axis of the incoming beam, while at other angles the beam is completely transmitted. In the case of high-resolution

imaging, this allows the arrangement of atoms within the crystal lattice to be deduced. The main components of the TEM are indicated in Fig. 2.12.

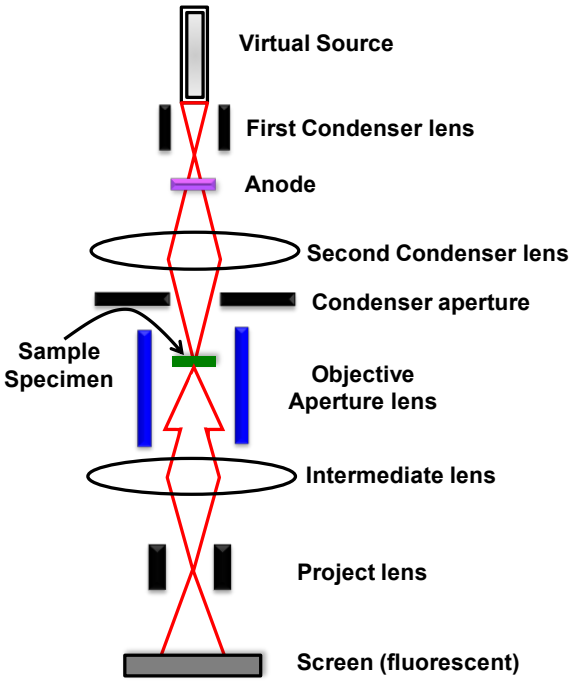

Figure 2.12 *Schematic diagram of Transmission Electron Microscopy.*

Morphology of amphiphilic aggregates formed in liquids has been imaged using a special TEM technique known as Cryo-TEM. Cryo-TEM is a form of electron microscopy and has great importance in the soft matter science because the direct imaging of liquids is not possible in a high-vacuum of TEM chamber due to the low vapor pressure of solvents and molecular diffusion. However, most of the self-assembled structures, with an extensive variety of shapes are stable only in their native solution conditions. However, Cryo-TEM provides in situ imaging of various delicate structures of soft matter, including liquid systems and can directly image in wide length scales ranging from a few nanometers to several micrometers. Cryo-TEM makes use of rapid quenching of the specimen to low temperatures so that the structures are preserved in an amorphous ice matrix and is imaged at low temperature.

By using Cryo-TEM one can easily differentiate between the topologies that are difficult to resolve by other techniques like scattering such as between small disk objects and spherical micelles, or between narrow ribbon elements and cylindrical micelles. Cryo-TEM has become a powerful complementary tool to small-angle X-ray and neutron scattering, light scattering, nuclear magnetic resonance, and rheological measurements in the study of soft matters.

Selected Area Electron Diffraction (SAED): Selected area electron diffraction patterns from the sample are obtained when TEM operates in the diffraction mode. Here, using an aperture in the image plane, a diffraction region from the specimen is selected. SAED patterns are a projection of the reciprocal lattice, with lattice reflections showing as sharp diffraction spots and can be used to identify crystal structures and measure lattice parameters.

2.5. UV-Visible Spectroscopy

Ultraviolet-visible (UV-visible) spectroscopy is widely utilized for both qualitative and quantitative characterization of organic and inorganic materials which shows electronic transitions in the UV-visible region of the electromagnetic spectrum. In this technique, a sample is irradiated with electromagnetic radiations in the UV-visible region (190-900 nm) and the characteristic wavelength of absorption and molar extinction coefficient are analyzed through the resulting spectrum. The absorption spectra arise from the allowed transition of electrons from lower energy ground state to higher energy excited state and the remaining light is transmitted through the sample. The transmittance (T) is defined as the ratio of the radiant power transmitted by the sample (I) to the radiant power incident (I_o) on the sample.

$$T = \frac{I}{I_0} \tag{2.33}$$

The basic principle of UV-visible spectroscopy is based on Beer-Lambert's law which relates to the absorbance by a sample, which is independent of the intensity of the incident beam and is related to the concentration of the absorbing species in the solutions as well as optical path length of the solutions. According to this law, when a beam of monochromatic light having intensity I_0 is traveled through a solution of an absorbing species, the rate of decrease of intensity of radiation with the thickness of the absorbing solution is proportional to the incident radiation as well as the concentration of the species. The analytical solution of this expression gives the following relations:

$$I = I_0 \exp(-\varepsilon bc) \tag{2.34}$$

$$A = \log\left(\frac{I_0}{I}\right) = -\log T = \varepsilon bc \tag{2.35}$$

where I and I_0 are the intensity of transmitted and incident light respectively, ε is molar absorption coefficient, which depends on the wavelength and the nature of the absorbing species, b is the optical path length of the light beam in the sample and c is the concentration of light-absorbing species in the sample (in moles per liter), A is the absorbance defined as the negative logarithm of transmittance. The absorption spectrum plots the absorbance by a sample as a function of spectral wavelength. The energy changes due to UV-visible radiation correspond to various molecular electronic transitions. For simple molecules, the lowest energy occupied molecular orbitals are σ orbital, then the π orbitals are at somewhat higher energy levels and the unoccupied or antibonding orbitals (π* and σ*) are the highest energy orbitals. The valence electrons available for transitions are located in σ (single bonding) orbitals, π (double/triple bonding) orbitals, and non-bonding orbitals (n) (which containing lone pair of electrons). The transition occurs from σ, π, and n orbitals, to antibonding

orbitals, π* and σ*. Some of the important transitions with increasing energies are: n to π*, n to σ*, π to π*, π to σ*, σ to π* and σ to σ*. The different wavelengths of light match the energy required for their respective transitions. The quantification of the exact concentration of unknown species in a mixture can be extracted by measuring the intensities of absorption for different concentrations of the sample and comparing it with the intensity of a standard sample using UV-visible spectroscopy.

The basic components of the spectrophotometer are: light source, monochromator, sample compartment, detector, amplifier, and recorder as shown in the figure below. The double beam recording spectrophotometer features a continuous change in the wavelength and an automatic comparison of the light intensities of the sample and the reference material. The instrument either plots the transmittance or the absorbance as a function of the wavelength of light.

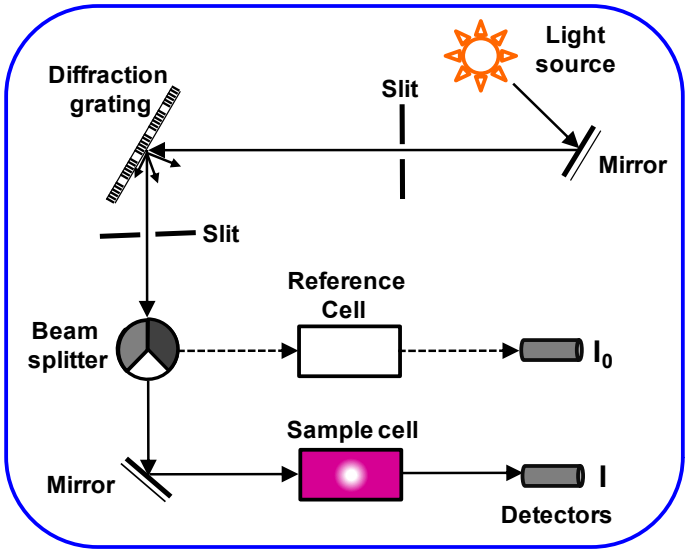

Figure 2.13 *Schematic representation of the components of a UV-visible spectrophotometer.*

2.6. Fourier Transform Infrared Spectroscopy

The vibrational spectroscopic technique like Fourier Transform Infrared Spectroscopy (FTIR) is a popular analytical technique used to identify mostly the

functional groups in organic and inorganic materials. It gives information about molecular vibrations or more precisely in transitions between vibrational and rotational energy levels in molecules. This information is of immense help to identify molecular components and their structures. The FTIR method is superior to conventional IR spectra due to the advantage of obtaining high-quality infrared spectra by mathematical conversion of an interference pattern into a spectrum. It simultaneously collects spectral data in a broad region of the spectrum in a short period of time and it has the advantages of high spectral resolution with good signal-to-noise ratios.

When Infrared (IR) radiation is passed through a sample, some radiation is absorbed by the sample and some transmitted and absorbed energy of light generates characteristic vibrational movements in molecules, such as stretching and bending modes. The frequency of light absorbed by a particular molecule is a function of the energy difference between the ground and excited vibrational states. These states are associated with a molecule's particular bonds, and consequently, each molecule has its own unique signatures. If the frequency of molecular vibrations corresponds to the frequency of IR radiation absorbed, the resulting signal at the detector is a spectrum representing a molecular 'fingerprint' of the sample. Hence, FTIR spectroscopy can be used to find the type of bond between two or more atoms and consequently identify functional groups, and it is also widely used to characterize the attachment of organic ligands to organic or inorganic nanoparticles and surfaces. The covalent bonds between the atoms or molecules vibrate at specific frequencies corresponding to their vibrational energy levels. These vibrational frequencies depend on several factors including bond strength and the atomic mass. Chemical bonds can be distorted in

different ways such as stretching (symmetrical and asymmetrical), scissoring, rocking, wagging, and twisting. The energy of a photon is given by the relation,

$$E = h\nu = \frac{E = hc}{\lambda} \qquad (3.36)$$

where λ is the wavelength of *t* radiation, *v* is the frequency, *h* = plank's constant, and *c* is the velocity of light.

Due to the relatively smaller amounts of energy associated with the IR radiation, photons are unable for electronic excitations but induce transitions between vibrational and rotational energy levels of a molecule. The molecular bonds vibrate at various frequencies depending on the elements and the type of bonds that leads to change in the dipole moment (necessary for the absorption of IR radiation) and this forms the basis of IR spectroscopy. For any given transition between two states, the light energy must exactly equal the difference in the energy between the ground state and the excited vibrational state. The vibrational energy levels of a molecule can be expressed by the relation,

$$E_v = (\nu + ½)\ \hbar\omega \qquad (3.37)$$

where, ω is the oscillations frequency, $\hbar = h/2\pi$, and *v* represents the vibrational quantum numbers which having values *v* = 0, 1, 2, 3, .etc, and the transition is restricted to $\Delta v = \pm 1$. The vibrational frequency is related to the force constant (*k*) and reduced mass (μ) of the molecule by the relation,

$$\nu = \frac{1}{2\pi c}\sqrt{\frac{k}{\mu}} \qquad (3.38)$$

An increase in bond strength and a decrease in the reduced mass results in the corresponding increase in the vibrational frequency. Various correction factors have been applied to the above equation for the anharmonic nature of vibrations.

The basic components of an infrared spectrometer are shown in Fig. 2.14. It consists of a light source having continuous radiations over the entire range of the infrared spectrum and intense enough for detection, an interferometer to modulate the wavelength from a broadband infrared source. The sample compartment also called the sampling area to put the sample for analysis; the monochromator disperses the light and then selects a narrow wavenumber range. The detector measures the intensity of transmitted or reflected light as a function of its wavelength and transforms it into an electric signal. The IR spectra are usually presented as plots of intensity versus wavenumber (in cm^{-1}) which is the reciprocal of the wavelength. The intensity can be plotted as the percentage of light transmittance or absorbance at each wavenumber. Samples in all states, solid, liquid or gas are characterized by IR spectroscopy.

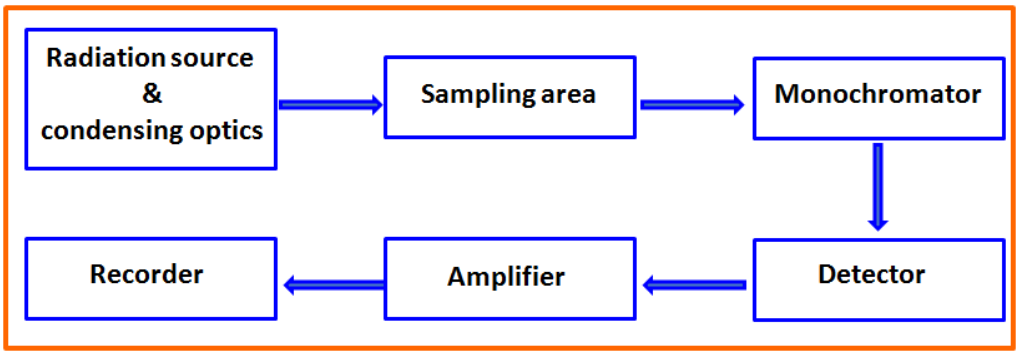

Figure 2.14 *Block diagram of major components of IR spectrophotometer*

The main components of conventional IR spectrophotometer are: IR sources, sample cells, monochromators, detectors, amplifiers, and recorder.

Fourier Transform: The ultimate performance of any IR spectrometer is determined by measuring its signal to noise ratio and this is best achieved by FTIR spectrometers. The term Fourier Transform Infrared Spectroscopy originates from the fact that a Fourier transform (a common algorithm/ mathematical process) is required to convert

the raw data (also called interferogram) into the actual spectrum. The commercial spectrometers use Michelson interferometers composed of a beam-splitter and two mirrors, one is fixed and another translates back and forth, very precisely (schematically shown in Fig. 2.15) with a variety of scanning mechanisms to produce the interference pattern. Once an interferogram is collected, it needs to be translated into a spectrum this process of conversion is through the Fast Fourier Transform algorithm.

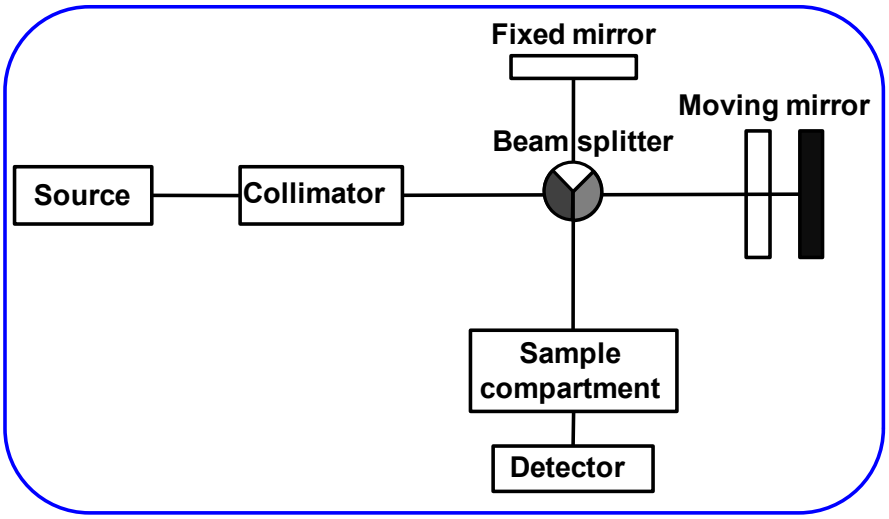

Figure 2.15 *Schematic diagram of Michelson interferometer.*

2.7. Magnetic Susceptibility Measurements

Magnetization represents the vector field which expresses the density of permanent or induced magnetic dipole moments in a magnetic material. The sources of the magnetic moments responsible for magnetization are electric currents resulting from the motion of unpaired electrons in atoms, and the spin of the electrons.[159] A single unpaired electron has a magnetic moment of 1 μB (Bohr magneton), where 1μB = $9.27402\times10^{-24}Am^2$. Magnetization also describes how a material responds to an applied magnetic field as well as the way the material changes the magnetic field and

can be used to calculate the forces that result from those interactions. If a magnetic field (*H)* induces magnetization (*M)* in a material, the material is said to possess a magnetic susceptibility (χ_m), and is given by,

$$M=\chi_m H \qquad (2.39)$$

where *M* and *H* are measured in units of Am^{-1}, where 1 $Am^{-1} = 4\pi/10^3$ Oe and χ_m is a dimensionless quantity and depends on the atomic structures of materials, temperature, and the applied magnetic field, which gives rise the characteristic sigmoidal shape to the M-H curve (Fig. 2.16) also called magnetization curve for magnetic materials. The $\chi_m H$ term represents the field-induced increase in the spontaneous magnetization at low field, while saturation of magnetization at high field. When the magnetization state reflects the previous states of magnetization, the material is said to be hysteretic, and the trajectory representing the response to the *H* is called the hysteresis loop. The shape of this curve depends on the nature of the material (ferromagnetic, ferrimagnetic, and superparamagnetic). The hysteresis loop shows that the magnetization increase with increasing applied field up to a point called the saturation magnetization. However, for materials that show hysteresis, when the field is removed, the magnetization is retained; even as the field is reduced to zero. This is called remanence magnetization which is retained due to the hysteresis. To reduce the magnetization back to zero, some amount of magnetic field of opposite direction has to be applied; this field is termed as coercivity. The magnetization vs. magnetic field (M-H) variations were used to estimate the saturation magnetization, hysteresis, and magnetic behavior of the material.

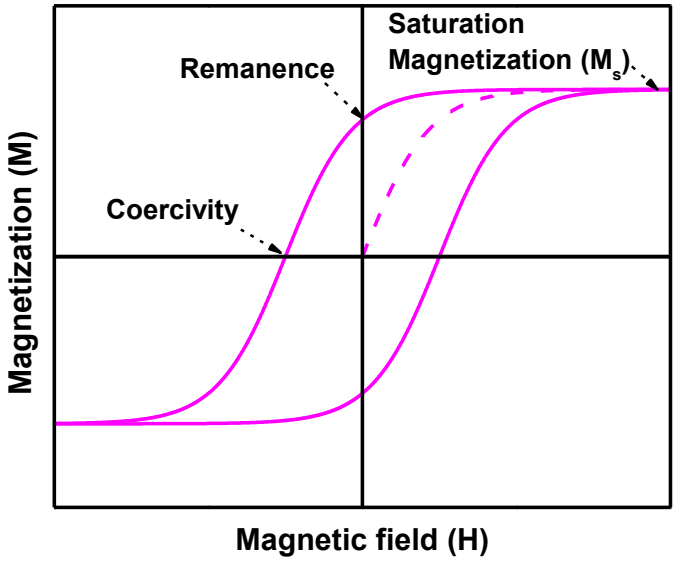

Figure 2.16 *Typical Magnetization (M) vs. applied magnetic field (H) representation of magnetic material*

2.8. Hyperthermia Studies

Magnetic materials possess the additional advantage of localized heating by application of external alternating current (AC) magnetic field. To estimate the heating efficiency of the magnetic nanoparticles, the time-dependent calorimetric measurements were done using an induction heating unit under the applied AC magnetic field which is necessary for use the magnetic nanoparticles in the thermal therapy. An instrument consists of an electromagnet, through which a high-frequency alternating current (AC) is passed. The frequency of AC required for effective heating depends on the particle size, material type, coupling (between the work coil and the object to be heated), and penetration depth. The relation between the heat generation/dissipation (P) and applied AC magnetic field is given by:[165]

$$P = \pi\mu_0\chi_m H^2 f \frac{2\pi f\tau_{eff}}{1+(2\pi f\tau_{eff})^2} \qquad (2.40)$$

where μ_0 is the permeability of free space, χ_m is the magnetic susceptibility, H is the applied magnetic field and τ_{eff} is the effective relaxation time. From equation 2.40 one

can say that the time required to reach the hyperthermia temperature (43-45 °C) decreases with an increase in the strength of the applied magnetic field. It may be noted that under appropriate conditions, the system temperature can be raised to a level required for hyperthermia in the presence of magnetic nanoparticles under the AC magnetic field. However, the application of the same field (335 Oe for 20 minutes) without magnetic nanoparticles did not produce significant heating.[166] In thermal activation of magnetic nanoparticles under the AC magnetic field, an increase in temperature is mainly due to the relaxation time (τ_{eff}), which is the combined effect of Néel and Brownian relaxations.[167] The Néel relaxation is associated with the magnetic moment rotations within the particles due to internal fluctuations of the magnetic moment with respect to the crystal lattice. The Brownian relaxation is related to the rotation of entire particles due to mechanical friction with the surrounding medium when NPs keep oscillating towards the field, keeping its magnetic moment fixed along the crystal axis. The relaxation times are given by the following equations:[165,167]

$$\tau_{eff} = \frac{\tau_N \tau_B}{\tau_N + \tau_B} \quad (2.41)$$

$$\tau_N = \tau_0 e^{KV_M/K_B T} \quad (2.42)$$

$$\tau_B = \frac{4\pi\eta {R_H}^3}{K_B T} \quad (2.43)$$

where τ_B is the Brownian relaxation time, τ_N is the Néel relaxation time, $\tau_0 \sim 10^{-9}$ s, K is the anisotropy constant, V_M is the volume of the magnetic nanoparticle, k_B is Boltzmann's constant, T is the temperature, η is the viscosity and R_H is the hydrodynamic radius of the particle. In the case of Fe_3O_4-based MNPs, heat generation from eddy current loss under AC magnetic field will be negligible.[168] Further, heat generation due to hysteresis loss will be negligible for

superparamagnetic NPs (as the particle size is less than the critical diameter/single domain).[169] The use of Fe_3O_4-based MNPs in hyperthermia therapy depends on their heating ability, which is expressed in terms of the specific absorption rate (SAR). The SAR value is dependent on various parameters such as the concentration of particles, magnitude of the applied field, frequency and physical properties of magnetic particles such as magnetization, particles size, size distribution etc.[170]

In the case of Fe_3O_4 MNPs, the SAR value (in W/g of Fe,) can be calculated from the Temperature (T) vs time (t) plot, using the following equation:[171]

$$SAR = C\frac{\Delta T}{\Delta t}\frac{1}{m_{Fe}} \quad (2.44)$$

where C is the specific heat of solvent ($C = C_{water}$ = 4.18 J/g ^{o}C), $\Delta T/\Delta t$ is the initial slope of the time-dependent temperature curve and m_{Fe} is the mass fraction of Fe. However, this SAR value is dependent on the applied frequency and field strength. Thus, the system-independent intrinsic loss power (ILP, measured in nHm^2kg^{-1}) can be obtained using the following equation:

$$ILP = \frac{SAR}{H^2 f} \quad (2.45)$$

where H is the field strength and f is the frequency.

Often the ILP parameter is used in preference to SAR when reporting the specific case of magnetic hyperthermia heating from ensembles of MNPs.

2.9. Other Complementary Techniques

2.9.1. Fluorescence Spectroscopy

Fluorescence spectroscopy (also known as Fluorometry) is a simple, fast, inexpensive and popular method to determine the concentration of analytes within the solution based on its fluorescence properties. This emission type of spectroscopy is

concerned with electronic and vibrational states of molecules; the species under study is first excited by a specific wavelength of light, that excites the electrons in molecules of certain compounds from its ground electronic state to one of the various vibrational states in the excited electronic state and intermolecular collisions cause the excited molecule to lose vibrational energy until it reaches the lowest vibrational state of the excited electronic state and causes them to emit light. Fluorescence is the phenomenon where a molecule absorbs light within its absorption band and then emits this light at longer wavelengths within its emission band. This phenomenon can be used to identify, quantify, and observe chemical changes in the molecules. The light that is emitted by the sample is generally measured at a 90-degree angle. The concentration level of the analyte compound within the solution is directly proportional to the intensity of emission spectrum, so by comparing with the fluorescence intensity with a standard sample under similar conditions, the quantification of unknown concentration of analytes can be easily done using fluorescence spectroscopy. It is the complementary technique for absorption spectroscopy.

2.9.2. Thermogravimetric Analysis

The TGA measurements are used mainly to determine the composition of materials and to assess their thermal stability with respect to temperature change. This measurement provides information about materials that exhibit weight loss or gain due to any physical process (phase transitions, absorption, and desorption) or chemical process (chemisorptions, evaporation, sublimation, thermal decomposition, oxidation, or dehydration, etc.) when subjected to change in temperature. Precise measurements of the weight of the specimen in a controlled atmosphere at different temperatures are obtained using a thermobalance. The effect of buoyancy in TGA measurements are

usually corrected by performing a blank measurement with a similar condition for sample measurement and then the resulting blank curve is subtracted from the sample measurement curve.[172] A typical block diagram of the TGA instrument is given in Fig. 2.17.

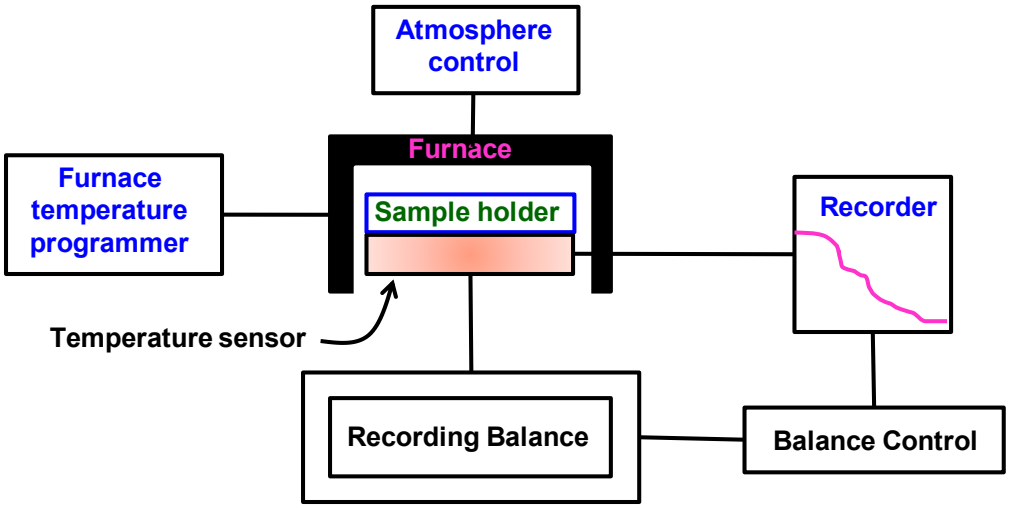

Figure 2.17 *Typical block diagram of Thermogravimetry*

2.10. Materials Used

Ferrous chloride tetra-hydrate ($FeCl_2.4H_2O$, ≥99%), ferric chloride hexa-hydrate ($FeCl_3.6H_2O$, ACS reagent, 97%), doxorubicin hydrochloride (DOX, 98%), 4-nitrophenyl chloroformate (NPC) and 1,1-diphenyl 2-picryl hydrazyl (DPPH), N-Hydroxysuccinimide (NHS), bovine serum albumin (BSA) and thiazolyl blue tetrazolium bromide (MTT) were purchased from Sigma-Aldrich, USA. Iron (III) acetylacetonate (98%) brought from Spectrochem. Pvt. Ltd., India. Ascorbic acid, ferrous ammonium sulfate (AR grade), 1, 10-phenanthroline monohydrate (Extrapure, AR grade), Ethylcarbodiimide hydrochloride (EDC) and dimethylformamide (DMF) were procured from Sisco Research Laboratories Pvt. Ltd., India. Triethylamine (TEA, ACS reagent, 99.5%), Methanol (HPLC grade), dichloromethane (DCM), and

Dimethyl sulfoxide (DMSO) was bought from SD Fine Chem. Ltd., India. Ammonia solution (25%, AR grade) and methylene blue were obtained from Thomas Baker Chemical Pvt. Ltd., India and Amurt industries, India, respectively. Dulbecco's modified eagle medium (DMEM) and fetal calf serum (FCS), Dialysis membrane-60, 0.5% trypsin–EDTA (10X) were procured from Himedia Laboratories Pvt. Ltd., India. D-mannitol, D-Sorbitol (extra pure), Fructose (AR grade), D-Glucose (Dextrose anhydrous, extra pure 99% purity), Sucrose LR grade (99%) were obtained from SD Fine Chemicals, India. Xylitol (≥99%) obtained from Sigma-Aldrich; Urea (AR grade) was purchased from Glaxo Laboratories (India) Ltd. Sodium chloride (NaCl) AR grade (99.9% purity) was acquired from Polypharm Pvt. Ltd., India. Glutaric acid, citric acid (99.7%) (Chemco fine chemicals, India), malic acid (99% Sisco Research Laboratories Pvt. Ltd. India), maleic acid (98%, Loba Chemie Pvt. Ltd.), oxalic acid, N-methyl urea, Acetamide was purchased from Sisco Research Laboratories Pvt. Ltd., India. Cetyltrimethylammonium Bromide (CTAB) AR grade (99% purity) was obtained from SD Fine Chemicals Pvt Ltd, India. Sodium dodecyl sulfate (SDS) and deuterated SDS were obtained from Sisco Research Labs and Sigma-Aldrich respectively. Triton X-100 (99%) was purchased from Sigma-Aldrich. Tween-80 (Polyoxyethylene monooleate) was obtained from E. Merck (India) Ltd. Dihexadecyl dimethyl ammonium bromide (DDAB), Sodium deoxycholate (SDC) Loba Chemie, India, Cetylpyridinium chloride (CPC) and Dioctyl sulfosuccinate sodium salt (AOT) 98% brought from Fluka Chemicals, Cholesterol (extra pure, Sisco Research Laboratories Pvt. Ltd. India), H-90 lipid. Curcumin (>99%) was received as a gift from Win Herbal Care, India. MTT reagent (thiazolyl blue tetrazolium bromide) was purchased from Sigma-Aldrich, USA. Mouse Skin Fibrosarcoma (WEHI-164), human breast cancer cells (MCF-7), human lung cancer (A549) and Chinese hamster ovary

(CHO) cells were obtained from National Centre for Cell Sciences (NCCS), Pune, India, and human normal lung cells (WI26VA) from Sigma. The acetate buffer (AB, pH 5) and phosphate-buffered saline (PBS, pH 7.4) were prepared using standard protocols. All other chemicals used were of AR grade unless otherwise specified and used as such without further treatment. All the aqueous solutions were prepared using nano-pure water from a Millipore-MilliQ system (resistivity ~18 MΩ cm) was used for preparing the solutions.

2.11. Instrument Details

SAXS: The SAXS experiments were performed using the Anton Paar SAXSpace instrument (line collimated sealed tube Cu-Kα source). The samples were placed in 1 mm quartz capillaries or paste cell and thermostated using Peltier controlled sample holder. The sample to detector distance was set to 305 mm. The scattering intensities were monitored in transmission geometry using a 2D CCD detector (pixel size 24 micron) to span a q (momentum transfer) range of 0.01 $Å^{-1}$ to 0.65 $Å^{-1}$. The data were processed using standard protocols.

SANS: SANS experiments were carried out using the SANS diffractometer at the Dhruva Reactor, Bhabha Atomic Research Centre, Trombay, India. The mean wavelength (λ) of the neutron beam is 5.2 Å. The angular distribution of the scattered neutrons was recorded using a one-dimensional position-sensitive detector (PSD) in the wave vector transfer range of 0.017-0.35 $Å^{-1}$. The samples were held in a quartz sample holder of 2 mm thickness. The measured SANS data were corrected and normalized to a cross-sectional unit, using standard procedures.

Dynamic Light Scattering: DLS experiments were performed on a Malvern 4800 Autosizer instrument employing a 7132 digital correlator and equipped with 5 mW He-Ne laser operated at 632.8 nm. All measurements were done at a scattering angle of 90^{o}. The samples were placed in 10 mm square cuvettes and thermostated using Peltier controlled sample holder.

Zeta-potential Measurements: Zeta potential measurements were made with a Zetasizer Nano instrument, Malvern Instruments, by phase analysis light scattering with an applied field strength of 2.5 x 10^3 V/m. The light source was a He-Ne laser operated at 632.8 nm operating at 4.0 mW. The experiment was carried out using a quartz cuvette (universal dip cell) with a 10 mm light pathway. The measurements were performed at 25 ^{o}C. The zeta potential (ζ) values are calculated from the electrophoretic mobility data using the Smoluchowsky approximation.

XRD Measurements: XRD measurements for all the samples were performed by a Phillips PW1729 diffractometer based on the Bragg-Brentano reflection geometry with Cu Kα (λ= 1.5405 nm) as incident radiation with a Ni filter. The crystallite size is estimated from the X-ray line broadening using the Debye-Scherrer formula (eq.2.31). The diffracted beam was monochromatized with a curved graphite single crystal. For the detection of X-rays, a proportional counter (argon filled) was attached to the diffractometer. The X-ray tube rating was maintained at 30 kV and 20 mA. The goniometer was calibrated for correct zero position using silicon standard. Samples were well-grounded and made in the form of a thin slide prior to mounting in the diffractometer.

Magnetic Measurements: The magnetic properties of the prepared nanoparticles were measured by using Vibrating Sample Magnetometer (VSM, LakeShore, Model-7410). The room temperature (300 K) field dependence magnetic measurements (M *vs.* H) were carried out on powder samples mounted tightly in the sample holder by varying magnetic fields from -20 to +20 kOe.

UV-Visible Measurements: UV-visible measurements were done using JASCO V-650, UV-visible spectrophotometer. The instrument allows absorbance measurements in the wavelength range of 190-900 nm, and all the measurements were done at the resolution of 1 nm.

FTIR: IR spectra were recorded using Bomen Hartman and Braun, MB series, FTIR machine having a range of 400-4000 cm^{-1} and with a resolution of 4 cm^{-1}. IR radiation was generated from a globar source (silicon carbide rod). The instrument used CsI single crystal, as the beam splitter and deuterated triglycine sulfate (DTGS) as a detector. Prior to IR measurements, the samples were ground into fine powder thoroughly by mixing with dry KBr powder (since KBr does not absorb infrared light in the interest region), using an agate mortar and the mixture is to admitted a pressure under a hydraulic press at 10,000 psi in a die, to produce a highly transparent thin plate or disc and introduced into the sample chamber of the instrument to record the FTIR spectra.

Fluorometry: The steady-state fluorescence measurements were carried out using Hitachi F-4500 fluorescence spectrophotometer, and for measuring the fluorescence intensity using a microplate reader, Gen1.0.5, SYNERGY/H1 microplate reader; Bio Tek, Germany used.

TEM: In the case of Fe_3O_4-based nanocarriers the samples for TEM were prepared by making clear dispersion of the MNPs in isopropyl alcohol using the ultrasonic bath (20 kHz, 500 W) for 10 min and putting a drop of the solution on a carbon-coated copper grid. The solution was allowed to evaporate under a UV lamp leaving behind the MNPs on the carbon grid. The structures and crystallite size of Fe_3O_4-based nanocarriers were studied using FEI Tecnai T-20 having LaB6 filament. TEM micrographs were digitally recorded on CCD camera and particle size was determined after examining at least 10 micrographs.

For observation of supercooled micelles, HR-TEM experiments were done using an FEI Talos F200C equipped with phase plates at Technion, Israel Institute of Technology, Israel. Images were recorded on both a CETA 16M camera and a Falcon 3-direct detector. For liposomes, a drop of liposomal formulations was put on holey carbon grids and then the excess sample was removed by blotting with filter paper. Thereafter, the grids were plunged into liquid ethane using an automated plunger and transferred into a grid holder kept in liquid nitrogen. The samples were mounted in a Cryo specimen holder and observed in the Cryo-TEM instrument.

TGA: The physico-chemical changes during thermal treatment were analyzed by TGA measurements using a 10 °C/min heating rate under inert (N_2) atmosphere in the range of 40 to 500 ºC, and the change in mass/weight (%) of the sample was plotted against temperature. The weight loss processes with different thermal decomposition rate was monitored in thermogravimetric analysis and other useful and complementary information obtained by using the first derivative of the TGA curve with respect to temperature or time. This shows the rate at which the mass of sample changes and is known as the differential thermogravimetric or DTG curve. In the case of Fe_3O_4

nanocarriers, the weight loss observed by TGA was further supported by the chemical method of iron estimation through the phenanthroline spectrophotometric method, which is useful to estimates the amount of organic moieties present on the surface of MNPs.

Density measurements: To estimate the SLD of the solvent, the density of the solvent matrix needs to be known. For solvent mixtures or solvents with additives for which the density is not known, density measurements were done by using a digital density meter, Model DSA 5000M (Anton Paar, Austria).

CHAPTER 3

SURFACE PASSIVATION OF Fe_3O_4 FOR ELECTROSTATIC BINDING OF DOXORUBICIN

3.1. Introduction

There are various reports attempting on the surface functionalization of MNPs with polymers, polysaccharides, etc. for imparting kinetic stability to aqueous dispersions.[102,173] In spite of the biocompatibility of these polymers, during in vivo experiments, they often detach from the surface of the nanoparticles, resulting in unfavorable aggregation. Also, the presence of large non-magnetic polymer shell will reduce the effect of the superparamagnetic properties of MNPs thereby limiting their applications in biomedical use. Only a limited number of studies exist on the functionalization of MNPs with small molecules like amino acids, sugars, vitamins, etc.[174,175] These multifunctional small molecule-based stabilizing agents can be an attractive option owing to its biocompatible and health supplement properties. These additives may allow better internalization of the MNPs inside the cells as health supplements are often absorbed by the cells and also provide the functional groups for conjugation of different bioactive molecules. The similarity of the chemical structure of sugar alcohols/polyols with polysaccharides and their good biocompatibility offer great promise as potential stabilizing agents. Among the other polyols, mannitol and sorbitol are extensively used in sweets and low-calorie foods and as a stabilizer during the freeze-drying of biological macromolecules.[176] Also, ascorbic acid (called vitamin-C) is a water-soluble essential vitamin, very well known for its anti-oxidant properties[177] and is of much interest in both pharmaceutical and food processing industries. As an anti-oxidant, ascorbic acid (AA) scavenges free radicals and reactive oxygen species.[178] Also, AA has a striking effect on the absorption of non-heme iron thereby increasing the bioavailability of iron and also it reduces and binds dietary non-heme iron.[179] These compounds (sugar alcohols and ascorbic acid) have significant biological (biodegradable, biocompatible, bioactive) and chemical properties (due to

the presence of reactive groups like –OH in sugar alcohols and, enol -OH groups, -OH groups and a carbonyl group in AA) amenable for the drug delivery applications.

Mannitol and sorbitol are widely used in the pharmaceutical industry as the water-soluble solid matrix of carrier materials and can improve the solubility of certain drugs. It has six hydroxyl groups that can easily form hydrogen bonds with water. Earlier studies indicate that mannitol opens the blood-brain barrier to hydrophilic molecules by stretching the tight junctions between the endothelial cells.[180] Moreover, AA, as well as its oxidized product dehydroascorbic acid (DHA) acted as a good capping ligand due to the chemical interaction of its carbonyl groups with metal ions. There have also been reports on the MRI contrast properties of AA and DHA coated MNPs.[181,182] AA is transported into cells in DHA form via facilitative glucose transporters (GLUTs). DHA can cross the BBB by means of GLUT1[183] and thus, AA coated MNPs can be useful as a carrier for brain drug delivery. However, the drug delivery capability of sugar alcohols and AA conjugated nanoparticles is not yet explored, and hence; significant interest lies in preparing highly water dispersible Fe_3O_4 MNPs using these compounds as capping agents for biomedical applications. Therefore, it is envisaged to use sugar alcohols and AA as effective coating agents for MNPs with desired colloidal stability and magnetic responsivity. A monolayer coating of these low molecular weight species is conducive for forming thin coatings for MNPs. Attempts were made to compare the drug loading and release behavior of these MNPs under different physiological conditions for cancer therapy applications.

3.2. Experimental

Synthesis of Functionalized Fe_3O_4 Magnetic Nanoparticles:

The functionalized Fe_3O_4 magnetic nanoparticles (MNPs) were prepared by a well-known co-precipitation method using the stoichiometric mixture of ferrous and ferric salts in an aqueous medium followed by in-situ coating of sugar alcohols/AA with slight modification. In a typical synthesis of ascorbic acid-coated Fe_3O_4 magnetic nanoparticles (AMNPs), 0.994 g of $FeCl_2.4H_2O$ and 2.703 g of $FeCl_3.6H_2O$ (molar ratio of Fe^{2+}/Fe^{3+} =1:2) were dissolved in 40 ml of oxygen-free Milli-Q water in a round bottom flask and temperature was slowly increased to 70 ^oC in under nitrogen atmosphere with constant stirring. The temperature was maintained at 70 ^oC for 30 min and then 15 ml of 25% ammonia solution was added instantaneously to the reaction mixture and kept for another 30 min at 70 ^oC. Then, 5 ml aqueous solution of coating agent AA (0.88 g) was added to the above reaction mixture. The temperature was slowly raised up to 90 ^oC and reacted for 60 min with continuous stirring for the functionalization of particles with AA. The obtained black colored precipitates were then thoroughly rinsed with Milli Q water (3-4 times) and separated from the supernatant using a permanent magnet of field strength ~ 2.5 kOe.

By using a similar protocol the mannitol and sorbitol-coated Fe_3O_4 magnetic nanoparticles (MMNPs and SMNPs, respectively) were prepared using D-mannitol and D-sorbitol as coating agents. The schematic representation of the synthetic protocol for functionalized Fe_3O_4 MNPs is shown in Fig. 3.1.

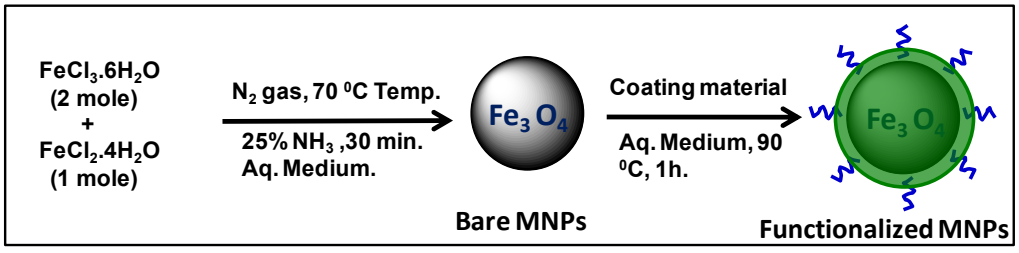

Figure 3.1 *Schematic representation of the synthesis of functionalized MNPs.*

3.3. Results and Discussion

3.3.1 Structural and Morphological Characterization of MNPs

XRD patterns of MNPs functionalized with mannitol, sorbitol, AA and bare iron oxide MNPs are shown in Fig. 3.2. The six diffraction peaks displayed in the XRD pattern corresponding to (220), (311), (400), (422), (511) and (440) confirmed the formation of single-phase inverse cubic spinel nanostructure. The lattice constant was found to be 8.378 Å, which is very close to the reported value of Fe_3O_4 (JCPDS Card No. 88-0315, a=8.375 Å). The spinel-structured magnetic iron oxide nanoparticles exist in two different phases such as magnetite (Fe_3O_4) and maghemite (γ-Fe_2O_3). Since the XRD patterns of magnetite and maghemite are very similar, it is difficult to distinguish these two phases simply from XRD patterns. The earlier studies such as X-ray photoelectron spectroscopy and temperature-dependent magnetization measurement performed on MNPs obtained by similar synthesis methods primarily suggested the presence of magnetite phase.[184,185] From X-ray line broadening, the average crystallite size was found to be around 10 nm for all the three functionalized MNPs.

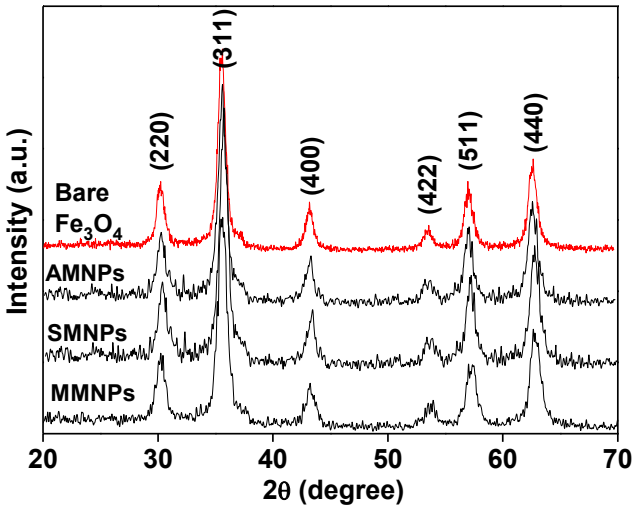

Figure 3.2 *X-ray diffraction patterns of functionalized MNPs along with bare MNPs.*

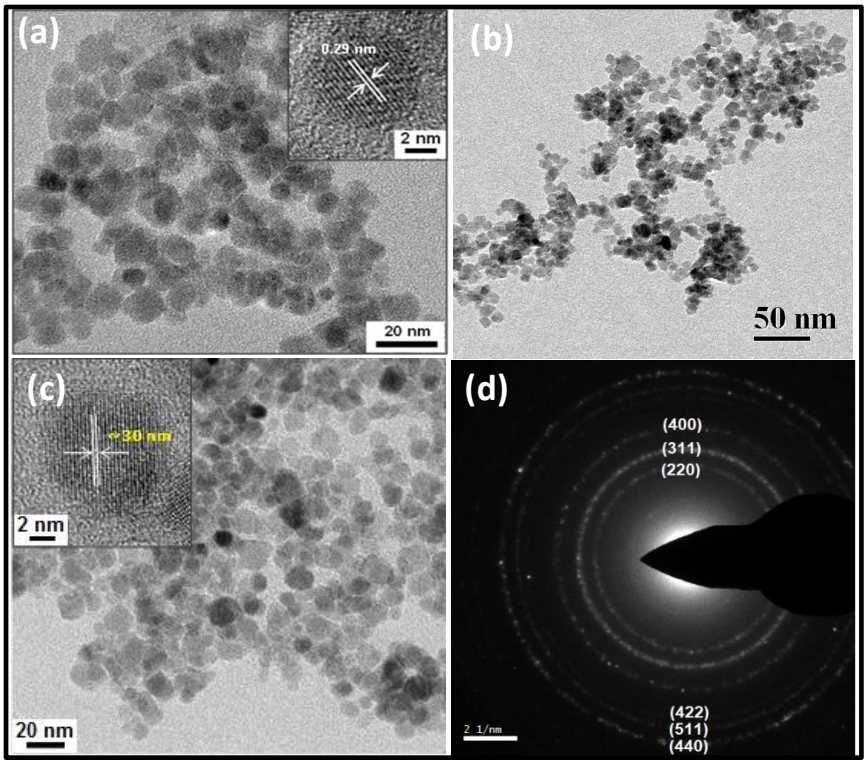

Figure 3.3 *TEM micrograph of (a) MMNPs, (b) SMNPs, (c) AMNPs (inset shows corresponding HRTEM micrograph revealing lattice spacing), and (d) Selected area electron diffraction pattern of AMNPs.*

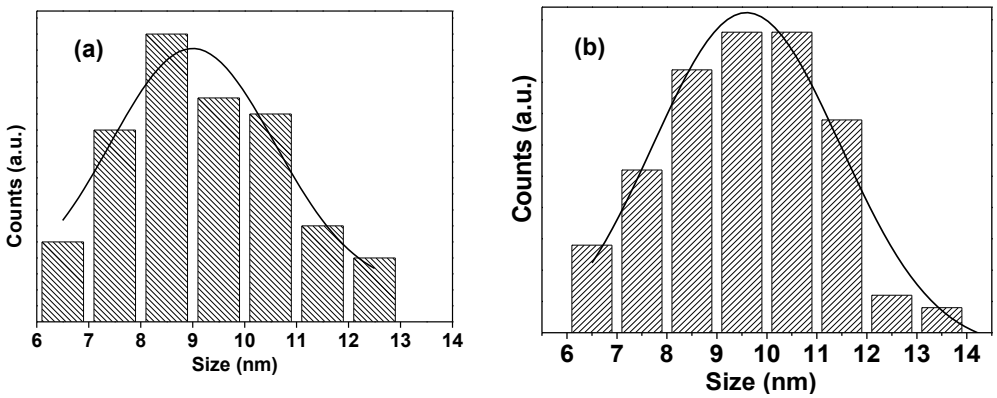

Figure 3.4 *Particle size distributions obtained from TEM micrograph of (a) MMNPs and (b) AMNPs.*

TEM micrograph (Fig. 3.3) shows that these MNPs are roughly spherical in shape with a fairly narrow size distribution having an average size of 10 nm (Fig. 3.4).

HRTEM analysis reveals highly crystalline and single-domain structures. The crystal lattice fringes (inset of Fig. 3.3) with the spacing of ~0.30 nm corresponds to the (220) spinel plane of Fe_3O_4.[177] Further, the selected area electron diffraction (SAED) pattern of AMNPs (Fig. 3.3d) exhibits bright and distinguishable diffraction rings corresponding to the reflections of (220), (311), (400), (422), (511) and (440) planes of spinel structure and also confirmed the high crystalline nature of these MNPs, which is consistent with the XRD result. All these results suggest that the oxide material formed primarily consists of Fe_3O_4 NPs.

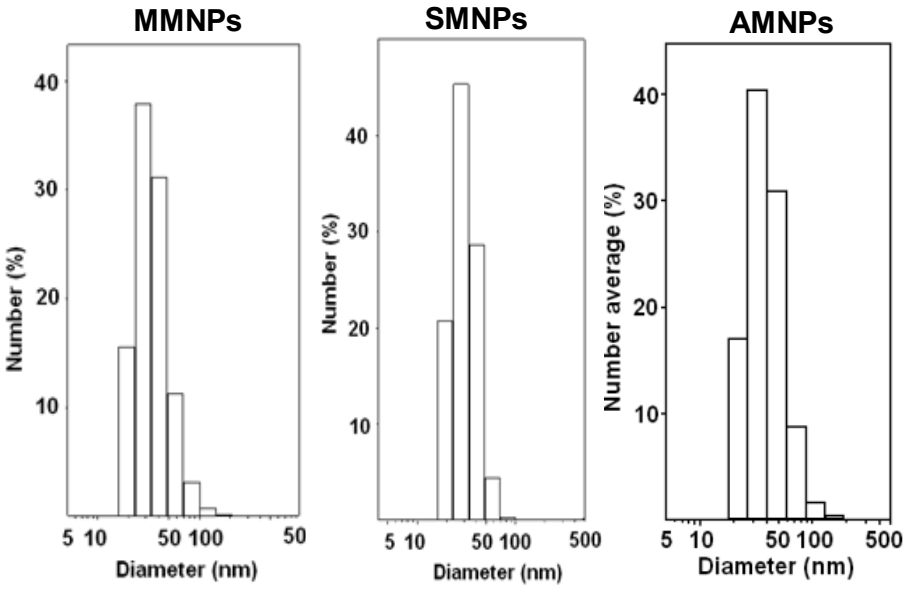

Figure 3.5 *Number weighted hydrodynamic size distributions of the MNPs.*

Further, dynamic light scattering (DLS) measurements were performed in order to determine the hydrodynamic diameter of these nanoparticles in the aqueous medium. DLS measurement (Fig. 3.5) indicates that these samples render stable aqueous colloidal suspension with the mean number weighted hydrodynamic diameter of about 31.0 nm, 37.0 nm and 40 nm for SMNPs, MMNPs and AMNPs respectively.

This is significantly larger than the size obtained by TEM analysis. The observed higher hydrodynamic diameter is possibly due to the presence of associated hydrated organic layers on the surface of MNPs particles.[186] Also, both the shape irregularity and polydispersity of MNPs could also contribute to the differences in particle size.[187] Some of the hydroxyl groups of sugar-alcohols strongly coordinate to iron cations on the Fe_3O_4 surface to form a robust coating, while uncoordinated hydroxyl groups extend into the water medium, conferring a high degree of water dispersibility.

The successful conjugation of sugar alcohols (mannitol and sorbitol) and AA on the surface of Fe_3O_4 MNPs are confirmed by FTIR and thermal analyses. The FTIR spectra of pure D-mannitol, D-sorbitol, AA, and corresponding MNPs along with their characteristic peak assignments in the range of 400-4000 cm^{-1} are shown in Fig. 3.6. The IR spectra of pure mannitol, sorbitol, and AA shows well-resolved vibration modes whereas those of their corresponding MNPs are relatively broad and a few peaks have merged. The intense peak appeared at around 588 cm^{-1} in spectra of all MNPs can be attributed to the Fe–O vibration of Fe_3O_4 MNPs.[171]

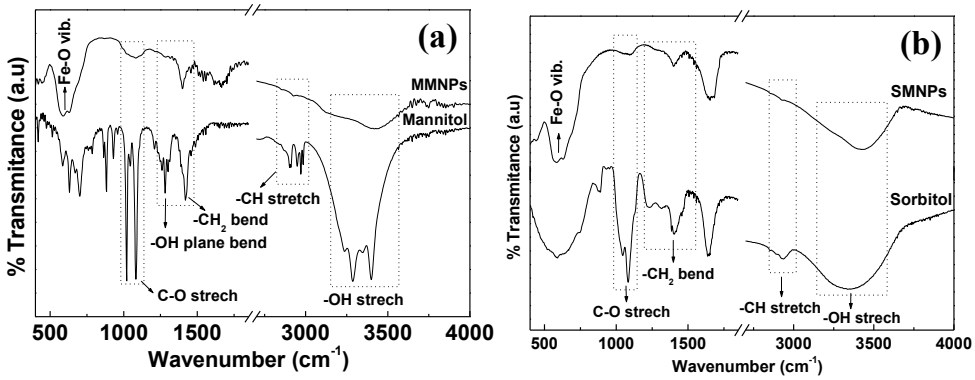

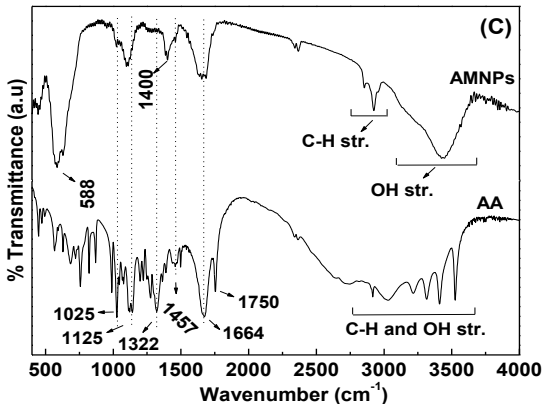

Figure 3.6 *FTIR spectra of (a) pure mannitol and MMNPs, (b) pure sorbitol and SMNPs and (c) Pure AA and AMNPs along with their characteristic peak assignments in the range of 400-4000 cm^{-1},*

The FTIR spectrum of pure mannitol and sorbitol shows strong stretching vibrations peaks of –OH and C–O, C–H.[188] The –OH in-plane bending and C–H bending vibrations of pure mannitol also appeared at 1422 and 1280 cm^{-1}. Several peaks of C–H bending vibrations are also observed in the FTIR spectrum of sorbitol between 1200 and 1500 cm^{-1}. Most of these characteristic bands appeared in the FTIR spectrum of MMNPs and SMNPs suggesting the presence of sugar alcohols on the surface of MNPs. Further, from FTIR spectra (Fig. 3.6c), it is seen that AA exhibited bands at 1750, 1664, and 1322 cm^{-1} for C=O stretching of five-member lactone ring, C=C stretching vibrations coupled with the neighboring vibrations along with the conjugated system and enol hydroxyl stretching vibrations, respectively.[189] The C=C and enol hydroxyl stretching vibrations of AA also appear in the FTIR spectrum of AMNPs. The absence of an intense C=O stretching band in AMNPs indicates the oxygen atom of the carbonyl group has coordinated to the Fe atoms of MNPs surface (through C=O···Fe interaction). This coordination is further confirmed by the appearance of a new intense vibrational band at 1400 cm^{-1}. However, it is difficult to predict whether Fe is co-ordinated with AA using one, two or three of its C=O groups

of the lactone ring. The band appearing at 1125 and 1025 cm^{-1} in pure AA can be associated with C–O groups of the lactone ring.[182] These peaks appeared in the spectrum of AMNPs with a slight shift in peak position. Further, the bands corresponding to different hydroxyl groups of AA in the range of 3210–3527 cm^{-1} appeared as broadband in the FTIR spectrum of AMNPs.

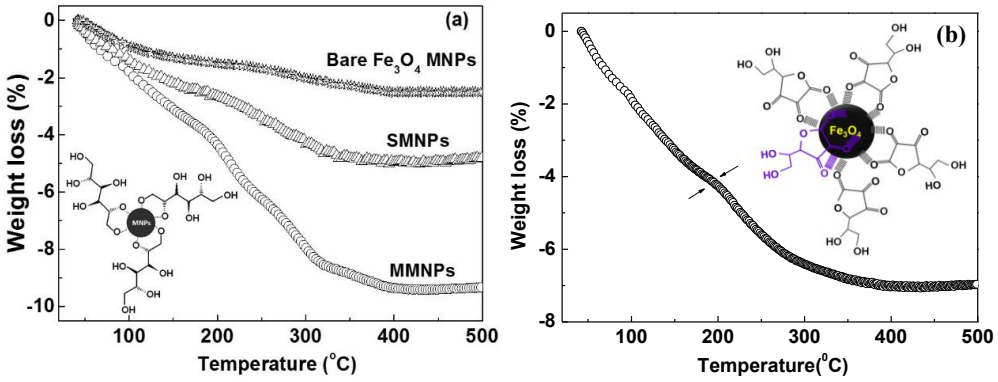

Figure 3.7 *TGA plots of (a) MMNPs, SMNPs, bare Fe_3O_4 MNPs and (b) AMNPs (Inset shows a proposed schematic representation showing conjugation of sugar alcohols and AA with MNPs).*

The organic modification of these nanoparticles was further evident from thermogravimetric analysis (TGA) shown in Fig. 3.7. All these MNPs show two steps thermal decomposition with a total weight loss of about 9.4%, 4.8%, and 7.0% for MMNPs, SMNPs, and AMNPs, respectively. The first step weight loss up to 200 ^oC can be ascribed to the removal of physically adsorbed water and organic moieties, whereas weight loss beyond this can be associated with the removal of chemically adsorbed coating molecules and water molecules from the surface of Fe_3O_4 MNPs. The bare Fe_3O_4 nanoparticles prepared by similar method (without using coating agent) exhibit only 2.5 % total weight loss in the temperature range from 25 to 500 ^oC owing to the removal of physically adsorbed water molecules. This result was consistent with reported weight loss of bare MNPs by a similar method.[169] The significantly higher weight loss associated with these particles suggests the

incorporation of organic molecules on the particle surface of NPs. It has been reported that pure D-mannitol, D-sorbitol, and AA starts decomposing at about 300 ºC, 250 ºC, and 191 ºC respectively.[190–192] The observed decomposition temperature of these additives in the presence of MNPs is slightly higher than that is reported for pure molecules. The shifting of decomposition temperature of these molecules upon coating with MNPs can be attributed to the chemical coordination of these molecules with Fe_3O_4 nanoparticles.

The weight loss observed by TGA is consistent with the iron estimation (by the spectrophotometric method using 1,10 phenanthroline).[193] The percentage of organic content in the particles as obtained from iron estimations are 10 %, 4.8%, and 8% for MMNPs, SMNPs, and AMNPs respectively. Thus, FTIR and TGA together provide clear evidence for effective capping of sugar-alcohols and AA on the surface of Fe_3O_4 NPs.

3.3.2 Colloidal Stability Studies

Light scattering measurements were performed to determine the hydrodynamic diameter and surface charge of these particles as well as their colloidal stability. From pH-dependent zeta-potential measurements (Fig. 3.8), the point of zero charge (PZC) of MMNPs, SMNPs and AMNPs were found to be around pH 5.3, 5.4 and 2.8 respectively, whereas PZC of bare Fe_3O_4 nanoparticles is 6.7.[194] This difference in their charge characteristics may be attributed to the degree of ionization of functional groups at different pH values and is conducive for electrostatic binding of drug molecules. Further, these particles possess negative values of zeta-potential in 0.1 M PBS medium (-22.7 mV, -16.2 mV and -26.0 mV, respectively for MMNPs, SMNPs, and AMNPs).

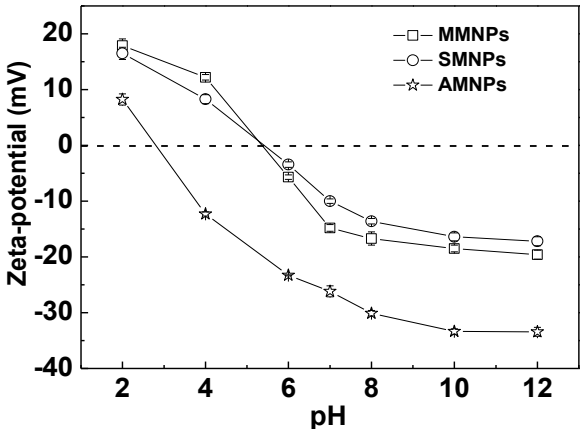

Figure 3.8 *The variation of zeta-potential as a function of pH of the MMNPs, SMNPs, and AMNPs suspensions.*

A negative zeta-potential at physiological pH implies that these MNPs posses negative surface charge under neutral conditions. Such negative surface potential of inorganic particles at physiological conditions have been reported for other hydroxyl-containing stabilizing agents. Stiufiuc et al. observed negative surface charge (-16.2 mV) on the surface of PEG-coated gold NPs.[195] Similar results were also observed by Marchetti et al. in hydroxyl functionalized core-shell poly(styrene-co-butadiene) NPs.[196] Also, Cai et al. reported the negative zeta-potential (-21 mV) form ethoxy polyethylene glycol-coated Fe_3O_4NPs in water.[197] Thus, the observed negative surface potential could provide electrostatic repulsion between the NPs leading to their colloidal stabilization.

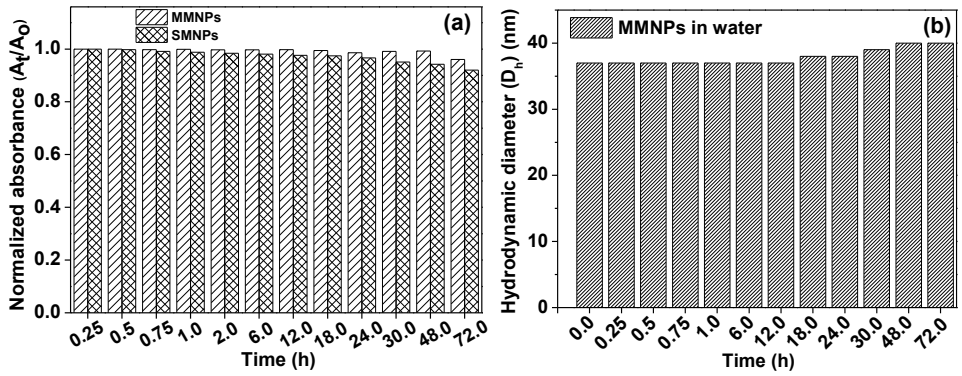

Figure 3.9 *Normalized absorbance vs. time plot indicating the stability of (a) MMNPs and SMNPs (0.1mg/ml) in water and (b) Variation in the hydrodynamic diameter of MMNPs with time.*

Light scattering techniques are often used to assess the stability of particles, by monitoring time-dependent changes in the hydrodynamic diameter (D_h) of the particles. Therefore, the aqueous colloidal stability of these MNPs were compared using the changes in D_h of MMNPs as well as their normalized absorbance (Fig. 3.9) as a function of time. The insignificant change in absorbance of particle suspension (0.1 mg/ml) in water and cell culture medium (DMEM with FBS) with time (even after 72 h) indicates their good colloidal stability (Fig. 3.10). Thus, it can be confirmed that small molecules like sugar-alcohols and AA can coordinate with iron oxide metal surface through the hydrophilic –OH group providing a high degree of colloidal stability to the particles by overcoming the attractive magnetic and van der Waals forces in the solvent medium through hydrogen bonding as well as electrostatic repulsive forces.

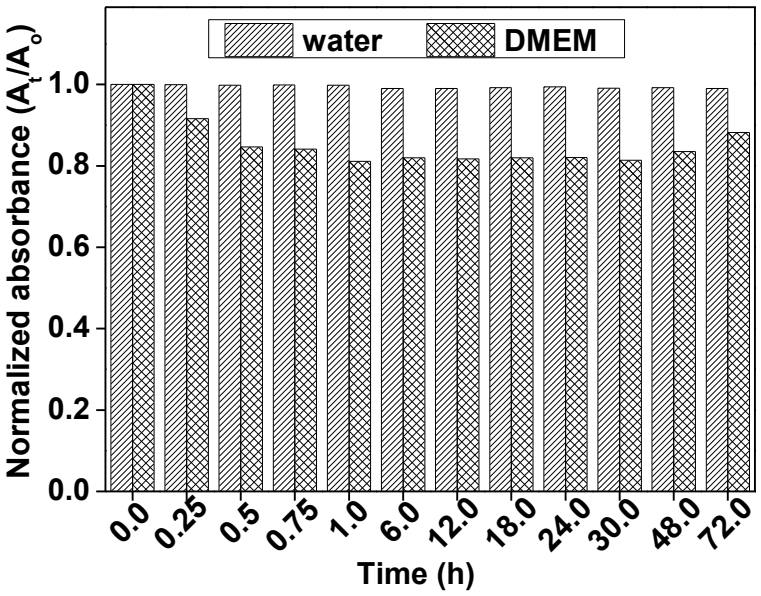

Figure 3.10 *Normalized absorbance vs time plot indicating the stability of AMNPs (0.1 mg/ml) in water and DMEM.*

3.3.3 Drug Loading and Release Study

Considering the negative surface charge and colloidal stability of the prepared MNPs, these particles were explored for electrostatic binding of cationic drugs. The anticancer drug, doxorubicin hydrochloride (DOX) was used as a model cationic drug to estimate the drug loading and release behavior of the functionalized MNPs. The interaction of DOX molecules with MNPs was observed from zeta-potential and UV-visible measurements. Any electrostatic interaction between oppositely charged species could lead to a decrease in the magnitude of the surface charge due to the neutralization of charges. Thus, it is envisaged that zeta-potential measurements could serve as a tool to monitor drug binding to the particle surface. As expected, upon incubating with an aqueous solution of 10 μg/mL of DOX, the zeta-potential of MNPs suspension (100 μg/mL) changed from a high negative value to less negative values. A change in the in surface charge of MMNPs, SMNPs, and AMNPs from -15.0, -13.5 and -26.2 mV to -1.0, -1.5, and -18.4mV respectively were observed after incubating with the drug (10 μg DOX and 100 μg MNPs, 1:10 drug to particle ratio). This change in zeta-potential arises from the binding of cationic DOX (protonated primary amine present on DOX induces a positive charge) with negatively charged hydroxyl moieties present on the surface of Fe_3O_4 NPs forming DOX bound MNPs. Such affinity of cationic DOX towards negatively charged particles are well reported by various research groups.[166,184,198] Further, the interaction of DOX molecules with MNPs was also evident from the decrease in the optical absorption spectra of the supernatant liquid after removal of the drug-loaded MNPs through magnetic separation (Fig. 3.12b). The schematic illustration of electrostatic binding of DOX with negatively charge MNPs are depicted in Fig. 3.11.

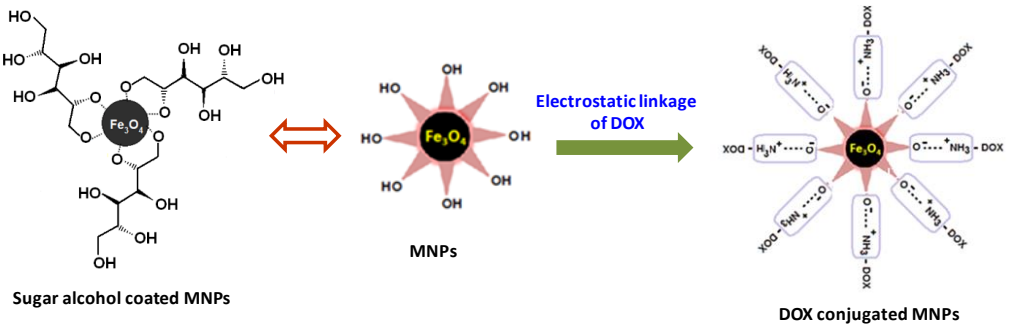

Figure 3.11 *Schematic representations showing electrostatic conjugation of DOX to the MNPs.*

To monitor the concentration of drug molecules bound with the particles, it is necessary to separate the free and bound drug molecules so that the interference of free drug in *in-vivo* parameters is minimized. In the case of MNPs, this process of separating the bound and free drug is relatively easy, due to the inherent magnetic separation of the particles. Clearly, the interaction of DOX molecules with MNPs is evident from the decrease in fluorescence intensity of the supernatant liquid after removal of the drug-loaded MNPs through magnetic separation. It may be noted that the binding efficiency of drug molecules to a given NPs depends very much on the drug to particle ratio. The fluorescence intensity of DOX in the supernatant decreases with increasing concentration of MNPs, suggesting an increase in the loading efficiency of DOX with increasing particle concentration, at fixed drug content. Typical fluorescence spectra of DOX present in the supernatant, at a different drug to particle weight ratio, is given in Fig. 3.12a. From this, it is inferred that the drug loading efficiency is strongly dependent on the DOX to particles ratio. Among the concentrations studied, the highest drug-loading efficiency could be achieved for AMNPs at 1:10 (w/w) DOX to particle ratio. A similar trend was also seen for MMNPs and SMNPs. The drug loading efficiency, obtained from fluorescence

measurements were also corroborated by UV-visible spectroscopic studies (Fig. 3.12b). The maximum loading efficiency obtained for the particles are 40, 68, and 60% for SMNPs, MMNPs, and AMNPs respectively, at DOX to particles ratio of 1:10. Though the binding of the drug to the particles is quite a fast process due to the electrostatic nature of the interaction, all measurements were done after incubating the drug with particles for 1h in dark. It has been observed that among the three, MMNPs show the maximum drug loading followed by AMNPs and then SMNPs. This could possibly arise from the higher in the organic coating content in MMNPs as observed from TGA measurements. Higher the organic content, the larger will be the number of -OH groups present on it providing more sites for adsorption of drug molecules. Considering the fact that molecules like mannitol, sorbitol, and ascorbic acid are generally accepted food ingredients and cryoprotectants, even relatively low loading efficiencies are acceptable.

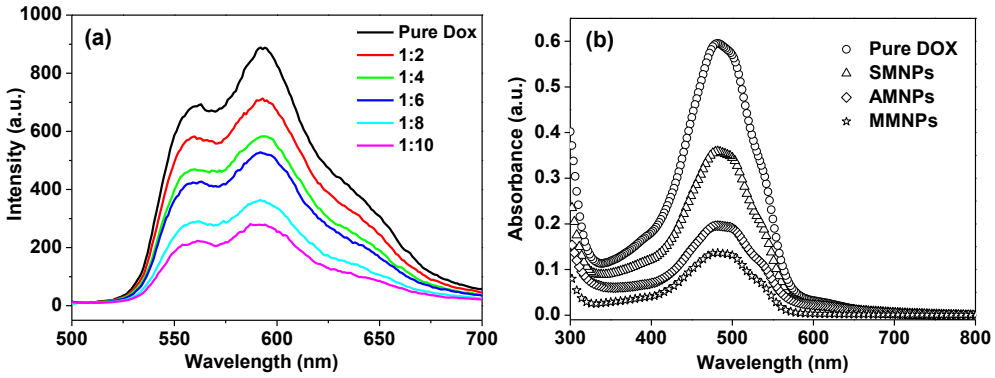

Figure 3.12 *(a) Variation in the fluorescence intensity of DOX present in the supernatant, at different DOX to particle (AMNPs) ratio (w/w), (b) UV-visible absorbance spectra of pure DOX in water and supernatant solution obtained after magnetic separation of MNPs-DOX.*

Having noticed good binding of DOX with MNPs, it is important to look into the release behavior of the drug at different pH conditions. This is important to

identify its site-specific release, as tumor cells exhibit relatively lower pH than normal cells. The pH-dependent drug release profile of DOX loaded MNPs were investigated under different reservoir-sink conditions (reservoir: pH 5/pH 7.4 and sink: pH 7.4) at a temperature of 37 °C (Fig.3.13). The physiological pH of the bloodstream is 7.4, while sub-cellular lysosomal compartments of tumor cells have pH less than 6.0. For the drug release experiments, the drug-loaded particles were immersed into 5 ml of respective release medium (AB pH 5 or PBS 7.4) and then put into a dialysis bag. The dialysis was performed against 200 ml of PBS (pH 7.4) under continuous stirring at 37 ^{o}C to mimic the cellular environment. One ml of the external medium was withdrawn at a fixed interval of time and replaced with fresh PBS pH 7.4 to maintain the sink conditions. The amount of DOX released was determined by measuring the fluorescence intensity at 594 nm (λ_{ex}: 490 nm) against the standard plot prepared under similar conditions. Each experiment was performed in triplicates and the standard deviation was given in the plots. Each experiment was performed in triplicates and the standard deviation was given in the plots.

The drug release studies under reservoir-sink conditions show a strong dependence of the release profile on the reservoir pH values. The release of drugs from drug-loaded MNPs follows a time-dependent release profile. It has been observed that drug molecules release slowly over a period of 70 h and the shape of the release profile suggests that the complete release of drug was not attained over the experimental period of time. The initial stage is characterized by a rapid release of the drug, followed by a slow, steady, and controlled release of the drug. The percentage of drug release from MMNPs-DOX, SMNPs-DOX, and AMNPs-DOX, after 72 h period is tabulated in Table 3.1.

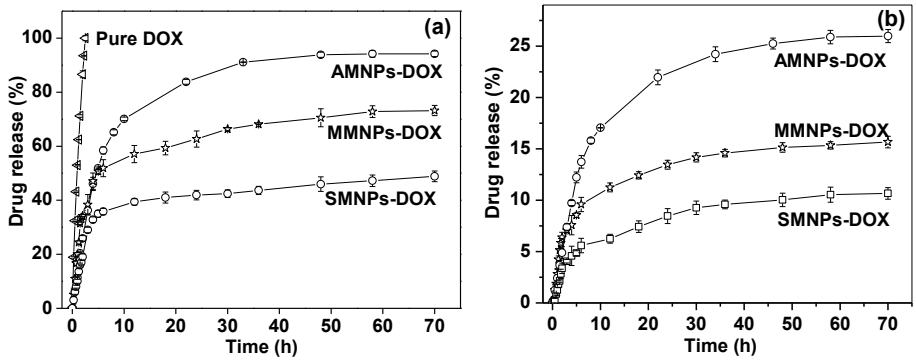

Figure 3.13 *Drug release profile of MNPs-DOX at 37 °C under reservoir-sink condition (a) reservoir: pH 5 and sink: pH 7.4 and (b) reservoir: pH 7.4 and sink: pH 7.4.*

The pure DOX shows the rapid release behavior of drugs with $t_{1/2}$ (the time need for 50 % release of the loaded drug) about 45 min at pH 5. However, DOX-MNPs show a sustained release profile with $t_{1/2}$ about 5 h. With the pH drop from 7.4 to 5.0, the zeta-potential of MNPs increases (discussed in section 3.3.1) which means that the surface of the MNPs becomes less negative. The less negative the surface, weaker the interactions between the MNPs and DOX. Thus, the enhanced release of DOX at lower pH could be attributed to the weakening of the electrostatic interactions between cationic DOX and partially neutralized hydroxyl groups on the surface of MNPs. This is desirable for cancer therapy as the relatively low pH in tumors will stimulate the DOX release at the target site. It has been observed that about 48, 73 and 94 % of loaded drug molecules were released from the SMNPs-DOX, MMNPs-DOX and AMNCs-DOX system, respectively at pH 5.

Table 3.1 Percentage drug loading and release of drug-loaded MNPS system.

Drug loaded system	**Drug loading (%)**	**Drug release % (72 h)**	
		pH 5 vs 7.4	**pH 7.4 vs 7.4**
MMNPs-DOX	68	73	15
SMNPs-DOX	40	48	10
AMNPs-DOX	60	94	26

From the perspective of enhanced binding and pH-dependent release, we observed that compared to sugar-alcohol functionalized MNPs, the AMNPs show superior performance. The drug release percentage from AMNPs is the highest in both pH 5 and pH 7.4 conditions. Moreover, the amount of electrostatically bound drug released from AMNPs-DOX at reservoir pH 5 is higher than that reported for other DOX loaded particles reported. For example, DOX loaded citrate-stabilized Fe_3O_4 NPs show a maximum release percentage of about 60 %, at pH 5.[184] Similarly, the phosphate anchored Fe_3O_4 NPs show a 90 % release and folate conjugated bi-functional Fe_3O_4 NPs show 83 % at same pH.[166,199] The sustained/controlled release of DOX from MNPs-DOX is advantageous as it will help in maintaining the drug level below the acute toxicity limit. It is noteworthy to mention that less than 26% DOX release was observed from these MNPs-DOX systems at reservoir pH 7.4. This is desirable as it will impart minimum toxicity to normal cells. Next, we examined the interaction of these MNPs with bovine serum albumin (BSA) protein at physiological medium (0.01 M PBS, pH 7.3). Serum albumin is one of the major components of blood and adsorption of these proteins is one of the preliminary stages in the clearance of foreign objects when administered intravenously. So, appropriate surface characteristics that prevent protein adsorption is necessary to utilize them as an intravenous drug delivery system. Any adsorption of the protein on particle surface can be monitored by changes in the zeta-potential of the carrier. We observed that these MNPs do not show any significant change in zeta-potential (Table 3.2) even after interacting with BSA for 2h, revealing their protein resistance characteristic at a physiological medium. This suggests that the suspensions of these particles are suitable for applications under physiological conditions, which is essential for biomedical applications.

Table 3.2 Zeta-potential (ZP) results of MNPs (0.02 mg/ml) upon interacting with BSA (0.025 mg/ml) in 0.01M PBS.

Time (min)	ZP (mV) of SMNPs	ZP (mV) of MMNPs	ZP (mV) of AMNPs
0	-16.2	-22.4	-20.8
30	-16.4	-22.2	-21.4
60	-16.4	-22.4	-21.6
120	-16.6	-22.9	-21.9

3.3.4. Antioxidant Activity Studies of AMNPs

Elevated reactive oxygen species (ROS) levels have been perceived in most cancer cells. In cancer, ROS account for genomic instability, resistance to apoptosis, proliferation, invasion, and extravasation and growth into a distant metastasis site. The uses of antioxidant supplements, enzymes, and ROS inhibitors are logical interventions for reducing oxidative stress.[200] Dietary antioxidant, AA has the ability to maintain redox homeostasis in cells. Thus, the antioxidant behavior of AMNPs was investigated both by methylene blue (MB) degradation as well as by free radical scavenging capability (Fig.3.14).

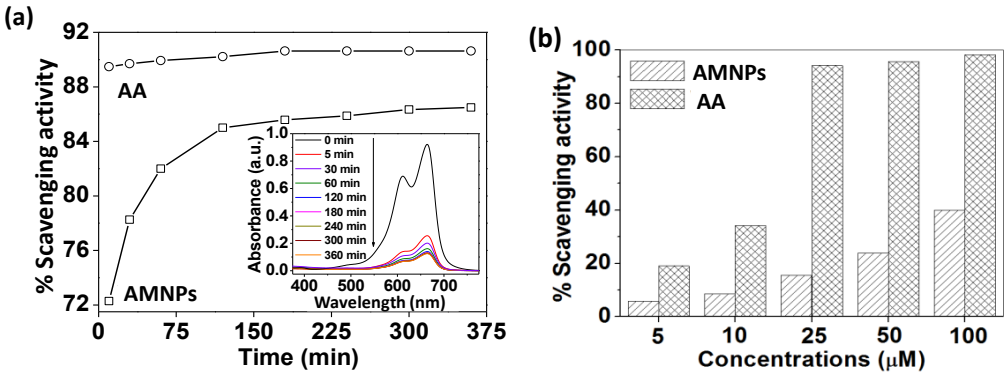

Figure 3.14 *(a) Time-dependent scavenging activity of AA and AMNPs (inset shows the catalytic degradation of MB using AMNPs at a different time) and (b) Concentration dependant scavenging activity of AA and AMNPs.*

AA is a well-known antioxidant and is inferred from the time-dependent increase in the formation of reduced MB. By comparing the efficacy of AMNPs with pure AA in converting the MB dye to its bleached form, leucomethylene blue (LMB), it is possible to assess its antioxidant activity.[201] It has been observed that pure AA reduced MB up to ~90% within 10 min, whereas AMNPs took 2 h to reduce 85% of MB (Fig. 3.14a), and it also depends on the AMNPs to MB ratio (Fig. 3.15). This suggests that AA can retain the antioxidant property upon conjugation with MNPs, though its rate of action is different from that of AA. The slow antioxidant behavior could arise from the chemical binding of AA to the particles. The antioxidant activities of AMNPs were further confirmed by the DDPH scavenging ability.

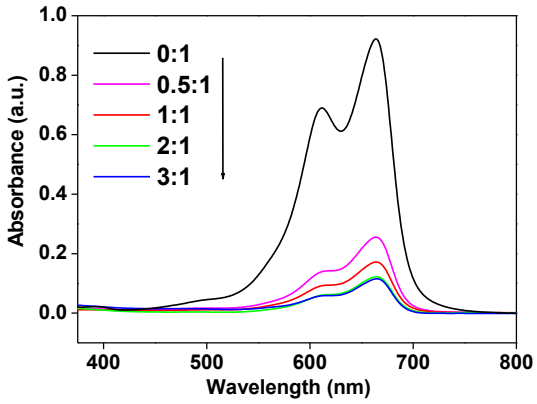

Figure 3.15 *Reduction of MB by AMNPs at different AA to MB mole ratio.*

The purple color of the DPPH solution was reduced to a yellow-colored product, diphenylpicryl hydrazine on the addition of AMNPs in a concentration-dependent manner.[202] AMNPs show a free radical scavenging ability of 40% at 100 μM of AA, whereas pure AA exhibited about 96% scavenging capability at an identical concentration (Fig. 3.14b). A concentration-dependent DPPH scavenging activity studies indicate that the scavenging ability can be increased by an increase in the concentration of particles. The poor lipo-solubility of AA limits its cumulative

amount in the cells after permeating through the cell membrane. However, this can be enhanced with the help of nanocarriers. Thus, the AMNPs have the capability to protect adjacent normal cells from oxidative stress up to a certain extent.

The surface modification of MNPs using the above molecules produces functionalized exteriors with high densities of negatively charged hydroxyl moieties for electrostatic binding of positively charged anticancer drugs, DOX. In all these MNPs systems, the drug release increased significantly upon changing the pH of release medium from 7.4 to 5.0. Specifically, the high loading affinity for these functionalized MNPs for DOX with their sustained release profile, and protein resistance characteristic makes them suitable for drug delivery applications. In addition, AA coated Fe_3O_4 NPs showed the antioxidant and free radical scavenging activities. AMNPs showed the time-dependent gradual increase in antioxidant property and free radical scavenging ability of 40% at 100 μM of AA. Moreover, sugar-alcohols and AA coated MNPs can serve as a springboard for the creation of complex multifunctional particles through the addition of functional and bioactive groups at the MNPs surface, which further augments the range of applications.

3.4. Conclusion

In summary, sugar-alcohols and AA functionalized iron oxide nanoparticles were prepared through co-precipitation of Fe^{+2} and Fe^{3+} ions in basic medium followed by in-situ coating. XRD and TEM analysis confirmed the formation of crystalline spinel nanostructure with an average particle size of 10 nm. The surface passivation of these nanoparticles was evident from FTIR, TGA, and zeta-potential measurements. Light scattering measurements indicate that these particles render good aqueous colloidal stability and possess pH-dependent charge conversant behavior and

protein resistant characteristics in the physiological medium. The loading efficiency of the drug as well as their pH-triggered release is strongly dependent on the drug to particle ratio and the coating agent. These functionalized MNPs showed a high loading affinity for DOX and their pH-dependent sustained release, which makes them suitable for drug delivery. Further, the presence of ascorbic acid shell on the surface of nanocarriers not only provides the binding sites for the drug but also possesses the capability to the reduction of oxidative stress. Specifically, the developed pH-sensitive drug delivery carrier has the ability to minimize the loss of drug during their blood circulation and trigger after internalized by the target cells. In addition, the functionalized exterior of these MNPs having free hydroxyl groups can provide the available sites for conjugation of various bioactive molecules for a variety of biomedical applications.

CHAPTER 4

COVALENT IMMOBILIZATION OF DOXORUBICIN TO Fe_3O_4 USING pH LABILE LINKAGES FOR SPECIFIC RELEASE IN CANCER CELLS

4.1. Introduction

Conventional chemotherapies for cancer suffer from the disadvantage of toxicity to normal cells and non-specific bio-distribution leading to toxicities to organs like liver, kidneys, etc.[203] The targeting of the drug to the tumors can be achieved by incorporating the active ingredient in suitable nanostructured materials with desired size, charge, and surface characteristics.[204] MNPs conjugated with drugs have been assessed as a strategy to deliver an anticancer agent to the tumor sites and its site-specific release characteristics.[205] In addition to the targeting capability, most of these nanocarriers solve other limitations of conventional drug delivery systems in terms of solubility, systemic toxicity, and drug degradation. The rationale behind this approach is to increase efficacy while reducing systemic side-effects.

Although many non-covalent approaches have been employed for delivering anticancer drugs, the *in-vivo* stability of the drug delivery system constructed using a non-covalent method is still challenging. The drug delivery systems formed by covalent approaches (via chemical bonds) provide more stability to the drug as well as their selective release than those constructed using non-covalent linkages.[206–209] In this aspect, polymer-drug conjugates are extensively developed by using pH-labile chemical bonds such as hydrazone, cis-acotinyl, carbamate, and acetal bonds.[210–212] The presence of acid-labile linkages between drug and polymeric carrier permits drug release either in the mild acidic extracellular environment of a tumor or after endocytosis in endosomes/lysosomes in tumor cells.

Therefore, attempts have been made to develop pH-labile magnetic nanocarriers for the effective delivery of an anticancer drug, DOX to cancer cells. DOX was covalently bound to the ascorbic acid-coated Fe_3O_4 magnetic nanoparticles

(AMNPs), through carbamate and hydrazone linkage (see Fig. 4.1). The pH-triggered drug release studies were carried out under various reservoir-sink conditions, and also investigated the selective cytotoxicity of AMNPs, toward different cancer cells and normal cells. Further uptake study was performed to check the capability of this AMNPs for the intracellular delivery of an anticancer drug.

4.2. Experimental Methods

4.2.1. Covalent Conjugation of DOX to Ascorbic Acid Functionalized Fe_3O_4 Magnetic Nanocarriers (AMNPs)

AMNPs were prepared by the co-precipitation method as discussed in the previous chapter. The covalent conjugation of DOX with AMNPs was carried out through carbamate and hydrazone linkage using the modified protocol reported by Hu et al. for the preparation of biodegradable block copolymer-doxorubicin conjugates.[212] The detailed reaction pathway for the covalent conjugation of DOX with AMNPs is shown in the reaction scheme (Fig. 4.1). In the proceeding sections, the DOX conjugated AMNPs through carbamate linkage and hydrazone linkage are abbreviated as AMNPs-CL-DOX and AMNPs-HL-DOX, respectively.

For covalent conjugation of the drug, AMNPs were first activated with 4-nitrophenyl chloroformate (NPC). Briefly, AMNPs (600 mg) was dissolved in 20 ml of dichloromethane (DCM, CH_2Cl_2). Then, 100 mg of NPC and 200 µl triethylamine (TEA*)* were added dropwise to the above solution at 0 ^oC (molar ratio of AMNPs:NPC:TEA is 1:1.2:4) (with respect to OH groups, calculated based on TGA results). The reaction mixture was stirred at 0 ^oC for 4 h, and finally, the NPC activated AMNPs was obtained through magnetic separation and washed 3-4 times with DCM to remove unreacted reagents.

a) Covalent Conjugation via Carbamate Linkage (AMNPs-CL-DOX)

The NPC activated AMNPs (20 mg) dissolved in DMF (5 ml) was reacted with DOX (2 mg) in the presence of TEA (10 µl) for 48 h at room temperature under nitrogen atmosphere. The obtained product (AMNPs-CL-DOX) was then separated and washed 3-4 times with DMF through magnetic separation.

b) Covalent Conjugation via Hydrazone Linkage (AMNPs-HL-DOX)

The NPC activated AMNPs (50 mg) were dissolved in DCM (3 ml) and hydrazine monohydrate (NH_2-NH_2.H_2O) (22 µl) was slowly added into it. The reaction was carried out for 2 h at room temperature and hydrazine modified AMNPs was separated and washed 3-4 times through magnetic separation. This hydrazine modified AMNPs (20 mg) dissolved in DMF (5 ml) was reacted with DOX (2 mg) in the presence of TEA (50 µl) for 48 h at room temperature. The DOX conjugated AMNPs (AMNPs-HL-DOX) was separated using a magnet and washed 3-4 times by DMF.

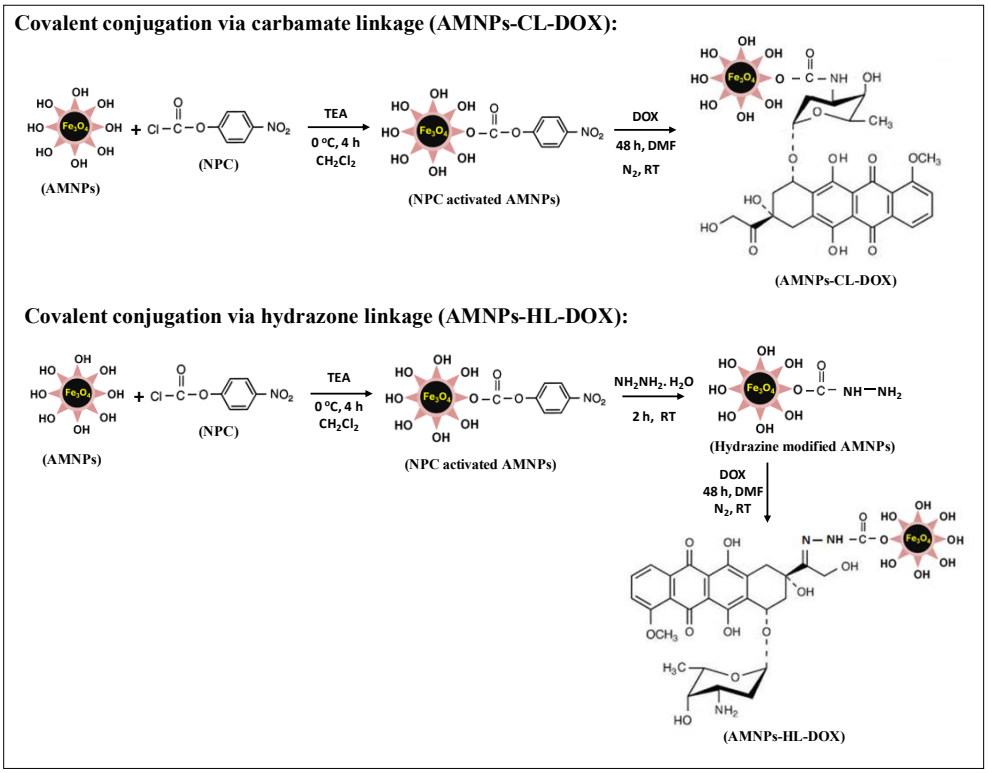

Figure 4.1 *Schematic of the reaction pathway for covalent linkage of DOX to AMNPs*

4.3. Results and Discussion

4.3.1. Drug Conjugation Studies

The capability of AMNPs as a drug carrier was investigated by a covalently conjugating anticancer drug, DOX through carbamate and hydrazone linkages. The interaction of DOX molecules with AMNPs was evident from the decrease in fluorescence intensity measured at 594 nm (λ_{ex}: 490 nm) of the supernatant liquid obtained after removal of the drug-loaded AMNPs through magnetic separation (Fig.4.2). The fluorescence intensities of supernatants (washed drug molecules were also taken into consideration for calculations) against that of pure DOX solution (prepared with appropriate mediums to maintain a similar condition) were used to

determine the loading efficiency. The loading efficiency (% w/w) was calculated using the following relation:

$$Loading\ efficiency\ (\%) = \frac{I_{DOX} - I_S - I_W}{I_{DOX}}\ X\ 100 \qquad (4.1)$$

where I_{DOX} is the fluorescence intensity of pure DOX solution, I_S the fluorescence intensity of supernatant and I_W the fluorescence intensity of washed DOX (physically adsorbed DOX molecules).

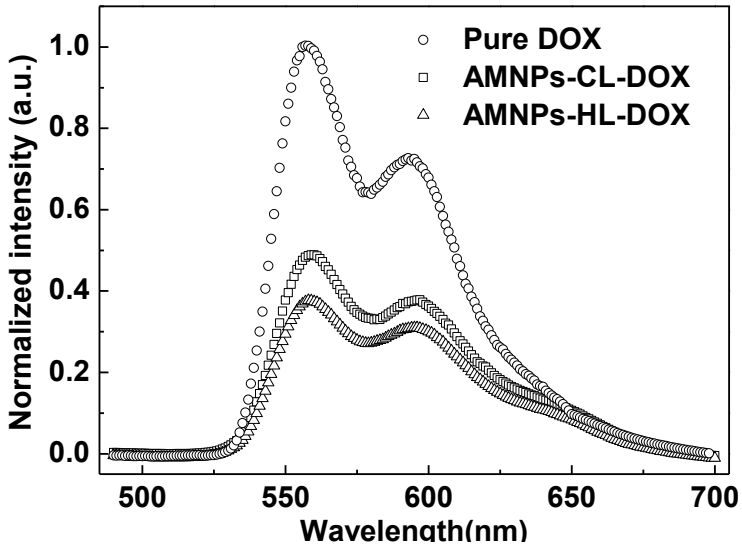

Figure 4.2 *Fluorescence spectra showing the interaction of DOX with AMNPs.*

The drug loading efficiencies of 48 and 57% were obtained for AMNPs-CL-DOX and AMNPs-HL-DOX, respectively at DOX to particles ratio of 1:10. Slightly higher loading efficiency was observed for hydrazone linkage than carbamate linkage. As evident from Fig.4.1, the conjugation of DOX through carbamate linkage formed by direct reaction between NPC activated AMNPs and amine group of DOX, whereas that occurred by hydrazone linkage proceeds through the reaction between hydrazine modified AMNPs and the carbonyl group of DOX. The nucleophilic reaction ability of hydrazine modified AMNPs may be higher than that of the amine group of DOX.

Though the exact reason is not yet known, we believe that the reaction yield of DOX conjugation by hydrazone linkage probably higher than that through carbamate linkage. These pH-sensitive linkages (hydrazone and carbamate) can be cleaved at mildly acidic pH, thus provide opportunities for designing pH-responsive nanocarriers. The hydrodynamic diameter and surface charges of drug-loaded AMNPs were also investigated as these parameters are important criteria for drug delivery and provided in Table 4.1 along with those of AMNPs. Further, TEM images of drug-loaded AMNPs confirmed the insignificant change in morphology of AMNPs after conjugation of DOX (Fig.4.3).

Table 4.1 Hydrodynamic diameter (number weighted) and surface charges of AMNPs, AMNPs-CL-DOX, and AMNPs-HL-DOX.

MNPs system	Zeta Potential (mV)	Hydrodynamic diameter (nm)	Polydispersity Index
AMNPs	-26.6	40	0.2
AMNPs-HL-DOX	-6.6	54	0.3
AMNPs-CL-DOX	-12.4	48	0.3

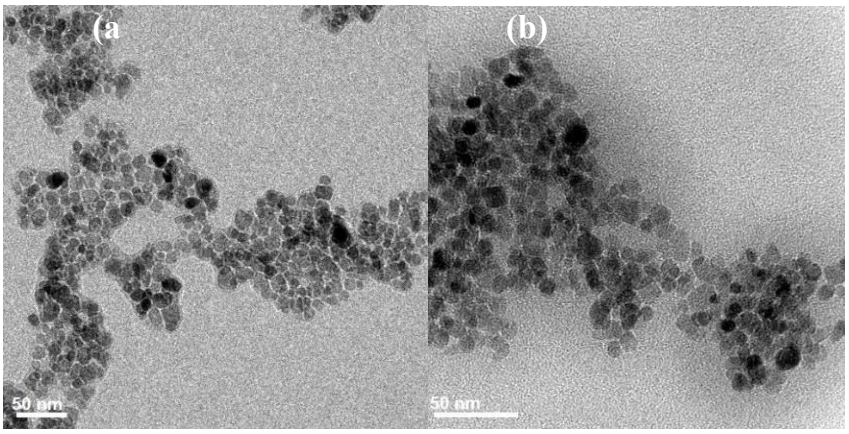

Figure 4.3 *TEM micrographs (a) AMNPs-HL-DOX and (b) AMNPs-CL-DOX.*

4.3.2. Drug Release Studies

The pH-triggered drug release studies were carried out under reservoir (r) - sink (s) conditions (reservoir: pH 5/pH 7.4 and sink: pH 7.4) at a temperature of 37 °C (Fig.4.4 a-b). The details about experimental setup was explained in the section 3.3.3 above. The drug release studies (Fig. 4.4) show a strong dependence of the release profile on the reservoir pH values. Under these conditions, drug molecules release slowly over a period of 70 hr with the initial rapid release, followed by a slow, steady, and controlled release of the drug. The percentages of drug release from different drug-loaded systems are shown in Table 4.2. Similar to our results, Aydin et al. reported a much slower release of DOX from the cryogel system prepared through a relatively stable covalent bonding.[213] This is mainly due to the formation of stable linkage between drug and nanocarriers. Between the two systems, the release rate of DOX from AMNPs-HL-DOX is slightly higher compared to AMNPs-CL-DOX due to higher stability of carbamate linkage.[213]

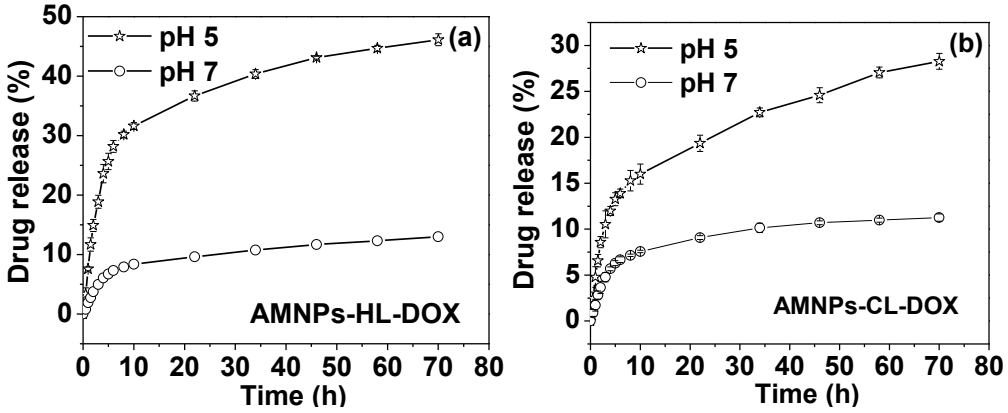

Figure 4.4 *pH-dependent drug release profile of (a) AMNPs-HL-DOX, and (b) AMNPs-CL-DOX at 37 °C.*

Further, the potential of developed nanocarrier for delivery of doxorubicin was evident from our short-term drug release study (Fig. 4.5) in serum conditions

(prepared by adding 10% FCS to respective buffer medium) under the similar conditions as mentioned above. It showed a pH-dependent release of doxorubicin similar to that observed in buffer mediums (higher in acidic pH, see Table 4.2). The long-term (>10 hr) release study could not be performed as fungal growth/ protein aggregation was observed in release mediums beyond 10 hr, is due to the presence of 10 % fetal calf serum (FCS) in release medium incubated at 37 ^{o}C. Further, it is noteworthy to mention that the release rate of DOX is higher at low pH for both the cases as carbamate and hydrazone linkage are prone to faster hydrolysis in acidic conditions. Thus, the release of DOX from nanocarriers would increase in the acidic environment of the endosomal intracellular compartments after their internalization. The observed drug release characteristic is desirable for cancer therapy as DOX will be released at the targeted site. For instance, Prabaharan et al. reported that covalently conjugated DOX-amphiphilic multi-arm-block copolymer reduces the chance of premature drug release outside of the tumor tissue and shows excellent *in vivo* stability for targeting the drugs to cancer cells.[214] A significant difference in these covalently linked systems is that the percentage of drug release is much lower than that observed from non-covalently linked systems.[184,198]

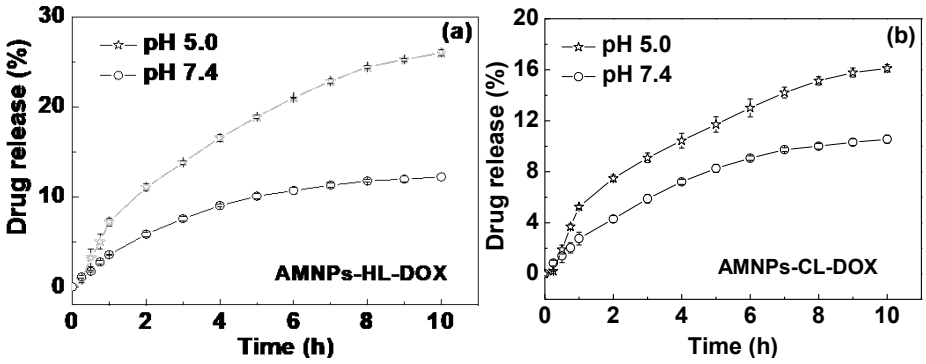

Figure 4.5 *pH-dependent drug release profile of (a) AMNPs-HL-DOX and (b) AMNPs-CL-DOX in serum medium (prepared by adding 10% FCS to respective buffer) at 37 °C.*

Table 4.2 The percentage of drug release at different reservoir pH in buffer and serum mediums

Drug loaded systems	Buffer mediums after 70 h		Serum mediums after 10 h	
	pH 5	pH 7.4	pH 5	pH 7.4
AMNPs-HL-DOX	45	13	26	12
AMNPs-CL-DOX	28	11	16	11

4.3.3. Cytotoxicity and Cell Uptake Studies

MTT assay was used to investigate the cytotoxicity of AMNPs, DOX loaded AMNPs (AMNPs-CL-DOX, AMNPs-HL-DOX) and pure DOX against three different cancer cell lines, such as WEHI-164 (mouse fibrosarcoma cells), MCF-7 (human breast cancer cells) and A549 (human lung cancer cells) and one normal cell line, WI26VA (human normal lung cells) see the Fig. 4.6 and Fig. 4.7. Cells were cultured in DMEM supplemented with 10% FCS and antibiotics (100 U mL^{-1} penicillin and 100 µg mL^{-1} streptomycin) in a humidified atmosphere of 5% CO_2 at 37 °C. Cells (5000) were seeded in 96-well plates containing 100 µl of culture medium for overnight in culture conditions. For determining the cytotoxicity, the cells were treated with different concentrations of drug-loaded AMNPs/controls followed by incubation at culture conditions for 48 h. After this, the culture media of each well was replaced by fresh media containing 0.5 mg/mL MTT and further incubated for 3 hr at culture conditions. Following this, the MTT solution was aspirated, and formazan crystals were solubilized by adding 100 µl of DMSO to each well. For determining the cytotoxicity, the absorbance was measured in a microplate reader (Tecan Infinite 200 PRO, Switzerland) at 544 nm. The cell toxicity was obtained by comparing the absorption of treated cells to that of the control, which was defined as

100%. Each experiment was performed in triplicates and the standard deviation was given in the plot.

Here we observed that an increase in cytotoxicity (30-60 %) in these cancer cells when cells were treated with increasing concentration of AMNPs-CL-DOX/ AMNPs-HL-DOX. But the increase in cytotoxicity was not in a perfect dose-dependent manner (Fig. 4.6). This could be attributed to the slow release of covalently bounded DOX molecules from nanocarrier as cleavage of both carbamate and hydrazone linkages are quite a slow process. The toxicity observed was in a similar range across the three cancer cell lines used for both the drug-loaded AMNPs system. However, DOX loaded AMNPs showed relatively lower cytotoxicity as compared to pure DOX. This could be ascribed to the slower release of DOX from nanocarriers. It is noteworthy to mention that AMNPs-CL-DOX/AMNPs-HL-DOX showed significantly lower cytotoxicity (up to 20 %) in human normal lung cells (WI26VA4) suggesting its relatively selective toxicity to cancer cells than normal cells. Moreover, the toxicity of AMNPs without conjugation of DOX observed in WI26VA4 was further lower (up to 20 %) suggesting their biocompatibility (Fig. 4.7). The higher toxicity of AMNPs-CL-DOX/ AMNPs-HL-DOX in normal cells than AMNPs without conjugation of DOX may be attributed to the presence of DOX, which may impose higher inherent toxicity in normal cells.

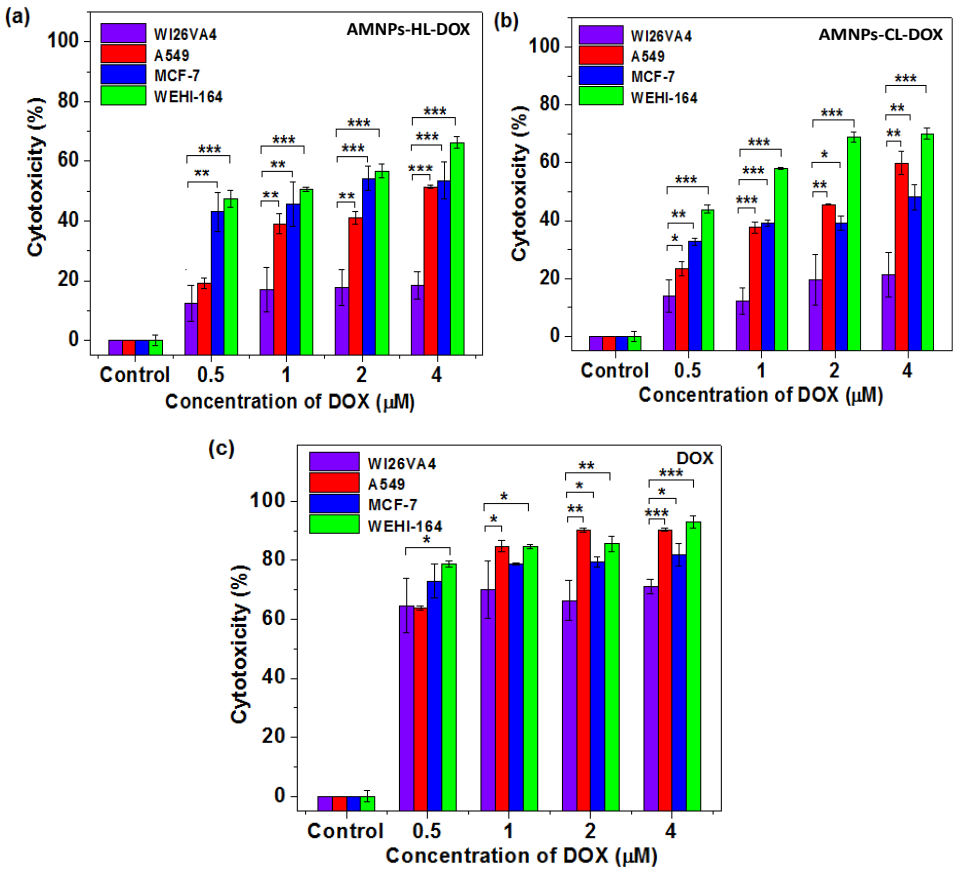

Figure 4.6 *Cytotoxicity results of (a) AMNPs-HL-DOX, (b) AMNPs-CL-DOX and (c) pure DOX towards cancer cells (WEHI-164, MCF-7, A549) and normal cell (WI26VA4) after 48 h incubation at culture conditions. (data represent the mean ± SD (n = 3), the statistically significant values were obtained using t-test by comparing toxicity of cancer cells with respect to normal cells, * p < 0.1, ** p < 0.01, *** p < 0.001).*

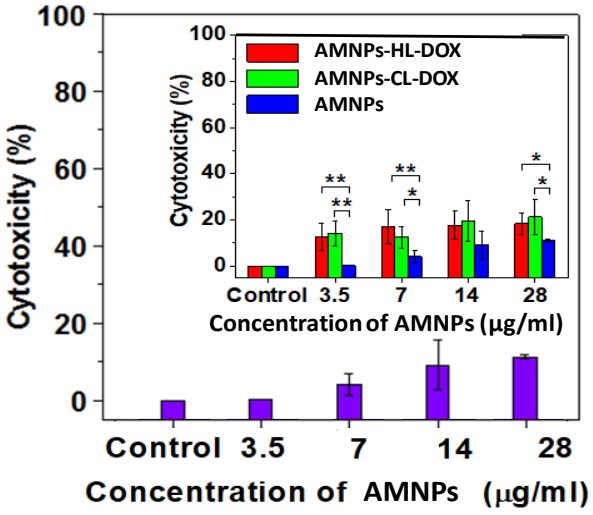

Figure 4.7 *Cytotoxicityresults of AMNPs (without conjugation with DOX) in human normal lung cells (WI26VA4) after 48 h incubation at culture condition (data represent the mean ± SD, n = 3). Inset shows its comparison with equivalent amount AMNPs used in DOX loaded AMNPs systems (the corresponding DOX concentrations in DOX loaded AMNPs systems were 0, 0.5, 1, 2, 4 µM, the statistically significant values were obtained using t-test by comparing the toxicity of DOX loaded AMNPs systems with respect to AMNPs, * p < 0.1, ** p < 0.05).*

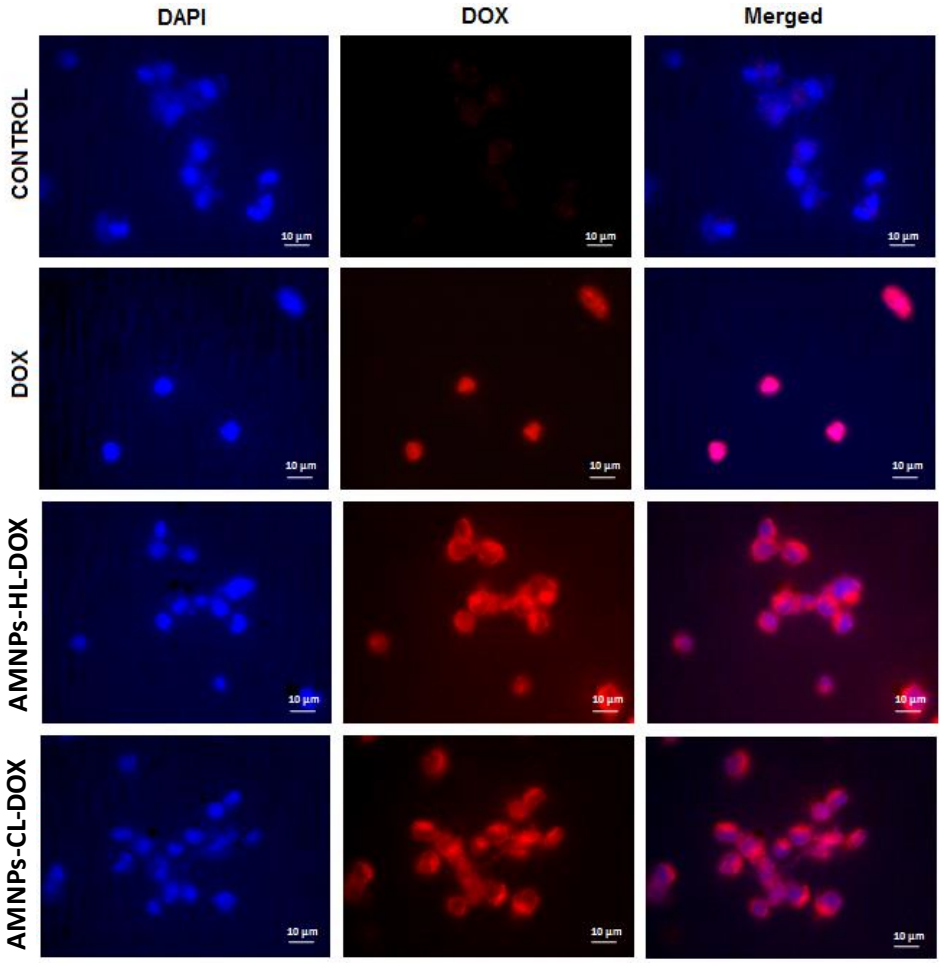

Figure 4.8 *Fluorescence microscopy images of WEHI-164 cells after incubation with pure DOX and DOX loaded AMNPs for 3 h under culture conditions (red filter for DOX and blue filter for DAPI, control cell with DAPI staining is provided for comparative purpose).*

Further, we have investigated the cellular uptake of DOX loaded AMNPs systems in WEHI-164 cells and compared them with that of pure DOX by

fluorescence microscopy. For fluorescence imaging, cells (0.5×10^6) were seeded on glass coverslips and cultured overnight. The cells were then treated with AMNPs-CL-DOX/AMNPs-HL-DOX (at a DOX concentration of 4 μM) and incubated for 3 hr under culture conditions, followed by washing with PBS. The untreated control cells and the cells treated with drug-loaded AMNPs were mounted on a glass slide in cell mounting medium (Invitrogen, USA) containing DAPI for nuclear staining and then imaged by fluorescence microscopy (Nikon eclipse Ti, Japan) using a red filter for DOX and a blue filter for DAPI.

In order to explore the sub-cellular localization of DOX, the nucleus of the cells was stained with DAPI. The blue fluorescence image shows emission from DAPI stained nuclei. As shown in Fig. 4.8, WEHI-164 cells exposed to free DOX (magenta color arise from the merged image of DOX and DAPI) showed nuclear internalization after 3 hr, consistent with the earlier studies.[215,216] The accumulation of DOX in the nucleus for free DOX occurred as intracellular DOX molecules in the cytosol were observed rapidly diffuse to the nucleus. In the case of DOX loaded AMNPs, red fluorescence signal coming up from DOX emissions was observed mainly in the cytoplasm. Thus, these nanocarriers have a strong capability for the intracellular delivery of the anticancer drug.

4.4. Conclusion

In summary, DOX was covalently conjugated to ascorbic acid functionalized Fe_3O_4 magnetic nanocarriers (~10 nm) for pH-triggered slow and sustained delivery of the drug to cancer cells with minimal side effects. It has been found that the loading efficiency of the drug as well as their pH-triggered release is strongly dependent on the nature of the bonding. The uniqueness of this drug delivery system lies in the

covalent conjugation DOX through carbamate and hydrazone linkage, resulting in slow and sustained drug release profile at different environmental conditions. The drug-loaded nanocarriers exhibit sustained pH triggered release of drug molecules at mildly acidic environment of tumor, due to the faster hydrolysis of carbamate and hydrazone linkage and substantial cellular internalization with significant toxicity towards the proliferation of mouse skin fibrosarcoma (WEHI-164) cells, human breast cancer (MCF-7), and human lung cancer (A549) cells. However, it showed significantly lower toxicity in human normal lung (WI26VA) cells, which is essential for cancer therapy. Specifically, the developed drug-nanocarrier conjugate would minimize the amounts of drug leaching out in the blood (pH 7.4) and enable intracellular drug release upon internalized by the target cells (pH 5). Taken together, our results suggest the ability of these nanoparticles for pH-sensitive release of DOX and selective cytotoxicity to cancer cells. The free hydroxyl group present on the surface of nanocarriers can provide the accessible surface for conjugation of various biomolecules/bio-labeling for a variety of other biomedical applications.

CHAPTER 5

FABRICATION OF BIO-COMPATIBLE Fe_3O_4 MAGNETIC NANOPARTICLES FOR IMPROVED HYPERTHERMIA APPLICATIONS

5.1. Introduction

The current existing methods for cancer treatment such as chemotherapy, and radiotherapy, are not conducive to treat all types of cancers and have side effects associated with it, depending on the nature, location, and grades of the disease. Therefore, a search for less aggressive and more effective treatments continues and becomes ever increasingly important. One of the promising and upcoming potentially effective approaches for cancer treatment is magnetic hyperthermia therapy. By subjecting magnetic nanoparticles to an external magnetic field, the carriers can be targeted to a specific tumor location and subject to hyperthermia without affecting the surrounding healthy tissues.[217,218] This approach is a fast emerging, non-invasive tool that has been proposed for cancer treatment by deactivation/killing (dead or driven to apoptosis) of cancer cells by raising the temperature of the cell to about 42-46 ^{o}C.[217,219] At this temperature range, the generated heat also increases the efficacy of different chemotherapeutic drugs. Therefore, the combination of conventional chemotherapy with hyperthermia provides a promising strategy, which can have synergistic therapeutic effects on tumor cells and reduce the required effective doses of anticancer drugs[220]. The heating efficiency of MNPs, often represented as the specific absorption rate (SAR), is directly related to the heat losses of the MNPs when exposed to the AC magnetic field.[221] Therefore, the SAR can be improved by increasing the saturation magnetization and also the coercive field of the MNPs. From a biomedical application perspective, to reduce the possibility of toxic effects, using a minimal amount of MNPs for hyperthermia treatment is highly recommended. This requires the heating efficiency of the currently used MNPs to be substantially high (as manifested from the SAR value), and also it should have other characteristics like good biocompatibility, protection from the immune system, high colloidal stability in

biological fluids, narrow size distribution, and long blood circulation time.[166] These are the main challenges in magnetic hyperthermia toward its practical use.

Among the others, the functionalized iron oxide MNPs (magnetite/maghemite NPs less than 20 nm size) have enjoyed significant attention owing to their potentials in various biomedical applications due to the excellent biocompatibility and unique superparamagnetic properties, ease of synthesis and relatively at low cost.[222] Often, at room temperature, the saturation magnetization of functionalized iron oxides is relatively low (for bulk Fe_3O_4 = 92 emu/g), especially if we compare it to those of other magnetic materials such as Fe (220 emu/g) and Co (166 emu/g). It has been reported that as the size of iron oxide NPs decreases, the saturation magnetization tends to decrease; for example, for 5 nm MNPs, saturation magnetization can be as small as 32 emu/g; because of the increased surface spin disorder.[223] As a result, moderate values of SAR have been reported for small size superparamagnetic iron oxide nanoparticles.[224] Moreover, MNPs-based therapeutics and diagnostics have generally been troubled by the agglomeration of NPs. The low stability of iron oxide NPs in aqueous solution and their destabilization due to the adsorption of plasma proteins are perhaps some of the intriguing difficulties for their therapeutic applications.

One of the effective remedies for this problem is the surface passivation of Fe_3O_4 NPs with the water-soluble and biocompatible material, which provide the colloidal stability to nano-formulations and increase the blood circulation time long enough to reach the target tissue in amounts suitable for therapeutic and/or detection purposes. In addition, the advancements in functionalization of MNPs enable such therapeutic treatments to selectively kill cancer cells by localized heating, without having to limit the extent of tissue penetration. Thus, the surface functionalization of

Fe_3O_4 NPs is extremely important to their design and subsequent application in hyperthermia, and to provides the selectivity for target analytes as well as improves liquid-solid interface stability. Moreover, it is important to identify if such biocompatible coating influences the magnetic properties of such materials. Here, we explore the influence of different biocompatible ingredients such as sugar-alcohols, ascorbic acid, and bovine serum albumin (BSA) on magnetic and hyperthermia effects of Fe_3O_4 MNPs.

5.2. Experimental Methods

5.2.1. Synthesis of Functionalized Fe_3O_4 MNPs for Hyperthermia

The synthesis and characterization of MMNPs, SMNPs, and AMNPs were discussed in the previous chapters. In addition to the above particles, protein conjugated MNPs were prepared by the thermal decomposition method. Protein decorated particles are highly desirable for intravenous administration. To prepare serum albumin protein conjugated particles, first, glutaric acid is used as a preliminary stabilizer at high-temperature synthesis. This is followed by the covalent conjugation of BSA to MNPs prepared by thermal decomposition. Briefly, in a typical reaction, thermal decomposition of iron (III) acetylacetonate (2.83 mmol) was carried out in presence of glutaric acid (2.83 mmol) as a stabilizer, in diethyl glycol (30 ml) as a solvent. The reaction mixture was heated first 100 ^oC to make a clear brown-reddish color solution and then temperature raised to 240 ^oC and it refluxed for 5 hr. Additionally, the grain size was controlled by changing the alkalinity of the solution using 2 g anhydrous sodium acetate (NaOAc). The formed black precipitate of Fe_3O_4 magnetic nanoparticles coated with glutaric acid (GMNPs) were separated out from the solvent by using a permanent magnet (field strength ~2.5 kOe) and thoroughly

rinsed with ethanol and water to remove solvent and unreacted materials. The prepared particles were nearly monodisperse and could be suspended in aqueous solution without extra surfactant/modification.

After the successful preparations of GMNPs, the BSA protein covalently conjugated with it by EDC-NHS reaction. In detail, 100 mg GMNPs dispersed in 40 ml of PBS (pH 6) and sonicated it for 30 min to get a homogeneous mixture. Then 2.5 ml of EDC.HCl (2 mg/ml, 0.032 mmol) added in the above solution and sonicated it for 20 min, and then 2 ml of NHS (1 mg/ml, 0.016mmol) added in it and again sonicated it for 20 min. Then 10 ml of BSA (1mg/ml) in PBS (pH 6) was added in the above reaction mixture and stirred it (300 rpm) for 5 h at room temperature. Then BSA conjugated MNPs (PGMNPs) were separated by using a permanent magnet of magnetic field strength (~2.5 kOe) and 2-3 times washing was given using 5 ml PBS (pH 6) each. Using the supernatant solution and pure BSA in PBS (pH 6), conjugations of BSA with GMNPs were estimated with the help of UV-visible and fluorescence spectrophotometer.

5.3. Results and discussion

5.3.1. Structural and Morphological Studies

The detailed structural characterization of MMNPs, SMNPs, and AMNPs were already discussed in the previous chapters. The crystal structure, crystallite size and surface morphology of the GMNPs have been carried out using XRD and TEM techniques. Fig. 5.1 shows the XRD pattern of the GMNPs. From the XRD patterns, a series of characteristic diffraction peaks were observed, at 2θ values of 20^{o}, 30^{o}, 35^{o}, 43^{o}, 57^{o}, and 63^{o}. These peak positions and relative peak intensities corresponded to

the characteristic diffraction peaks of (111), (220), (311), (400), (511), and (440) planes of Fe_3O_4, and are consistent with the inverse cubic spinel phase (magnetite, JCPDS Card No. 19-0629 Fig.5.1). There are no additional peaks corresponding to other phases of iron oxide such as maghemite (γ-Fe_2O_3) within the detection limits of XRD measurements (Fig.5.1). These results indicate the formation of highly crystalline, inverse cubic spinel Fe_3O_4 nanostructure.[225] The broadening of peaks observed here as compared to bulk Fe_3O_4 indicates the small crystallites with the mean crystallite size of around 5 nm.

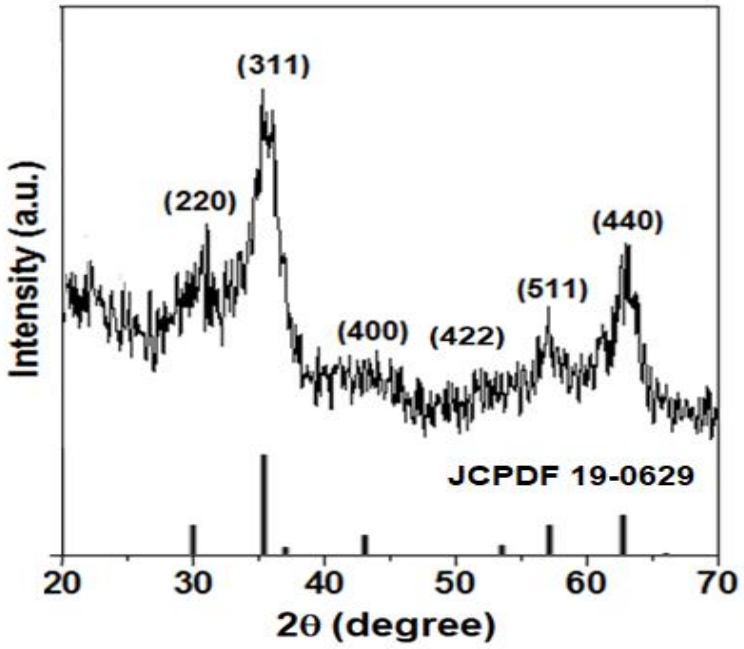

Figure 5.1 *XRD pattern of GMNPs and reference peaks from JCPDS file.*

The surface morphology and size of the GMNPs were further supported and confirmed by direct imaging, using TEM of GMNPs as shown in Fig.5.2. From the image, it is inferred that most of the Fe_3O_4 nanoparticles are quasi-spherical with a mean size of around 4.5 nm (See the particle size distribution obtained from TEM in the inset of Fig.5.2), which is in line with the size obtained from XRD.

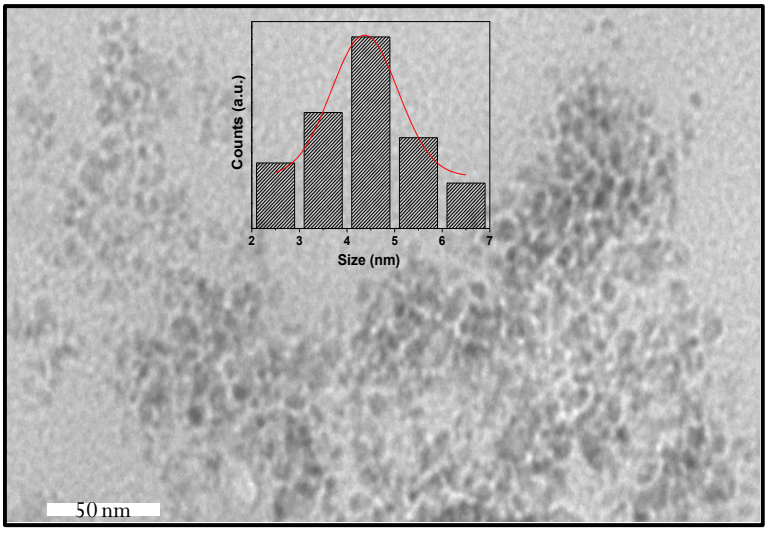

Figure 5.2 *TEM image of GMNPs (inset: Size distribution of GMNPs obtained from TEM analysis (red line shows Gaussian fit to find the mean size)).*

The conjugations of GMNPs with BSA protein were analyzed by the combined use of FTIR, DLS, TGA, fluorescence and zeta-potential measurements. The FTIR spectra of GMNPs, pure BSA protein, and BSA protein conjugated GMNPs (PGMNPs) are depicted in Fig. 5.3a. The broad band's seen at 1628 and 3419 cm^{-1} for all three samples can be assigned to the -OH vibrations. The two intense peaks observed between 580 cm^{-1} and 630 cm^{-1} are attributed to the stretching vibration mode associated with the metal-oxygen (Fe–O) bonds in the crystalline lattice of Fe_3O_4. These vibrations are characteristics of all spinel structures, in particular for ferrites.[226] Moreover, the peaks at 1619 $cm^{-1}$and 1385 cm^{-1} in GMNPs and PGMNPs arise from the asymmetric and symmetric stretching of the COO^- group, respectively.[184,227] It may be noted these peaks are observed at slightly higher wavenumbers (1649 cm^{-1} and 1396 cm^{-1}) in the BSA. These minor changes in the vibrational frequencies clearly show that the protein is successfully conjugated on the surface of the Fe_3O_4 nanoparticles.

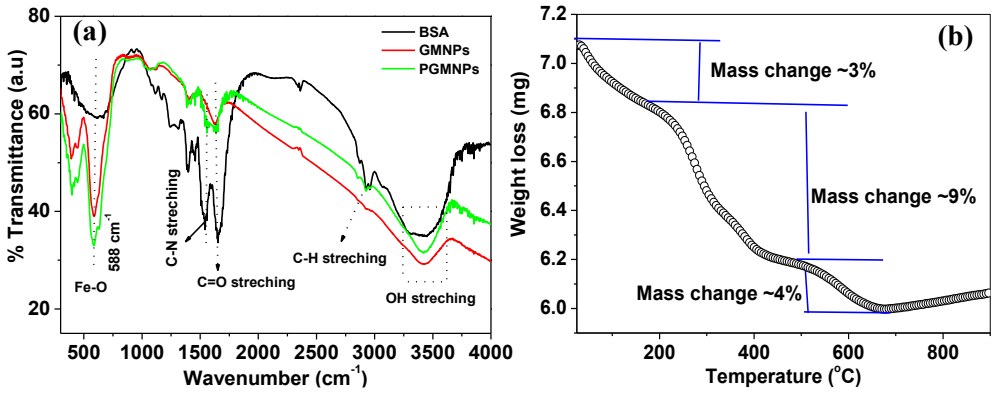

Figure 5.3 *(a) FTIR spectra of pure BSA protein, GMNPs, and PGMNPs along with their characteristic peak assignments in the range of 400-4000 cm^{-1} and (b) TGA plot of PGMNPs samples showing weight loss at different temperatures.*

The organic modification of Fe_3O_4 NPs was further evident from the thermogravimetric analysis. TGA showed four steps of thermal decomposition with a total weight loss of about 16% (Fig. 5.3b). The first step weight loss of around 3% up to 200 ^oC can be ascribed to the removal of physically adsorbed water and organic moieties onto the surface of Fe_3O_4 NPs. The weight loss observed beyond 200 ^oC can be ascribed to the removal of covalently conjugated BSA protein from the surface of MNPs due to the protein degradation process. The TGA pattern is consistent with the reported TGA curves of pure BSA.[228] The only difference in the TGA curves is that the decomposition temperature shifts to a higher temperature when BSA molecules are bound with MNPs. The weight loss observed by TGA was further supported by iron-estimation which showed that about 18% organic content is present in the sample. The amount of BSA conjugated on PGMNPs was also estimated from the measurement of free BSA in the supernatant solution after removal of the bound particles by magnetic separation and estimated from fluorescence measurements, as tryptophan residue in BSA is fluorescent in nature. From fluorescence studies, it is

observed that the loading of BSA contentto be ~87% i.e. 8.7 mg of BSA out of 10 mg (taken for synthesis of PGMNPs) conjugated to GMNPs (Fig. 5.4a).

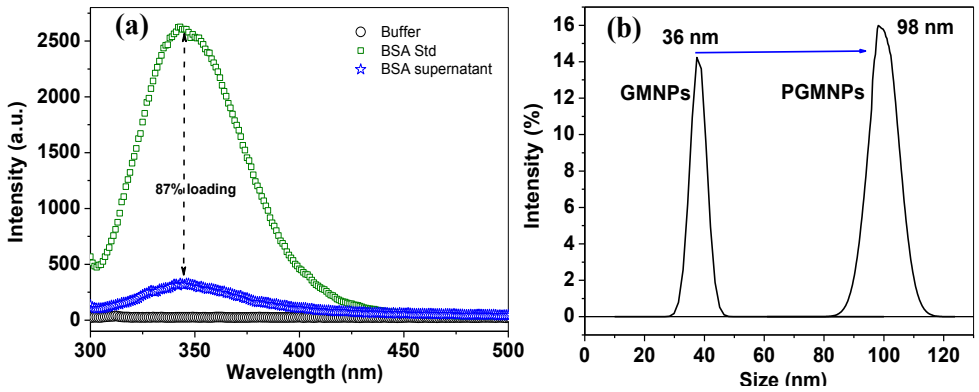

Figure 5.4 *(a) Fluorescence spectra showing the conjugation of BSA protein with GMNPs, (b) shows the change in hydrodynamic diameter of GMNPs from 36 to 98 nm after conjugation with BSA protein.*

The functionalization of BSA protein on the surface of GMNPs was confirmed by the DLS experiment. Fig.5.4b shows the change in hydrodynamic size distributions of GMNPs and PGMNPs. An aqueous solution of GMNPs show intensity weighted average hydrodynamic size 36 nm, while after covalent conjugation with BSA protein the mean hydrodynamic size increased to around 98 nm, with polydispersity index 0.16. This increase in the hydrodynamic diameter is an indication of the successful binding of BSA on MNPs. However, the increase in size from GMNPs to PGMNPs is much higher than that is expected from a monolayer coating of protein, since the protein hydrodynamic diameter is only ~5 nm. Thus, it is very likely that BSA molecules interconnect many MNPs forming a cluster of MNPs after BSA conjugation. Further, the reduction in surface charge from -24.5 ±1.2 mV to -16.8 ±2.4 mV, observed by zeta potential measurements after BSA conjugation, provides additional evidence for the effective binding of BSA on the surface of Fe_3O_4 nanoparticles.

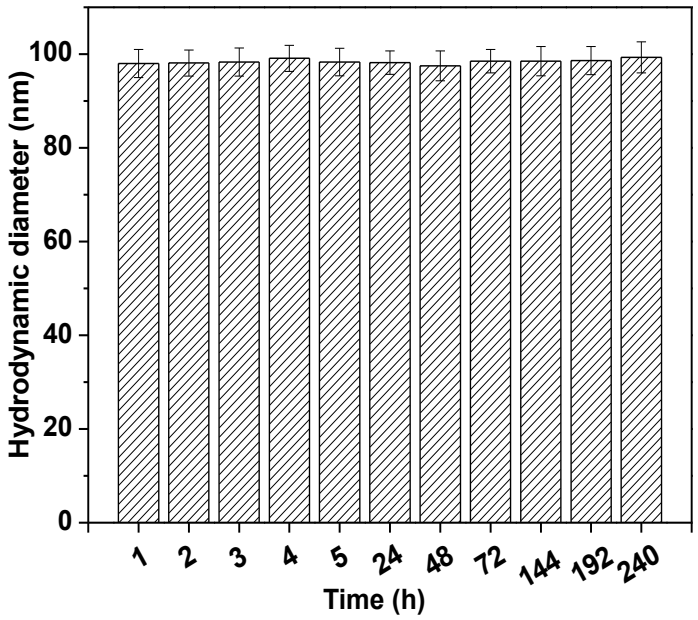

Figure 5.5 *Plot of aqueous colloidal stability of PGMNPs evaluated using the change in hydrodynamic diameter as a function of time.*

The observed surface charge and additional steric interactions arising from large protein sheath can have a positive impact on the stability of the NPs. In general, the negative surface charge is conducive to stabilization in blood. Since the blood cells and plasma possess a negative surface charge, MNPs with negative surface charge can minimize non-specific contact with these components through electrostatic repulsions.[229,230] The aqueous colloidal stability of PGMNPs was also assessed from the changes in D_h (Fig.5.5) as well as their normalized absorbance as a function of time (Fig.5.6a). The insignificant change in hydrodynamic diameter and absorbance of particle suspension (0.1 mg/ml) in water with time suggests their good colloidal stability. Further, the zeta-potential measurements show the pH-dependent charge conversant features of GMNPs and PGMNPs. The highly negative values of zeta-potential of these MNPs in water mediums also provide additional colloidal stability to the particles.

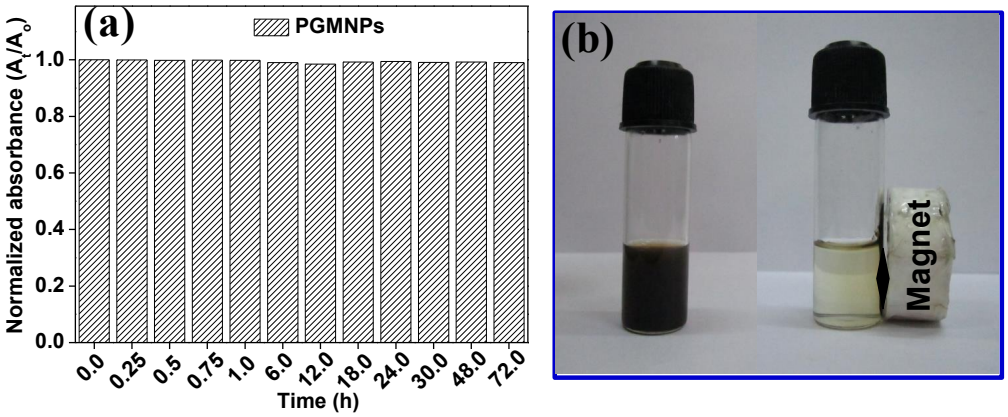

Figure 5.6 *(a) Typical plot of normalized absorbance vs time indicating the stability of PGMNPs (0.1 mg/ml) in water and (b) The response of MNPs to an external magnetic field having field strength ~2.5 kOe.*

In the present case, we believe that the organic shell (free carboxyl groups of glutaric acid on GMNPs, and both free carboxyl and amine groups of BSA on PGMNPs) can provide good compatibility with polar solvents through hydrogen bonding. This will be conducive to overcoming the attractive magnetic and van der Waals forces in water or physiological medium. Additionally, the electrostatic repulsive forces originating from the ionization of the surface groups may also provide stability to particles. Recent studies indicate that the electrostatic repulsive forces originating from the negatively charged ligands coated on Fe_3O_4 nanoparticles provide significant colloidal stability[184]. Thus, the electrostatic repulsion instigated among BSA protein conjugated NPs also contributes to their colloidal stabilization. We also explored the interaction of these nanoparticles with BSA protein at physiological medium (0.01 M PBS, pH 7.3). Interestingly, the PGMNPs do not show any significant change in zeta-potential and D_h even after incubation with BSA for 2h, revealing their protein resistance characteristic at the physiological medium.

5.3.2. Magnetic Properties of Functionalized MNPs

Both ferromagnetic and ferrimagnetic materials exhibit a behavior called hysteresis, and gives the characteristic sigmoidal shape of the M-H curve, with M approaching a saturation value at large values of *H* (see discussion in Chapter 2). It may be noted that the particle size of ferromagnetic materials also have a deciding role in the shapes of M-H curves. Experimental investigation of the dependence of coercivity on particle size showed behavior similar to that schematically illustrated in Fig.5.7. For large particles (micron-sized or more) there is a multi-domain ground state that leads to a narrow hysteresis loop since it takes relatively little field energy to make the domain walls move. As we reduce the particle size, a critical size is reached where domain walls can no longer be accommodated and the whole particle behaves as a single domain. Single domain particles have broad hysteresis loops and the coercivity increases to a maximum and then decreases towards zero. When the size of single-domain particles further decreases below a critical diameter, the coercivity becomes zero, and such particles are known as superparamagnetic particles.

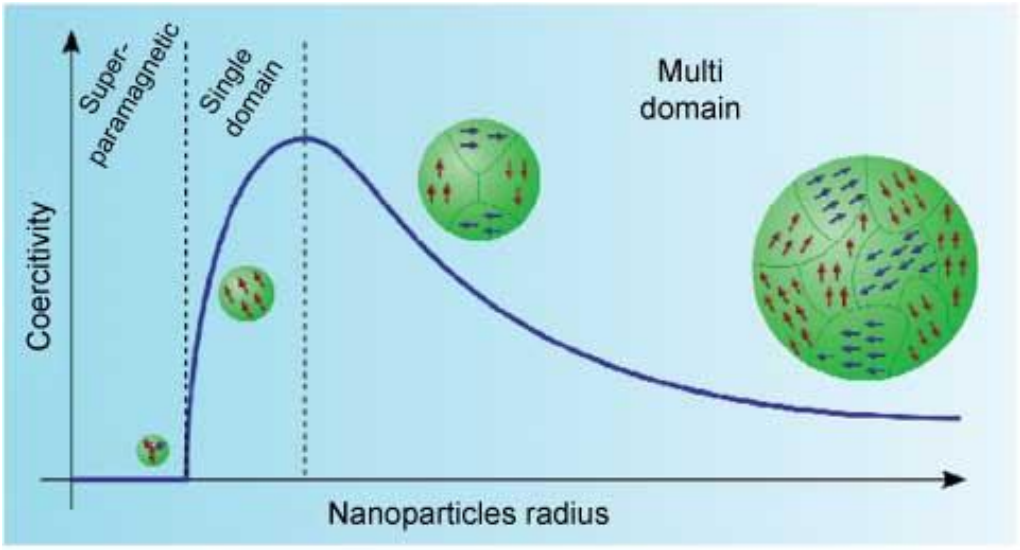

Figure 5.7 *Schematic illustrations of variation of coercivity with NPs size. [Figure is taken from ref:*[231]*]*

The magnetization behavior of MNPs after successful conjugation with organic moieties needs to be investigated for their application in hyperthermia. Fig.5.8 shows the magnetization data of different surface-functionalized Fe_3O_4 MNPs as a function of the applied magnetic field of ±20 kOe at 300 K temperature,

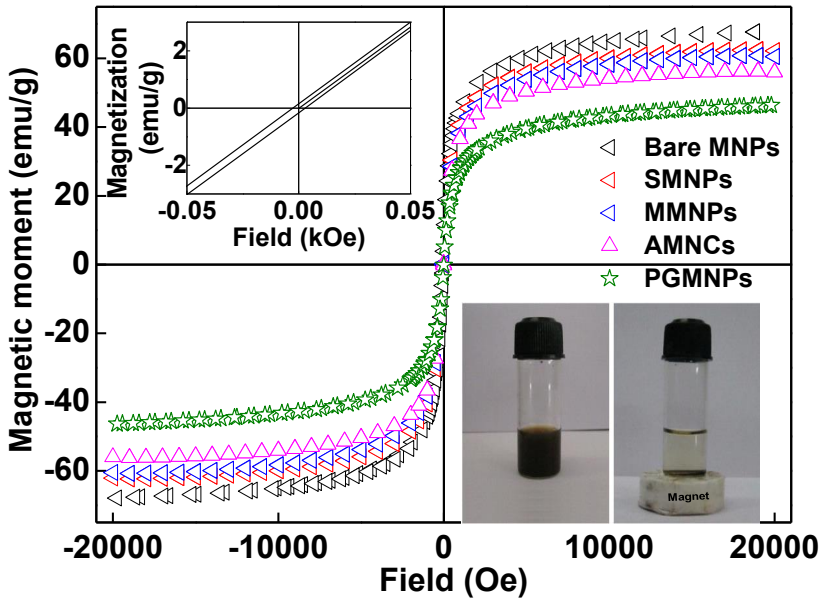

Figure 5.8 *Field dependent magnetization (M vs. H) plot of bare MNPs, SMNPs, MMNPs, AMNPs, and PGMNPs at 300K (top inset shows a typical plot of expanded field-dependent magnetization of MMNPs at the low-field region and bottom inset shows the typical photographs of an aqueous colloidal suspension of AMNPs in absence and presence of magnetic field).*

From magnetic measurement, it has been observed that at low magnetic fields, the magnetization response is steep and approximately linear as the particles begin to align with the applied field. However, at higher fields, the particles are almost completely aligned with the field, and the magnetization approaches saturation. The expanded field-dependent magnetization plot (shown only for MMNPs) at the low-field region revealing negligible coercivity (2.75 Oe) and remanence (0.15 emu/g) is shown in the top inset of Fig.5.8. These results suggest that these MNPs possess superparamagnetic behavior at room temperature. This phenomenon is particularly

important for fast separation of MNPs within a short time from the solvent at the time of synthesis, and the driving of drug carrier to specific organs or tissues by applying an external magnetic field. Also, the superparamagnetic properties of these MNPs are advantageous in localized hyperthermia therapy. The maximum magnetization of these MNPs was found to be 67.6, 62.1, 60.5, 56.0, and 46.4 emu/g for bare MNPs, SMNPs, MMNPs, AMNPs, and GMNPs respectively at 20 kOe. The observed magnetization value is less than that of bulk Fe_3O_4 (92 emu/g)) possibly due to the combined effect of nano-sized particles and non-magnetic organic coating. However, the maximum magnetization of all MNPs prepared here are higher than that of aqueous stable Fe_3O_4 nanoparticles (43.2 emu/g) prepared by thermal decompositon[171]. Results obtained for these MNPs are also comparable with the result reported for carboxyl decorated Fe_3O_4 nanoparticles (58 emu/g) by Barick et al.[232] It is worthy of note that the use of non-magnetic material for coating may cause mitigation in the magnetic properties of nanoparticles. The reduction in M_s value these MNPs is not very surprising due to the quenching of magnetic moment through electron exchange between organic molecules and surface atoms.[233] Nevertheless, an abundant magnetic property was still retained for these MNPs to provide fast separation using permanent magnets and promising hyperthermia effects, as discussed later. Further, these nanoparticles are also highly stable against aggregation after re-dispersion in the aqueous medium. In presence of an external magnetic field (~2.5 kOe), the opaque homogeneous dispersion of MNPs changed to a clear and transparent solution within a few minutes (AMNPs shown inset of Fig.5.8 and PGMNPs shown in Fig.5.6b). Thus, the superparamagnetic nature of these MNPs with good magnetic field responsivity and aqueous colloidal stability makes them suitable for the heat-activated killing of cancer cells.

5.3.3. Heating Ability of MNPs

The heating efficiency of these colloidally stable MNPs was studied by the magnetic hyperthermia experiments. It may be noted that there is a specific tolerance range of frequency and amplitude of the applied magnetic field for hyperthermia in humans. Often, these limits were given by a maximum field-frequency product (H*f) of 4.85×10^8 $A\cdot m^{-1}\cdot s^{-1}$, called the Atkinson–Brezovich limit[234]. However, in practice, such a limit depends on the area of application in the body as well,[217] and there exists a less rigid criterion, i.e. H*f should not exceed $5\times10^9 Am^{-1}s^{-1}$, as proposed by Hergt et al.[235] By accepting this criterion and based on the sensitivity and parameters of our induction heating unit, we have performed hyperthermia experiments at the field strength of 423 Oe (33.6 kA/m) and frequency of 300 kHz. The heating ability of MNPs suspensions were measured from the time-dependent measurements. For hyperthermia studies, to minimize the heat loss, MNPs samples (1 ml) were taken in a polypropylene sample holder (Eppendrof) with suitable arrangements and placed into a coil connected to a power generator, which allows us to control the amplitude of the AC field inside the coil. While the field is applied, a fiber optic temperature sensor inserted into the eppendorf with the solution records the increase in temperature, and from the initial slope of this temperature versus time curves, one can obtain the SAR values. The measurements are done for different concentrations and different solvent to evaluate the heating efficacy which is expressed in terms of SAR (measured in W/g of Fe) of the MNPs.[171] Instead of SAR values, often a system-independent intrinsic loss power (ILP, measured in nHm^2kg^{-1}) is used to express the heating ability of magnetic materials.

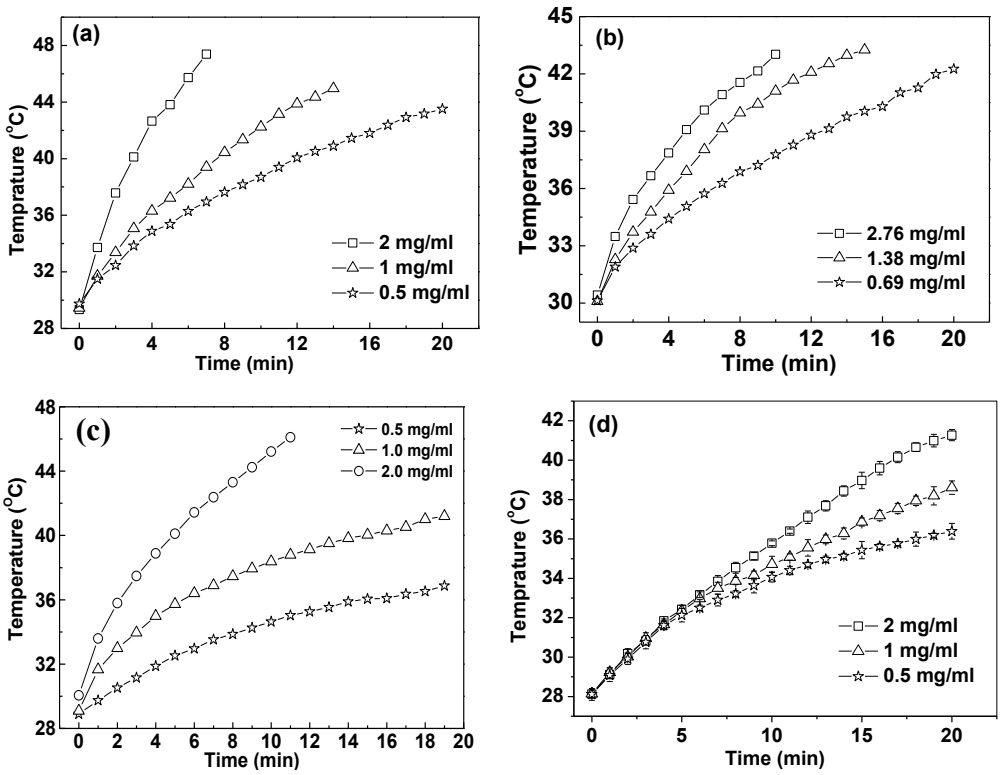

Figure 5.9 *Time-dependent AC magnetic field induced calorimetric measurements of (a) SMNPs, (b) MMNPs, (c) AMNPs, and (d) GMNPs suspension in water at different Fe concentrations.*

The time-dependent calorimetric behavior of aqueous suspensions of these functionalized MNPs were investigated in detail. Fig.5.9 shows the temperature *vs.* time plot for an aqueous suspension of these functionalized MNPs under the AC magnetic field. The results showed a gradual increase in temperature of the MNPs suspension under the applied AC magnetic field. The applied AC magnetic field (507 Oe for SMNPs, MMNPs, and AMNPs, and 423 Oe for GMNPs and PGMNPs are used) and frequency of 300 kHz is able to produce enough energy for raising the temperature of 1 mg/ml of Fe suspension to hyperthermia temperature (42-43^{o}C) within 20 min. It has been observed that the time required for reaching hyperthermia temperature decreases with an increase in the concentration of Fe in suspension. Here one thing we observed that compared to GMNPs (small size MNPs prepared by

thermal decomposition method) sugar-alcohol and ascorbic acid-coated MNPs (prepared by co-precipitation) shows a higher heating rate (see Fig.5.9). This observed different heating rate may be due to differences in the magnetization properties, size of NPs, applied field and the amount of coating agent present on the MNPs. The SAR values and corresponding system-independent ILP values for these MNPs were provided in Table 5.1. Muller et al.[236] developed iron oxide ferrofluids having a SAR value of 87 W/g at H=11 kA/m and f=410 kHz (particle size: 13 nm, ILP: 1.75 nHm^2/kg). Fortin et al.[237] reported SAR parameter of 1650 W/g at H=24.8 kA/m and f=700 kHz for IONPs (particle size: 16.5 nm, ILP: 3.8 nHm^2/kg). The ILP values obtained in the present study are less than these synthetic IONPs. However, they are in the range of those reported for commercially available ferrofluids such as Nanomag-D-spio, BNF-01808, and BNF-01708 (Manufacturer: Micromod).[238] Further, the SAR value decreases with an increase in the concentration of particles in suspension. This could be attributed to the increase in NPs aggregation and dipolar interactions with the increase in the concentration of particles. Piñeiro-Redondo et al.[239] demonstrated that heat production efficiency decreases with increasing the concentration of polyacrylic acid-coated Fe_3O_4 nanoparticles due to the higher inter-particle dipolar interaction. A similar SAR dependence of the particle concentration was also observed by Rana et al.[124] for starch and polyaniline coated Fe_3O_4 nanoparticles.

Table 5.1 SAR and ILP parameters obtained for functionalized MNPs at different concentrations of Fe.

MNPs	**SAR (W/g)**			**IPL (nHm^2/kg)**		
	0.5 mg/ml	1.0 mg/ml	2 mg/ml	0.5 mg/ml	1.0 mg/ml	2 mg/ml
SMNPs	92.0	71.1	39.7	0.188	0.144	0.079
MMNPs	158.9	104.6	100.5	0.324	0.213	0.204
AMNCs	111.0	87.1	71.7	0.226	0.177	0.146
GMNPs	108.73	50.21	29.31	0.319	0.147	0.086
PGMNPs	115.0	69.0	40.0	0.339	0.203	0.118

Our studies indicate that compared to GMNPs, PGMNPs show a higher heating rate (see Fig.5.10a). It was stated elsewhere that isotropic clusters of BSA were formed under the AC magnetic field, and this may be responsible for raising the temperature of a nanoparticle system[240].

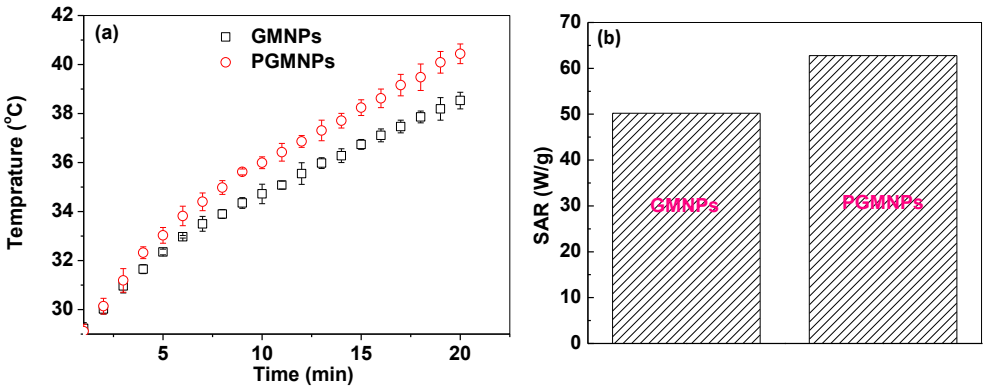

Figure 5.10 *(a) Comparison of Time-dependent calorimetric plots of GMNPs and PGMNPs suspensions (1 mg/ml of Fe) in water medium) in presence of AC magnetic field (423 Oe) (b) SAR values (W/g of Fe_3O_4) of GMNPs and PGMNPs suspensions (1 mg/ml of Fe).*

A comparison of the heating ability of GMNPS and PGMNPs and the corresponding SAR values are presented in Fig.5.10b, The SAR value of the PGMNPs (69.0W/g) is higher than that of GMNPs (50.21 W/ g). This increased SAR could arise from the preventions of fibrous aggregation of NPs under the AC magnetic field, as reported earlier. In general, fibrous aggregation increases the critical size of the NPs in a solution and hence decreases the specific heat of the system. It is well reported that the aggregation of NPs decreases the SAR value significantly[241]. Prevention of aggregation by BSA conjugation might have thus enhanced the SAR value of the system. Further, it has been observed that the heating efficacy is strongly dependent on the stabilizing medium in addition to the concentrations of MNPs (Fig.5.11).

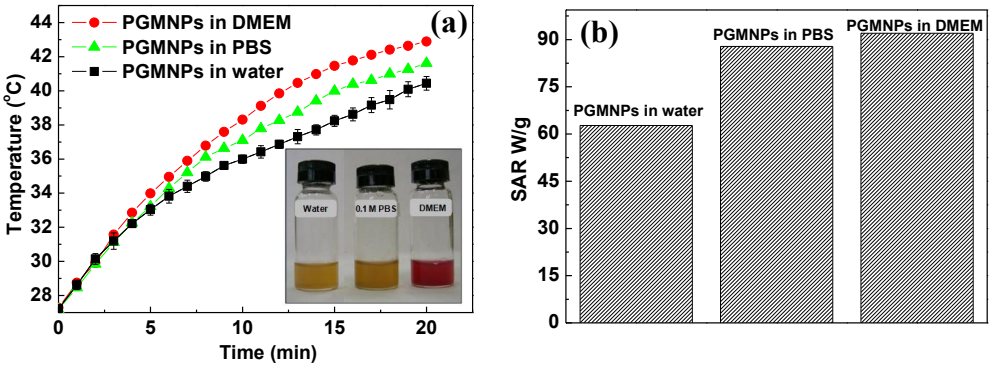

Figure 5.11 *(a) Time-dependent calorimetric plots (inset shows the colloidally stable PGMNPs suspensions (1 mg/ml of Fe) in a different medium), and (b) Corresponding SAR values (W/g of Fe_3O_4) of PGMNPs suspension.*

It is important to identify the heating ability of MNPs in different media to ensure its properties under in-vivo conditions. Investigation of the heating ability of PGMNPS in PBS, water, and DMEM indicates that PGMNPs show a higher heating rate in the physiological (PBS) and culture (DMEM) mediums, compared to in the water. The heating rate increases in the order water< PBS< DMEM medium (Fig.5.10a). The particles are found to be stable in all mediums (inset of Fig.5.10a) and showed the highest SAR value in DMEM (Fig.5.10b). The ILP values computed for PGMNPs are 0.203, 0.254, and 0.278 nHm^2kg^{-1} in water, PBS, and DMEM respectively, and it was seen to be in the range of those reported for commercially available ferrofluids.[238] The observed good SAR values of PGMNPs combined with good colloidal stability and magnetic field responsivity makes it an attractive material for hyperthermia.[242] The main contributions to the AC field-induced heating are through energy loss processes such as hysteresis loss, Néel relaxation, Brownian relaxation, and eddy current loss.[198] Considering the superparamagnetic nature of the samples, one would expect negligible heat generation from the hysteresis loss. The poor electrical conductivity of Fe_3O_4 (ρ =~10^2 Ohm-cm) ensures a negligible contribution from eddy current loss as well. Thus, it is likely that the major

contribution to ILP arises from Brownian (heat due to friction arising from total particle oscillations) and Néel (heat due to rotation of the magnetic moment with each field oscillation) relaxation loss processes. Thus, a comparison of the hyperthermia effects of different surface passivated NPs suggests that protein stabilized particles are superior to mannitol, sorbitol or ascorbic acid-coated particles. This provides the opportunity to use human serum proteins as appropriate stabilizing agents for the preparation of high water-dispersible Fe_3O_4 MNPs and its application as an effective heating source for hyperthermia therapy.

5.4. Conclusions

Colloidally stable functionalized Fe_3O_4 MNPs with different stabilizing agents such as sugar-alcohols, ascorbic acid, and BSA protein were prepared successfully. The structural, morphological, and interfacial properties of these MNPs have been carried out by XRD, TEM, FTIR, TGA, DLS, Zeta-potential, and Fluorescence spectroscopy, and it was confirmed that there is the formation of single-phase inverse spinel nanostructure with a successful coating of the stabilizing agent. Light scattering measurements indicate that these MNPs render good colloidal stability in aqueous and physiological medium. The magnetic studies demonstrated that the presence of an organic layer reduces the saturation magnetization of the MNPs. Nevertheless, this passivation does not change the superparamagnetic nature of the Fe_3O_4 NPs, as shown by the negligible coercivity and remanence magnetization at 300 K. In addition, these MNPs show self-heating ability under the ACMF with good system-independent ILP values. The heating efficacy and SAR of these MNPs were found to be strongly dependent on the concentration of particles and stabilizing media. Among various organic modifications, BSA conjugated MNPs show superior hyperthermia properties for application in cancer therapy.

CHAPTER 6

A NEW ORGANIC SOLVENT-FREE PROCESS FOR THE PRODUCTION OF SURFACE CHARGE TUNED LIPOSOMES

6.1. Introduction

Among the others, nanostructured soft material-based drug delivery carriers such as micelles, liposomes/vesicles, solid lipid nanoparticles, microemulsions, etc. are the widely used drug carriers in cancer therapy. These carriers have a unique structure in which the hydrophilic or hydrophobic compartments with a dimension of a few nanometers to sub-micrometer are dispersed in a solvent and exist in a thermodynamic equilibrium state. These structural features of amphiphilic assemblies make them efficient carriers for the encapsulation of several drug molecules. Among them, micelles and liposomes are mostly used drug carriers in the cancer treatment, due to their unique properties like good colloidal stability, long blood circulation time, ability to load hydrophobic as well as hydrophilic drug molecules, their small particle size, good thermodynamic solution stability, extended-release of various drugs and prevention of rapid clearance by the RES. Also, their surface can be functionalized with different targeting moieties to make the targeted drug delivery system. The nanocarriers such as vesicles/liposomes can be effective at targeting cancer cells and play a key role in the development of nano-particulate carriers for cancer therapy. Liposomes are mostly composed of phospholipids. Other additives or modified lipids are added to impart additional functionality to the liposomes. The rigidity of the bilayer can be varied by adding cholesterol.[243] Stealth characteristics can be achieved by covalently binding polyethylene glycol (PEG) chains to the lipid and have been successfully used in the delivery of doxorubicin for the treatment of solid tumors and are presently marketed as ‘Doxil’ or ‘Caelyx’.[244] A variety of therapeutic agents (both hydrophobic as well as hydrophilic) have been incorporated into liposomes and are

widely used in the pharmaceutical industry as DDS, foods, and beverages as well as in cosmetic formulations.

The currently available methods[245] of liposomes preparation are: lipid dry film hydration followed by extrusion, reverse-phase evaporation, and solvent injection method including mechanical (sonication and micro-emulsification) and solvent dispersion methods. In the dry film hydration method, the constituent lipids of the bilayer are dissolved in an organic solvent and a dry film of the lipid is formed by evaporating the solution in a rotary evaporator. The dry lipid film formed on the walls of the flask is hydrated by an aqueous solution or PBS. In the reverse-phase evaporation method, the dry lipid film is first reconstituted in diethyl ether/isopropyl ether, followed by addition of the aqueous phase. Then, the organic phase is removed by the purging of nitrogen. In the solvent injection method, first, the lipid is dissolved in a water-miscible solvent such as ethanol and then the solution is slowly injected into the aqueous phase. The main drawbacks connected with most of the liposome preparation methods are the use of one or more organic solvents to achieve adequate distribution of the constituents of a lipid bilayer and poor stability of the liposomes upon storage. When liposomes are administered intravenously, as a drug delivery vehicle, it is necessary to ensure that it is free from any organic solvents. For instance, a chlorinated solvent such as chloroform is undesirable in intravenous injection products. Moreover, the use of water-immiscible organic solvents puts additional constraints with respect to workplace safety and release to the environment. Further, the stability of liposomes for long term storage and reproducibility for scale-up are also a matter of concern. Also, the surface charge of the liposomes needs to be controlled to enhance transfection efficiency. Thus, there is a need to devise methods

for producing liposomes having improvements in safety, stability issues with controlled interfacial properties.

In this context, attempts were made for a versatile method to produce liposomes of narrow size distribution with a controlled surface charge without using volatile/toxic and flammable organic solvents such as chloroform, methylene chloride, hexane or cyclohexane or other additives that are not approved for use in pharmaceutical applications. First, we developed a dynamically frozen water-free micellar system by using a supercooled matrix comprising sugar or sugar alcohol and urea or its analogs. The supercooled micelles were used as a precursor for solubilization of lipids or other bilayer forming amphiphiles. It was observed that the dissolution of this supercooled matrix in water leads to the spontaneous formation of vesicles or liposomes with a controlled surface charge. Further, these liposomes were used to improve the effectiveness of drug formulation. To investigate the suitability of this method for drug encapsulation, we employed curcumin as a model hydrophobic compound and observed around 10 fold increase in cellular uptake of curcumin using liposomal formulation. This offers a novel way of creating liposomes with tunable surface charge and high drug loading capacity. The above approach does not involve any organic solvents or other energy-intensive size reduction procedures such as sonication or extrusion.

6.2. Experimental and Methods

6.2.1. Preparation of Water-Free Supercooled Micelles

Water-free supercooled micelles can be prepared in a variety of solvents. Typically, the solvent includes a mixture of hydrophilic compounds like sugar or sugar alcohols and a hydrogen bonding compound like urea, its derivatives or any other

amide group-containing molecules. In a typical preparation, first, a mixture of sugar and urea at a weight ratio of 3:2 is placed in a mortar and ground well to form a homogenous powder. The appropriate amount of solid surfactant was also added before grinding using a mortar and pestle. For example, to prepare 10% SDS water-free micelles in the fructose-urea melt, a mixture of 0.54 gm fructose, 0.36 g urea, and 0.1 g SDS are taken in a mortar. The well ground powder is transferred to a glass vial, sealed and placed in an oil bath maintained at 90 ^{o}C. The melting started at around 68 ^{o}C and a homogenous solution was obtained at 90 ^{o}C (fructose-urea mixture becomes homogenous at 80 ^{o}C while glucose-urea needs 90 ^{o}C). Care should be taken not to raise the temperature high, to avoid any charring of sugar. Occasional stirring helps to dissolve easily. Once a homogenous solution is formed the vial is placed in a temperature-controlled water bath kept at 15 ^{o}C. The mixture reached a temperature of 15 ^{o}C within a span of 30 seconds. This supercooled melt is sticky initially which gets hardened with time, depending on the composition. For in-situ SAXS analysis, the well ground powder is loaded in a metallic paste cell (Anton Paar, Austria) with Kapton window and heated/cooled using the Peltier sample holder.

6.2.2 Preparation of Liposomes

The above-mentioned procedure is employed to solubilize lipids in a supercooled solvent so as to form emulsions or micro-emulsions. The dissolution of this micelle or emulsion with appropriate lipids in water or buffer leads to the spontaneous formation of liposomes. The flow chart of a typical organic solvent-free process for liposome preparation using a supercooled micelle/emulsion dissolution process (SEMSOL) is given in Fig. 6.1.

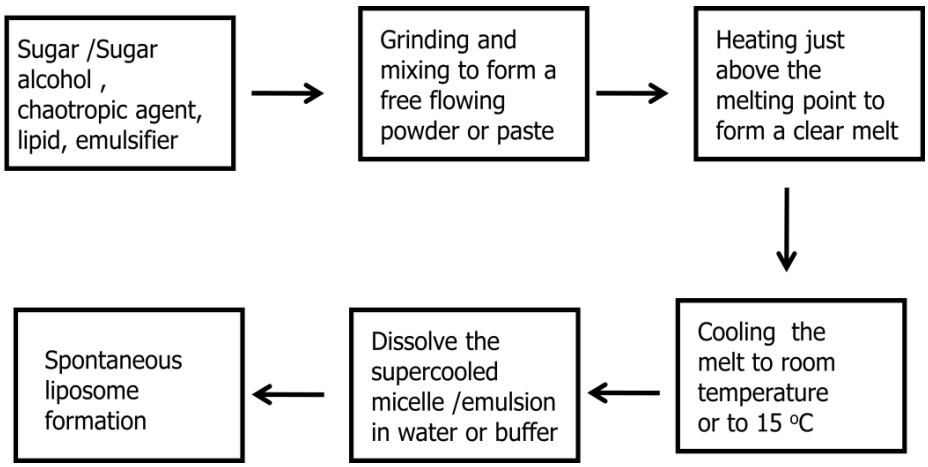

Figure 6.1 *Flow chart of the process for the spontaneous formation of liposomes by supercooled micelle/emulsion dissolution (SEMSOL).*

6.3 Results and Discussion

6.3.1. SDS Micelles in Supercooled Fructose-Urea Melt

A typical three-component system that forms supercooled micelles consists of fructose, urea, and SDS, at a weight ratio of 54:36:10. The micelles are first prepared at a temperature above the matrix melting point and subsequent cooling of the melt leads to the formation of trapped micelles. The supercooled liquid formed by melting and subsequent cooling of the above mixture is optically transparent and viscous enough to hold its own weight.

Using SAXS, we followed the evolution of micellar structures as a function of temperature (Fig. 6.2a). At 25 °C, the SAXS pattern of the sample (fructose-urea-SDS 54:36:10 w/w) shows characteristic lamellar peaks of SDS. The peaks occur at q values of 0.1595, 0.3199, and 0.4799 $Å^{-1}$. The ratio of the peak positions is close to 1:2:3, with a lattice parameter of 3.93 nm, as expected for lamellar crystals.[246] Upon sample heating, to 50 °C, the lamellar peaks intensity decrease and a broad peak appear at q value close to 0.105 $Å^{-1}$. At 70 °C, the contribution from the lamellar

structure becomes negligible and the system mostly comprises micellar aggregates as shown by the broad peak at q value 0.115 $Å^{-1}$. This peak arises from the short-range inter-micellar correlations, as observed for micelles in liquids.[247] At 80 °C, the lamellar structure completely disappears and the SAXS pattern is reminiscent of pure micelles. Moreover, upon cooling these preformed micelles to 15 °C (within a span of 30 s), the micelles SAXS pattern is retained, indicating kinetically trapped supercooled micelles.

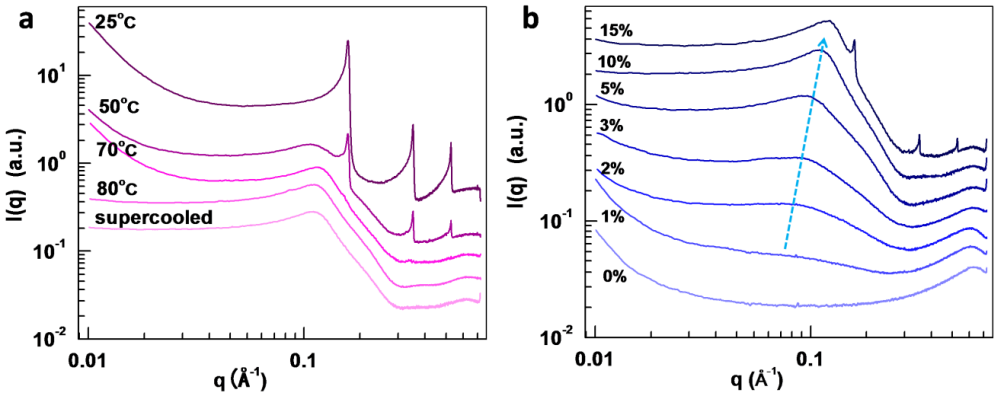

Figure 6.2 *(a) Temperature-dependent SAXS patterns of SDS in the fructose-urea mixture. (b) SAXS pattern of micelles formed in the fructose-urea melt at different SDS concentrations.*

SAXS profiles of supercooled samples indicate that micelles exclusively exist up to at least 10% SDS (Fig. 6.2b). Moreover, as expected for globular micelles, the position of the correlation peak is shifted to higher q values with increasing SDS concentration (see the trend line). This is because the increase in the number density of the micelles decreases the inter-particle distance ($d=2\pi/q_{max}$) between micelles, provided that the aggregation number of the micelles remains practically unchanged. At 15% SDS surfactant, the SAXS pattern shows features of micelles superimposed with characteristic peaks of lamellar structures, indicating the coexistence of micelles and lamellar SDS crystals in the melt. This is different from the phase behavior of

SDS in water,[248] where globular micelles exist up to a concentration of 36% w/w, and lamellar crystals form only above ~70% w/w. Thus, we demonstrate that SDS can be solubilized in an organic melt up to a concentration of at least 10% w/w, without any phase separation or transition to lamellar crystals.

To understand the structure of micelles in such a supercooled matrix, a systematic investigation of the SAXS pattern, taking into account the scattering length density of the solvent is necessary. As the structure of SDS micelles in water is well documented, it is appropriate to look into the effect of these additives in aqueous micelles and how does the micelles in sugar-urea melt compares with micelles in water.

6.3.2 Structure of SDS Micelles in Fructose-Urea Mixtures

The effect of the fructose-urea mixture on the structure of SDS micelles can be understood from the series of SAXS patterns from 10% SDS solution, at the different additive concentrations (Fig. 6.3a). The use of such a mixed additive permits variation of solvent SLD in the entire concentration range, including supercooled melt. No crystalline peaks were observed in any of the SAXS patterns indicating the existence of micelle-like aggregates at all compositions. This ensures that micellar aggregates are present even in the water-free system, fructose-urea melt. As the concentration of solid content increases from 0 to 100 %, one can see the evolution of the correlation peak due to the structure factor. This peak which was absent in the case of micelles in water becomes evident when the additive concentration becomes 30%. The position of the correlation peak shifted continuously to higher q value. This could arise from a change in the number density of the micelles or changes in the solvent SLD or both. A systematic analysis of the SAXS data using the known SLD of solvent can reveal this

structural information. The quantitative analysis of the SAXS pattern using model fitting confirms that the axial and equatorial radii of the micelle core remain more or less the same with the increasing concentrations of the fructose-urea mixture (Fig.6.3b and Table 6.1a). However, beyond 40% additive concentration, due to the minor difference between the SLD of shell and solvent, the thickness of the hydrophilic shell is kept constant. Analysis of the data in the supercooled melt indicates that the shell thickness decreases, as compared to that in water. This has resulted in a decrease in the surface charge of water-free micelles.

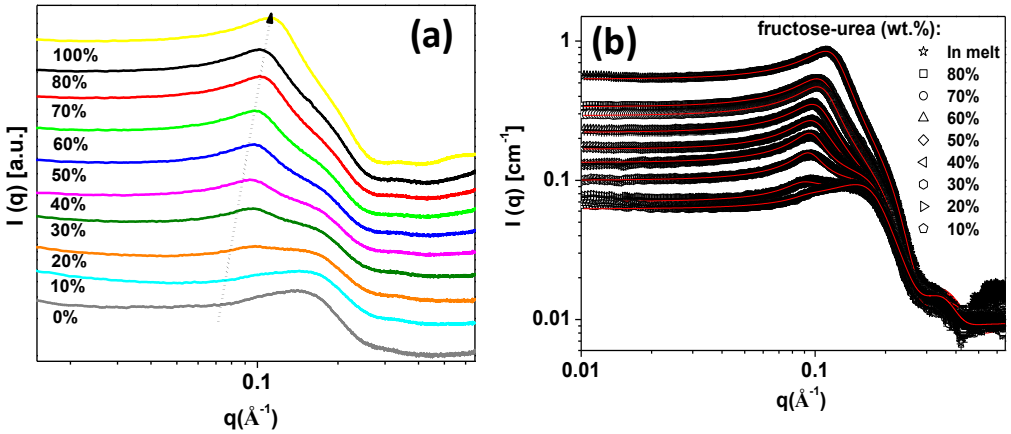

Figure 6.3 *(a) SAXS pattern of 10% SDS micelles at different concentration of fructose-urea (3:2) in water, (0% corresponds to micelles in water and 100% corresponds to water-free micelles in the fructose-urea supercooled melt (data are scaled vertically for clarity), and (b) corresponding background subtracted SAXS pattern (in absolute scale) along with fitted curves.*

Table 6.1 Structural parameters of 10% aqueous SDS micelles at different concentrations of fructose-urea, as obtained from SAXS and SANS analysis using core-shell ellipsoidal model, with constant polydispersity (0.1) in the semi-minor core. The structure factor is taken into account using screened Coulomb potential (Hayter-Penfold Mean spherical approximation).

6.1a. Micellar parameters obtained from SAXS analysis

Fructose-Urea (wt. %)	**Semi-minor core (Å)**	**Semi-major core (Å)**	**Shell thickness (Å)**	**Charge (e.u.)**	**SLD (10^{-6} Å^{-2})**			χ^2
					core	shell	Solv.	
0	13.1 ±0.2	18.2 ±0.1	11.0 ±0.1	38.3 ±2.5	7.21	10.14 ±0.1	9.44	3.7
10	13.1 ±0.2	17.4 ±0.3	10.6 ±0.2	38.2 ±1.4	7.21	10.43 ±0.2	9.73	2.1
20	13.1 ±0.1	17.8 ±0.2	10.0 ±0.2	38.8 ±1.2	7.21	10.56 ±0.1	10.0	3.4
30	13.0 ±0.2	16.6 ±0.2	9.1 ±0.3	37.5 ±1.6	7.21	10.79 ±0.2	10.3	4.3
40	13.0 ±0.2	16.5 ±0.2	6.0 ±0.2	38.2 ±0.3	7.21	11.23 ±0.1	10.7	4.1
50	13.4 ±0.1	16.6 ±0.2	6.0	38.0 ±0.2	7.21	11.36 ±0.1	11.0	5.1
60	13.4 ±0.2	16.8 ±0.1	6.0	38.8 ±0.2	7.21	11.41 ±0.1	11.3	4.4
70	13.8 ±0.3	16.4 ±0.2	6.0	38.9 ±0.3	7.21	11.56 ±0.2	11.6	5.0
80	13.6 ±0.2	16.8 ±0.2	6.0	38.6 ±0.4	7.21	11.78 ±0.3	11.9	7.1
100 (Supercooled matrix)	14.1 ±0.2	17.0 ±0.1	5.6 ±0.1	13.7 ±0.1	7.21	13.1 ±0.2	12.5	14.1

6.1b. Micellar parameters obtained from SANS analysis

Fructose-Urea (wt. %)	**Semi-minor core (Å)**	**Semi-major core (Å)**	**Shell thickness (Å)**	**Charge (e.u.)**	**SLD (10^{-6} Å^{-2})**			χ^2
					core	shell	solvent	
0	15.1 ±0.2	24.6 ±0.1	4.6 ±0.2	38.2 ±0.2	-0.37	4.59 ±0.1	6.39	5.4
10	14.2 ±0.6	24.1 ±0.5	4.4 ±0.3	38.8 ±0.4	-0.37	4.53 ±0.1	6.11	2.1
20	14.1 ±0.5	23.8 ±0.6	3.9 ±0.4	37.2 ±0.4	-0.37	4.38 ±0.1	5.81	2.9
40	13.9 ±0.2	22.3 ±0.4	3.7 ±0.2	38.2 ±0.3	-0.37	4.32 ±0.2	5.11	2.7
60	13.8 ±0.2	19.6 ±0.1	3.6 ±0.2	37.5 ±0.4	-0.37	3.91 ±0.3	4.24	3.2
80	13.9 ±0.3	16.3 ±0.2	3.5 ±0.2	38.3 ±0.4	-0.37	3.16 ±0.2	3.23	2.8

Above, observations of altering the contrast while retaining the micelle structure intact with the addition of fructose-urea mixture are supplemented by SANS data. For this, SANS measurements were carried out on micelles prepared in D_2O, in the presence of different concentrations fructose-urea mixture (Fig. 6.4). The correlation peak due to the inter-particle structure factor is clearly seen for micelles in D_2O. As observed from SAXS, the position of the peak shifts to higher q values with an increase in additive content. However, due to the decrease in the neutron SLD of

solvent with increasing additive, the contrast diminishes and the scattering intensity decreases drastically at 80% solid. Quantitative analysis of the SANS pattern shows excellent agreement with micelle parameters obtained from SAXS analysis (Table 6.1a and 6.1b). Through a systematic analysis of SAXS and SANS data, we inferred that the SDS micelles with similar core dimensions can be formed in water as well as a fructose-urea melt. This provides an opportunity to use such mixtures as efficient additives to alter the SLD of the solvent as well as prepare a water-free matrix for forming micelles. However, while employing contrast variation methods to study the structure of a wide range of aggregates using such additives, it should be kept in mind that it can modify the micelle structure and/or interaction, depending on the nature of the system.

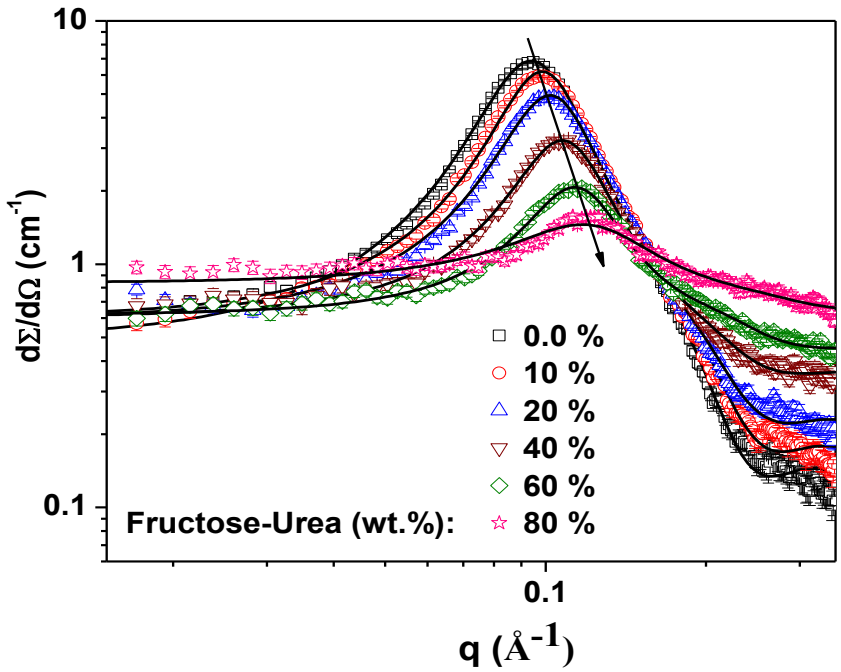

Figure 6.4 *Background subtracted SANS pattern and the best-fit curves for 10% SDS in D_2O at different concentration (wt.%) of fructose-urea (3:2).*

Thus, quantitative SANS and SAXS analysis showed that the dimensions of the supercooled micelles are in the same range as that was observed in water.

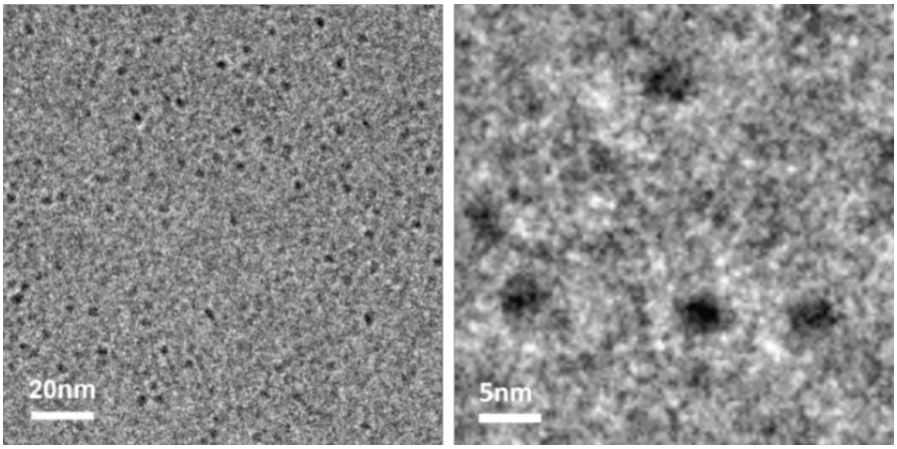

Figure 6.5 *TEM images of 2% SDS in fructose urea melt at ambient conditions*.

The structural features of micelles formed in the fructose-urea melt are further analyzed, directly, by transmission electron microscopy (TEM) studies. As can be seen in Fig. 6.5, nearly globular micelles with a diameter of ~4 nm are observed when 2% SDS is dissolved in fructose-urea melt. The micelles are similar to those found in water and an excellent agreement with the scattering findings. It may be noted that the micelles prepared in the melt (80 °C) are quenched in liquid nitrogen (-196 °C) and further examined at ambient temperature using HR-TEM and phase plate TEM. This way, there is no need to use cryogenic conditions during imaging, which simplifies the imaging procedure compared to conventional Cryo-TEM analysis. It may be noted that as self-assembled structures such as micelles or liposomes are sensitive to the presence of additives, there could be a slight difference in the structure of micelles in water and sugar melt. However, the absence of any crystal formation in the matrix is advantageous to visualize the structures at ambient conditions. The structures revealed by HR-TEM are consistent with those detected by scattering measurements. The features in the TEM images originate from the hydrocarbon core of the micelles with associated high SLD counterions. However, a precise demarcation of the core and shell morphology is difficult to achieve by TEM due to the lack of a sharp interface.

Often, the continuous counterions distribution and rough interface of the micelles, along with poor scattering contrast make it difficult to ascertain the core-shell morphology in TEM. Thus, the determination of the precise morphology of the micelles necessitates the combination of both scattering and electron microscopy. One notable feature in the TEM images is the narrow polydispersity in size, as is observed in the case of equilibrium structures formed via self-assembly.[249] It may be noted that such direct images of micelles were previously observed only at cryogenic temperature, upon vitrification of suspensions. Here, all observations are made at ambient temperature, and imaging of the micelles was possible due to the supercooled nature of the system. In summary, the formation of supercooled micelles in a water-free environment can be schematically represented as Fig. 6.6.

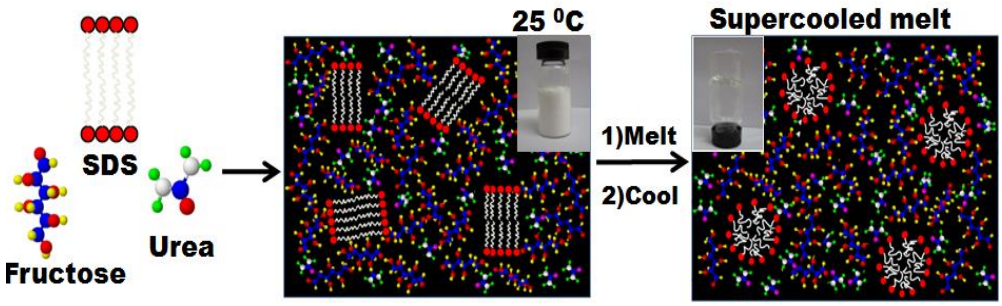

Figure 6.6 *Schematic illustrations of surfactant dissolution in the fructose-urea melt at 80 °C and subsequent trapping of micelles in a supercooled state at 15 °C.*

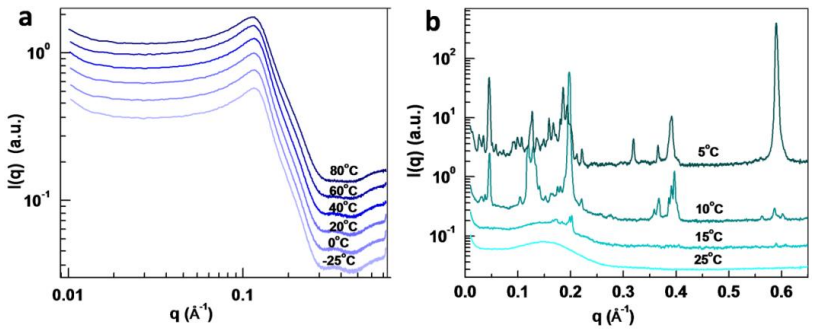

Figure 6.7 *Micelles in organic melt sustain subzero degree Celsius (a) Temperature-dependent SAXS patterns of 10% SDS in the fructose-urea melt (3:2) at 80 °C and*

subsequent cooling of the sample to -25 °C. (b) Temperature-dependent SAXS patterns of 10% SDS in water indicating crystallization of the surfactant below 15 °C.

One notable feature of the micelles in sugar-urea melt is that these micelles can exist below 0 °C. The similarity of SAXS patterns recorded upon cooling the melt containing micelles at temperatures ranging from 80 °C to -25 °C (Fig. 6.7a) confirms that the aggregates are kinetically trapped and remain in the micellar form at least up to -25 °C. This is contrary to what is observed for SDS micelles in water, where the surfactant starts crystallizing at ~15 °C, and diffraction peaks corresponding to SDS crystals are found already at 5 °C (Fig. 6.7b).

The above phenomenon of micelle formation in sugar-urea melt is not limited to SDS. Non-ionic and cationic micelles can also be formed in such molten solvents. For example, non-ionic TritonX-100 micelles can be formed in a mixture of glucose and urea at appropriate concentrations.

6.3.3. TritonX-100 Micelles in Glucose-Urea (GU) Melt

Fig. 6.8(a) shows the background subtracted SAXS patterns recorded at 25 °C, for the aggregates formed by solubilizing different concentrations (1, 3, 5, and 10% w/w) of TritonX-100 (TX-100) in GU (3:2) melt. The SAXS pattern shows the signature of nanostructure formation, as revealed by an increase in the scattering at small q values. The scattering pattern is analogous to those of globular micelles formed in other non-aqueous solvents such as ionic liquids or DESs.[250,251] However, the SAXS pattern is strikingly different from those of typical non-ionic micelles in water.[252] Fig. 6.8(b) shows the SAXS pattern of TX-100 micelles in water at 25 °C, at different surfactant concentrations. SAXS data of micelles in water show a pronounced peak at q ~0.16 Å^{-1}, characteristic of core-shell morphology

of the micelles.[253] On the other hand, the SAXS pattern in the supercooled solvent shows a monotonic decrease with an increase in q values. This difference in the pattern could arise from a change in the morphology of the aggregates or changes in the scattering contrast between the solvated shell of the micelle and solvent. With an increase in surfactant concentration, the scattering intensity increases and the peak at high q value can be clearly resolved.

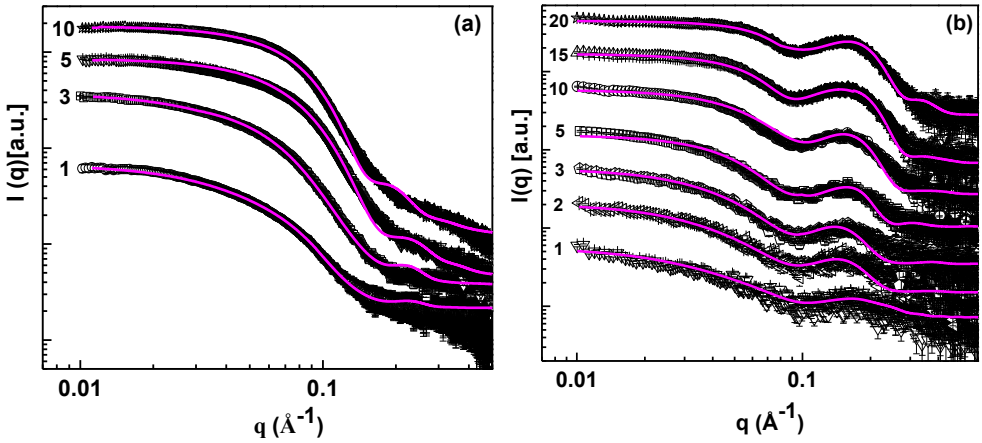

Figure 6.8 *SAXS patterns of TX-100 (a) in supercooled Glucose-Urea melt and (b) in the water at different surfactant concentrations (% w/w) at 25 °C, (The solid lines show simulated model fit data are scaled vertically for clarity).*

The PDDF obtained from GIFT analysis of the SAXS data supports the core-shell morphology of aggregates. The PDDF, *p(r)*, gives the distribution of paired distances within the micelles weighted by the SLD of the points connected by them. The PDDF of micelles in water (Fig. 6.9(a)) shows a clear hump at a small distance of ~1.3 nm, followed by a peak at 4.3 nm. The hump at a small distance arises from the peak observed at high q values in the scattering pattern. This is a signature of the core-shell morphology of the aggregates due to differing scattering length of the hydrophobic core and

hydrophilic shell. The peak observed at high *q* region is analogous to those of aggregates formed by peptide amphiphiles in water.[254] Aaron Lau et al. demonstrated that the changes in the hydrophilic segment of the lipopeptides alter the high *q* peak observed in the SAXS pattern. The peak at small distances in the PDDF, observed for micelles in water disappears for micelles formed in the melt. The electron density profile of the micelles were obtained from deconvolution of the p(r) function (Fig. 6.9(b)) it shows that the high electron density observed for the solvated shell of the micelles in water disappeared in GU melt, with a systematic variation of electron density from the core to that of solvent.

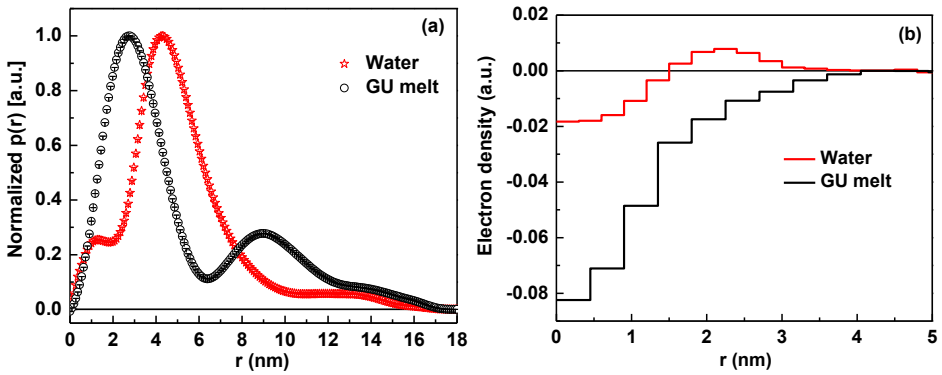

Figure. 6.9 *(a) The Pair distance distribution function of 5% TX-100 micelles in water and Glucose-Urea melt, as obtained from Indirect Fourier Transformation of the SAXS data, and (b) their corresponding electron density profile.*

The information obtained from the PDDF can be used to develop a suitable model to analyze the scattering pattern. Here, a core-shell sphere model with continuously varying electron density at the shell interface (graded interface) is employed. This is a reasonably good approximation, instead of a sharp interface between shell and solvent, as it is well known that the penetration of solvent at the hydrophilic region alters the SLD of the shell matrix. The SLD of the core, dry shell

and solvent are calculated from the molecular structure parameters (discussed in chapter 2). In the case of TX-100 micelles, the SLD of the core is obtained as 8.08 x 10^{-6} Å^{-2} and the dry shell is 10.33 x 10^{-6} Å^{-2}, as per the structure of hydrophobic and hydrophilic part of surfactant. The SLD of the dry shell is around ~9.4% higher than that of water (9.44 x 10^{-6} Å^{-2}), while SLD of the core is around 14.4 % lower. Hence, by using X-ray scattering the core-shell structure of TX-100 aqueous micelles can be easily resolved.

The X-ray scattering intensity from spherically symmetric non-ionic micelles can be best described in terms of core-shell particles with a graded interface to account for the solvated hydrophilic shell. The form factor *P(q),* for such micelles, can be calculated as,

$$P(q) = \frac{f^2}{V_{particle}} \tag{6.2}$$

where $f = f_{core} + f_{dry\ shell} + f_{shell\ interface} + f_{solvent}$

Here we assume that the SLDs of the core and the solvent are constant against *r* and considered a sharp interface between the core and dry shell while a diffused interface has been considered between dry shell and solvent. The SLD at the interface between shell and solvent is computed using an error function with a characteristic width (thickness of the interface). The solid lines in Fig. 6.9 shows the fitted curve using polydisperse core-shell particles with a graded interface. The polydispersity in the core radius is kept at 0.1 and the variables used in the fit are core radius, dry shell thickness, and the interface thickness. To calculate the volume fraction of the micelles, the degree of solvation in the corona region of micelles is taken as around 50%. The structural parameters of TX-100 micelles in both solvents at different surfactant concentrations obtained

from the model fit are summarized in Table 6.1. The result obtained from model fitting is consistent with results from model-independent IFT analysis.

Table 6.2 SAXS parameters of TX-100 at different surfactant concentrations (% w/w) in GU supercooled melt and in water obtained by model fitting with the core-shell spherical model and 0.1 polydispersity (Schulz) in core radius.

(a) TX-100 in Glucose-Urea supercooled melt:

TX-100 (% w/w)	**Core radius (Å)**	**Dry Shell thickness (Å)**	**Shell interface (Å)**	**SLD_{Shell} [10^{-6} Å^{-2}]**	χ^2
1	25.0 ±0.5	12.1 ±0.2	0.0 ±0.2	12.19 ±0.02	2.8
3	24.2 ±0.2	15.3 ±0.3	0.0 ±0.2	12.31 ±0.02	3.2
5	24.8 ±0.2	17.9 ±0.2	0.0 ±0.1	12.43 ±0.03	6.1
10	24.6 ±0.3	14.3 ±0.2	7.3 ±0.2	12.49 ±0.02	7.4

(b) TX-100 in water:

TX-100 (% w/w)	**Core radius (Å)**	**Dry Shell thickness (Å)**	**Shell interface (Å)**	**SLD_{Shell} [10^{-6} Å^{-2}]**	χ^2
1	15.1 ±0.4	0.0 ±0.1	34.9 ±0.2	10.33 ±0.02	1.1
2	15.3 ±0.2	0.0 ±0.1	34.6 ±0.2	10. 34 ±0.03	1.2
3	15.2 ±0.2	0.0 ±0.1	34.7 ±0.2	10.33 ±0.02	1.4
5	15.3 ±0.2	0.0 ±0.1	32.7 ±0.2	10.33 ±0.03	2.1
10	14.8 ±0.2	2.5 ±0.2	20.8 ±0.2	10.33 ±0.02	3.2
15	14.6 ±0.2	2.7 ±0.2	17.1 ±0.2	10.32 ±0.02	3.8
20	14.5 ±0.2	2.9 ±0.2	16.4 ±0.2	10.29 ±0.02	5.8

To assess the solvent-mediated changes in the scattering contrast and its impact on scattering patterns we first examined the scattering patterns of micelles at different SLDs of solvent. Here the solvent SLD has been varied by the addition of different concentrations of GU mixture. Fig.6.10a shows the variation in the scattering pattern of 5% aqueous TX-100 micelles at different concentrations (% w/w) of GU. To understand the evolution of the scattering pattern upon systematic variation of the solvent electron density, the patterns

were simulated using continuous variation in the SLD of the solvent (Fig.6.10). To simulate the scattering pattern, the core radius, dry shell SLD and shell thickness were kept constant while the SLD of solvent is calculated from the measured densities of the solvent at different GU concentrations in aqueous solution (Fig.6.10a).

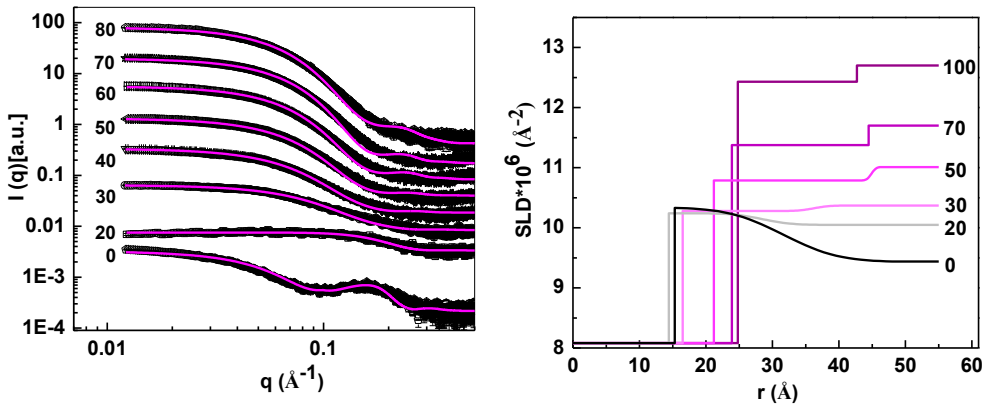

Figure 6.10 *(a) SAXS intensity pattern of 5% TX-100 aqueous micelles at different Glucose-Urea concentration (The solid lines show the simulated model fit). The data are scaled vertically. (b) Its corresponding SLD profile obtained by model fitting.*

Table 6.3 Structural parameters of 5% TX-100 micelles at different concentrations of Glucose-Urea in water, as obtained from fitting the SAXS data with the core-shell spherical model. (The SLD of the core is fixed as: 8.08 X10^{-6} Å^{-2}).

GU (% w/w)	Core Radius (Å)	Dry Shell thickness (Å)	Shell interface (Å)	SLD_{shell} [10^{-6} Å^{-2}]	$SLD_{solv.}$ [10^{-6} Å^{-2}]	χ^2
0	15.3 ±0.2	0.0 ±0.1	32.7 ±0.2	10.33 ±0.03	9.44	2.1
5	14.3 ±0.2	0.0 ±0.2	29.8 ±0.2	10.31 ±0.02	9.58	1.2
10	14.1 ±0.2	3.5 ±0.2	21.9 ±0.2	10.16 ±0.03	9.72	1.1
20	14.5 ±0.3	5.4 ±0.2	17.2 ±0.2	10.24 ±0.02	10.05	1.0
30	16.4 ±0.2	15.1 ±0.2	9.3 ±0.2	10.28 ±0.02	10.37	1.1
40	19.1 ±0.2	21.2 ±0.2	5.1 ±0.2	10.49 ±0.02	10.70	1.1
50	21.2 ±0.1	22.3 ±0.2	2.8 ±0.1	10.79 ±0.02	11.01	1.2
60	22.2 ±0.1	22.5 ±0.2	0.0 ±0.1	11.05 ±0.02	11.35	3.6
70	23.9 ±0.1	20.6 ±0.2	0.0 ±0.1	11.37 ±0.02	11.7	7.4
80	24.4 ±0.3	18.4 ±0.2	0.0 ±0.1	11.53 ±0.02	12.06	8.7
100	24.8 ±0.2	17.9 ±0.2	0.0 ±0.1	12.43 ±0.02	12.7	6.1

The experimental SAXS data were fitted with the above model and the variation in the micellar parameters obtained from the best fit values are summarized in Table 6.3. The solid lines in Fig.6.10a shows the best-fit curves for the SAXS data. The resulting SLD profile of the micelles in solvents with different GU concentration are summarized in Fig. 6.10b. The major inference derived from the SAXS analysis is that the conformation of the hydrophilic head group at the interface region is significantly different in the melt as compared to those found in the presence of water. In aqueous micelles as well as in the presence of GU, the hydrophilic PEO chain is highly solvated and the SLD varies monotonically over a length scale of ~30 Å. However, in the absence of water (i.e in GU melt) the interface thickness decreases drastically by ~12 Å, indicating the collapse of the polyoxyethylene chain at the surface. This is followed by a systematic increase in the radius of the core of the micelles. Such collapse of the ethylene oxide units as compared to that in water has been reported in other non-aqueous solvents such as ethyl ammonium nitrate (EAN). SANS studies using deuterated-PEO in EAN shows that the radius of gyration of the polymer chain in EAN is less than that is observed in water.[255] SAXS studies of micelles formed by Pluronic P123 in EAN shows compact PEO chains at the micelle surface.[256] The stabilization of micelles in GU melt can be attributed to the opposing effects of glucose and urea on PEO chains of micelles.[257,258]

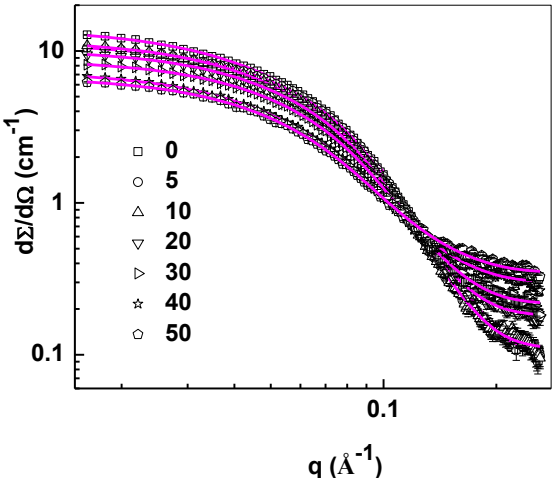

Figure 6.11 *SANS pattern of 5% TX-100 micelles in d-water at different Glucose-Urea concentration (solid lines show model fit).*

Further, the changes in the core radius of the micelles were also inferred from SANS studies (Fig. 6.11). As opposed to SAXS, in the SANS data, the contribution from the shell is marginal. This is due to the poor contrast between the solvated corona and the solvent SLD for SANS. Hence, the SANS data are best fitted using the polydisperse core-shell sphere model with a graded interface. A good agreement has been found between the dimension of the micelles obtained from SAXS and SANS. It may be noted that at high concentrations of GU, the scattering contrast from neutrons is poor and hence SANS experiments could not be performed beyond 50% GU addition. However, the micellar radius obtained from SANS in the concentration range studied here agrees well with SAXS parameters. The detailed model fit parameters obtained from SANS analysis are given in Table 6.4 below. The increase in the core diameter with the addition of GU mixture to aqueous TX-100 micelles can be thought of as a consequence of the changes in the curvature of assemblies due to the conformational reorientation of the EO chains. The effective interfacial area per surfactant decreases with an increase in the concentration of GU, resulting in closer packing of monomers in the aggregate.

Table 6.4 SANS parameters of 5% TX-100 at different concentrations of Glucose-Urea in d-water obtained from the model fitting by using polydisperse core-shell sphere model with the graded interface. The polydispersity (Schulz distribution) in the core radius was kept at 0.1.

Glucose-Urea (% w/w)	Core Radius (Å)	Shell interface (Å)	SLD_{shell} x 10^6 [Å $^{-2}$]	$SLD_{solvent}$ x 10^6 [Å^{-2}]	χ^2
0	16.8 ±0.1	36.6 ±1.2	5.72 ±0.1	6.39	4.1
5	17.1 ±0.3	36.2 ±2.4	5.48 ±0.1	6.28	1.5
10	18.3 ±0.2	35.5 ±2.2	5.34 ±0.3	6.14	4.3
20	18.6 ±0.2	34.4 ±2.1	4.97 ±0.2	5.81	1.8
30	19.2 ±0.2	31.1 ±1.4	4.62 ±0.3	5.53	3.4
40	21.8 ±0.2	28.7 ±2.2	4.35 ±0.1	5.14	4.7
50	25.4 ±0.3	16.5 ±1.6	3.43 ±0.2	4.75	4.9

6.3.4. Arrested Dynamics of Micelles in Supercooled Melt

One of the important implications of having micelles in a supercooled state is its ability to arrest its global motion. Colloids have been employed as model systems to understand glass transition and have shown to undergo dynamical arrest upon approaching the glass transition.[259] Here, a typical example of TX-100 micelles formed in the glucose-urea mixture at different concentrations of water (20% to 95%) are studied using DLS measurements, which indicates arrested diffusion of the micelles in the supercooled state (Fig.6.12).

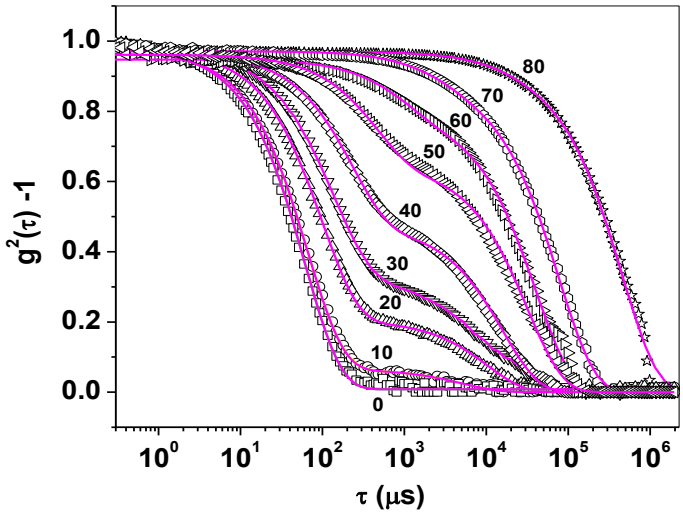

Figure 6.12 *The frozen diffusion of supercooled micelles: Evolution of DLS pattern (intensity correlation function at a scattering angle of 90^0) upon dilution*

of 5% TX-100 micelles formed in the sugar-urea melt at different water concentration (20% to 95%), and the solid lines are fit to a double exponential decay.

To obtain a correlation function in DLS, the presence of water was necessary, presumably due to the poor scattering contrast and frozen dynamics of the micelles in the melt. As compared to micelles formed in 95% water, a six order of magnitude decrease in the diffusion coefficient of the micelles is observed when the micelles are present in 20% water, the rest being glucose, urea, and surfactant. The evolution of the micelles correlation function with a decrease in water concentration is analogous to that observed in colloids under the jammed state.[259,260] In particular, the correlation function changes from a single exponential to a double exponential function as is observed in the case of arrested macromolecules in a crowded environment.[261] The solid lines in Fig. 6.12 represents fit to the data using the equation 2.29 and the corresponding variation in the diffusion coefficient for the TX-100 micelles obtained from the fast mode is depicted in Fig. 6.13a and their corresponding relaxation times are shown in Fig. 6.13b. The bi-exponential nature of colloids in a crowded environment has been reported by various colloidal systems and is often explained in terms of walking confined diffusion.[260] The fast mode (τ_1) corresponds to the diffusion of the micelles within a confined space formed by the clustering of additives around the micelle surface. The slow mode (τ_2) arises from the motion of micelles together with the associated clusters of micelles and additive. What is more interesting is that the diffusion coefficient due to the fast motion of the micelles decreases drastically when the concentration of GU reaches above 50%, indicating immobilization of the micelles in the GU matrix.

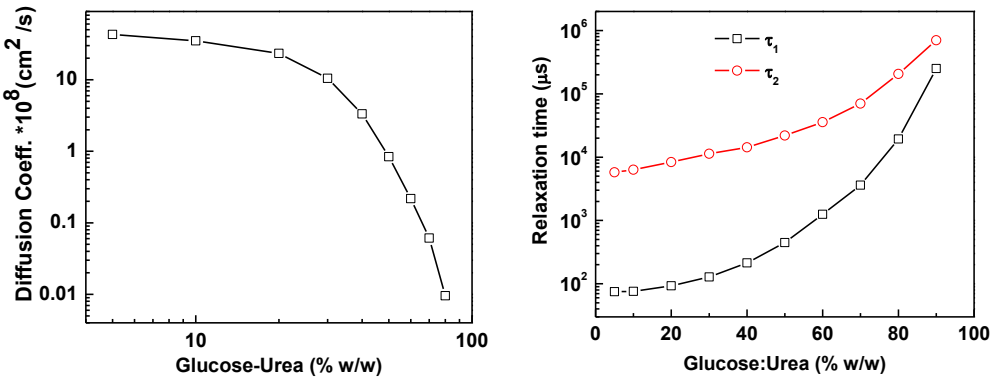

Figure 6.13 *(a) Variation of the diffusion coefficient of 5% TX-100 micelles, as obtained from the fast mode, with Glucose-Urea concentrations (% w/w) in water and (b) Variations in the relaxation times due to fast and slow modes of the intensity autocorrelation function of micelles.*

Thus, micelle formation in a supercooled sugar matrix is found to be a more general case in which a variety of other matrices can be investigated. We found that cationic, anionic and non-ionic surfactants can self-assemble in other sugars and sugar alcohols in the presence of additives like urea, urea-analogs (acetamide, N-methyl urea, etc.) and also small molecular organic acids such as citric acid, malic acid, maleic acid, oxalic acid, and which can remain in a supercooled state at room temperature, leading to dynamically frozen micelles.

We believe that the identification of mixed additives that can supercool and stabilize micelles at temperatures much lower than room temperature will pave way for the design of new formulation strategies. Moreover, the above approach could be extended to develop nanostructured drug delivery systems using primarily biocompatible solid ingredients. To explore such arrested micelles to control diffusion mediated growth of lipid-based drug delivery systems, hydrogenated soya lecithin is solubilized using different types of surfactants such as cationic, anionic and non-ionic. Dissolution of the supercooled matrix in water leads to the spontaneous formation of vesicles or liposomes with controlled surface charge.

6.3.5. Liposome Preparation Using Supercooled Micelles

Usually, various organic solvents were used during the preparation of liposomes, which introduce the chemical toxicity and decrease the biocompatibility of the carrier system. It has been reported that cationic liposomes specifically target angiogenic vessels in tumors and sites of chronic inflammation. In this aspect, attempts were made to prepare surface charge-controlled liposomes formulation by using the supercooled micelles as a precursor to avoid the chemical toxicity associated with most organic solvents. A process/method for the production of liposomes by using supercooled micelles or emulsions comprising sugars, chaotropic agent and lipid/amphiphiles are demonstrated. The matrix is chosen from the category of water-soluble sugar or sugar alcohols and the chaotropic agent is urea or its derivatives, acetamide, glycerol, ethylene glycol, citric acid, ascorbic acid, butanol, etc. or a mixture thereof which are capable of forming hydrogen bonding with sugar.

The liposome with positive surface charge can be made by adding ingredients like long-chain amines, long-chain pyridinium compounds such as cetylpyridinium chloride (CPC), quaternary ammonium compounds such as cetyltrimethylammonium bromide (CTAB), dihexadecyl dimethyl ammonium bromide (DDAB) or mixtures thereof. The preferred ingredients for producing negatively charged liposomes are dioctyl sulphosuccinate sodium salt (AOT), sodium dodecyl sulfate (SDS), sodium deoxycholate (SDC), certain long-chain fatty acids and mixtures thereof. For non-ionic liposomes, non-ionic surfactants like TritonX-100 (TX-100), Tween-80 (TW-80) are used. Optional ingredients like cholesterol can be added to alter the rigidity of the membrane. PEG coating can be introduced by adding ethoxylated surfactants such as Poloxamer or Tween. Also, passive targeting molecules can be included in the vesicles, it can be a polyoxyethylene chain attached to a hydrophobic alkyl chain or a

hydrophobic block of a block copolymer. Such polymers get anchored on liposomes by interdigitations in the bilayer membrane. Preferred amphiphilic targeting molecules are neutral polyoxyethylene sorbitan esters, Pluronic block copolymers, polysorbates, etc. Further, the hydrophobic compound "curcumin" is used as a model hydrophobic drug, owing to its excellent fluorescence intensity, and cellular internalization are studied with different cell lines.

The solubilizations of hydrogenated soya lecithin (Phospholipon 90H) in supercooled micelles were studied using different types of surfactants such as cationic, anionic, and non-ionic. The above lipid can be solubilized in a variety of micelles comprising different surfactants such as SDS, AOT, Tween 80, SDC, DDAB, CPC, and CTAB, forming trapped micelles or microemulsions. In a typical supercooled micelle containing 1% DDAB as a cationic emulsifier, about 6% w/w of phospholipid can be solubilized forming mixed micelles or microemulsions. However, above 6% lipid, SAXS pattern shows characteristic features of emulsions containing solid lipids. Dissolution of this supercooled matrix in water leads to the spontaneous formation of vesicles or liposomes. SAXS data of such melt containing different types of emulsifiers such as SDS, SDC, AOT, CTAB, and TW-80, etc. reveal that structure of the preformed supercooled micelles changes upon dissolution of the matrix leading to liposome formation (Fig. 6.14a). By model fitting the SAXS data using an SLD pattern for multi-lamellar structures as indicated in Fig. 6.14b, the thickness of the bilayer can be estimated. The solid lines in Fig. 6.14a shows the simulated scattering curves and the corresponding bilayer structural parameters are given in Table 6.5.

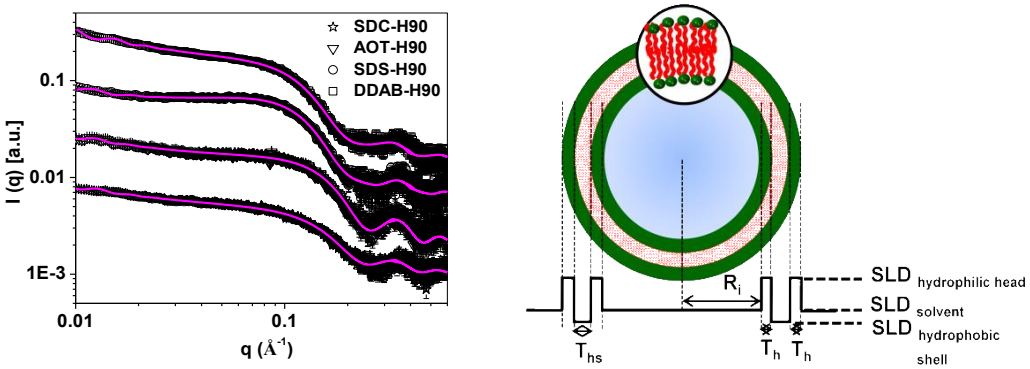

Figure 6.14 *(a) SAXS pattern of liposomes prepared by dissolution of the supercooled micelle in water using different emulsifiers. (b) Schematic of X-ray scattering length density profile of liposome.*

Table 6.5 Structural parameters of liposomes at different types of emulsifiers, as obtained from fitting the SAXS data with sphere core multi-shell model.

Emulsifier	Inner hydrophilic shell thickness(Å)	Hydrophobic shell thickness (Å)	Outer hydrophilic Shell thickness (Å)	SLD of inner hydrophilic shell (10^{-6}Å^{-2})	SLD of hydrophobic shell (10^{-6}Å^{-2})	SLD of outer hydrophilic shell (10^{-6} Å^{-2})	χ^2
DDAB	8.9 ±0.3	27.1 ±0.3	8.9±0.4	13.6 ±0.2	7.2 ±0.2	9.8 ±0.2	1.2
SDC	5.3± 0.1	27.5 ±0.4	5.5±0.4	13.4±0.3	7.9±0.1	11.1±0.2	1.1
SDS	5.6 ±0.2	27.8 ±0.3	5.3±0.4	13.9 ±0.1	7.8 ±0.2	11.4 ±0.2	1.3
AOT	5.3± 0.1	27.1 ±0.4	5.4±0.4	15.0±0.3	7.1±0.1	13.0±0.2	1.1

Further, Cryo-TEM studies reveal the formation of vesicular structures with an average size ~200 nm (Figure 6.15).

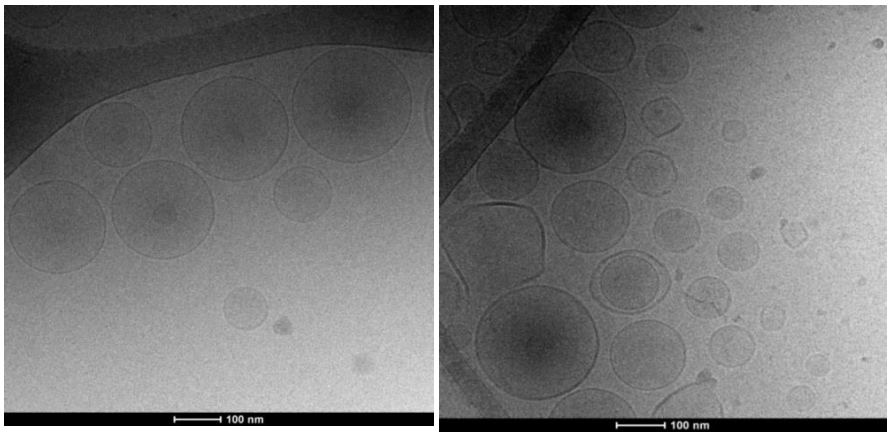

Figure 6.15 *Typical Cryo-TEM images of the liposomes indicating spherical uni-lamellar structure, with less than 200 nm size.*

Further, to investigate the colloidal stability of these liposomal formulations the zeta-potential and DLS experiments were carried out. The size distribution and the zeta-potential of these liposomes are determined immediately after preparation and after 3 months to estimate the colloidal stability. For optimized formulations, no significant change in the particle size was observed confirming colloidal stability. The surface charge was successfully controlled by using different types of emulsifiers from positive, negative or neutral (Fig. 6.16). It was observed that liposome surface charge provides good colloidal stability to the liposomal formulations, either through electrostatic or steric means. From the DLS measurements it was observed that all liposomal formulations have an average hydrodynamic size less than 200 nm with narrow size distributions (see Fig. 6.17).

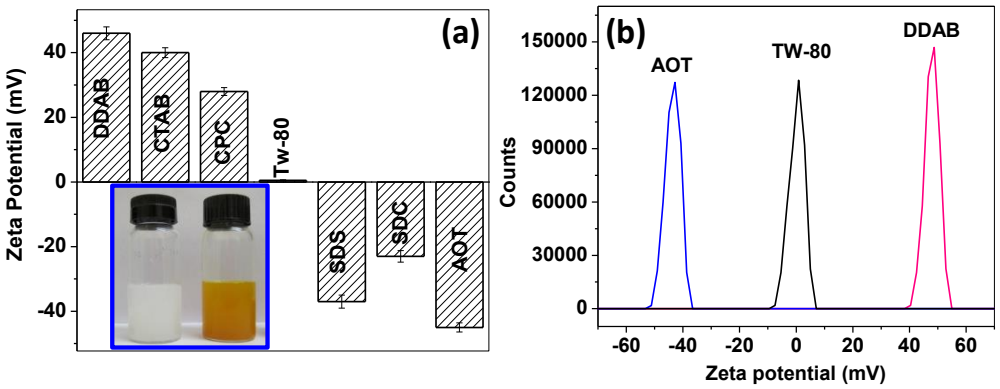

Figure 6.16 *(a) Zeta potential of the liposomes formed by phospholipon 90H using different emulsifiers (inset shows the photographs of stable liposomal and drug-loaded liposomal formulations) and (b) Typical zeta-potential distribution plots of liposomes containing AOT, Tween-80 (TW-80) and DDAB indicating surface charge changes.*

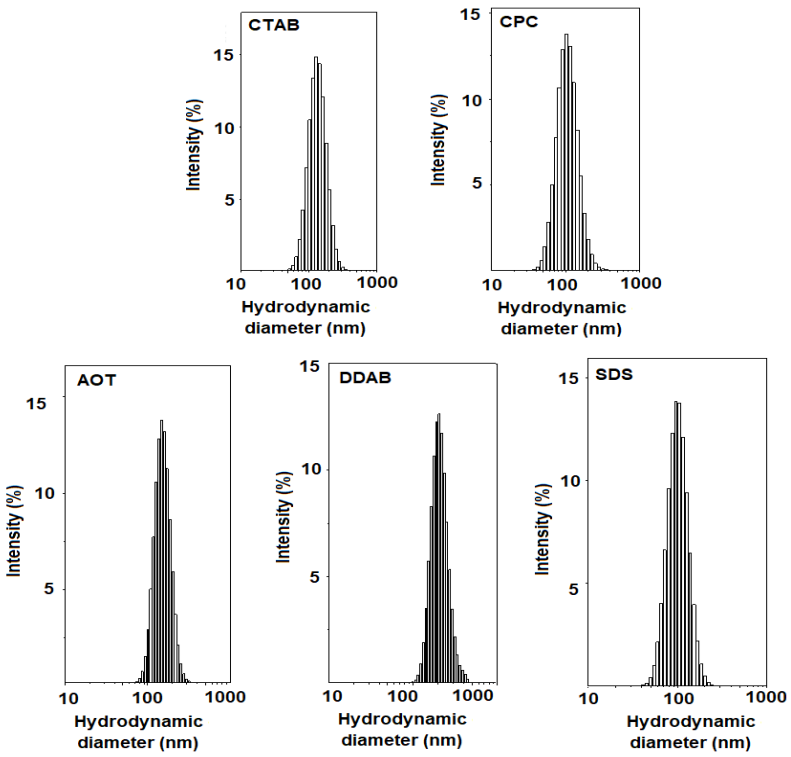

Figure 6.17 *Particle size distribution of liposomes formed by Phospholipon 90 H using different emulsifiers*.

Further, to investigate the suitability of this method for drug encapsulation, curcumin is employed as a model hydrophobic compound. For this, curcumin is mixed along with other ingredients during supercooled matrix formation in the initial stage of liposome preparation and hence it can be incorporated in the liposome through passive encapsulation. It was observed that up to 50 mg of curcumin can be loaded per gram of lipid, leading to liposomes having aqueous colloidal stability for more than six months. It may be noted that these liposomes with and without curcumin encapsulation can be diluted to any extent without any phase separation or leaching out of active ingredients. From the cell culture experiments, it was observed that there is a decrease in the viability of the cells when the cells were treated with increasing concentrations of curcumin loaded liposome. The drug-loaded liposomal formulation show increased cytotoxicity towards MCF-7 and CHO cell line compared to that of

pure curcumin (see Fig. 6.18). Also from cellular internalization study, it was seen that curcumin loaded cationic liposomal formulations shows almost 10 times enhancement in the uptake of curcumin in MCF-7 cell lines compare to pure curcumin (see Fig.6.19), and serve as good drug delivery carrier.

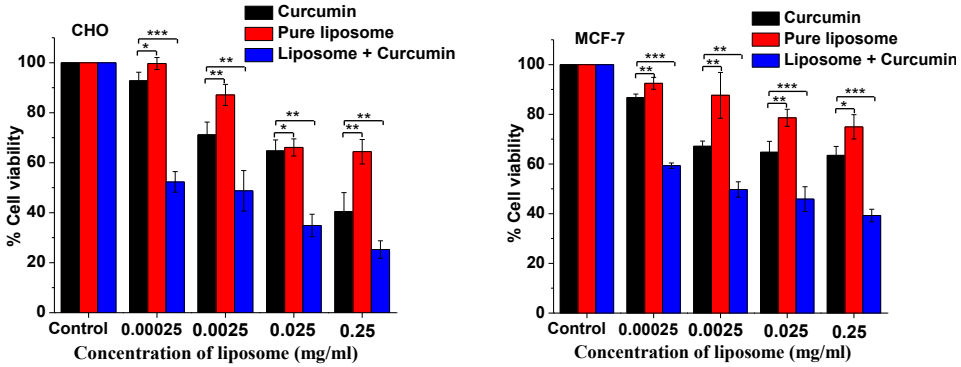

Figure 6.18 *Cell viability results in CHO and MCF-7 cell lines after 48 h of incubation at culture conditions. (Concentration of curcumin in 0.25mg/ml of liposome is 680 µM). (data represent the mean ± SD (n = 3), the statistically significant values were obtained using t-test by comparing viability of cancer cells with treatment of pure liposome and curcumin loaded liposome with respect to curcumin, * $p < 0.1$, ** $p < 0.01$, *** $p < 0.001$).*

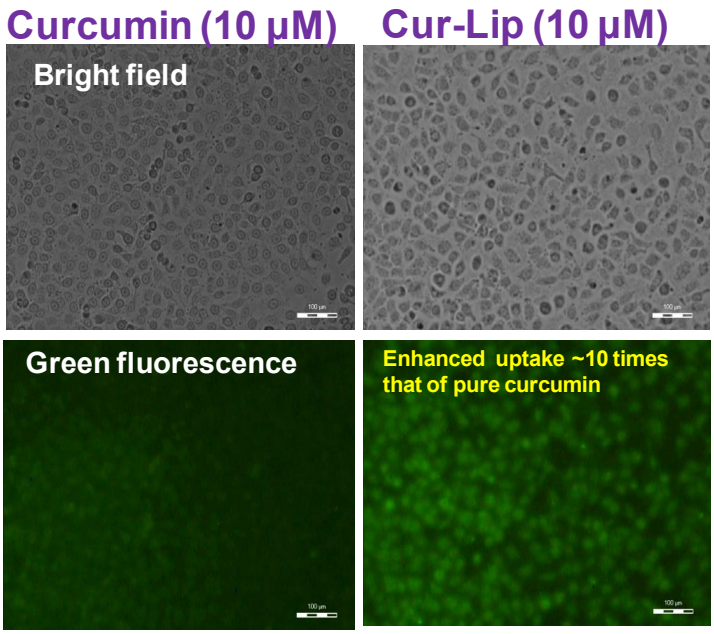

Figure 6.19 *Fluorescence microscopy images of MCF-7 cell lines after incubation with pure curcumin and curcumin loaded liposomes for 3 h under culture conditions.*

This offers a novel way of creating liposomes with tunable surface charge and high drug loading capacity using supercooled micelles and microemulsions as a precursor. The above approach does not involve any organic solvents or other energy-intensive size reduction procedures such as sonication or extrusion. These liposomal formulations have good biocompatibility and a strong ability for intracellular drug delivery and serve as a good drug delivery carrier.

6.4. Conclusion

A water-free supercooled micellar system is developed using the sugar-urea matrix and used as precursors to produce liposomes of narrow size distribution with a controlled surface charge without using toxic and flammable organic solvents. Room temperature supercooled solvents comprising sugars and other additives have been explored for the first time as a solvent for micellization. Micelle and microemulsion formation in such a matrix has been confirmed using SAXS, SANS, and HR-TEM. Further, this matrix is used in the production of liposomes, as a drug delivery system. This has the advantage of enhanced safety of the formulations for human use as well as in plant scale production, as no volatile solvents are involved. Also, the liposomal formulations prepared by this route have a good capability of incorporating active pharmaceutical agents. This offers a scalable method for the productions of liposomes through a spontaneous dissolution of supercooled micelles or emulsions in water or buffer. Further, this method does not require any additional steps of size processing such as extrusion processing, ultra-sonication, and high-pressure homogenization.

CHAPTER 7

SUMMARY AND FUTURE PERSPECTIVES

Summary

In summary, this thesis discussed a few novel surface functionalization strategies that can be adopted for commercial implementation of magnetic nanoparticles in cancer therapy. Also, a new methodology for the production of surface charge tuned organic nanocarriers were developed for effective drug encapsulation and delivery.

The effects of different biocompatible ingredients such as sugar alcohols and ascorbic acid as surface passivation agents for Fe_3O_4 MNPs were investigated. The effects of these coating materials on particle size, surface potential and colloidal stability were successfully investigated. For that Fe_3O_4 MNPs were synthesized through co-precipitation of Fe^{+2} and Fe^{3+} ions in basic medium followed by in-situ coating. XRD and TEM analysis revealed the formation of a highly crystalline spinel nanostructure of Fe_3O_4 MNPs with an average crystallite size of 10 nm. The surface passivation of these MNPs was evident from FTIR spectra, TGA, and zeta-potential measurements. Light scattering measurements indicate that such approaches provide nano-formulations with good colloidal stability and pH-dependent charge reversal behavior. This offers an efficient route for electrostatic binding of drugs like doxorubicin hydrochloride and protein resistant characteristics in the physiological medium. The loading efficiency of the drug as well as their pH-triggered release is strongly dependent on the drug to particle ratio and the coating agent. These functionalized MNPs showed a high loading affinity for DOX and their pH-dependent sustained release, which makes them suitable for drug delivery. In addition, the functionalized exterior of these MNPs having free hydroxyl groups can provide the available sites for conjugation of various bioactive molecules for a variety of

biomedical applications.

Further, covalent immobilization of anticancer drug DOX to Fe_3O_4 MNPs were carried out using pH-labile linkages for sustained delivery of anticancer drug DOX to the tumor cells with minimal side effects. The covalent conjugation DOX through carbamate and hydrazone linkage resulted in a slow and sustained drug release profile at different environmental conditions. The drug-loaded nanocarriers exhibit sustained pH-triggered release of drug molecules at mildly acidic environment of tumor, due to the faster hydrolysis of carbamate and hydrazone linkage and substantial cellular internalization with significant toxicity towards the proliferation of mouse skin fibrosarcoma (WEHI-164) cells, human breast cancer (MCF-7), and human lung cancer (A549) cells. Moreover, it showed significantly lower toxicity in human normal lung (WI26VA) cells, which is essential for cancer therapy. Specifically, the developed drug-nanocarrier conjugate would minimize the amounts of drug leaching out in the blood (pH 7.4) and enable intracellular drug release upon internalized by the target cells (pH 5). The covalent conjugation and pH-triggered drug release make the nanocarriers more specific towards the targeting site and minimize premature drug release from carriers at the physiological conditions.

The application of surface-functionalized Fe_3O_4 MNPs in magnetic hyperthermia has also been investigated. The magnetic studies demonstrated that the presence of the coating layer reduces the magnetic saturation of the MNPs. Nevertheless, this passivation does not change the superparamagnetic nature of the Fe_3O_4 nanoparticles, as shown by the absence of coercivity and remanence magnetization at 300 K. These MNPs shows the very high magnetic response for external magnetic field and shows self-heating ability under AC magnetic field. The

effects of surface modification on the heating efficacy of these MNPs are monitored by time-dependent induction heating studies under the AC magnetic field. These studies revealed that the heating efficacy and specific absorption rate (SAR) of these MNPs strongly dependent on the concentration of particles and stabilizing matrix. Further, serum proteins such as BSA can be used as a coating material for MNPs with enhanced heating efficacy.

An organic solvent-free process for the preparation of surface charge controlled liposomes were developed using supercooled micelles and emulsions. Room temperature supercooled solvents comprising sugars and other additives have been explored for the first time as a solvent for micellization. Hydrogenated soya lecithin is solubilized using cationic, anionic and non-ionic surfactants as emulsifiers. Dissolution of the supercooled micelle and emulsion in water leads to the spontaneous formation of liposomes with controlled surface charge. To investigate the suitability of this method for drug encapsulation, curcumin is employed as a model hydrophobic compound. Curcumin loaded formulations show 10 fold enhanced cellular uptake in cancer cells, as compared to that of pure curcumin. Thus, the liposomal formulations prepared by this route have a good capability of incorporating active pharmaceutical agents. This offers a scalable method for the productions of liposomes through the spontaneous dissolution of supercooled micelles or emulsions in water or buffer.

Future Perspectives

Inspired by the extensive research on nano-drug delivery systems and its application in cancer therapy, very few have reached commercial deployment. This is primarily due to the lack of specificity of the carrier to the tumor cells. Therefore, it is necessary to put more efforts to develop new modalities that will specifically target

the site of action. Photodynamic/thermal therapy using efficient photosensitizers with target specific receptors or immunotherapy agents are some of the new modalities that are not yet explored. Among the immunotherapy options, a MUC1 glycoprotein is an attractive option for cancer therapy. MUC1 is often found overexpressed in tumor cells from various cancer types. Since its discovery MUC1 has been an attractive target for antitumor immunotherapy. Recent studies indicate the possibility of new T-cell vaccine strategies capable of inducing MUC1-specific cytotoxicity in tumor cells. Another key research area includes the separation of circulating tumor cells (CTC) from cancer patients and offers a personalized medicine platform. Despite their potential role in cancer healthcare, CTC methods are still at its infancy due to the difficulties caused by CTC heterogeneity, unavailability of unique CTC separation methods from the blood, and a lack of thorough clinical validation. Therefore, it is necessary to pursue extensive research on standardization and clinical application of various CTC technologies for cancer diagnosis and therapy. Dual-modality drug delivery-contrast agent systems that can track and treat cancer will emerge as a new modality for advanced health care. One such strategy will be to employ existing imaging techniques such as MRI or ultrasound to track the delivery system and release the cargo upon an external stimulus such as ultrasound. This area is also not yet fully explored. Ultrasound mediated delivery of drugs in a precisely controlled manner could pave the way for effective chemotherapy in a clinical environment. Another approach is to use functionalized particles with proteins or peptides that can translocate across the plasma membrane and intracellularly deliver the payload. Often a peptide residue that contains domains of less than 20 amino acids, mostly basic, termed as cell-penetrating peptides (CPPs) are used to target tumor cells. CPPs have been recognized as a promising strategy as they possess the ability to translocate

across the cell membrane. Different therapeutic moieties that are mostly hydrophilic in nature and/or are of high molecular weight can be tagged to CPPs and transported across the cell membrane.

Production of organic nanoparticles using biocompatible ingredients such as cholesterol or lipoproteins with controlled size distribution and a surface charge is still a challenge. Room temperature supercooled solvents have been identified as a new solvent matrix for self-assembly of amphiphiles. These matrices have the ability to arrest the motion of preformed nuclei during nanoparticle synthesis. Thus, the application of supercooled solvent for the production of organic as well as inorganic particles will emerge as a new area for research in nanotherapeutics.

.

References

1. Mirza, A. Z. & Siddiqui, F. A. Nanomedicine and drug delivery: a mini review. *Int. Nano Lett.* **4**, 94 (2014).
2. Verweij, J., Hendriks, H. R. & Zwierzina, H. Innovation in oncology clinical trial design. *Cancer Treat. Rev.* **74**, 15–20 (2019).
3. Hossen, S. *et al.* Smart nanocarrier-based drug delivery systems for cancer therapy and toxicity studies: A review. *J. Adv. Res.* **15**, 1–18 (2019).
4. Kohane, D. S. & Langer, R. Biocompatibility and drug delivery systems. *Chem. Sci.* **1**, 441–446 (2010).
5. Moore, T. L. *et al.* Nanoparticle colloidal stability in cell culture media and impact on cellular interactions. *Chem. Soc. Rev.* **44**, 6287–6305 (2015).
6. Jiang, X. *et al.* Quantitative analysis of the protein corona on FePt nanoparticles formed by transferrin binding. *J. R. Soc. Interface* **7 Suppl 1**, S5–S13 (2010).
7. Shen, S., Wu, Y., Liu, Y. & Wu, D. High drug-loading nanomedicines: progress, current status, and prospects. *Int. J. Nanomedicine* **12**, 4085–4109 (2017).
8. Din, F. U. *et al.* Effective use of nanocarriers as drug delivery systems for the treatment of selected tumors. *Int. J. Nanomedicine* **12**, 7291–7309 (2017).
9. Langer, R. New methods of drug delivery. *Science (80-.).* **249**, 1527 LP – 1533 (1990).
10. Au, J. L.-S., Jang, S. H. & Wientjes, M. G. Clinical aspects of drug delivery to tumors. *J. Control. Release* **78**, 81–95 (2002).
11. Allen, T. M. & Cullis, P. R. Drug delivery systems: entering the mainstream. *Science* **303**, 1818–1822 (2004).

12. McDonald, D. M. & Baluk, P. Significance of blood vessel leakiness in cancer. *Cancer research* **62**, 5381–5385 (2002).

13. Matsumura, Y. & Maeda, H. A new concept for macromolecular therapeutics in cancer chemotherapy: mechanism of tumoritropic accumulation of proteins and the antitumor agent smancs. *Cancer Res.* **46**, 6387–6392 (1986).

14. Maeda, H. The enhanced permeability and retention (EPR) effect in tumor vasculature: the key role of tumor-selective macromolecular drug targeting. *Adv. Enzyme Regul.* **41**, 189–207 (2001).

15. Moore, R. G. & Maclaughlan, S. Current clinical use of biomarkers for epithelial ovarian cancer. *Curr. Opin. Oncol.* **22**, 492–497 (2010).

16. Haubner, R. *et al.* Glycosylated RGD-containing peptides: tracer for tumor targeting and angiogenesis imaging with improved biokinetics. *J. Nucl. Med.* **42**, 326–336 (2001).

17. Owens, D. E. 3rd & Peppas, N. A. Opsonization, biodistribution, and pharmacokinetics of polymeric nanoparticles. *Int. J. Pharm.* **307**, 93–102 (2006).

18. Voycheck, C. L. and Tan, J. S. Ion-Containing Polymers and Their Biological Interactions. in *Polyelectrolytes: Science and Technology* (ed. Hara, M.) 299–388 (CRC Press, USA, 1992).

19. Yoo, J.-W. & Mitragotri, E. C. and S. Factors that Control the Circulation Time of Nanoparticles in Blood: Challenges, Solutions and Future Prospects. *Current Pharmaceutical Design* **16**, 2298–2307 (2010).

20. D'Amico, A. V. US Food and Drug Administration approval of drugs for the treatment of prostate cancer: a new era has begun. *Journal of clinical oncology : official journal of the American Society of Clinical Oncology* **32**,

362–364 (2014).

21. Knop, K., Hoogenboom, R., Fischer, D. & Schubert, U. S. Poly(ethylene glycol) in drug delivery: pros and cons as well as potential alternatives. *Angew. Chem. Int. Ed. Engl.* **49**, 6288–6308 (2010).

22. Hao, G., Xu, Z. P. & Li, L. Manipulating extracellular tumour pH: an effective target for cancer therapy. *RSC Adv.* **8**, 22182–22192 (2018).

23. Alvarez-Lorenzo, C. & Concheiro, A. Smart drug delivery systems: from fundamentals to the clinic. *Chem. Commun.* **50**, 7743–7765 (2014).

24. Park, H. *et al.* Multifunctional nanoparticles for combined doxorubicin and photothermal treatments. *ACS Nano* **3**, 2919–2926 (2009).

25. Zhao, Y.-Z., Du, L.-N., Lu, C.-T., Jin, Y.-G. & Ge, S.-P. Potential and problems in ultrasound-responsive drug delivery systems. *Int. J. Nanomedicine* **8**, 1621–1633 (2013).

26. Giner-Casares, J. J., Henriksen-Lacey, M., Coronado-Puchau, M. & Liz-Marzán, L. M. Research. *Mater. Today* **19**, 19–28 (2016).

27. Edwards, P. P. & Thomas, J. M. Gold in a metallic divided state--from Faraday to present-day nanoscience. *Angew. Chem. Int. Ed. Engl.* **46**, 5480–5486 (2007).

28. Kong, F.-Y. *et al.* Unique Roles of Gold Nanoparticles in Drug Delivery, Targeting and Imaging Applications. *Molecules* **22**, (2017).

29. Prusty, K. & Swain, S. K. Nano silver decorated polyacrylamide/dextran nanohydrogels hybrid composites for drug delivery applications. *Mater. Sci. Eng. C. Mater. Biol. Appl.* **85**, 130–141 (2018).

30. Dhar, S., Reddy, E. M., Shiras, A., Pokharkar, V. & Prasad, B. L. V. Natural gum reduced/stabilized gold nanoparticles for drug delivery formulations.

Chemistry **14**, 10244–10250 (2008).

31. McNamara, K. & Tofail, S. A. M. 10 - Biomedical applications of nanoalloys. in (ed. Calvo, F. B. T.-N.) 345–371 (Elsevier, 2013). doi:https://doi.org/10.1016/B978-0-12-394401-6.00010-2

32. Sabale, S. *et al.* Superparamagnetic MFe2O 4 (M = Ni, Co, Zn, Mn) nanoparticles: synthesis, characterization, induction heating and cell viability studies for cancer hyperthermia applications. *J. Mater. Sci. Mater. Med.* **26**, 127 (2015).

33. Renu, G., Rani, V. V. D., Nair, S. V, Subramanian, K. R. V & Lakshmanan, V.-K. Development of Cerium Oxide Nanoparticles and Its Cytotoxicity in Prostate Cancer Cells. *Advanced Science Letters* **6**, 17–25

34. Bavnhøj, C. G., Knopp, M. M., Madsen, C. M. & Löbmann, K. The role interplay between mesoporous silica pore volume and surface area and their effect on drug loading capacity. *Int. J. Pharm. X* **1**, 100008 (2019).

35. Andersson, J., Rosenholm, J., Areva, S. & Lindén, M. Influences of Material Characteristics on Ibuprofen Drug Loading and Release Profiles from Ordered Micro- and Mesoporous Silica Matrices. *Chem. Mater.* **16**, 4160–4167 (2004).

36. Huang, I.-P. *et al.* Enhanced chemotherapy of cancer using pH-sensitive mesoporous silica nanoparticles to antagonize P-glycoprotein-mediated drug resistance. *Mol. Cancer Ther.* **10**, 761–769 (2011).

37. Barick, K. C., Nigam, S. & Bahadur, D. Nanoscale assembly of mesoporous ZnO: A potential drug carrier. *J. Mater. Chem.* **20**, 6446–6452 (2010).

38. Yuan, Q., Hein, S. & Misra, R. D. K. New generation of chitosan-encapsulated ZnO quantum dots loaded with drug: synthesis, characterization and in vitro drug delivery response. *Acta Biomater.* **6**, 2732–2739 (2010).

39. Tripathy, N., Ahmad, R., Ko, H. A., Khang, G. & Hahn, Y.-B. Enhanced anticancer potency using an acid-responsive ZnO-incorporated liposomal drug-delivery system. *Nanoscale* **7**, 4088–4096 (2015).

40. Desai, D. *et al.* Lipid Bilayer-Gated Mesoporous Silica Nanocarriers for Tumor-Targeted Delivery of Zoledronic Acid in Vivo. *Mol. Pharm.* **14**, 3218–3227 (2017).

41. Han, N. *et al.* Hybrid Lipid-Capped Mesoporous Silica for Stimuli-Responsive Drug Release and Overcoming Multidrug Resistance. *ACS Appl. Mater. Interfaces* **7**, 3342–3351 (2015).

42. Vivero-Escoto, J. L., Slowing, I. I., Wu, C.-W. & Lin, V. S.-Y. Photoinduced Intracellular Controlled Release Drug Delivery in Human Cells by Gold-Capped Mesoporous Silica Nanosphere. *J. Am. Chem. Soc.* **131**, 3462–3463 (2009).

43. Bikram, M., Gobin, A. M., Whitmire, R. E. & West, J. L. Temperature-sensitive hydrogels with SiO2-Au nanoshells for controlled drug delivery. *J. Control. Release* **123**, 219–227 (2007).

44. Chen, F.-H., Zhang, L.-M., Chen, Q.-T., Zhang, Y. & Zhang, Z.-J. Synthesis of a novel magnetic drug delivery system composed of doxorubicin-conjugated Fe3O4 nanoparticle cores and a PEG-functionalized porous silica shell. *Chem. Commun.* **46**, 8633–8635 (2010).

45. Barick, K. C. *et al.* Covalent bridging of surface functionalized Fe3O4 and YPO4:Eu nanostructures for simultaneous imaging and therapy. *Dalt. Trans.* **44**, 14686–14696 (2015).

46. Fang, W., Yang, J., Gong, J. & Zheng, N. Photo- and pH-Triggered Release of Anticancer Drugs from Mesoporous Silica-Coated Pd@Ag Nanoparticles. *Adv.*

Funct. Mater. **22**, 842–848 (2012).

47. Shen, S. *et al.* CMCTS stabilized Fe3O4 particles with extremely low toxicity as highly efficient near-infrared photothermal agents for in vivo tumor ablation. *Nanoscale* **5**, 8056–8066 (2013).

48. Parveen, S. & Sahoo, S. K. Polymeric nanoparticles for cancer therapy. *J. Drug Target.* **16**, 108–123 (2008).

49. Patra, J. K. *et al.* Nano based drug delivery systems: recent developments and future prospects. *J. Nanobiotechnology* **16**, 71 (2018).

50. Hu, Y. *et al.* Synthesis and characterization of chitosan-poly(acrylic acid) nanoparticles. *Biomaterials* **23**, 3193–3201 (2002).

51. Conti, B. *et al.* Microencapsulation of cetylpyridinium chloride with a bioadhesive polymer. *Proc. Control. Release Soc.* **25**, 822–823 (1998).

52. Mitra, S., Gaur, U., Ghosh, P. C. & Maitra, A. N. Tumour targeted delivery of encapsulated dextran-doxorubicin conjugate using chitosan nanoparticles as carrier. *J. Control. Release* **74**, 317–323 (2001).

53. De Campos, A. M., Sanchez, A. & Alonso, M. J. Chitosan nanoparticles: a new vehicle for the improvement of the delivery of drugs to the ocular surface. Application to cyclosporin A. *Int. J. Pharm.* **224**, 159–168 (2001).

54. Anselmo, A. C. & Mitragotri, S. An overview of clinical and commercial impact of drug delivery systems. *J. Control. Release* **190**, 15–28 (2014).

55. Tomoda, K. *et al.* Enhanced transdermal permeability of estradiol using combination of PLGA nanoparticles system and iontophoresis. *Colloids Surf. B. Biointerfaces* **97**, 84–89 (2012).

56. Cheng, F.-Y., Su, C.-H., Wu, P.-C. & Yeh, C.-S. Multifunctional polymeric nanoparticles for combined chemotherapeutic and near-infrared photothermal

cancer therapy in vitro and in vivo. *Chem. Commun. (Camb).* **46**, 3167–3169 (2010).

57. Ruttala, H. B. & Ko, Y. T. Liposomal co-delivery of curcumin and albumin/paclitaxel nanoparticle for enhanced synergistic antitumor efficacy. *Colloids Surf. B. Biointerfaces* **128**, 419–426 (2015).

58. Han, J., Wang, Q., Zhang, Z., Gong, T. & Sun, X. Cationic bovine serum albumin based self-assembled nanoparticles as siRNA delivery vector for treating lung metastatic cancer. *Small* **10**, 524–535 (2014).

59. Son, S. *et al.* Self-crosslinked human serum albumin nanocarriers for systemic delivery of polymerized siRNA to tumors. *Biomaterials* **34**, 9475–9485 (2013).

60. Elzoghby, A. O., Saad, N. I., Helmy, M. W., Samy, W. M. & Elgindy, N. A. Ionically-crosslinked milk protein nanoparticles as flutamide carriers for effective anticancer activity in prostate cancer-bearing rats. *Eur. J. Pharm. Biopharm.* **85**, 444–451 (2013).

61. Van Tomme, S. R., Storm, G. & Hennink, W. E. In situ gelling hydrogels for pharmaceutical and biomedical applications. *Int. J. Pharm.* **355**, 1–18 (2008).

62. Qi, X. *et al.* Fabrication and Characterization of a Novel Anticancer Drug Delivery System: Salecan/Poly(methacrylic acid) Semi-interpenetrating Polymer Network Hydrogel. *ACS Biomater. Sci. Eng.* **1**, 1287–1299 (2015).

63. Ghosh, R., Goswami, U., Ghosh, S. S., Paul, A. & Chattopadhyay, A. Synergistic anticancer activity of fluorescent copper nanoclusters and cisplatin delivered through a hydrogel nanocarrier. *ACS Appl. Mater. Interfaces* **7**, 209–222 (2015).

64. Lombardo, D., Kiselev, M., magazù, S. & Calandra, P. Amphiphiles Self-Assembly: Basic Concepts and Future Perspectives of Supramolecular

Approaches. *Adv. Condens. Matter Phys.* **2015**, 1–22 (2015).

65. Kundu, A., Verma, P. K. & Cho, M. Role of Solvent Water in the Temperature-Induced Self-Assembly of a Triblock Copolymer. *J. Phys. Chem. Lett.* **8**, 3040–3047 (2017).

66. Dierking, I. & Al-Zangana, S. Lyotropic Liquid Crystal Phases from Anisotropic Nanomaterials. *Nanomaterials* **7**, (2017).

67. von Hippel, P. H. The Hydrophobic Effect. Formation of Micelles and Biological Membranes. Charles Tanford. Wiley-Interscience, New York, 1973. viii, 200 pp., illus. $12.50. *Science (80-.).* **184**, 559 LP – 560 (1974).

68. Israelachvili, J. N., Mitchell, D. J. & Ninham, B. W. Theory of self-assembly of hydrocarbon amphiphiles into micelles and bilayers. *J. Chem. Soc. Faraday Trans. 2 Mol. Chem. Phys.* **72**, 1525–1568 (1976).

69. Nagarajan, R. Molecular Packing Parameter and Surfactant Self-Assembly: The Neglected Role of the Surfactant Tail. *Langmuir* **18**, 31–38 (2002).

70. Abdulrahiman Hassan, P. & L. Gawali, S. Directing Amphiphilic Self-Assembly: From Microstructure Control to Interfacial Engineering. *Langmuir* **35**, 9635–9646 (2018).

71. RAY, A. Solvophobic Interactions and Micelle Formation in Structure Forming Nonaqueous Solvents. *Nature* **231**, 313–315 (1971).

72. Talelli, M. *et al.* Core-crosslinked polymeric micelles: Principles, preparation, biomedical applications and clinical translation. *Nano Today* **10**, 93–117 (2015).

73. Ulbrich, K. *et al.* Targeted Drug Delivery with Polymers and Magnetic

Nanoparticles: Covalent and Noncovalent Approaches, Release Control, and Clinical Studies. *Chem. Rev.* **116**, 5338–5431 (2016).

74. Dhand, C. *et al.* Methods and strategies for the synthesis of diverse nanoparticles and their applications: a comprehensive overview. *RSC Adv.* **5**, 105003–105037 (2015).

75. Behari, J. Principles of nanoscience: An overview. *Indian J. Exp. Biol.* **48**, 1008–1019 (2010).

76. Blanco-Andujar, C., Ortega, D., Pankhurst, Q. A. & Thanh, N. T. K. Elucidating the morphological and structural evolution of iron oxide nanoparticles formed by sodium carbonate in aqueous medium. *J. Mater. Chem.* **22**, 12498–12506 (2012).

77. Gonsalves, K. E., Rangarajan, S. P. & Wang, J. Chapter 1 - Chemical synthesis of nanostructured metals, metal alloys, and semiconductors. in (ed. Nalwa, H. S. B. T.-H. of N. M. and N.) 1–56 (Academic Press, 2000). doi:https://doi.org/10.1016/B978-012513760-7/50004-6

78. Massart, R. Preparation of aqueous magnetic liquids in alkaline and acidic media. *IEEE Trans. Magn.* **17**, 1247–1248 (1981).

79. Roca, A. G. *et al.* Design strategies for shape-controlled magnetic iron oxide nanoparticles. *Adv. Drug Deliv. Rev.* **138**, 68–104 (2019).

80. Kang, Y. S., Risbud, S., Rabolt, J. F. & Stroeve, P. Synthesis and Characterization of Nanometer-Size Fe3O4 and γ-Fe2O3 Particles. *Chem. Mater.* **8**, 2209–2211 (1996).

81. Rao, C. N. R., Ramakrishna Matte, H. S. S., Voggu, R. & Govindaraj, A. Recent progress in the synthesis of inorganic nanoparticles. *Dalt. Trans.* **41**, 5089–5120 (2012).

82. Sun, S. & Zeng, H. Size-Controlled Synthesis of Magnetite Nanoparticles. *J. Am. Chem. Soc.* **124**, 8204–8205 (2002).

83. Zeng, H., Li, J., Liu, J. P., Wang, Z. L. & Sun, S. Exchange-coupled nanocomposite magnets by nanoparticle self-assembly. *Nature* **420**, 395–398 (2002).

84. Lattuada, M. & Hatton, T. A. Functionalization of Monodisperse Magnetic Nanoparticles. *Langmuir* **23**, 2158–2168 (2007).

85. Wu, W., He, Q. & Jiang, C. Magnetic iron oxide nanoparticles: synthesis and surface functionalization strategies. *Nanoscale Res. Lett.* **3**, 397–415 (2008).

86. Du, J.-J. *et al.* Facile one-pot hydrothermal synthesis of Pt nanoparticles and their electrocatalytic performance. *Int. J. Hydrogen Energy* **39**, 17634–17637 (2014).

87. Wang, J., Sun, J., Sun, Q. & Chen, Q. One-step hydrothermal process to prepare highly crystalline Fe3O4 nanoparticles with improved magnetic properties. *Mater. Res. Bull.* **38**, 1113–1118 (2003).

88. Qiu, H. *et al.* Novel Fe3O4@ZnO@mSiO2 Nanocarrier for Targeted Drug Delivery and Controllable Release with Microwave Irradiation. *J. Phys. Chem. C* **118**, 14929–14937 (2014).

89. Nanophase materials by a novel microwave-hydrothermal process . *Pure and Applied Chemistry* **74**, 1537 (2002).

90. Burda, C., Chen, X., Narayanan, R. & El-Sayed, M. A. Chemistry and Properties of Nanocrystals of Different Shapes. *Chem. Rev.* **105**, 1025–1102 (2005).

91. Behnajady, M. A., Eskandarloo, H., Modirshahla, N. & Shokri, M. Investigation of the effect of sol–gel synthesis variables on structural and

photocatalytic properties of TiO2 nanoparticles. *Desalination* **278**, 10–17 (2011).

92. Barick, K. C., Aslam, M., Dravid, V. P. & Bahadur, D. Controlled fabrication of oriented co-doped ZnO clustered nanoassemblies. *J. Colloid Interface Sci.* **349**, 19—26 (2010).

93. del Monte, F. *et al.* Formation of γ-Fe2O3 Isolated Nanoparticles in a Silica Matrix. *Langmuir* **13**, 3627–3634 (1997).

94. Suslick, K. S. Sonochemistry. *Science (80-.).* **247**, 1439 LP – 1445 (1990).

95. Okitsu, K., Ashokkumar, M. & Grieser, F. Sonochemical Synthesis of Gold Nanoparticles: Effects of Ultrasound Frequency. *J. Phys. Chem. B* **109**, 20673–20675 (2005).

96. Abu Mukh-Qasem, R. & Gedanken, A. Sonochemical synthesis of stable hydrosol of Fe3O4 nanoparticles. *J. Colloid Interface Sci.* **284**, 489—494 (2005).

97. Saez, V. & Mason, T. Sonoelectrochemical Synthesis of Nanoparticles. *Molecules* **14**, 4284–4299 (2009).

98. Giersig, M. & Mulvaney, P. Preparation of ordered colloid monolayers by electrophoretic deposition. *Langmuir* **9**, 3408–3413 (1993).

99. Ibrahim, A., El-Lat, M. & Selim, M. Effect of Polyethyleneimine Stabilizer on Size and Morphology of Gold Nanoparticles. *Asian J. Appl. Sci.* **9**, 178–184 (2016).

100. Díaz-Núñez, P. *et al.* Effect of Organic Stabilizers on Silver Nanoparticles Fabricated by Femtosecond Pulsed Laser Ablation. *Applied Sciences* **7**, (2017).

101. Sahoo, Y. *et al.* Aqueous Ferrofluid of Magnetite Nanoparticles: Fluorescence Labeling and Magnetophoretic Control. *J. Phys. Chem. B* **109**, 3879–3885

(2005).

102. Dias, A. M. G. C., Hussain, A., Marcos, A. S. & Roque, A. C. A. A biotechnological perspective on the application of iron oxide magnetic colloids modified with polysaccharides. *Biotechnol. Adv.* **29**, 142–155 (2011).

103. Ashtari, P., He, X., Wang, K. & Gong, P. An efficient method for recovery of target ssDNA based on amino-modified silica-coated magnetic nanoparticles. *Talanta* **67**, 548–554 (2005).

104. Yi, D. K. *et al. Silica-Coated Nanocomposites of Magnetic Nanoparticles and Quantum Dots*. *Journal of the American Chemical Society* **127**, (American Chemical Society, 2005).

105. Mandal, M. *et al.* Magnetite nanoparticles with tunable gold or silver shell. *J. Colloid Interface Sci.* **286**, 187–194 (2005).

106. Wu, W., He, Q., Chen, H., Tang, J. & Nie, L. Sonochemical synthesis, structure and magnetic properties of air-stable Fe3O4/Au nanoparticles. *Nanotechnology* **18**, 145609 (2007).

107. Stoeva, S. I., Huo, F., Lee, J.-S. & Mirkin, C. A. Three-Layer Composite Magnetic Nanoparticle Probes for DNA. *J. Am. Chem. Soc.* **127**, 15362–15363 (2005).

108. Hong, R. Y. *et al.* Preparation, characterization and application of Fe3O4/ZnO core/shell magnetic nanoparticles. *Mater. Res. Bull.* **43**, 2457–2468 (2008).

109. Barakat, N. S. Magnetically modulated nanosystems: a unique drug-delivery platform. *Nanomedicine (Lond)*. **4**, 799–812 (2009).

110. Hanini, A. *et al.* Evaluation of iron oxide nanoparticle biocompatibility. *Int. J. Nanomedicine* **6**, 787–794 (2011).

111. Gupta, A. K. & Gupta, M. Synthesis and surface engineering of iron oxide

nanoparticles for biomedical applications. *Biomaterials* **26**, 3995–4021 (2005).

112. Kwei, G. H. *et al.* Structure and valence from complementary anomalous X-ray and neutron powder diffraction. *J. Mol. Struct.* **223**, 383–406 (1990).

113. Cornell, R. M. & Schwertmann, U. *The iron oxides : structure, properties, reactions, occurrence, and uses*. (Weinheim : VCH, 1996).

114. Friák, M., Schindlmayr, A. & Scheffler, M. Ab initiostudy of the half-metal to metal transition in strained magnetite. *New J. Phys.* **9**, 5 (2007).

115. Pirayesh Islamian, J. *et al.* Targeted superparamagnetic nanoparticles coated with 2-deoxy-d-gloucose and doxorubicin more sensitize breast cancer cells to ionizing radiation. *Breast* **33**, 97–103 (2017).

116. Ye, P. *et al.* Fe3O4 nanoparticles and cryoablation enhance ice crystal formation to improve the efficiency of killing breast cancer cells. *Oncotarget* **8**, 11389–11399 (2017).

117. Zhang, Y. *et al.* Cisplatin-loaded polymer/magnetite composite nanoparticles as multifunctional therapeutic nanomedicine. *Chinese J. Polym. Sci.* **32**, 1329–1337 (2014).

118. Ebrahimi, E. *et al.* In vitro study and characterization of doxorubicin-loaded magnetic nanoparticles modified with biodegradable copolymers. *Artif. cells, nanomedicine, Biotechnol.* **44**, 550–558 (2016).

119. Mu, X. *et al.* EGFR-targeted delivery of DOX-loaded Fe(3)O(4)@ polydopamine multifunctional nanocomposites for MRI and antitumor chemo-photothermal therapy. *Int. J. Nanomedicine* **12**, 2899–2911 (2017).

120. Jia, Y. *et al.* Co-encapsulation of magnetic Fe3O4 nanoparticles and doxorubicin into biodegradable PLGA nanocarriers for intratumoral drug delivery. *Int. J. Nanomedicine* **7**, 1697–1708 (2012).

121. Mao, X. *et al.* Daunorubicin Loaded Fe3O4 Nanoparticles Induce Apoptosis of Glioma Cells and Disrupt Tight Junction at Blood-Brain Barrier. *J. Nanosci. Nanotechnol.* **16**, 12356–12361 (2016).

122. GILCHRIST, R. K. *et al.* Selective inductive heating of lymph nodes. *Ann. Surg.* **146**, 596–606 (1957).

123. Johannsen, M. *et al.* Clinical hyperthermia of prostate cancer using magnetic nanoparticles: presentation of a new interstitial technique. *Int. J. Hyperth. Off. J. Eur. Soc. Hyperthermic Oncol. North Am. Hyperth. Gr.* **21**, 637–647 (2005).

124. Rana, S., Jadhav, N. V, Barick, K. C., Pandey, B. N. & Hassan, P. A. Polyaniline shell cross-linked Fe3O4 magnetic nanoparticles for heat activated killing of cancer cells. *Dalton Trans.* **43**, 12263–12271 (2014).

125. Bulte, J. W. M. In vivo MRI cell tracking: clinical studies. *AJR. Am. J. Roentgenol.* **193**, 314–325 (2009).

126. Toth, G. B. *et al.* Current and potential imaging applications of ferumoxytol for magnetic resonance imaging. *Kidney Int.* **92**, 47–66 (2017).

127. Lind, K., Kresse, M., Debus, N. P. & Muller, R. H. A novel formulation for superparamagnetic iron oxide (SPIO) particles enhancing MR lymphography: comparison of physicochemical properties and the in vivo behaviour. *J. Drug Target.* **10**, 221–230 (2002).

128. Schmitz, S. A., Albrecht, T. & Wolf, K. J. MR angiography with superparamagnetic iron oxide: feasibility study. *Radiology* **213**, 603–607 (1999).

129. Di Marco, M. *et al.* Physicochemical characterization of ultrasmall superparamagnetic iron oxide particles (USPIO) for biomedical application as MRI contrast agents. *Int. J. Nanomedicine* **2**, 609–622 (2007).

130. Jun, Y.-W. *et al.* Nanoscale size effect of magnetic nanocrystals and their utilization for cancer diagnosis via magnetic resonance imaging. *J. Am. Chem. Soc.* **127**, 5732–5733 (2005).

131. Matsumura, Y. *et al.* Phase I clinical trial and pharmacokinetic evaluation of NK911, a micelle-encapsulated doxorubicin. *Br. J. Cancer* **91**, 1775–1781 (2004).

132. Kato, K. *et al.* Phase I study of NK105, a paclitaxel-incorporating micellar nanoparticle, in patients with advanced cancer. *J. Clin. Oncol.* **24**, 2018 (2006).

133. Lungu, I. I., Grumezescu, M. A., Volceanov, A. & Andronescu, E. Nanobiomaterials Used in Cancer Therapy: An Up-To-Date Overview. *Molecules* **24**, (2019).

134. Bhattacharjee, J. *et al.* Tween 80−Sodium Deoxycholate Mixed Micelles: Structural Characterization and Application in Doxorubicin Delivery. *J. Phys. Chem. B* **114**, 16414–16421 (2010).

135. Maswal, M. *et al.* Solubilization and co-solubilization of Carbamazepine and Nifedipine in mixed micellar systems: insights from surface tension, electronic absorption, fluorescence and HPLC measurements. *RSC Adv.* **5**, 7697–7712 (2015).

136. Jatinder V. Yakhmi, R. R. Nanotechnological approaches toward cancer chemotherapy. in *Nanostructures for Cancer Therapy* 211–240 (Elsevier, 2017). doi:10.1016/B978-0-323-46144-3.00008-8

137. Bulbake, U., Doppalapudi, S., Kommineni, N. & Khan, W. Liposomal Formulations in Clinical Use: An Updated Review. *Pharmaceutics* **9**, (2017).

138. Franzé, S., Selmin, F., Samaritani, E., Minghetti, P. & Cilurzo, F. Lyophilization of Liposomal Formulations: Still Necessary, Still Challenging.

Pharmaceutics **10**, 139 (2018).

139. Laouini, A., Charcosset, C., Fessi, H., Holdich, R. G. & Vladisavljević, G. T. Preparation of liposomes: a novel application of microengineered membranes - investigation of the process parameters and application to the encapsulation of vitamin E. *RSC Adv.* **3**, 4985 (2013).

140. Tyndall, J. IV. On the blue colour of the sky, the polarization of skylight, and on the polarization of light by cloudy matter generally. *Proc. R. Soc. London* **17**, 223–233 (1869).

141. Strutt, J. W. XXXVI. On the light from the sky, its polarization and colour. *London, Edinburgh, Dublin Philos. Mag. J. Sci.* **41**, 274–279 (1871).

142. Mie, G. Beiträge zur Optik trüber Medien, speziell kolloidaler Metallösungen. *Ann. Phys.* **330**, 377–445 (1908).

143. Rademeyer, P., Carugo, D., Lee, J. Y. & Stride, E. Microfluidic system for high throughput characterisation of echogenic particles. *Lab Chip* **15**, 417–428 (2015).

144. Fan, X., Zheng, W. & Singh, D. J. Light scattering and surface plasmons on small spherical particles. *Light Sci. Appl.* **3**, e179–e179 (2014).

145. Ross, D. J. & Sigel, R. Mie scattering by soft core-shell particles and its applications to ellipsometric light scattering. *Phys. Rev. E* **85**, 56710 (2012).

146. Hong, S.-H. & Winter, J. Size dependence of optical properties and internal structure of plasma grown carbonaceous nanoparticles studied by in situ Rayleigh-Mie scattering ellipsometry. *J. Appl. Phys.* **100**, 64303 (2006).

147. Glatter, O. & Kratky, O. *Small angle x-ray scattering*. (Academic Press, 1982).

148. Brumberger, H. *Modern Aspects of Small-Angle Scattering*. (Springer Netherlands, 1995). doi:10.1007/978-94-015-8457-9

149. *Soft Matter Characterization*. (Springer Netherlands, 2008). doi:10.1007/978-1-4020-4465-6

150. Ballauff, M. Analysis of Polymer Colloids by Small-Angle X-Ray and Neutron Scattering: Contrast Variation. *Adv. Eng. Mater.* **13**, 793–802 (2011).

151. Svergun, D. I. & Koch, M. H. J. Small-angle scattering studies of biological macromolecules in solution. *Reports Prog. Phys.* **66**, 1735–1782 (2003).

152. Franke, D. & Svergun, D. I. DAMMIF, a program for rapid ab-initio shape determination in small-angle scattering. *J. Appl. Crystallogr.* **42**, 342–346 (2009).

153. Debye, P. Zerstreuung von Röntgenstrahlen. *Ann. Phys.* **351**, 809–823 (1915).

154. Glatter, O. *Scattering Methods and their Application in Colloid and Interface Science*. (Elsevier, 2018). doi:10.1016/C2016-0-04640-5

155. Pedersen, J. S. Form factors of block copolymer micelles with spherical, ellipsoidal and cylindrical cores. *J. Appl. Crystallogr.* **33**, 637–640 (2000).

156. SASview documentation.

157. Kotlarchyk, M. & Chen, S. Analysis of small angle neutron scattering spectra from polydisperse interacting colloids. *J. Chem. Phys.* **79**, 2461–2469 (1983).

158. Stein, R. S. & Rowell, R. L. The Scattering of Light and Other Electromagnetic Radiation. Milton Kerker. Academic Press, New York, 1969. xviii + 670 pp., illus. $33.50. *Science (80-.).* **167**, 861 (1970).

159. Cullity, B. D. *Elements of X-ray diffraction*. (Addison-Wesley Publishing Company, 1959).

160. M, von L. Concerning the detection of X-ray interferences. *Nobel Lect.* (1920).

161. Friedrich, W., Knipping, P. & Laue, M. Interferenzerscheinungen bei Röntgenstrahlen. *Ann. Phys.* **346**, 971–988 (1913).

162. Hull, A. W. A NEW METHOD OF CHEMICAL ANALYSIS. *J. Am. Chem. Soc.* **41**, 1168–1175 (1919).

163. Jensen, H. *et al.* Determination of size distributions in nanosized powders by TEM, XRD, and SAXS. *J. Exp. Nanosci.* **1**, 355–373 (2006).

164. Fultz, Brent, Howe, J. M. *Transmission Electron Microscopy and Diffractometry of Materials*. (Springer Berlin Heidelberg, 2008). doi:10.1007/978-3-540-73886-2

165. Rosensweig, R. E. Heating magnetic fluid with alternating magnetic field. *J. Magn. Magn. Mater.* **252**, 370–374 (2002).

166. Sharma, P. *et al.* Biocompatible phosphate anchored Fe3O4 nanocarriers for drug delivery and hyperthermia. *New J. Chem.* **38**, 5500–5508 (2014).

167. Joshi, H. M. *et al.* Effects of shape and size of cobalt ferrite nanostructures on their MRI contrast and thermal activation. *J. Phys. Chem. C. Nanomater. Interfaces* **113**, 17761–17767 (2009).

168. Ghosh, R. *et al.* Induction heating studies of Fe3O4 magnetic nanoparticles capped with oleic acid and polyethylene glycol for hyperthermia. *J. Mater. Chem.* **21**, 13388–13398 (2011).

169. Majeed, J. *et al.* Water-dispersible polyphosphate-grafted Fe3O4 nanomagnets for cancer therapy. *RSC Adv.* **5**, 86754–86762 (2015).

170. Samanta, B. *et al.* Protein-passivated Fe3O4nanoparticles: low toxicity and rapid heating for thermal therapy. *J. Mater. Chem.* **18**, 1204–1208 (2008).

171. Barick, K. C. *et al.* Novel and efficient MR active aqueous colloidal Fe3O4 nanoassemblies. *J. Mater. Chem.* **19**, 7023–7029 (2009).

172. Wagner, M. *Thermal Analysis in Practice*. (Carl Hanser Verlag GmbH & Co. KG, 2017). doi:10.3139/9781569906446

173. Kim, D. K. *et al.* Starch-Coated Superparamagnetic Nanoparticles as MR Contrast Agents. *Chem. Mater.* **15**, 4343–4351 (2003).

174. Culita, D. C. *et al.* Superparamagnetic nanomagnetites modified with histidine and tyrosine. *Mater. Chem. Phys.* **111**, 381–385 (2008).

175. Goloverda, G., Jackson, B., Kidd, C. & Kolesnichenko, V. Synthesis of ultrasmall magnetic iron oxide nanoparticles and study of their colloid and surface chemistry. *J. Magn. Magn. Mater.* **321**, 1372–1376 (2009).

176. Shen, B., Hohmann, S., Jensen, R. G. & Bohnert, a H. Roles of sugar alcohols in osmotic stress adaptation. Replacement of glycerol by mannitol and sorbitol in yeast. *Plant Physiol.* **121**, 45–52 (1999).

177. Mowry, S. & Ogren, P. J. Kinetics of Methylene Blue Reduction by Ascorbic Acid. *J. Chem. Educ.* **76**, 970 (1999).

178. Sies, H. Vitamin C: Its Chemistry and Biochemistry. (Reihe: Royal Society of Chemistry Paperbacks.) Von M. B. Davies, J. Austin und D. A. Partridge. The Royal Society of Chemistry, London, 1991, X, 154 S., Broschur $ 13.50. – ISBN 0-85186-333-7. *Angew. Chemie* **104**, 948 (1992).

179. Frei, B. & Lawson, S. Vitamin C and cancer revisited. *Proc. Natl. Acad. Sci.* **105**, 11037–11038 (2008).

180. Ikeda, M., Bhattacharjee, A. K., Kondoh, T., Nagashima, T. & Tamaki, N. Synergistic effect of cold mannitol and Na(+)/Ca(2+) exchange blocker on blood-brain barrier opening. *Biochem. Biophys. Res. Commun.* **291**, 669–674 (2002).

181. Sreeja, V., Jayaprabha, K. N. & Joy, P. A. Water-dispersible ascorbic-acid-coated magnetite nanoparticles for contrast enhancement in MRI. *Appl. Nanosci.* **5**, 435–441 (2015).

182. Gupta, H., Paul, P., Kumar, N., Baxi, S. & Das, D. P. One pot synthesis of water-dispersible dehydroascorbic acid coated Fe3O4 nanoparticles under atmospheric air: blood cell compatibility and enhanced magnetic resonance imaging. *J. Colloid Interface Sci.* **430**, 221–228 (2014).

183. Agus, D. B. *et al.* Vitamin C crosses the blood-brain barrier in the oxidized form through the glucose transporters. *J. Clin. Invest.* **100**, 2842–2848 (1997).

184. Nigam, S., Barick, K. C. & Bahadur, D. Development of citrate-stabilized Fe3O4 nanoparticles: Conjugation and release of doxorubicin for therapeutic applications. *J. Magn. Magn. Mater.* **323**, 237–243 (2011).

185. Singh, S., Barick, K. & Bahadur, D. Inactivation of bacterial pathogens under magnetic hyperthermia using Fe3O4–ZnO nanocomposite. *Powder Technol.* **269**, 513–519 (2015).

186. Wong, J. E., Gaharwar, A. K., Muller-Schulte, D., Bahadur, D. & Richtering, W. Magnetic nanoparticle-polyelectrolyte interaction: a layered approach for biomedical applications. *J. Nanosci. Nanotechnol.* **8**, 4033–4040 (2008).

187. Lim, J., Yeap, S. P., Che, H. X. & Low, S. C. Characterization of magnetic nanoparticle by dynamic light scattering. *Nanoscale Res. Lett.* **8**, 381 (2013).

188. Burger, A. *et al.* Energy/temperature diagram and compression behavior of the polymorphs of D-mannitol. *J. Pharm. Sci.* **89**, 457–468 (2000).

189. Xiao, L. *et al.* Water-Soluble Superparamagnetic Magnetite Nanoparticles with Biocompatible Coating for Enhanced Magnetic Resonance Imaging. *ACS Nano* **5**, 6315–6324 (2011).

190. Govindaraj, K., Velraj, R. & Iniyan, S. Thermal Analysis of D-mannitol for Use as Phase Change Material for Latent Heat Storage. *J. Appl. Sci.* **11**, 3044–3048 (2011).

191. Birta, N., Doca, N., Vlase, G. & Vlase, T. Kinetic of sorbitol decomposition under non-isothermal conditions. *J. Therm. Anal. Calorim. - J THERM ANAL CALORIM* **92**, 635–638 (2008).

192. Juhász, M., Kitahara, Y., Takahashi, S. & Fujii, T. Thermal stability of vitamin C: Thermogravimetric analysis and use of total ion monitoring chromatograms. *J. Pharm. Biomed. Anal.* **59**, 190–193 (2012).

193. Ding, B., Xia, S., Hayat, K. & Zhang, X. Preparation and pH stability of ferrous glycinate liposomes. *J. Agric. Food Chem.* **57**, 2938–2944 (2009).

194. Chang, Y.-C. & Chen, D.-H. Preparation and adsorption properties of monodisperse chitosan-bound Fe3O4 magnetic nanoparticles for removal of Cu(II) ions. *J. Colloid Interface Sci.* **283**, 446–451 (2005).

195. Stiufiuc, R. *et al.* One-step Synthesis of Pegylated Gold Nanoparticles with Tunable Surface Charge. *J. Nanomater.* **2013**, 88:88--88:88 (2013).

196. Marchetti, P., Mechelhoff, M. & Livingston, A. G. Tunable-Porosity Membranes From Discrete Nanoparticles. *Sci. Rep.* **5**, 17353 (2015).

197. Cao, X., Zhang, B., Zhao, F. & Feng, L. Synthesis and Properties of MPEG-Coated Superparamagnetic Magnetite Nanoparticles. *J. Nanomater.* **2012**, 1–6 (2012).

198. Barick, K. *et al.* pH-Responsive Peptide Mimic Shell Cross-Linked Magnetic Nanocarriers for Combination Therapy. *Adv. Funct. Mater.* **22**, 4975–4984 (2012).

199. Rana, S. *et al.* Folic acid conjugated Fe3O4 magnetic nanoparticles for targeted delivery of doxorubicin. *Dalt. Trans.* **45**, 17401–17408 (2016).

200. Morry, J., Ngamcherdtrakul, W. & Yantasee, W. Oxidative stress in cancer and fibrosis: Opportunity for therapeutic intervention with antioxidant compounds,

enzymes, and nanoparticles. *Redox Biol.* **11**, 240–253 (2017).

201. Galagan, Y. & Su, W.-F. Reversible photoreduction of methylene blue in acrylate media containing benzyl dimethyl ketal. *J. Photochem. Photobiol. A Chem.* **195**, 378–383 (2008).

202. Olugbami, J. O., Gbadegesin, M. A. & Odunola, O. A. In vitro free radical scavenging and antioxidant properties of ethanol extract of Terminalia glaucescens. *Pharmacognosy Res.* **7**, 49–56 (2015).

203. Tannock, I. F. Conventional cancer therapy: promise broken or promise delayed? *Lancet (London, England)* **351 Suppl**, SII9-16 (1998).

204. Shi, J., Kantoff, P. W., Wooster, R. & Farokhzad, O. C. Cancer nanomedicine: progress, challenges and opportunities. *Nat. Rev. Cancer* **17**, 20–37 (2017).

205. Yang, H.-W., Hua, M.-Y., Liu, H.-L., Huang, C.-Y. & Wei, K.-C. Potential of magnetic nanoparticles for targeted drug delivery. *Nanotechnol. Sci. Appl.* **5**, 73–86 (2012).

206. Zhu, Y.-J. & Chen, F. pH-responsive drug-delivery systems. *Chem. Asian J.* **10**, 284–305 (2015).

207. Sawant, R. M. *et al.* 'SMART' drug delivery systems: double-targeted pH-responsive pharmaceutical nanocarriers. *Bioconjug. Chem.* **17**, 943–949 (2006).

208. Aryal, S., Hu, C.-M. J. & Zhang, L. Polymer−Cisplatin Conjugate Nanoparticles for Acid-Responsive Drug Delivery. *ACS Nano* **4**, 251–258 (2010).

209. Zhang, Y. *et al.* Co-delivery of doxorubicin and curcumin by pH-sensitive prodrug nanoparticle for combination therapy of cancer. *Sci. Rep.* **6**, 21225 (2016).

210. Liu, Y., Wang, W., Yang, J., Zhou, C. & Sun, J. pH-sensitive polymeric

micelles triggered drug release for extracellular and intracellular drug targeting delivery. *Asian J. Pharm. Sci.* **8**, 159–167 (2013).

211. Rollas, S. & Küçükgüzel, Ş. G. Hydrazone, Amide, Carbamate, Macromolecular and Other Prodrugs of Doxorubicin. *Open Drug Deliv. J.* **2**, 77–85 (2008).

212. Hu, X., Liu, S., Huang, Y., Chen, X. & Jing, X. Biodegradable Block Copolymer-Doxorubicin Conjugates via Different Linkages: Preparation, Characterization, and In Vitro Evaluation. *Biomacromolecules* **11**, 2094–2102 (2010).

213. Aydin, D., Arslan, M., Sanyal, A. & Sanyal, R. Hooked on Cryogels: A Carbamate Linker Based Depot for Slow Drug Release. *Bioconjug. Chem.* **28**, 1443–1451 (2017).

214. Prabaharan, M., Grailer, J. J., Pilla, S., Steeber, D. A. & Gong, S. Amphiphilic multi-arm-block copolymer conjugated with doxorubicin via pH-sensitive hydrazone bond for tumor-targeted drug delivery. *Biomaterials* **30**, 5757–5766 (2009).

215. Gillies, E. R. & Frechet, J. M. J. pH-Responsive copolymer assemblies for controlled release of doxorubicin. *Bioconjug. Chem.* **16**, 361–368 (2005).

216. Zhao, H. & Yung, L. Y. L. Selectivity of folate conjugated polymer micelles against different tumor cells. *Int. J. Pharm.* **349**, 256–268 (2008).

217. Ortega, D. & Pankhurst, Q. A. Magnetic hyperthermia. in *Nanoscience: Volume 1: Nanostructures through Chemistry* **1**, 60–88 (The Royal Society of Chemistry, 2013).

218. Ivkov, R. Magnetic nanoparticle hyperthermia: a new frontier in biology and medicine? *International journal of hyperthermia : the official journal of*

European Society for Hyperthermic Oncology, North American Hyperthermia Group **29**, 703–705 (2013).

219. Muela, A. *et al.* Optimal Parameters for Hyperthermia Treatment Using Biomineralized Magnetite Nanoparticles: Theoretical and Experimental Approach. *J. Phys. Chem. C* **120**, 24437–24448 (2016).

220. Sasikala, A. R. K. *et al.* A smart magnetic nanoplatform for synergistic anticancer therapy: manoeuvring mussel-inspired functional magnetic nanoparticles for pH responsive anticancer drug delivery and hyperthermia. *Nanoscale* **7**, 18119–18128 (2015).

221. Carrey, J., Mehdaoui, B. & Respaud, M. Publisher's Note: "Simple models for dynamic hysteresis loop calculations of magnetic single-domain nanoparticles: Application to magnetic hyperthermia optimization" [J. Appl. Phys. 109, 083921 (2011)]. *J. Appl. Phys.* **109**, 83921 (2011).

222. Mahmoudi, M., Sant, S., Wang, B., Laurent, S. & Sen, T. Superparamagnetic iron oxide nanoparticles (SPIONs): development, surface modification and applications in chemotherapy. *Adv. Drug Deliv. Rev.* **63**, 24–46 (2011).

223. Goya, G. F. *et al.* Magnetic Hyperthermia With Fe$_{3}$O$_{4}$ Nanoparticles: The Influence of Particle Size on Energy Absorption. *IEEE Trans. Magn.* **44**, 4444–4447 (2008).

224. Ma, M. *et al.* Size dependence of specific power absorption of Fe3O4 particles in AC magnetic field. *J. Magn. Magn. Mater.* **268**, 33–39 (2004).

225. Mahadevan, S., Gnanaprakash, G., Philip, J., Rao, B. P. C. & Jayakumar, T. X-ray diffraction-based characterization of magnetite nanoparticles in presence of goethite and correlation with magnetic properties. *Phys. E Low-dimensional Syst. Nanostructures* **39**, 20–25 (2007).

226. Waldron, R. D. Infrared Spectra of Ferrites. *Phys. Rev.* **99**, 1727–1735 (1955).

227. Cheraghipour, E., Javadpour, S. & Mehdizadeh, A. Citrate capped superparamagnetic iron oxide nanoparticles used for hyperthermia therapy. *J. Biomed. Sci. Eng.* **05**, 715–719 (2012).

228. Adamiano, A., Lesci, I. G., Fabbri, D. & Roveri, N. Adsorption of bovine serum albumin onto synthetic Fe-doped geomimetic chrysotile. *J. R. Soc. Interface* **12**, 20150186 (2015).

229. Danafar, H., Manjili, H. K. & Najafi, M. Study of Copolymer Composition on Drug Loading Efficiency of Enalapril in Polymersomes and Cytotoxicity of Drug Loaded Nanoparticles. *Drug Res. (Stuttg).* **66**, 495–504 (2016).

230. Andalib, S., Molhemazar, P. & Danafar, H. In vitro and in vivo delivery of atorvastatin: A comparative study of anti-inflammatory activity of atorvastatin loaded copolymeric micelles. *J. Biomater. Appl.* **32**, 1127–1138 (2018).

231. Fojtik, A., Horák, D., Piksová, K., Trung, T. Q. & Škeren, T. *Magnetic and metallic nanoparticles for biomedical application*. *NANOCON 2009 - 1st International Conference, Conference Proceedings* (Nano Con, 2009).

232. Barick, K. C. *et al.* Carboxyl decorated Fe3O4 nanoparticles for MRI diagnosis and localized hyperthermia. *J. Colloid Interface Sci.* **418**, 120–125 (2014).

233. Van Leeuwen, D. *et al.* Quenching of Magnetic Moments by Ligand-Metal Interactions in Nanosized Magnetic Metal Clusters. *Phys. Rev. Lett.* **73**, 1432–1435 (1994).

234. Atkinson, W. J., Brezovich, I. A. & Chakraborty, D. P. Usable frequencies in hyperthermia with thermal seeds. *IEEE Trans. Biomed. Eng.* **31**, 70–75 (1984).

235. Hergt, R., Dutz, S., Müller, R. & Zeisberger, M. Magnetic particle hyperthermia: nanoparticle magnetism and materials development for cancer

therapy. *J. Phys. Condens. Matter* **18**, S2919–S2934 (2006).

236. Müller, R., Hergt, R., Zeisberger, M. & Gawalek, W. Preparation of magnetic nanoparticles with large specific loss power for heating applications. *J. Magn. Magn. Mater.* **289**, 13–16 (2005).

237. Fortin, J.-P. *et al.* Size-Sorted Anionic Iron Oxide Nanomagnets as Colloidal Mediators for Magnetic Hyperthermia. *J. Am. Chem. Soc.* **129**, 2628–2635 (2007).

238. Kallumadil, M. *et al.* Suitability of commercial colloids for magnetic hyperthermia. *J. Magn. Magn. Mater.* **321**, 1509–1513 (2009).

239. Piñeiro-Redondo, Y. *et al.* The influence of colloidal parameters on the specific power absorption of PAA-coated magnetite nanoparticles. *Nanoscale Res. Lett.* **6**, 383 (2011).

240. Sun, J. F., Liu, X., Chen, Y., Zhang, Y. & Gu, N. Exploiting BSA to Inhibit the Fibrous Aggregation of Magnetic Nanoparticles under an Alternating Magnetic Field. *Int. J. Mol. Sci.* **14**, 5775–5783 (2013).

241. Branquinho, L. C. *et al.* Effect of magnetic dipolar interactions on nanoparticle heating efficiency: Implications for cancer hyperthermia. *Sci. Rep.* **3**, 2887 (2013).

242. Laurent, S. *et al.* Magnetic Iron Oxide Nanoparticles: Synthesis, Stabilization, Vectorization, Physicochemical Characterizations, and Biological Applications. *Chem. Rev.* **108**, 2064–2110 (2008).

243. Gracià, R. S., Bezlyepkina, N., Knorr, R. L., Lipowsky, R. & Dimova, R. Effect of cholesterol on the rigidity of saturated and unsaturated membranes: fluctuation and electrodeformation analysis of giant vesicles. *Soft Matter* **6**, 1472–1482 (2010).

244. Immordino, M. L., Dosio, F. & Cattel, L. Stealth liposomes: review of the basic science, rationale, and clinical applications, existing and potential. *Int. J. Nanomedicine* **1**, 297–315 (2006).

245. Akbarzadeh, A. *et al.* Liposome: classification, preparation, and applications. *Nanoscale Res. Lett.* **8**, 102 (2013).

246. Battaglia, G. & Ryan, A. J. The evolution of vesicles from bulk lamellar gels. *Nat. Mater.* **4**, 869–876 (2005).

247. Yaghmur, A. & Glatter, O. Characterization and potential applications of nanostructured aqueous dispersions. *Adv. Colloid Interface Sci.* **147**–**148**, 333–342 (2009).

248. Kékicheff, P., Grabielle-Madelmont, C. & Ollivon, M. Phase diagram of sodium dodecyl sulfate-water system: 1. A calorimetric study. *J. Colloid Interface Sci.* **131**, 112–132 (1989).

249. van Zanten, R. & Zasadzinski, J. A. Using cryo-electron microscopy to determine thermodynamic and elastic properties of membranes. *Curr. Opin. Colloid Interface Sci.* **10**, 261–268 (2005).

250. Li, Q., Yao, M., Yue, X. & Chen, X. Effects of a Spacer on the Phase Behavior of Gemini Surfactants in Ethanolammonium Nitrate. *Langmuir* **33**, 4328–4336 (2017).

251. Li, Q. *et al.* Phase behaviours of a cationic surfactant in deep eutectic solvents: from micelles to lyotropic liquid crystals. *Phys. Chem. Chem. Phys.* **20**, 12175–12181 (2018).

252. He *et al.* Comparison of Small-Angle Scattering Methods for the Structural Analysis of Octyl-β-maltopyranoside Micelles. *J. Phys. Chem. B* **106**, 7596–7604 (2002).

253. Jensen, G. V. *et al.* Direct Observation of the Formation of Surfactant Micelles under Nonisothermal Conditions by Synchrotron SAXS. *J. Am. Chem. Soc.* **135**, 7214–7222 (2013).

254. Lau, K. H. A. *et al.* Self-assembly of ultra-small micelles from amphiphilic lipopeptoids. *Chem. Commun.* **53**, 2178–2181 (2017).

255. Werzer, O., Warr, G. G. & Atkin, R. Conformation of Poly(ethylene oxide) Dissolved in Ethylammonium Nitrate. *J. Phys. Chem. B* **115**, 648–652 (2011).

256. Chen, Z., Greaves, T. L., Caruso, R. A. & Drummond, C. J. Amphiphile Micelle Structures in the Protic Ionic Liquid Ethylammonium Nitrate and Water. *J. Phys. Chem. B* **119**, 179–191 (2015).

257. Kaizu, K. & Alexandridis, P. Micellization of polyoxyethylene–polyoxypropylene block copolymers in aqueous polyol solutions. *J. Mol. Liq.* **210**, 20–28 (2015).

258. Lage, E. V *et al.* Urea induced changes in self-assembly and aggregate microstructures of amphiphilic star block copolymers with widely different hydrophobicity. *Colloids Surfaces A Physicochem. Eng. Asp.* **537**, 259–267 (2018).

259. Mattsson, J. *et al.* Soft colloids make strong glasses. *Nature* **462**, 83–86 (2009).

260. Sentjabrskaja, T. *et al.* Anomalous dynamics of intruders in a crowded environment of mobile obstacles. *Nat. Commun.* **7**, 11133 (2016).

261. Zhao, K. & Mason, T. G. Shape-designed frustration by local polymorphism in a near-equilibrium colloidal glass. *Proc. Natl. Acad. Sci.* **112**, 12063–12068 (2015).

Thesis Highlight

Name of the Student: Santosh Lala Gawali

Name of the CI: Bhabha Atomic Research Centre **Enrolment No.: CHEM01201504019**

Thesis Title: "Interfacial Modification of Nanomaterials for Biomedical Applications"

Discipline: Chemical Sciences **Sub-Area of Discipline:** Novel Drug Delivery Systems

Date of viva voce: 12/08/2020

Improving the efficacy of drugs and minimizing its side effects have been a topic of great interest in cancer therapy and this has been attempted using different approaches such as delivering drugs in a controlled manner or selective targeting to the site of action. In this respect, interfacial modification of nanoparticles plays a crucial role to achieve improved delivery of drugs, targeted delivery with minimal side effect on normal tissue or co-delivery of two or more drugs for combination therapy.

This thesis describes the construction of surface functionalized colloidal materials for cancer therapeutics. In particular,using self-assembly of organic molecules at the interface of inorganic nanoparticles, various surface functionalized superparamagnetic particles were developed for application in cancer therapy. Biocompatible additives such as sugar alcohols, vitamins and proteins were used as the passivating agents for Fe_3O_4 based magnetic nano-carriers. The uniqueness of this drug delivery carrier lies in the covalent conjugation of chemotherapeutic drug through carbamate and hydrazone linkages, resulting in slow and sustained drug release profile at tumor site. They showsubstantial cellular internalization with significant toxicity towards the cancer cells and can also be used for hyperthermia therapy of cancer.

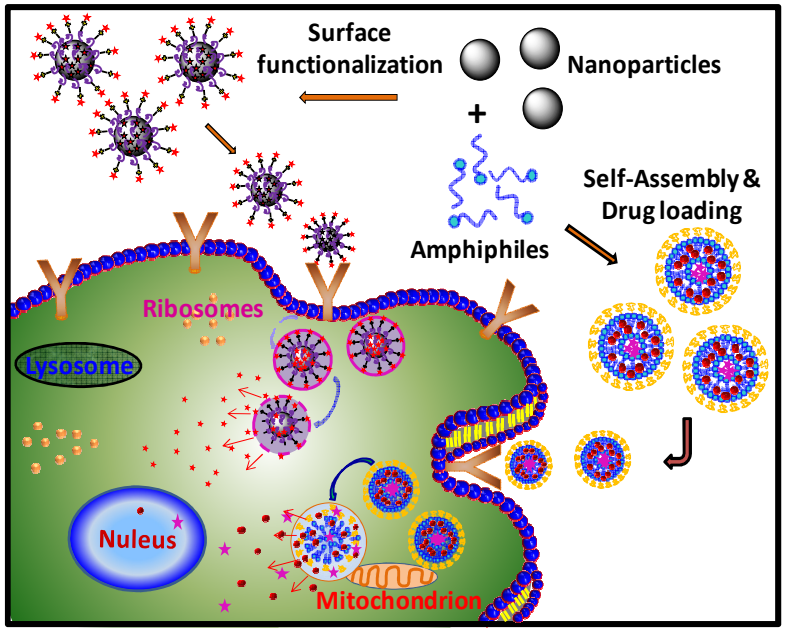

Figure 1. *Schematic of cellular internalization and drug release of functionalized nanocarriers.*

This thesis also demonstrated a method to immobilize micelles in supercooled matrices at ambient temperature. The existence of frozen micelles in a supercooled sugar-urea melt was proved by complementary tools like X-ray scattering, neutron scattering, HR-TEM, etc. Further, this matrix was employed to solubilize lipids and produce surface charge tuned liposomes for drug delivery applications. In summary, the present thesis demonstrated the ability of self-assembly approach in developing new surface functionalized materials that has both fundamental and technological relevance.